National Technical University of Athens

Department of Physics

Neutron induced reactions on Ir and Au and production of isomeric states

PhD Thesis

Antigoni Kalamara

Supervisor: Rosa Vlastou-Zanni, Professor NTUA

January 2019

Operational Programme
Human Resources Development, Education and Lifelong Learning
Co-financed by Greece and the European Union

National Technical University of Athens

Department of Physics

Neutron induced reactions on Ir and Au and production of isomeric states

PhD Thesis

Antigoni Kalamara

Examination Committee

N. Patronis, Assoc. Prof. at University of Ioannina (Adv. Committee)
A. Lagoyannis, Researcher B, NCSR "Demokritos" (Adv. Committee)
M. Kokkoris, Prof. NTUA
N. Colonna, Researcher, INFN, Bari, Italy
T.J. Mertzimekis, Assoc. Prof. at University of Athens
I. Stamatelatos, Researcher A, NCSR "Demokritos"
M. Diakaki, Researcher, CEA-Cadarache, France

Operational Programme
Human Resources Development, Education and Lifelong Learning
Co-financed by Greece and the European Union

Εθνικο Μετσοβιο Πολυτεχνειο

Τομεας Φυσικης

Αντιδράσεις νετρονίων σε Ir και Au και παραγωγή ισομερών καταστάσεων

Διδακτορικη Διατριβη

Αντιγόνη Καλαμαρά

Επιβλέπουσα: Ρόζα Βλαστού-Ζάννη, Καθηγήτρια ΕΜΠ

Ιανουάριος 2019

Επιχειρησιακό Πρόγραμμα
Ανάπτυξη Ανθρώπινου Δυναμικού,
Εκπαίδευση και Διά Βίου Μάθηση
Με τη συγχρηματοδότηση της Ελλάδας και της Ευρωπαϊκής Ένωσης

Επιχειρησιακό Πρόγραμμα
Ανάπτυξη Ανθρώπινου Δυναμικού,
Εκπαίδευση και Διά Βίου Μάθηση

Με τη συγχρηματοδότηση της Ελλάδας και της Ευρωπαϊκής Ένωσης

Το έργο συγχρηματοδοτείται από την Ελλάδα και την Ευρωπαϊκή Ένωση (Ευρωπαϊκό Κοινωνικό Ταμείο) μέσω του Επιχειρησιακού Προγράμματος «Ανάπτυξη Ανθρώπινου Δυναμικού, Εκπαίδευση και Διά Βίου Μάθηση», στο πλαίσιο της Πράξης «Πρόγραμμα Χορήγησης Υποτροφιών για Μεταπτυχιακές Σπουδές Δευτέρου Κύκλου Σπουδών» (ΜΙΣ-5003404), που υλοποιεί το Ίδρυμα Κρατικών Υποτροφιών (ΙΚΥ).

This research is co-financed by Greece and the European Union (European Social Fund-ESF) through the Operational Programme "Human Resources Development, Education and Lifelong Learning" in the context of the project "Scholarships programme for post-graduate studies - 2^{nd} Study Cycle" (MIS-5003404), implemented by the State Scholarships Foundation (IKY).

Operational Programme
Human Resources Development,
Education and Lifelong Learning

Co-financed by Greece and the European Union

All is made for humans and humans are made for all.
John Kalamaras

To my parents…

John Kalamaras along with his (two out of five) grandchildren, Antigoni and John Kalamaras (Porto Heli 1990).

John Kalamaras (1915-2005) has served as an officer in the Greek Navy and during World War II he was a Radio Operator-Maintener in Warships. In 1942, he was tortured, in his own home, in order to provide classified information and just after that, he was found moribund in the bathtub shown in the photo. He did not give in torturing and later on, he denied to accept the money award which was offered to all the War Heroes, due to the fact that he considered that he should not been paid for doing his duty.

Όλα είναι για του άνθρωπο κι ο άνθρωπος για όλα.
Ιωάννης Καλαμαράς

Στους γονείς μου...

Ιωάννης Καλαμαράς μαζί με τα (δύο από τα πέντε) εγγόνια του, Αντιγόνη και Γιάννη Καλαμαρά (Πόρτο Χέλι 1990).

Ο Ιωάννης Καλαμαράς (1915-2005) υπηρέτησε ως αξιωματικός του Πολεμικού Ναυτικού και κατά τη διάρκεια του Β΄ Παγκοσμίου Πολέμου ήταν ασυρματιστής σε πολεμικά πλοία. Το 1942, βασανίστηκε στο ίδιο του το σπίτι για να δώσει απόρρητες πληροφορίες και μετά από λίγο βρέθηκε ετοιμοθάνατος στην μπανιέρα που φαίνεται στην φωτογραφία. Δεν υπέκυψε στο βασανισμό και πολύ αργότερα αρνήθηκε να δεχθεί την χρηματική αποζημίωση που προσφέρθηκε σε όλους τους Ήρωες Πολέμου, λόγω του ότι θεωρούσε πως δεν θα έπρεπε να πληρωθεί επιπλέον, γιατί έκανε απλά το καθήκον του.

Contents

Acknowledgements

This year, another study cycle is closing for me; a rather memorable cycle of life. The latter began in 2010, when I had the chance to join the Nuclear Physics Group of the National Technical University of Athens (NTUA) and to be trained for my Diploma, for my M.Sc. and finally for my PhD thesis. All these years, I learned many interesting things, I traveled in several places, I met a lot of people, but the most important for me is that I had a reason to wake up every morning. In good and bad times, I never forgot that I had a goal to achieve and that gave me strength to carry on.

This amazing journey started the moment I knocked on Rosa's door. I'm not sure if I can find the words to express my gratefulness towards her, but I will try. It was not only the field of nuclear physics that led me to look for the door with the "Rosa Vlastou-Zanni" label, but also it was a premonition of mine that we could have a very warm collaboration. All these years, my feeling proved to be more than right! I was very lucky to work with Rosa, because she is not only an ideal supervisor, with knowledge and patience, but also a very beautiful person, with strength and understanding. She is the exact definition of a role model for both her intellectual skills and her warm soul. "Rosa I want to thank you for the trust, the support, for everything!".

Moreover, I would like to express my gratitude to the second person who gave me his full support all this time. He is known by the name "Michael Kokkoris" and he is the man who always gives good advise, finds solutions, makes everything to seem like a piece of cake and most importantly, cheers you up! He is so passionate with his work that he drags you with him. "Mike I want to thank you for believing in me, more than I did!"

Furthermore, although he lives and works far from Athens, it is impossible to have an unsuccessful collaboration with Nikolas Patronis. I met him when I was an undergraduate student and every time I see him ever since, I get to appreciate him more and more. He has a brilliant mind, he is always well organized and he is eager to help everyone who needs him. It is really nice to work and spend time with him. "Nikola I want to thank you for making me feel special!".

We had the chance to collaborate only during experimental measurements at NSCR

"Demokritos", but this experience was enough to make me feel lucky that I met him. He is Tassos Lagoyannis and he is always willing to help in any arising difficulty. Moreover, I would like to thank Sotirios Harissopulos and all the staff members of the Tandem Accelerator Laboratory of NCSR "Demokritos" for their invaluable assistance all these years. They are Michael Axiotis, Miltos Andrianis, Vasilis Andreopoulos, Manos Tsopanakis and Nikolaos Papakostopoulos. "I want to thank you all for the nice collaboration!".

Of course I could not forget to thank Michael Serris and Nicolaos Nicolis for the beautiful discussions we had, from time to time, all these years and also Costas Kalfas for always providing me the latest versions of the SPECTRW program and for helping me immediately, had a problem been occurred.

Furthermore, I could not forget to thank Ion Stamatelatos from the Institute of Nuclear and Radiological Sciences, Energy, Technology & Safety at NCSR "Demokritos" and his team, for being eager to help anytime.

Moreover, I would like to thank all the members of the NTUA Nuclear Physics Group (from 2010 to present), which helped me every time needed and namely Mary Diakaki, Andrea Tsinganis, Frosso Androulakaki, George Eleftheriou, Valentina Paneta, Filothei Pappa, Kostas Preketes, Veatriki Michalopoulou, Eleni Ntemou, Tassos Kanellakopoulos, Konstantina Krokidi, Sotiris Chasapoglou, Dimitris Sigalos and Nassos Spiliotis.

Special thanks to my colleague and partner in life Thanos Stamatopoulos. We shared the same office during our PhD studies, he always took care of me, helped me when I had a problem and encouraged me when I had bad days."I want to thank you for all the love and support that you gave me!".

Last but not least, I would like to thank my parents for always doing their best to support me and for giving me the opportunity and the luxury to make dreams and try to achieve them without having to worry how to make ends meet. In addition, I would like to thank my family and close friends for making everything better with their love and support.

This research is co-financed by Greece and the European Union (European Social Fund-ESF) through the Operational Programme "Human Resources Development, Education and Lifelong Learning" in the context of the project "Scholarships programme for post-graduate studies - 2^{nd} Study Cycle" (MIS-5003404), implemented by the State Scholarships Foundation (IKY).

Περίληψη

Η μελέτη ενεργών διατομών πυρηνικών αντιδράσεων νετρονίων παρουσιάζει ιδιαίτερο ενδιαφέρον τόσο για την Βασική Έρευνα της Πυρηνικής Φυσικής και της Αστροφυσικής, όσο και για τον τομέα των Εφαρμογών στην πυρηνική τεχνολογία, τη δοσιμετρία, την ιατρική και τη βιομηχανία. Πιο συγκεκριμένα, τα πειραματικά δεδομένα ενεργών διατομών είναι αναγκαία για τον έλεγχο των πυρηνικών μοντέλων και τον ακριβή προσδιορισμό των παραμέτρων τους. Ιδιαίτερα οι ενεργές διατομές των ισομερών καταστάσεων παρέχουν πληροφορίες για τη μελέτη του μηχανισμού αποδιέγερσης του σύνθετου πυρήνα, λόγω του ότι ο εποικισμός τους εξαρτάται άμεσα από το σπίν των ενεργειακών σταθμών που τροφοδοτούν τις ισομερείς καταστάσεις καθώς και από την κατανομή των σπίν στην περιοχή του συνεχούς. Για αυτούς τους λόγους χρειάζονται πυρηνικά δεδομένα υψηλής ακρίβειας σε μεγάλο ενεργειακό φάσμα, που σήμερα δεν υπάρχουν στις βάσεις δεδομένων.

Έτσι, σκοπός της παρούσας διατριβής είναι η πειραματική και θεωρητική μελέτη των ενεργών διατομών των αντιδράσεων ^{197}Au(n,2n)^{196}Au, ^{191}Ir(n,2n)^{190}Ir, ^{191}Ir(n,3n)^{189}Ir και ^{193}Ir(n,2n)^{192}Ir με τη μέθοδο της ενεργοποίησης, καθώς και ο ανεξάρτητος πειραματικός προσδιορισμός των ενεργών διατομών για τις δύο ισομερείς στάθμες των παραγόμενων πυρήνων: ^{197}Au(n,2n)^{196}Au^{m2} και ^{191}Ir(n,2n)^{190}Ir^{m2}.

Οι πειραματικές μετρήσεις πραγματοποιήθηκαν στο Εργαστήριο του Επιταχυντή 5.5 MV Tandem T11/25 του ΕΚΕΦΕ ¨Δημόκριτος¨ για ενέργειες δέσμης νετρονίων από 15.3 έως 20.9 MeV, με τη μέθοδο της ενεργοποίησης. Η παραγωγή των νετρονίων έγινε μέσω της αντίδρασης ^{3}H(d,n)^{4}He (D-T) και η ενεργειακή κατανομή τους έχει ήδη μελετηθεί, μέσω της μεθόδου πολλαπλής ενεργοποίησης (multiple foil activation). Η ροή των νετρονίων, η οποία είναι απαραίτητη για τον προσδιορισμό της ενεργού διατομής των έξι αντιδράσεων, υπολογίζεται μέσω των ενεργών διατομών αντιδράσεων αναφοράς: ^{27}Al(n,α)^{24}Na και ^{93}Nb(n,2n)^{92}Nb^{m}. Μετά το πέρας των ακτινοβολήσεων, η ενεργότητα των υπό μελέτη δειγμάτων και των στόχων αναφοράς μετρήθηκε μέσω φασματοσκοπίας-γ με ανιχνευτές υπερκαθαρού γερμανίου (HPGe).

Τις πειραματικές μετρήσεις συνόδευσαν Monte Carlo προσομοιώσεις των πειραματικών διατάξεων. Συνδυάστηκαν οι κώδικες NeuSDesc και MCNP5 για την προσομοίωση της διάδοσης της δέσμης των νετρονίων, ενώ MCNP5 προσομοιώσεις χρησιμοποιήθηκαν επίσης, για τον προσδιορισμό της ενδοαπορρόφησης των ακτίνων-γ μέσα στα ακτινοβοληθέντα δείγματα. Στα

πλαίσια της παρούσας διατριβής, μία πρόσφατα εφαρμοσμένη μέθοδος χρησιμοποιήθηκε για τον προσδιορισμό της ενεργού διατομής της αντίδρασης ^{193}Ir(n,2n)^{192}Ir, η οποία μολύνεται από την αντίδραση ^{191}Ir(n,γ)^{192}Ir που ενεργοποιείται από χαμηλοενεργειακά, παρασιτικά νετρόνια.

Επιπλέον, υλοποιήθηκαν θεωρητικοί υπολογισμοί των ενεργών διατομών των έξι αντιδράσεων ενδιαφέροντος, στα πλαίσια της θεωρίας Hauser-Feshcbach, χρησιμοποιώντας τις τελευταίες εκδόσεις των κωδίκων EMPIRE και TALYS. Οι θεωρητικοί υπολογισμοί πραγματοποιήθηκαν για ένα μεγάλο εύρος ενεργειών, μεταξύ 10^{-8} και 35 MeV, με σκοπό χρησιμοποιώντας τις ίδιες παραμέτρους, να γίνει η αναπαραγωγή της ενεργού διατομής για διάφορα κανάλια αντιδράσεων, όπως (n, elastic), (n,2n), (n,3n), (n,p), (n,α) και (n,total). Η αναπαραγωγή των ενεργών διατομών των αντιδράσεων που οδηγούν σε ισομερείς καταστάσεις, ^{197}Au(n,2n)^{196}Au^{m2} και ^{191}Ir(n,2n)^{190}Ir^{m2}, συνέστησε σημαντικό περιορισμό στους θεωρητικούς υπολογισμούς, λόγω της μεγάλης ευαισθησίας τους σε μικρές αλλαγές των τιμών των παραμέτρων εισόδου (input parameters).

Abstract

Neutron induced reaction cross sections are of considerable importance for technological applications such as nuclear technology, dosimetry, medicine and industry. Also, they play a significant role in Nuclear Physics and Astrophysics fundamental research. More specifically, cross section experimental data is necessary when the nuclear models need to be checked and their parameters be accurately determined. Especially, cross sections of isomeric states provide important supplementary information for the study of the compound nucleus de-excitation mechanism due to the fact that their population directly depends on the spin of the levels from which the isomeric states are fed and on the spin distribution in the continuum. For the aforementioned reasons, highly accurate nuclear data in a wide energy range, that does not exist in the databases, is needed.

Thus, the purpose of the present thesis is the experimental and theoretical study of the cross sections of the ^{197}Au(n,2n)^{196}Au, ^{191}Ir(n,2n)^{190}Ir, ^{191}Ir(n,3n)^{189}Ir and ^{193}Ir(n,2n)^{192}Ir reactions, as well as the independent experimental cross section determination for the two isomeric states of the produced nuclei, namely the: ^{197}Au(n,2n)^{196}Au^{m2} and ^{191}Ir(n,2n)^{190}Ir^{m2} ones. The measurements were performed at the 5.5 MV Tandem T11/25 Accelerator Laboratory of NCSR “Demokritos" for neutron beam energies ranging from 15.3 to 20.9 MeV using the activation technique. The neutrons were produced by means of the ^{3}H(d,n)^{4}He (D-T) reaction and their energy distribution has already been studied, implementing the multiple foil activation technique. The neutron flux, which is necessary for the determination of the cross sections of the six reactions, is determined relative to the ^{27}Al(n,α)^{24}Na and ^{93}Nb(n,2n)^{92}Nb^{m} reference reaction cross sections. After the end of the irradiations, the induced activity in the target and reference foils was measured by γ-ray spectroscopy, using High Purity Germanium detectors (HPGe).

The experimental measurements are accompanied by Monte Carlo simulations of the experimental setups. A combination of the MCNP5 and NeuSDesc codes is implemented for the simulation of the neutron beam transfer, while the MCNP5 code is also used in order to determine the γ-ray self-absorption in the irradiated samples. In the framework of the present thesis, a recently applied methodology was implemented for the determination of the ^{193}Ir(n,2n)^{192}Ir reaction cross section which is contaminated by the ^{191}Ir(n,γ)^{192}Ir reaction

which is activated by low energy parasitic neutrons.

Furthermore, the study concerning the six reactions is accompanied by theoretical cross section calculations performed in the framework of the Hauser-Feshcbach theory, using the latest versions of the EMPIRE and TALYS codes. The theoretical calculations are carried out over a wide energy range between 10^{-8} and 35 MeV in order to reproduce several experimental reaction channels using the same parametrization, such as the (n, elastic), (n,2n), (n,3n), (n,p), (n,α) and the (n,total) ones. The reproduction of the cross section for the two isomeric states of the produced nuclei in the ^{197}Au(n,2n)^{196}Au^{m2} and ^{191}Ir(n,2n)^{190}Ir^{m2} reactions constitutes a significant constraint due to their enhanced sensitivity for small changes in the input parameter values.

Εκτεταμένη Περίληψη

Εκτεταμένη Περίληψη

Εισαγωγή

Η μελέτη πυρηνικών αντιδράσεων νετρονίων παρουσιάζει ιδιαίτερο ενδιαφέρον τόσο για την Βασική Έρευνα της Πυρηνικής Φυσικής και της Αστροφυσικής, όσο και για τον τομέα των Εφαρμογών στην πυρηνική τεχνολογία, τη δοσιμετρία, την ιατρική και τη βιομηχανία [1, 2]. Από την εποχή που ανακαλύφθηκε το νετρόνιο [3], έγιναν προσπάθειες για την κατανόηση της επίδρασής του σε ιστούς, οι οποίες οδήγησαν στην χρήση των νετρονίων για την αντιμετώπιση του καρκίνου. Σε αντίθεση με τα φορτισμένα σωμάτια ή τα φωτόνια, που οδηγούν σε άμεση απελευθέρωση ηλεκτρονίων, τα νετρόνια αλληλεπιδρούν με τους πυρήνες του στόχου και παράγουν ποικίλα είδη φορτισμένων σωματίων, όπως πρωτόνα, σωμάτια α ή και βαρύτερα σωμάτια. Έτσι, η κατανόηση της αλληλεπίδρασης νετρονίου-πυρήνα είναι αναγκαία για τον ακριβή υπολογισμό της δόσης και το σχεδιασμό μίας θεραπείας [4]. Επομένως, μία από τις σημαντικές εφαρμογές της δοσιμετρίας είναι η χρήση της σε νοσοκομεία που εφαρμόζουν νετρονικές θεραπείες. Ένα άλλο θέμα είναι ότι, καθώς περνούν τα χρόνια, η ανάγκη για την διαχείριση των ραδιενεργών πυρηνικών αποβλήτων που περιέχουν πλουτώνιο και άλλες ακτινίδες, γίνεται όλο και πιο έντονη. Οι ακτινίδες εκπέμπουν νετρόνια είτε από την αυθόρμητη σχάση τους, είτε από αντιδράσεις (α,n) [5]. Ως εκ τούτου, ο ακριβής υπολογισμός των νετρονίων που εκπέμπονται από τα πυρηνικά απόβλητα είναι πολύ σημαντικός, τόσο για το περιβάλλον, όσο και για τους ανθρώπους.

Ιδιαιτέρα οι αντιδράσεις κατωφλίου (n,xn) σε ισότοπα του Au και του Ir, που μελετώνται στην παρούσα διατριβή, προτείνονται για δοσιμετρία υψηλοενεργειακών νετρονίων [6–8]. Η χρήση διαφορετικών ραδιοχημικών ανιχνευτών και διαφορετικών πυρηνικών αντιδράσεων επιτρέπει τον προσδιορισμό διαφόρων ενεργειακών περιοχών του φάσματος της ροής των νετρονίων σε νετρονικά περιβάλλοντα (π.χ αντιδραστήρες σύντηξης) και γι αυτό χρειάζονται ακριβή δεδομένα ενεργών διατομών. Η παθητική μέθοδος της δοσιμετρίας νετρονίων που λειτουργεί ενεργοποιώντας κατάλληλα υλικά (όπως Au και Ir), που συνήθως αναφέρονται ως ¨ανιχνευτές ενεργοποίησης¨ ("activation detectors"), έχει αποδειχθεί ως η πιο ευαίσθητη μεταξύ άλλων μετρητικών οργάνων. Για παράδειγμα, στον σχεδιασμό προσωπικών δοσιμέτρων, οι ¨ανιχνευτές ενεργοποίησης¨ θεωρούνται οι πιο κατάλληλοι για τη δοσιμετρία νετρονίων, λόγω του ότι έχουν μεγάλη

ευαισθησία και χαμηλώνουν το κατώτερο όριο της δόσης που μπορεί να ανιχνευθεί. Πρέπει να σημειωθεί ότι ιδιαίτερα οι ενεργές διατομές των αντιδράσεων (n,2n), αλλά και γενικότερα των (n,xn), στον Au, συμπεριλαμβάνονται στην Λίστα Πυρηνικών Δεδομένων Πρώτης Προτεραιότητας του Οργανισμού Πυρηνικής Ενέργειας (NEA Nuclear Data High Priority Request List).

Εκτός από τις παραπάνω Τεχνολογικές Εφαρμογές των αντιδράσεων (n,xn) στον Au και στο Ir, υπάρχουν και άλλα θέματα που αφορούν αυστηρά στην Βασική Έρευνα της Πυρηνικής Φυσικής. Οι παραγώμενοι πυρήνες από τις αντιδράσεις (n,2n) στον ^{197}Au και στο ^{191}Ir, έχουν ισομερείς στάθμες υψηλού σπίν. Οι ενεργές διατομές των τελευταίων, δίνουν σημαντικές πληροφορίες για τη μελέτη του μηχανισμού αποδιέγερσης του σύνθετου πυρήνα, διότι ο εποικισμός τους εξαρτάται άμεσα από το σπίν των ενεργειακών σταθμών που τροφοδοτούν τις ισομερείς καταστάσεις καθώς και από την κατανομή των σπίν στην περιοχή του συνεχούς. Επιπλέον, όσον αφορά στις ενεργές διατομές των ισομερών καταστάσεων, τα υπάχοντα πειραματικά δεδομένα είτε παρουσιάζουν σημαντικές διαφορές μεταξύ τους, είτε είναι ελλιπή. Γι αυτό το λόγο, τα νέα δεδομένα είναι απαραίτητα και ακόμα, θα δώσουν μία ώθηση στις πειραματικές εφαρμογές, εφόσον δίνουν τη δυνατότητα μίας άμεσης και λιγότερο χρονοβόρας ανάλυσης, λόγω των μικρότερων χρόνων ημιζωής (σε σύγκριση με τη βασική στάθμη) που εμπλέκονται. Εκτός αυτού, τα νέα και ακριβή πειραματικά δεδομένα είναι πολύ σημαντικά για την αξιολόγηση (evaluation) των ενεργών διατομών αυτών των αντιδράσεων, εφόσον δεν υπάρχουν αξιολογήσεις για αυτές τις αντιδράσεις. Μία ακόμα συνεισφορά της παρούσας διατριβής στην πειραματική φυσική, είναι η πρόσφατα εφαρμοσμένη μέθοδος ανάλυσης που χρησιμοποιήθηκε για τον προσδιορισμό της ενεργού διατομής της αντίδρασης ^{193}Ir(n,2n)^{192}Ir, λόγω της μόλυνσης από την αντίδραση ^{191}Ir(n,γ)^{192}Ir. Αυτή η μέθοδος, διορθώνει τον αριθμό των γεγονότων που χρησιμοποιείται για τον υπολογισμό της ενεργού διατομής, ώστε να ληφθούν υπόψη τα γεγονότα που προκύπτουν από χαμηλοενεργεικά, παρασιτικά νετρόνια και μπορεί να εφαρμοσθεί σε κάθε μέτρηση που γίνεται με μονοενεργειακή δέσμη, σε διατάξεις που δεν έχουν τη δυνατότητα της μέτρησης του χρόνου πτήσης των νετρονίων (TOF - Time of Flight).

Βιβλιογραφία και Νέες Μετρήσεις

Στα πλαίσια της παρούσας διδακτορικής διατριβής μελετήθηκαν οι εξής έξι αντιδράσεις:

- ^{197}Au(n,2n)^{196}Au
- ^{197}Au(n,2n)^{196}Au^{m2}
- ^{191}Ir(n,2n)^{190}Ir
- ^{191}Ir(n,2n)^{190}Ir^{m2}
- ^{191}Ir(n,3n)^{189}Ir
- ^{193}Ir(n,2n)^{192}Ir

και τα υπάρχοντα πειραματικά δεδομένα στην βιβλιογραφία [9], για την κάθε μία, φαίνονται στο Σχήμα 3.

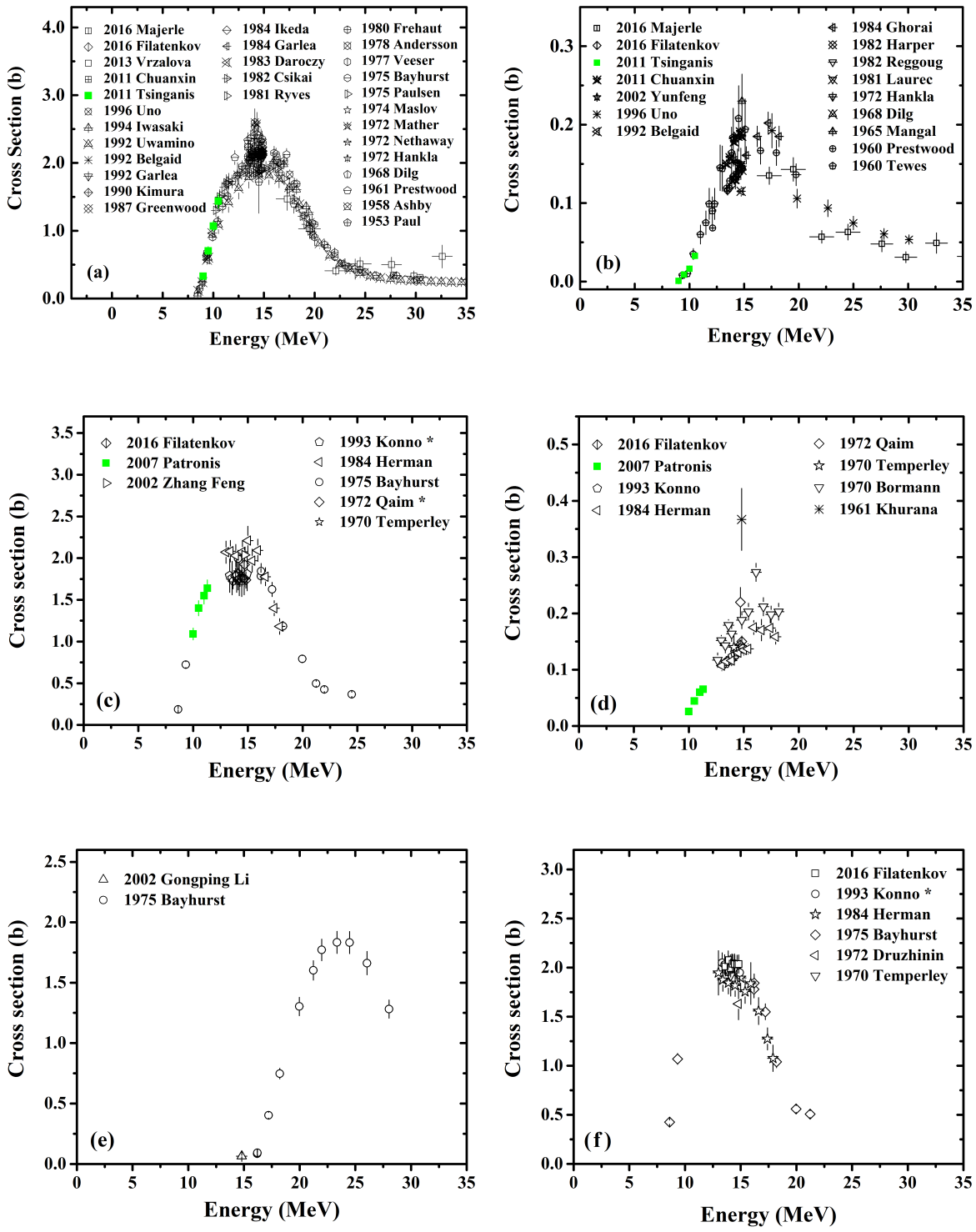

Figure 3: Πειραματικά δεδομένα που υπάρχουν στην διεθνή βιβλιογραφία [9] για τις ενεργές διατομές (cross section)των έξι αντιδράσεων που μελετώνται στα πλαίσια της παρούσας διατριβής:
(a)^{197}Au(n,2n)^{196}Au, (b)^{197}Au(n,2n)^{196}Au^{m2},
(c) ^{191}Ir(n,2n)^{190}Ir, (d) ^{191}Ir(n,2n)^{196}Ir^{m2},
(e) ^{191}Ir(n,3n)^{189}Ir and (f) ^{193}Ir(n,2n)^{192}Ir.
Τα πράσινα σημεία είναι παλιές μετρήσεις της ομάδας Πυρηνικής Φυσικής του ΕΜΠ [10], που δημοσιεύθηκαν το 2007 και 2011, από τον Ν. Πατρώνη κ. ά [11] και τον Α. Τσιγγάνη κ. ά [12], αντίστοιχα. Η παρούσα εργασία αποτελεί συνέχεια της προηγούμενης, με σκοπό να προσδιορισθούν οι ενεργές διατομές σε υψηλότερες ενέργειες νετρονίων.

Για ενέργειες πάνω από 15 MeV, μόνο πέντε σετ μετρήσεων υπάρχουν στην βιβλιογραφία [13–17] και τα αντίστοιχα δεδομένα παρουσιάζουν σημαντικές διαφορές μεταξύ τους. Για την ενεργό διατομή της αντίδρασης ^{191}Ir(n,2n)^{190}Ir, για το άθροισμα της βασικής και της πρώτης μετασταθούς στάθμης (g+m1) (βλέπε Σχήμα 3c) μόνο έξι σετ μετρήσεων υπάρχουν [11, 18–22], τα οποία έχουν λίγα πειραματικά σημεία για ενέργειες πάνω από 15 MeV. Μία ακόμα χειρότερη περίπτωση, είναι αυτή της δεύτερης μετασταθούς στάθμης του πυρήνα ^{190}Ir (Σχήμα 3d), διότι παρόλο που υπάρχουν δύο σετ δεδομένων [21, 23] στο ενεργειακό εύρος μεταξύ 15 και 18 MeV, παρουσιάζουν σημαντικές διαφορές μεταξύ τους, ενώ για μεγαλύτερες ενέργειες, δεν υπάρχουν καθόλου πειραματικά δεδομένα. Όσον αφορά στην ενεργό διατομή της αντίδρασης ^{191}Ir(n,3n)^{189}Ir (Σχήμα 3e), υπάρχουν μόνο δύο σετ δεδομένων σε όλο το ενεργειακό εύρος, με λίγα πειραματικά σημεία. Τέλος, για την αντίδραση ^{193}Ir(n,2n)^{192}Ir (Σχήμα 3f), έξι σετ δεδομένων υπάρχουν στην βιβλιογραφία [18–21, 24, 25], αλλά η πλειοψηφία των σημείων βρίσκεται στην περιοχή του πλατώ. Για ενέργειες κάτω από 13 και πάνω από 16 MeV, είναι εμφανές ότι χρειάζονται και άλλα πειραματικά σημεία.

Επομένως, ο σκοπός της παρούσας διατριβής είναι ο πειραματικός προσδιορισμός των ενεργών διατομών των έξι παραπάνω αντιδράσεων, για ενέργειες δέσμης νετρονίων μεταξύ 15 και 21 MeV. Επιπλέον, στα πλαίσια αυτής της εργασίας, αναλύθηκαν πειραματικά δεδομένα που είχαν ληφθεί το 2005 και 2006, με δέσμες νετρονίων μεταξύ 10 και 11.3 MeV, ειδικά για την ενεργό διατομή της αντίδρασης ^{193}Ir(n,2n)^{192}Ir. Τα δεδομένα που είχαν ληφθεί από τις ίδιες ακτινοβολήσεις για την αντίδραση ^{191}Ir(n,2n), δημοσιεύθηκαν το 2007 από τον Ν. Πατρώνη *κ. ά* [11].

Πειραματικό Μέρος

Οι μετρήσεις πραγματοποιήθηκαν στο Εργαστήριο του Επιταχυντή Tandem 5.5 MV του ΕΚΕΦΕ ¨Δημόκριτος¨ στην Αθήνα (βλέπε Σχήμα 4).

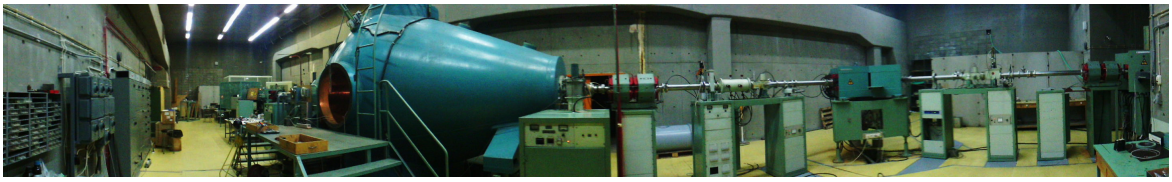

Σχήμα 4: Εργαστήριο του Επιταχυντή Tandem 5.5 MV του ΕΚΕΦΕ ¨Δημόκριτος¨ στην Αθήνα [26].

Η παραγωγή των μονοενεργειακών δεσμών νετρονίων έγινε μέσω της αντίδρασης ^{3}H(d,n)^{4}He (D-T). Η μεγάλη τιμή Q (Q = 17.59 MeV) και ο χαμηλός ατομικός αριθμός έχουν σαν αποτέλεσμα την αποδοτική παραγωγή υψηλοενεργειακών νετρονίων, για χαμηλές ενέργειες εισερχόμενων δευτερίων [27]. Η ενεργός διατομή της αντίδρασης D-T φαίνεται στο Σχήμα 5 για ένα ευρύ φάσμα ενεργειών.

Στις μετρήσεις της παρούσας διατριβής, οι ενέργειες των δευτερίων κυμάνθηκαν από 1 έως 4.3 MeV, ενώ η ενεργός διατομή της αντίδρασης για αυτές τις ενέργειες φαίνεται στο Σχήμα 6.

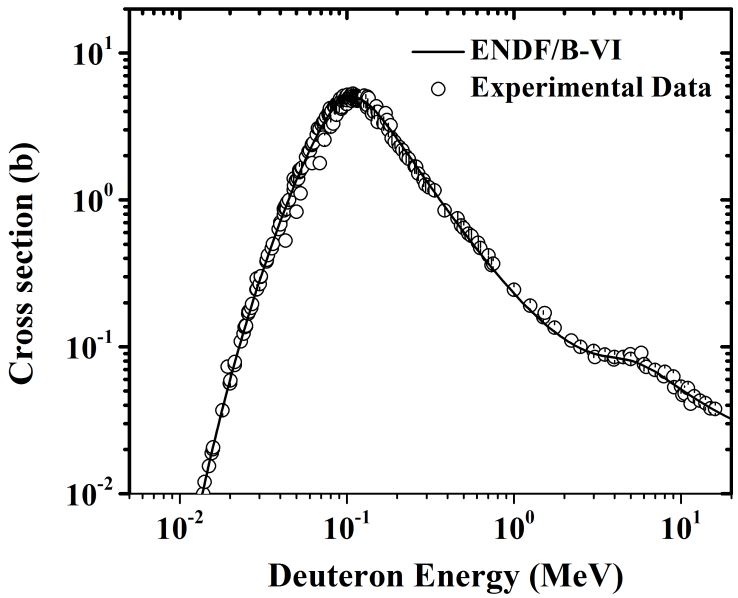

Σχήμα 5: Πειραματικά δεδομένα και η καμπύλη αξιολόγησης της βιβλιοθήκης ENDF/B-VI για την ενεργό διατομή της αντίδρασης ^{3}H(d,n)^{4}He (D-T), συναρτήσει της ενέργειας της δέσμης δευτερίων [9, 28].

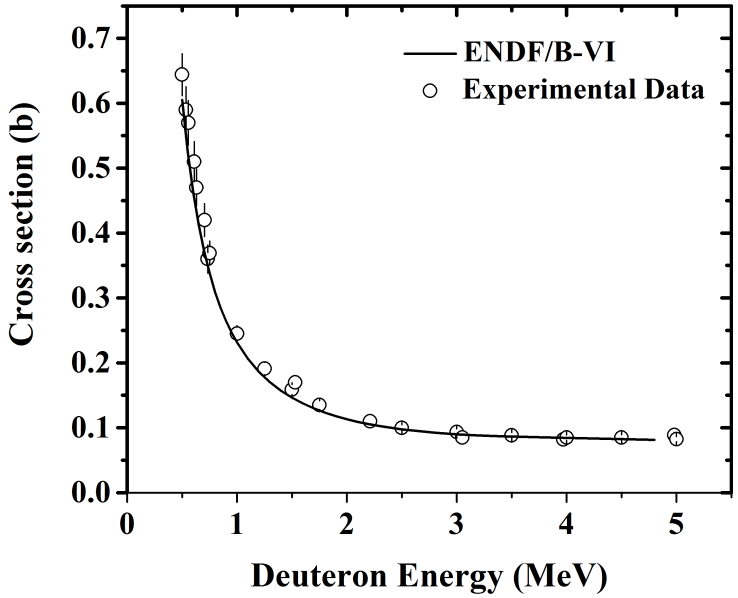

Σχήμα 6: Πειραματικά δεδομένα και η καμπύλη αξιολόγησης της βιβλιοθήκης ENDF/B-VI για την ενεργό διατομή της αντίδρασης ^{3}H(d,n)^{4}He (D-T), συναρτήσει της ενέργειας της δέσμης δευτερίων, εστιασμένα στην περιοχή ενδιαφέροντος [9, 28].

Αξίζει να αναφερθεί ότι, μονοενεργειακή πηγή νετρονίων είναι αυτή που δίνει ένα φάσμα νετρονίων που αποτελείται από μία πολύ λεπτή κορυφή, σε μία ενέργεια. Τέτοια νετρόνια μπορούν να προκύψουν μόνο από αντιδράσεις δύο-σωματίων, γι αυτό στην πράξη εκτός από τα νετρόνια της κύριας ενέργειας παράγονται επιπλέον νετρόνια "υποβάθρου" [29]. Αυτά τα νετρόνια, αναφέρονται και ως παρασιτικά, ενώ ξεκινούν από ενέργειες θερμικών νετρονίων και φθάνουν έως μερικά MeV [30].

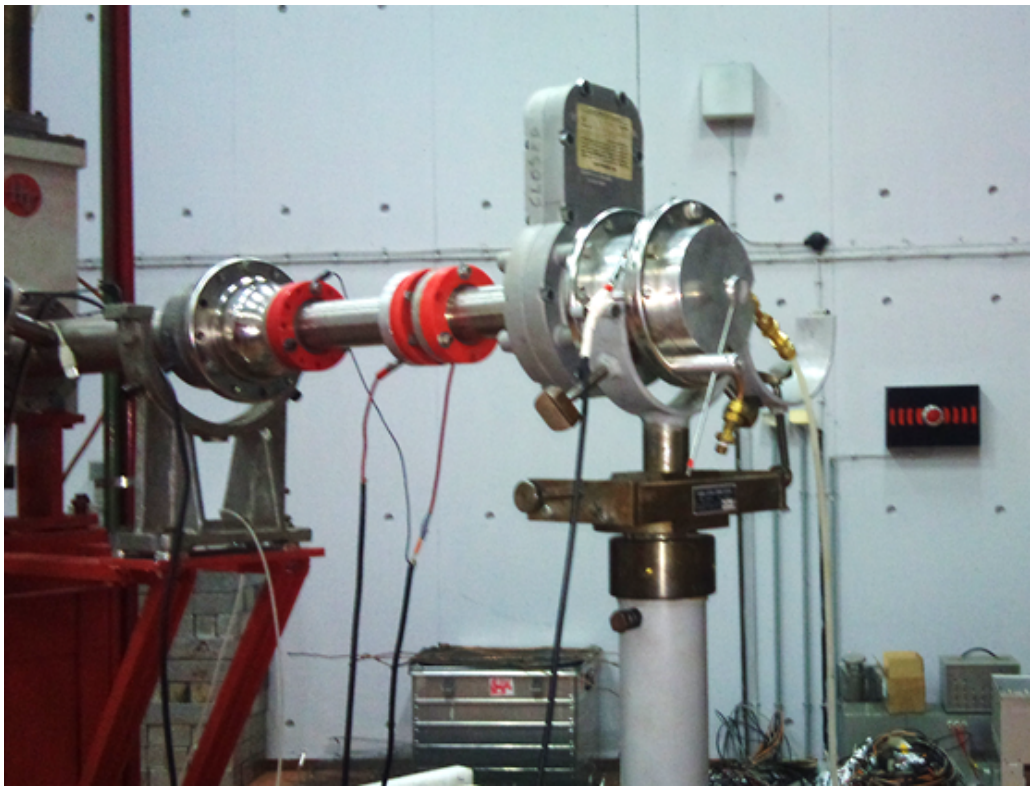

Σχήμα 7: Η άκρη της γραμμής ακτινοβόλησης στον πειραματικό χώρο του Εργαστηρίου του Επιταχυντή Tandem 5.5 MV στον ¨Δημόκριτο¨.

Οι αντιδράσεις που μπορούν να οδηγήσουν στην παραγωγή παρασιτικών νετρονίων παρουσιάζονται στον Πίνακα 1:

Πίνακας 1: Οι βασικές αντιδράσεις παραγωγής παρασιτικών νετρονίων, μαζί με την προέλευσή τους, τα ενεργειακά κατώφλια και τις αντίστοιχες τιμές Q. Όλες οι τιμές υιοθετήθηκαν από την βιβλιοθήκη NNDC από τον "υπολογιστή τιμών Q" (Q-value calculator) [31].

Προέλευση	Αντίδραση	Κατώφλι (MeV)	Κύρια Ενέργεια Δέσμης Νετρονίων (MeV) *	Τιμή Q (MeV)
Στόχος (Εμφύτευση)	^{2}H(d,n)^{4}He	0.000	-	3.269
Στόχος (Built up)	^{12}C(d,n)^{13}N	0.328	14.960	-0.281
Γραμμή Ακτινοβόλησης	^{16}O(d,n)^{17}F	1.829	17.710	-1.625
Αντιδράσεις Διάλυσης	^{3}H(d,np)^{3}H	3.710	20.304	-2.225
Αντιδράσεις Διάλυσης	^{3}H(d,2n)^{3}He	4.984	21.841	-2.988
Αντιδράσεις Διάλυσης	^{3}H(d,nd)^{2}H	10.435	-	-6.257
Αντιδράσεις Διάλυσης	^{3}H(d,2np)^{2}H	14.145	-	-8.482
Αντιδράσεις Διάλυσης	^{3}H(d,3n)2p **	17.876	-	-10.707

* Η κύρια ενέργεια της δέσμης νετρονίων υπολογίστηκε με τον κώδικα NeuSDesc, ο οποίος λειτουργεί για ενέργειες δέσμης δευτερίων μέχρι 10 MeV.
** Οι ενέργειες κατωφλίου και οι τιμές Q υιοθετήθηκαν από την αναφορά [32].

Προκειμένου να παρακολουθείται και να καταγράφεται η διακύμανση της δέσμης των νετρονίων κατά τη διάρκεια των ακτινοβολήσεων, ένας απαριθμητής τριφθοριούχου βορίου (BF_3, βλέπε Σχήμα 8) τοποθετήθηκε σε απόσταση $\sim$3 m από την πηγή των νετρονίων.

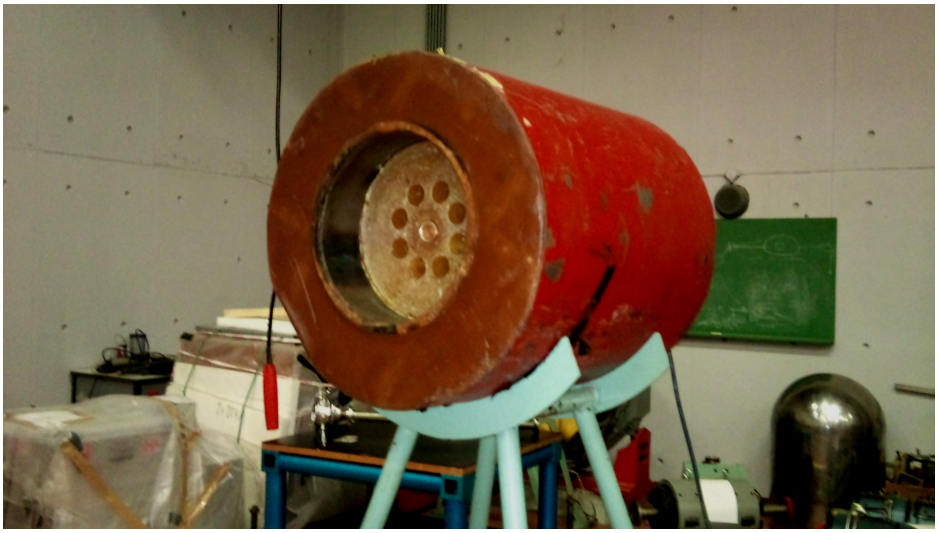

Σχήμα 8: Απαριθμητής BF_3 που χρησιμοποιείται για την παρακολούθηση των διακυμάνσεων της δέσμης των νετρονίων, κατά τη διάρκεια των ακτινοβολήσεων.

Τα δεδομένα του BF_3 αποθηκεύονταν ανά τακτά χρονικά διαστήματα μέσω ενός πολυκαναλικού αναλυτή (MCS) και αυτή η πληροφορία που αφορά στις αστάθειες της δέσμης (βλέπε Σχήμα 9), λήφθηκε υπόψη στην ανάλυση που έγινε μεταγενέστερα, ώστε να γίνει η απαραίτητη διόρθωση για τους πυρήνες που παρήχθηκαν και αποδιεγέθηκαν κατά τη διάρκεια της ακτινοβόλησης (παράγοντας f_c).

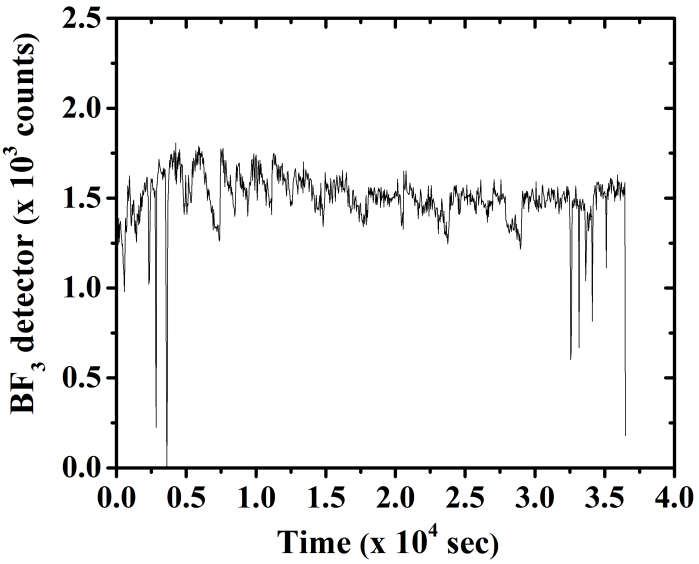

Σχήμα 9: Οι διακυμάνσεις της δέσμης νετρονίων για την ακτινοβόληση στα 20.0 MeV. Η ακτινοβόληση διήρκεσε 36480 s και τα δεδομένα του απαριθμητή BF_3 αποθηκεύοταν κάθε 40 s.

Πρέπει να σημειωθεί ότι ο απαριθμητής BF_3 λειτουργεί μόνο ως μετρητής νετρονίων και δε μπορεί να παρέχει πληροφορία, ούτε για την ενέργεια των νετρόνιων, αλλά ούτε για το πλήθος τους. Η απόλυτη ροή των υψηλοενεργειακών νετρονίων υπολογίζεται μέσω των αντιδράσεων αναφοράς, ενώ στη πλαίσια της παρούσας διατριβής αναπτύχθηκε μία μέθοδος ανάλυσης για την ποσοτική και ποιοτική εκτίμηση της χαμηλοενεργειακής περιοχής των νετρονίων.

Στα πλαίσια αυτής της εργασίας έγιναν έξι ακτινοβολήσεις στο Εργαστήριο του Επιταχυντή Tandem 5.5 MV στο ΕΚΕΦΕ "Δημόκριτος", οι λεπτομέρειες των οποίων παρουσιάζονται στον Πίνακα 2.

Πίνακας 2: Η ενέργεια δέσμης των δευτερίων (E_d), η ενέργεια δέσμης των νετρονίων (E_n), το τυπικό ρεύμα της δέσμης δευτερίων (I) και η διάρκεια της κάθε ακτινοβόλησης.

E_d (MeV)	E_n (MeV)	I (μA)	Διάρκεια (h)
1.0	15.3 ± 0.5	1.5	26.1
1.5	17.1 ± 0.3	1.0	96.1
2.0	17.9 ± 0.3	0.3	9.7
2.7	18.9 ± 0.3	0.5	27.8
3.5	20.0 ± 0.2	0.2	10.1
4.3	20.9 ± 0.2	0.3	32.4

Προκειμένου να μελετηθεί η δέσμη των νετρονίων σε διάφορες ενεργειακές περιοχές, χρησιμοποιήθηκαν αντιδράσεις με διαφορετικά ενεργειακά κατώφλια (βλέπε Πίνακα 3).

Πίνακας 3: Χρόνοι ημιζωής, ενέργειες ακτίνων-γ, εντάσεις των πιο εντατικών ακτίνων-γ και ενεργειακά κατώφλια (threshold), τόσο των μετρούμενων ατιδράσεων, όσο και των αντιδράσεων αναφοράς.

Αντίδραση	$T_{1/2}$	E_γ (keV)	I_γ (%)	$E_{threshold}$ (MeV)	$E_{threshold}$* (MeV)
Αντιδράσεις προς μέτρηση					
^{197}Au(n,2n)^{196}Au	6.183 d	355.7	87.0	8.11	8.25
^{191}Ir(n,2n)^{190}Ir	11.78 d	518.6	34.0	8.07	8.20
^{191}Ir(n,3n)^{189}Ir	13.2 d	245.1	6.0	14.48	15.00
^{193}Ir(n,2n)^{192}Ir	73.829 d	316.5	82.86	7.81	8.00
Αντιδράσεις αναφοράς					
^{27}Al(n,α)^{24}Na	14.9590 h	1368.6	100	3.25	6.75
^{93}Nb(n,2n)^{92}Nb^m	10.15 d	934.5	99.15	8.93	9.09
^{197}Au(n,γ)^{198}Au	2.6941 d	411.8	95.62	0.0	0.0
^{115}In(n,inl)^{115}In^m	4.486 h	336.2	45.9	0.0	0.5

* Αυτή η στήλη αντιστοιχεί στις ενέργειες των νετρονίων πάνω από τις οποίες οι αντιδράσεις έχουν αρκετή ενεργό διατομή ώστε να δίνουν υψηλούς ρυθμούς ενεργοποίησης (reaction rates).

Η διάταξη των στόχων που ακτινοβολήθηκαν παρουσιάζεται στο Σχήμα 10 για κάθε ακτινοβόληση. Σε κάθε περίπτωση, χρησιμοποιήθηκαν υψηλής καθαρότητας φύλλα Al, Au και Ir (πάχους 0.4-0.5 mm και διαμέτρου 13-14 mm), ενώ τα δείγματα προς μέτρηση τοποθετήθηκαν κοντά σε δείγματα αναφοράς, προκειμένου να είναι δυνατός ο ακριβής υπολογισμός της νετρονικής ροής. Αξίζει να σημειωθεί, ότι κατά τη διάρκεια των ακτινοβολήσεων που πραγματοποιήθηκαν στα πλαίσια της παρούσας διδακτορικής διατριβής, κάποια επιπλέον δείγματα τοποθετήθηκαν στις διατάξεις (όπως Am, Hf και Er, βλέπε Σχήμα 10), τα οποία είναι μέρος διαφορετικών εργασιών και δεν αφορούν την παρούσα διατριβή.

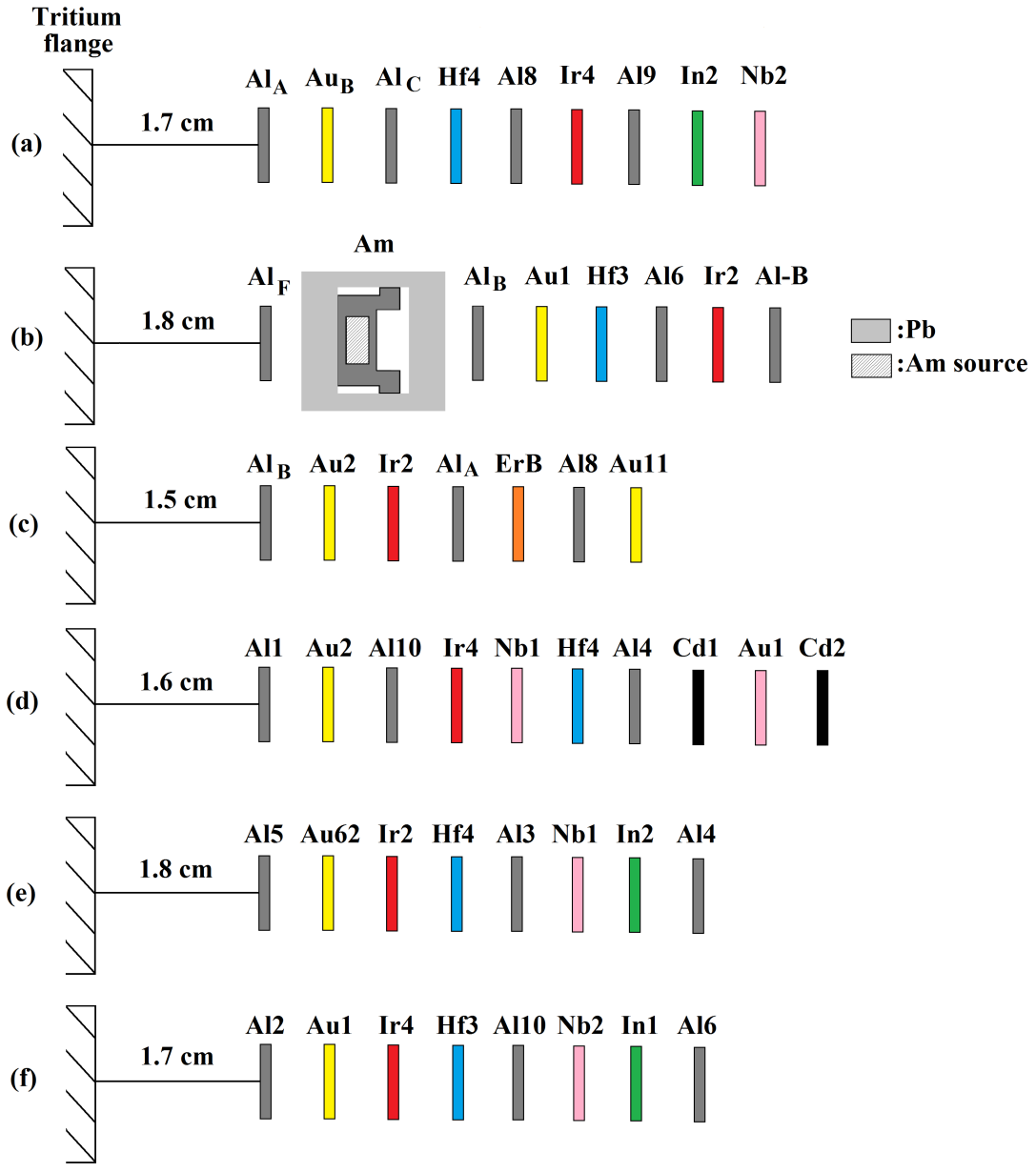

Σχήμα 10: Σχηματική αναπαράσταση των πειραματικών διατάξεων κατά τη διάρκεια των ακτινοβολήσεων σε ενέργειες δέσμης νετρονίων: (a) 15.3 MeV, (b) 17.1 MeV, (c) 17.9 MeV, (d) 18.9 MeV, (e) 20.0 MeV και (f) 20.9 MeV, αντίστοιχα.

Επιπλέον, δεν υπάρχει κενό μεταξύ των διαδοχικών στόχων, αλλά παρουσιάζονται έτσι στο Σχήμα 10 για λόγους ευκρίνειας. Ακόμα, τα δείγματα Cd1 και Cd2 στο Σχήμα 10d τοποθετήθηκαν μπροστά και πίσω από το δείγμα Au1, ως απορροφητές χαμηλοενεργειακών νετρονίων.

Όπως φαίνεται στο Σχήμα 10, όλοι οι στόχοι τοποθετήθηκαν σε απόσταση ∼2 cm από τον στόχο του TiT, ώστε να βρίσκονται εντός γωνιακού ανοίγματος ±19°, όπου η δέσμη των νετρονίων μπορεί να θεωρηθεί μονοενεργειακή (βλέπε Σχήμα 11).

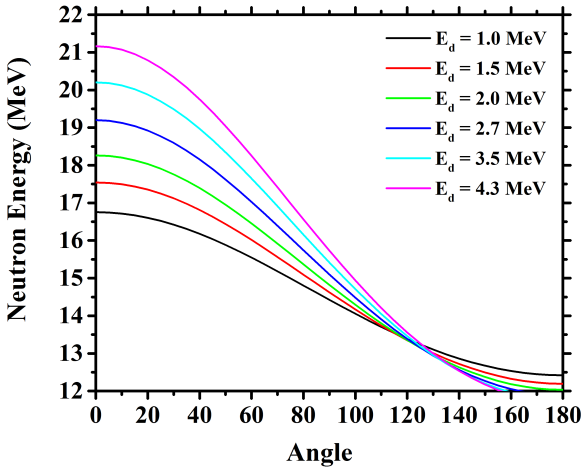

Σχήμα 11: Η ενέργεια των νετρονίων συναρτήσει της γωνίας, για κάθε ακτιβόληση, σύμφωνα με την κινηματική της αντίδρασης D-T (πρόγραμμα "Cire", Παράρτημα Δ, Αναφορά [33]).

Στα Σχήματα 12a και 12b παρουσιάζονται φωτογραφιές που λήφθηκαν πρίν την έναρξη των ακτινοβολήσεων στα 15.3 και 17.1 MeV, αντίστοιχα.

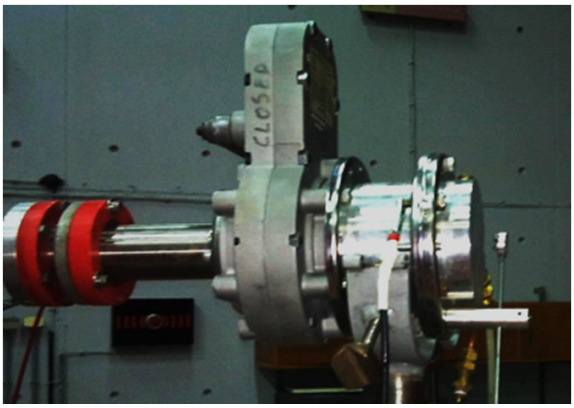

(a) Ακτινοβόληση με νετρόνια ενέργειας 15.3 MeV.

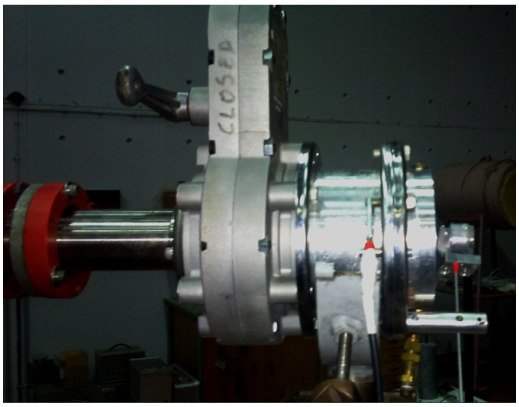

(b) Ακτινοβόληση με 17.1 MeV νετρόνια.

Σχήμα 12: Φωτογραφίες που λήφθηκαν πρίν την έναρξη των ακτινοβολήσων.

Η μελέτη της ενεργειακής κατανομής των νετρονίων πραγματοποιήθηκε με τους κώδικες NeuSDesc [34] και MCNP5 [35]. Οι ενέργειες των νετρονίων, καθώς και οι αβεβαιότητές τους, παρουσιάζονται στον Πίνακα 2 και στο Σχήμα 13, ενώ τα αποτελέσματα των προσομοιώσεων, τα οποία συμφωνούν με τις πειραματικά προσδιορισμένες ροές των νετρονίων σε κάθε ακτινοβόληση, παρουσιάζονται στο Σχήμα 14 μαζί με τις πειραματικές τιμές της ροής των νετρονίων.

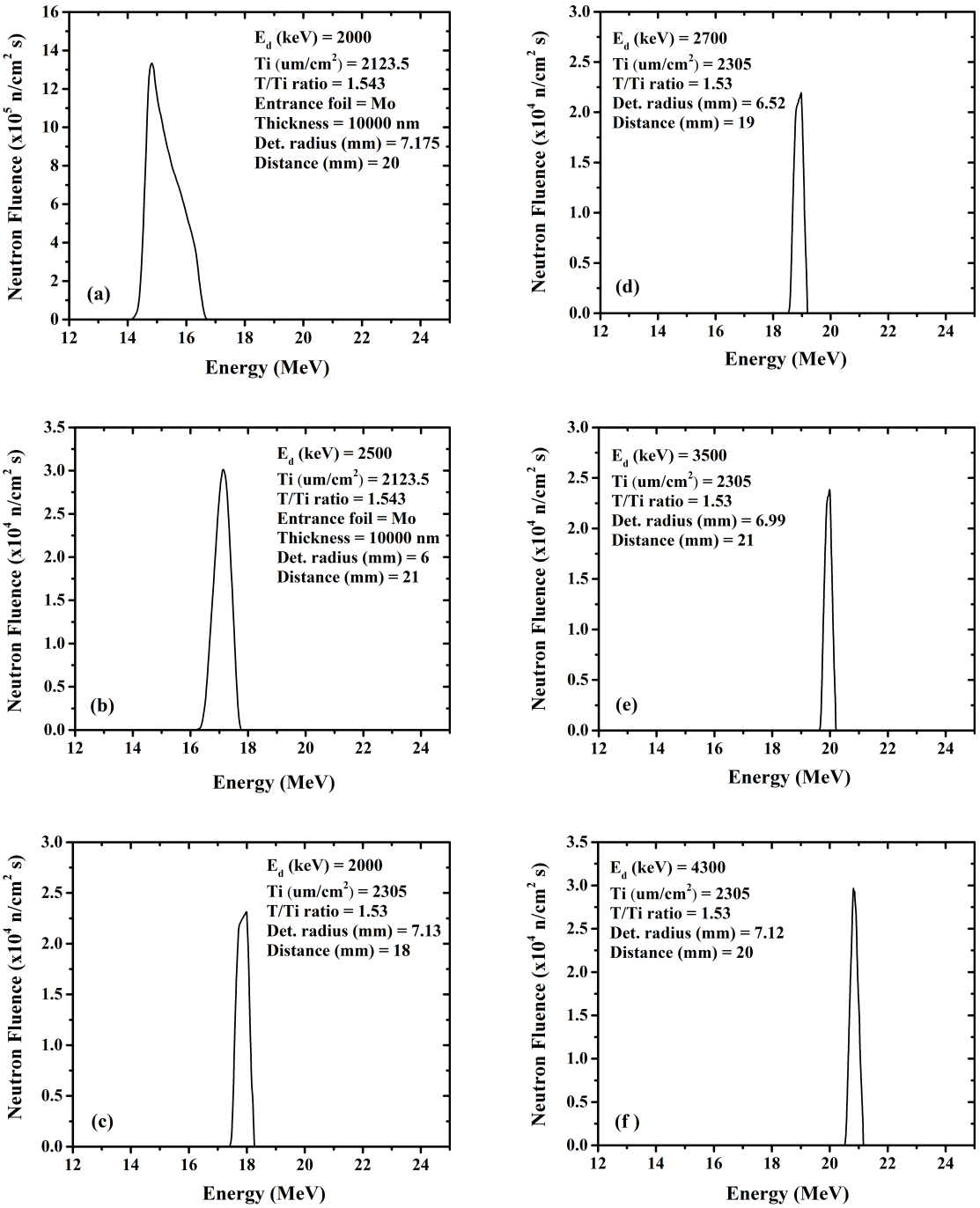

Σχήμα 13: Η κύρια κορυφή στο ενεργειακό φάσμα των νετρονίων για τις ακτινοβολήσεις σε ενέργειες (a) (15.3 ± 0.5) MeV, (b) (17.1 ± 0.3) MeV, (c) (17.9 ± 0.3) MeV, (d) (18.9 ± 0.3) MeV, (e) (20.0 ± 0.2) MeV και (f) (20.9 ± 0.2) MeV, σύμφωνα με τον κώδικα NeuSDesc [34]. Επίσης, δίνονται οι παράμετροι που εισήχθησαν στον κώδικα NeuSDesc για κάθε ακτινοβόληση, εκτός από την γωνία εκπομπής των νετρονίων (neutron emission angle) και το μέσο ρεύμα (typical deuteron beam current), τα οποία ήταν 0° και 1 μA αντίστοιχα, σε κάθε περίπτωση. Η ακτίνα του ανιχνευτή (detector radius) θεωρήθηκε ως η ακτίνα του πρώτου (σε σχέση με την πηγή των νετρονίων) στόχου Al, ενώ οι αποστάσεις από τον στόχο του τριτίου υιοθετήθηκαν από το Σχήμα 10 και αυξήθηκαν κατά 3 mm, τα οποία αντιστοιχούν στο υπόστρωμα του στόχου (Cu, πάχους 1 mm) και στο πάχος του παραθύρου της φλάντζας (Al, 2 mm).

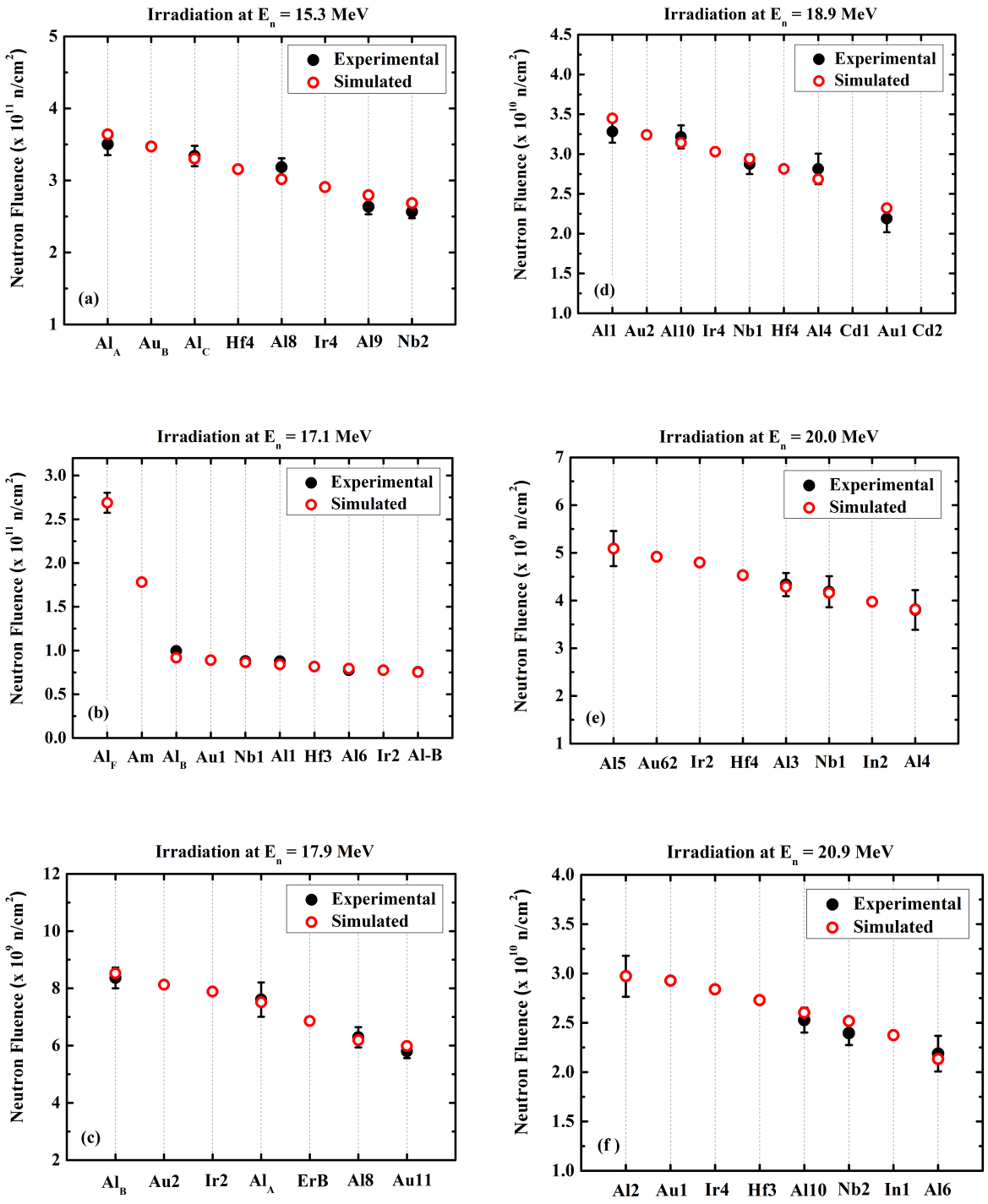

Σχήμα 14: Πειραματικά προσδιορισμένες ροές νετρονίων στους στόχους αναφοράς και ροές νετρονίων από προσομοιώσεις με τον κώδικα MCNP5 για τις ακτινοβολήσεις σε ενέργειες νετρονίων: (a) (15.3 ± 0.5) MeV, (b) (17.1 ± 0.3) MeV, (c) (17.9 ± 0.3) MeV, (d) (18.9 ± 0.3) MeV, (e) (20.0 ± 0.2) MeV και (f) (20.9 ± 0.2) MeV. Οι αποστάσεις των πρώτων στόχων Al από την φλάντζα με τον στόχο του τριτίου στις γεωμετρίες που προσομοιώθηκαν είναι: (a) 2.0 cm, (b) 2.0 cm, (c) 2.0 cm, (d) 1.9 cm, (e) 1.8 cm και (f) 1.7 cm, αντίστοιχα. Στο Σχήμα 14d, η προσομοιωμένη ροή των νετρονίων δεν υπολογίστηκε για τα φύλλα Cd1 και Cd2, εφόσον τοποθετήθηκαν στο μπροστά και πίσω μέρος του στόχου Au1 ως απορροφητές χαμηλοενεργειακών νετρονίων.

Όπως φαίνεται στο Σχήμα 14, τα αποτελέσματα των προσομοιώσεων έχουν πολύ καλή συμφωνία με τα πειραματικά για όλες τις ακτινοβολήσεις.

Μετά το πέρας των ακτινοβολήσεων, η ενεργότητα των υπό μελέτη στόχων (Au, Ir) και των στόχων αναφοράς, μετρήθηκε με ανιχνευτές γερμανίου υψηλής καθαρότητας (HPGe) σχετικής ανιχνευτικής απόδοσης 100, 80, 56 και 16%.

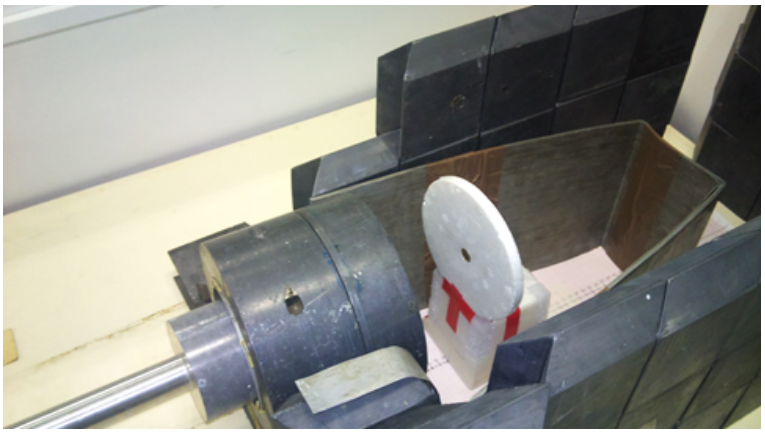

Σχήμα 15: Ο ανιχνευτής γερμανίου με 100% σχετική ανιχνευτική απόδοση, ο οποίος είχε κατάλληλη θωράκιση, ώστε να μειωθεί η συνεισφορά της ακτινοβολίας υποβάθρου στις μετρήσεις.

Οι μετρήσεις της ενεργότητας όλων των στόχων έγιναν σε απόσταση 10 cm από το παράθυρο του ανιχνευτή, ώστε να μην χρειάζονται διορθώσεις για φαινόμενα συσσώρευσης (pile-up) ή άθροισης (summing) παλμών. Στην ίδια απόσταση τοποθετήθηκε μία σημειακή πηγή ^{152}Eu, για τον υπολογισμό της απόλυτης απόδοσης του κάθε ανιχνευτή. Στο Σχήμα 16 παρουσιάζεται ένα τυπικό διάγραμμα απόλυτης απόδοσης ανιχνευτή, που αντιστοιχεί στον ανιχνευτή του Σχήματος 15.

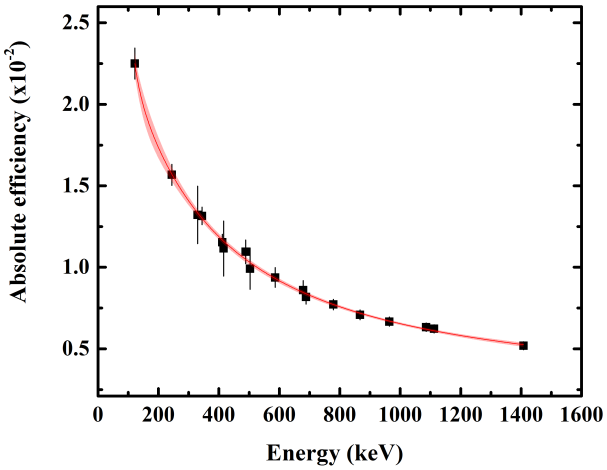

Σχήμα 16: Η απόλυτη απόδοση συναρτήσει της ενέργειας των ακτίνων-γ, για τον ανιχνευτή σχετικής ανιχνευτικής απόδοσης 100% του Σχήματος 15. Η κόκκινη γραμμοσκιασμένη περιοχή δηλώνει τα διαστήματα εμπιστοσύνης (condidence bands) εντός 95%.

Τυπικά φάσματα ακτίνων-γ των στόχων Au και Ir, τα οποία λήφθηκαν μετά το πέρας των ακτινοβολήσεων με ανιχνευτές γερμανίου (HPGe), παρουσιάζονται στο Σχήμα 17.

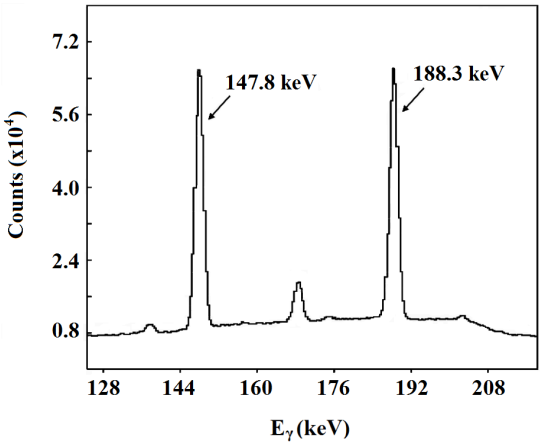

(a) Ο χρόνος της μέτρησης ήταν 16 h.

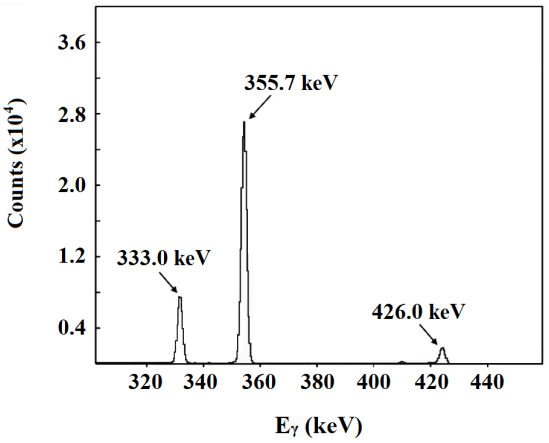

(b) Ο χρόνος της μέτρησης ήταν 19 h.

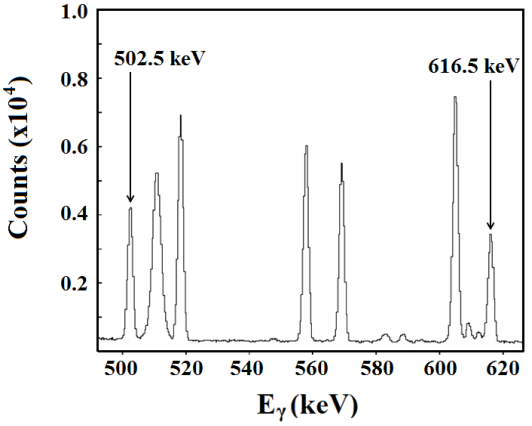

(c) Ο χρόνος της μέτρησης ήταν 10 h.

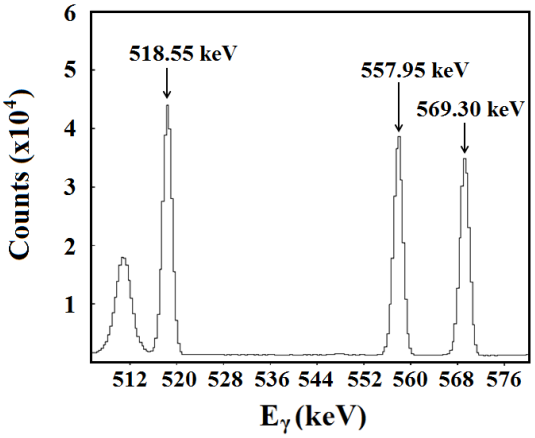

(d) Ο χρόνος της μέτρησης ήταν 72 h.

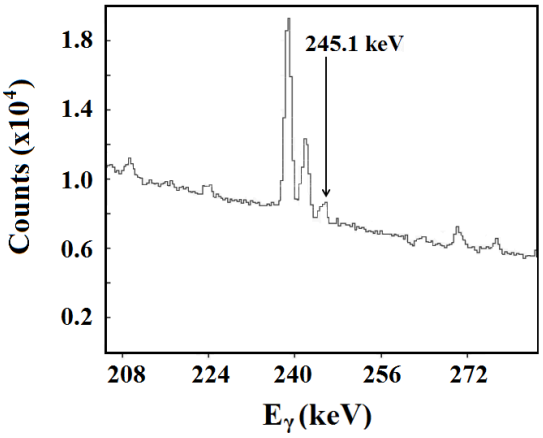

(e) Ο χρόνος της μέτρησης ήταν 56 h.

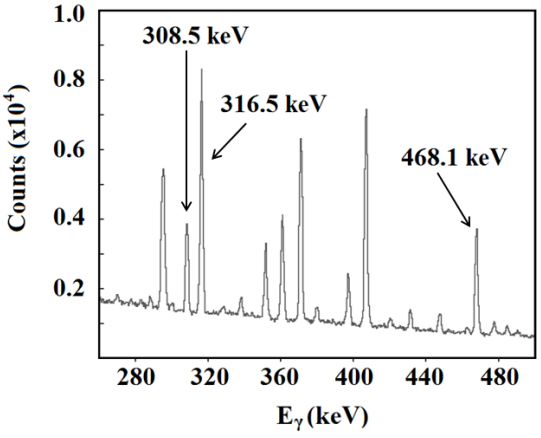

(f) Ο χρόνος της μέτρησης ήταν 54 h.

Σχήμα 17: Φάσματα ακτίνων-γ που λήφθηκαν μετά το τέλος των ακτινοβολήσεων στα: (a) 15.3 MeV, (b) 15.3 MeV, (c) 15.3 MeV, (d) 15.3 MeV, (e) 20.9 MeV και (f) 17.1 MeV, για τον προσδιορισμό των ενεργών διατομών των αντιδράσεων:
(a) ^{197}Au(n,2n)^{196}Au^{m2}, (b) ^{197}Au(n,2n)^{196}Au$^{g+m1+m2}$,
(c) ^{191}Ir(n,2n)^{190}Ir^{m2}, (d) ^{191}Ir(n,2n)^{190}Ir$^{g+m1+0.086\,m2}$,
(e) ^{191}Ir(n,3n)^{189}Ir και (f) ^{193}Ir(n,2n)^{192}Ir.

Ανάλυση Δεδομένων

Οι πειραματικές ενεργές διατομές των έξι υπό μελέτη αντιδράσεων υπολογίσθηκαν από τη σχέση:

$$\sigma_{measured} = \sigma_{reference} \cdot \frac{N_{\gamma_{measured}}}{N_{\gamma_{reference}}} \cdot \frac{(\varepsilon_\gamma \cdot I_\gamma \cdot F \cdot D \cdot f_c \cdot N_\tau)_{\,reference}}{(\varepsilon_\gamma \cdot I_\gamma \cdot F \cdot D \cdot f_c \cdot N_\tau)_{\,measured}} \cdot C_\Phi \tag{1}$$

όπου N_γ είναι το ολοκλήρωμα της κορυφής των ακτίνων-γ στο φάσμα που λήφθηκε με τον ανιχνευτή γερμανίου (HPGe), ε_γ είναι η απόλυτη απόδοση του ανιχνευτή στην αντίστοιχη ενέργεια, I_γ είναι η ένταση της ακτίνας-γ και F είναι ένας διορθωτικός παράγοντας που υπολογίζεται μέσω προσομοιώσεων Monte Carlo (MCNP5 [36]) για την ενδοαπορρόφηση των ακτίνων-γ στο δείγμα. Επιπλέον, χρησιμοποιείται ένας διορθωτικός παράγοντας για τον τρόπο λήψης των δεδομένων:

$$D = e^{-\lambda \cdot t_1} - e^{-\lambda \cdot t_2} \tag{2}$$

όπου t_1 και t_2 είναι τα χρονικά διαστήματα που μεσολαβούν από το τέλος της ακτινοβόλησης μέχρι την αρχή και το τέλος της μέτρησης με τον ανιχνευτή γερμανίου, αντίστοιχα και λ είναι η σταθερά αποδιέγερσης του παραγώμενου πυρήνα. Οι διακυμάνσεις της δέσμης και οι παραγώμενοι πυρήνες που διασπώνται κατά την διάρκεια της ακτινοβόλησης λαμβάνονται υπόψη μέσω του παράγοντα f_c:

$$f_c = \frac{\int_0^{t_B} e^{\lambda t}\, f(t)\, dt}{\int_0^{t_B} f(t)\, dt}\, e^{-\lambda\, t_B} \tag{3}$$

όπου f(t) είναι η ροή των νετρονίων σε τυχαίες μονάδες, όπως δίνεται από τον ανιχνευτή BF_3, ανά τακτά χρονικά διαστήματα dt και t_B είναι η διάρκεια της ακτινοβόλησης. Ακόμα, ο αριθμός των πυρήνων του στόχου, N_τ, υπολογίστηκε μέσω της διορθωμένης μάζας (m) για την αφθονία του κάθε ισοτόπου ($Abund$), τον μαζικό αριθμό A και τον αριθμό του Avogadro μέσω της σχέσης:

$$N_\tau = N_A\, \frac{m \cdot Abund}{A} \tag{4}$$

Ο παράγοντας C_Φ, που αντιστοιχεί στον λόγο της ροής των νετρονίων στον στόχο αναφοράς προς τη ροή στον υπό μελέτη στόχο:

$$C_\Phi = \frac{\Phi_{reference}}{\Phi_{measured}} \tag{5}$$

υπολογίστηκε με καλή συμφωνία μέσω πειραματικών αποτελεσμάτων και προσομοιώσεων Monte Carlo, με χρήση του κώδικα MCNP5. Επιπλέον, οι τιμές της ενεργού διατομής της αντίδρασης αναφοράς ^{27}Al(n,α)^{24}Na ($\sigma_{reference}$) υιοθετήθηκαν από την βιβλιοθήκη δεδομένων IRDFF 1.05 [28]. Τα δεδομένα που χρησιμοποιήθηκαν για τις αποδιεγέρσεις των παραγώμενων πυρήνων, τόσο για τις υπό μελέτη αντιδράσεις, όσο και για τις αντιδράσεις αναφοράς, συνοψίζονται στον Πίνακα 4.

Πίνακας 4: Δεδομένα που χρησιμοποιήθηκαν για τις αποδιεγέρσεις των παραγώμενων πυρήνων.

Αντίδραση	$T_{1/2}$	Eγ (keV)	Iγ (%)	Αναφορά
^{197}Au(n,2n)^{196}Au$^{g+m1+m2}$	6.183 d	355.7	87.0	[37]
		333.0	22.9	[37]
		426.0	7.0	[37]
^{197}Au(n,2n)^{196}Au^{m2}	9.6 h	147.8	43.0	[37]
		188.3	37.4 & 34.0	[37] & [38]
^{191}Ir(n,2n)^{190}Ir$^{g+m1+0.086\,m2}$	11.78 d	518.6	34.0	[39]
		558.0	30.1	[39]
		569.3	28.5	[39]
^{191}Ir(n,2n)^{190}Ir^{m2}	3.087 h	616.5	90.14	[39]
		502.5	89.38	[39]
^{191}Ir(n,3n)^{189}Ir	13.2 d	245.1	6.0	[39]
^{193}Ir(n,2n)^{192}Ir	73.829 d	316.5	82.86	[39]
		468.1	47.84	[39]
		308.5	29.7	[39]
^{27}Al(n,α)^{24}Na	14.959 h	1368.6	100	[37]

Μία σύνοψη των αβεβαιοτήτων όλων των βασικών μεγεθών που χρησιμοποιούνται για τον προσδιορισμό της ενεργού διατομής δίνεται στον Πίνακα 5.

Πίνακας 5: Σύνοψη αβεβαιοτήτων.

Μέγεθος	Αβεβαιότητα (%)
Ενέργεια νετρονίων	1-3
Ροή νετρονίων	4-7
Στατιστική στους στόχους αναφοράς	1-2
Στατιστική στους υπό μελέτη στόχους	1-29
Απόδοση του ανιχνευτή	2-11
Ενεργός διατομή αντίδρασης αναφοράς	3
Υπό μελέτη ενεργός διατομή (Συνολική αβεβαιότητα)	5-30

Όπως φαίνεται στον Πίνακα 5, η κυρίαρχη αβεβαιότητα είναι αυτή της στατιστικής των υπό μελέτη στόχων, η οποία οφείλεται είτε σε χαμηλές τιμές της ενεργού διατομής (στην περίπτωση της αντίδρασης ^{191}Ir(n,3n)), είτε σε σημαντική επιμόλυνση από άλλη αντίδραση (στην περίπτω-

ση της αντίδρασης ^{193}Ir(n,2n)). Επιπλέον, η αβεβαιότητα της απόδοσης του ανιχνευτή είναι σημαντική σε κάποιες περιπτώσεις, εφόσον ποικίλει από 2 έως 11%, ανάλογα με την προσαρμογή (fit) των πειραματικών δεδομένων της απόλυτης απόδοσης του ανιχνευτή με συνάρτηση της IAEA (βλέπε Appendix C) και την ενεργειακή περιοχή. Αυτές οι αβεβαιότητες εκτιμήθηκαν μέσω ζωνών εμπιστοσύνης σε επίπεδο 95%. Επιπλέον, η αβεβαιότητα της ροής των νετρονίων συμπεριλαμβάνεται στην συνολική αβεβαιότητα και είναι εξίσου σημαντική, αφού αποτελεί το 4-7%. Η αβεβαιότητα των ενεργών διατομών των αντιδράσεων αναφοράς θεωρήθηκε 3% σε κάθε περίπτωση, ενώ αυτή της στατιστικής των στόχων αναφοράς μπορεί να θεωρηθεί αμελητέα (1-2%).

Συγκεκριμένα για την ανάλυση της ενεργού διατομής της αντίδρασης ^{193}Ir(n,2n)^{192}Ir, μία επιπλέον διόρθωση εφαρμόσθηκε λόγω της επιμόλυνσης από την αντίδραση ^{191}Ir(n,γ)^{192}Ir, η οποία ενεργοποιείται από χαμηλοενεργειακά, παρασιτικά νετρόνια. Μία μέθοδος ανάλυσης εφαρμόσθηκε πρόσφατα, η οποία βασίζεται σε ενημερωμένες βιβλιοθήκες ενεργών διατομών και σε προσομοιώσεις με τον κώδικα MCNP5. Η μέθοδος αυτή μπορεί να παρουσιαστεί σε τρία βήματα:

1. Προμοιώσεις με MCNP5
   Πραγματοποιούνται προσομοιώσεις της πειραματικής διάταξης ακτινοβόλησης, στις οποίες η γεωμετρία όλης της πειραματικής περιοχής περιγράφεται με λεπτομέρεια (βλέπε Σχήμα 18).

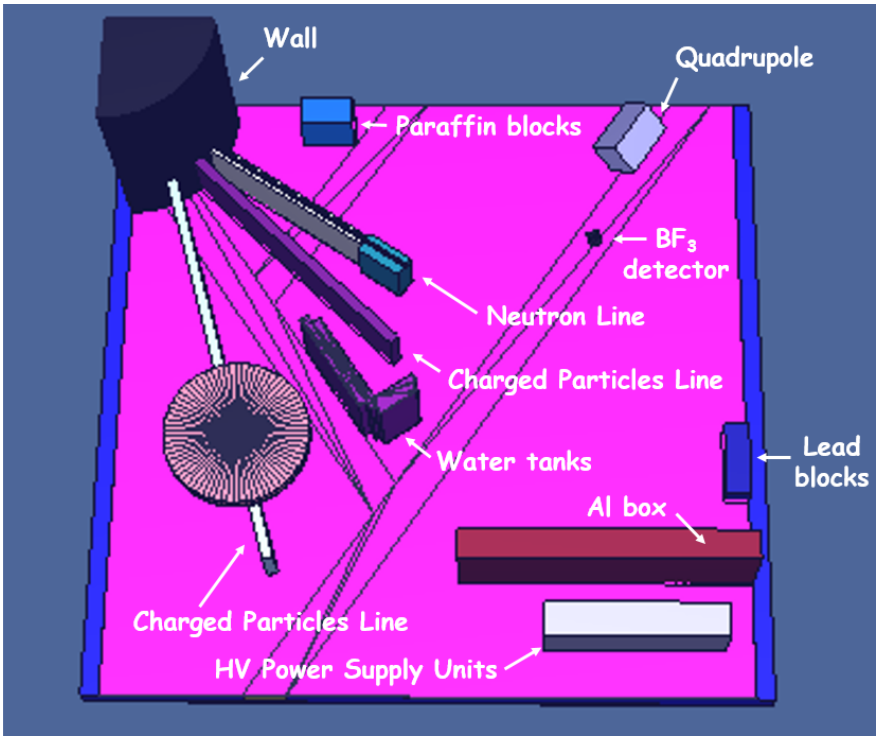

Σχήμα 18: Σχήμα 3-διαστάσεων που αναπαριστά την κάτοψη της πειραματικής περιοχής στο εργαστήριο του επιταχυντή Tandem στο ΕΚΕΦΕ ¨Δημόκριτος¨, όπως περιγράφεται με τον κώδικα MCNP5.

Αυτές οι προσομοιώσεις πραγματοποιούνται για καλή στατιστική, 10^9 προσομοιωμένα

σωματίδια (η εκτέλεση διαρκεί $\sim$ 11 d για κάθε ακτινοβόληση) και με χαμηλό ενεργειακό όριο διακοπής της παρακολούθησης των νετρονίων (10^{-11} MeV).

2. Επιβεβαίωση μέσω της αντίδρασης ^{197}Au(n,γ)
   Το αποτέλεσμα της προσομοίωσης φαίνεται στο Σχήμα 19.

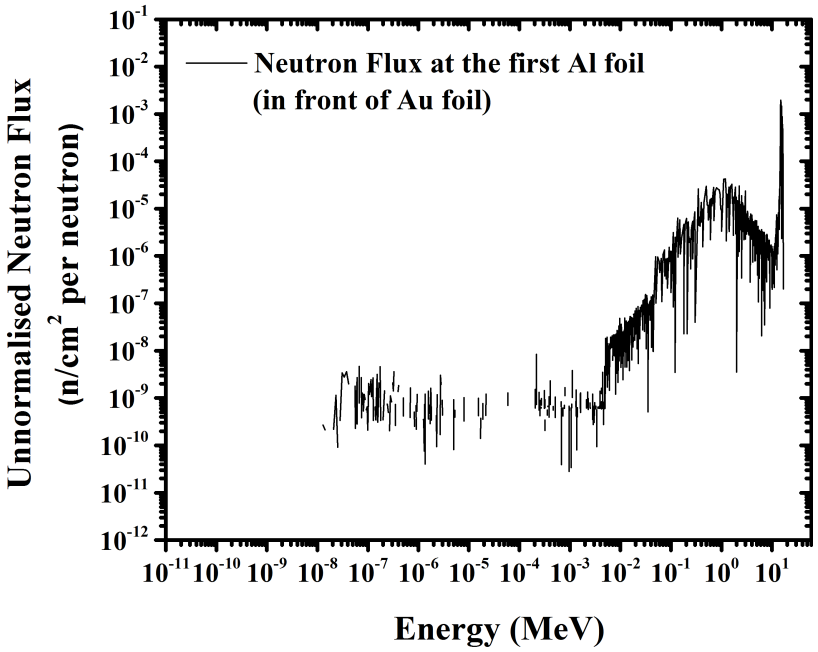

Σχήμα 19: Ενεργειακή κατανομή της ροής των νετρονίων σύμφωνα με την προσομοίωση με τον κώδικα MCNP5, για την ακτινοβόληση στα 15.3 MeV.

Αυτή η κατανομή (Σχήμα 19) κανονικοποιείται έτσι ώστε να συμφωνεί με το πείραμα και αυτό επιτυγχάνεται μέσω της αντίδρασης ^{197}Au(n,γ)^{198}Au. Η σχέση που χρησιμοποιείται για την κανονικοποίηση είναι η ακόλουθη:

$$\phi_{normalized}(E_i)\left(\frac{n}{cm^2\,s}\right) = \frac{\phi^{Au}_{experimental}\left(\frac{n}{cm^2\,s}\right)\cdot\phi_{mcnp}(E_i)}{\sum_{E_i=8MeV}^{30}\phi_{mcnp}(E_i)}\cdot Scale\,Factor \qquad (6)$$

όπου $\phi^{Au}_{experimental}\left(\frac{n}{cm^2\,s}\right)$ είναι η πειραματικά προσδιορισμένη ροή των νετρονίων που προσέπεσαν στον στόχο του Au κατά τη διάρκεια της ακτινοβόλησης και $\phi_{mcnp}(E_i)$ είναι η μη κανονικοποιημένη (unnormalized) ροή των νετρονίων, όπως δίνεται από τον κώδικα MCNP5. Η αρχική τιμή του $Scale\,Factor$ είναι 1 και υπάρχει στην Εξ. 6 για να διορθώσει για παρασιτικά νετρόνια που δεν έχουν συμπεριληφθεί στην προσομοίωση, όπως νετρόνια από αντιδράσεις (d,n) στα υλικά της γραμμής ακτινοβόλησης και νετρόνια από την αντίδραση D(d,n) που πραγματοποιείται λόγω δευτερίων που έχουν εμφυτευθεί στον στόχο TiT.

Χρησιμοποιώντας το $\phi_{normalized}(E_i)$, ο αναμενόμενος ρυθμός ενεργοποίησης (expected reaction rate, RR) υπολογίζεται από την σχέση:

$$RR_{expected} = \sum_{E_i}\sigma(E_i)\cdot\phi_{normalized}(E_i) \qquad (7)$$

όπου $\sigma\left(E_i\right)$ είναι η ενεργός διατομή της αντίδρασης ^{197}Au(n,γ)^{198}Au σε κάθε ενεργειακό διάστημα (βλέπε Σχήμα 20). Πρέπει να σημειωθεί ότι τα ενεργειακά διαστήματα έχουν υιοθετηθεί από την βιβλιοθήκη ENDF/B-VII.1 [28].

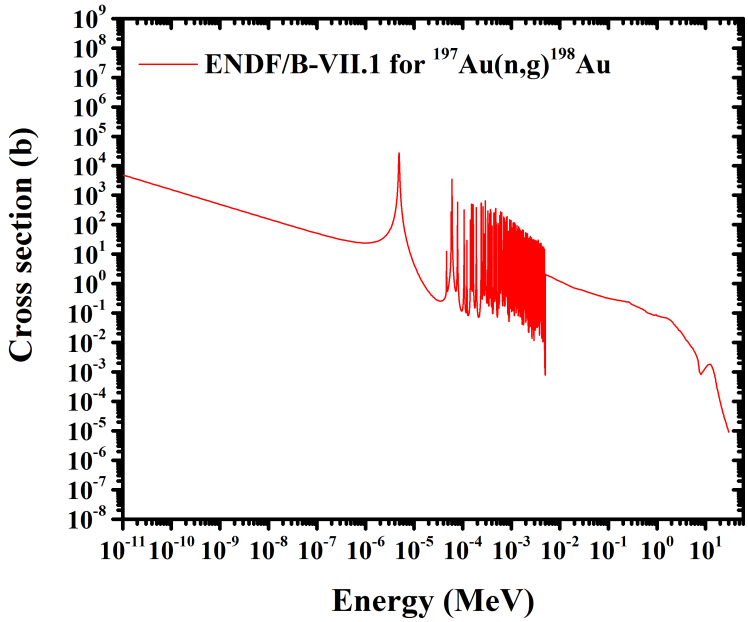

Figure 20: Ενεργός διατομή της αντίδρασης ^{197}Au(n,γ)^{198}Au συναρτήσει της ενέργειας των νετρονίων. Η καμπύλη αξιολόγησης αντιστοιχεί στην βιβλιοθήκη ENDF/B.VII.1 [28].

Επιπλέον, ο ρυθμός ενεργοποίησης μπορεί να προσδιορισθεί πειραματικά (experimental reaction rate) μέσω της ακόλουθης σχέσης:

$$RR_{experimental} = \frac{\lambda \cdot N_p}{N_\tau \left(1 - e^{\lambda t_B}\right)} \tag{8}$$

όπου N_p είναι ο αριθμός των πυρήνων που παρήχθησαν κατά τη διάρκεια της ακτινοβόλησης και δίνεται από την σχέση:

$$N_p = \frac{N_\gamma}{\varepsilon_\gamma \cdot I \cdot F \cdot D} \tag{9}$$

Συνδυάζοντας τις εξισώσεις 8 και 9, το ολοκλήρωμα του αριθμού των ακτίνων-γ, N_γ, δίνεται ως εξής:

$$N_\gamma = \frac{\varepsilon_\gamma \cdot I \cdot F \cdot D \cdot N_\tau \left(1 - e^{\lambda t_B}\right) \cdot RR_{experimental}}{\lambda} \tag{10}$$

ενώ ο αναμενόμενος αριθμός ακτίνων-γ, $N_{\gamma\, expected}$, χρησιμοποιώντας την προσομοιωμένη ροή των νετρονίων είναι:

$$N_{\gamma\, expected} = \frac{\varepsilon_\gamma \cdot I \cdot F \cdot D \cdot N_\tau \left(1 - e^{\lambda t_B}\right) \cdot RR_{expected}}{\lambda} \tag{11}$$

Όλα τα μεγέθη στην Εξ. 11 αντικαθιστώνται με αυτά που αντιστοιχούν στην ανάλυση της ακτίνας-γ στα 411.8 keV, που εκπέμπεται κατά την αποδιέγερση του πυρήνα ^{198}Au,

η τελική τιμή του $Scale\,Factor$ επιλέγεται έτσι ώστε το ολοκλήρωμα της ακτίνας-γ στα 411.8 keV να αναπαράγεται εντός του πειραματικού σφάλματος. Έτσι, ο τελικός σκοπός είναι να συμφωνεί το $N_{\gamma\,expected}$ με το $N_{\gamma\,experimental}$ για την ακτίνα-γ στα 411.8 keV.

Η πειραματικά προσδιορισμένη τιμή του $Scale\,Factor$ χρησιμοποιείται στο επόμενο βήμα, ώστε να γίνουν οι απαραίτητες διορθώσεις για τον υπολογισμό της ενεργού διατομής της αντίδρασης ^{193}Ir(n,2n)^{192}Ir, η οποία μολύνεται από την ^{191}Ir(n,γ)^{192}Ir.

3. Συνεισφορά της αντίδρασης ^{191}Ir(n,γ)
Μία κανονικοποίηση ανάλογη με αυτήν που εφαρμόσθηκε στο δεύτερο βήμα, εφαρμόζεται προκειμένου να προσδιορισθεί η ροή των νετρονίων στον στόχο του Ir, σύμφωνα με την σχέση:

$$\phi_{\,normalized}\left(E_i\right)\left(\frac{n}{cm^2\,s}\right)=\frac{\phi^{\,Ir}_{\,experimental}\left(\frac{n}{cm^2\,s}\right)\cdot\phi_{\,mcnp}\left(E_i\right)}{\sum_{E_i=8MeV}^{30}\phi_{\,mcnp}\left(E_i\right)}\cdot Scale\,Factor \tag{12}$$

όπου $\phi^{\,Ir}_{\,experimental}\left(\frac{n}{cm^2\,s}\right)$ είναι η πειραματικά προσδιορισμένη ροή των νετρονίων που προσέπεσαν στον στόχο του Ir κατά τη διάρκεια της ακτινοβόλησης, $\phi_{\,mcnp}\left(E_i\right)$ είναι η μη κανονικοποιημένη (unnormalized) ροή των νετρονίων, όπως δίνεται από τον κώδικα MCNP5 και ο $Scale\,Factor$ έχει προσδιορισθεί στο προηγούμενο βήμα. Επομένως, η κατανομή της ροής των νετρονίων είναι γνωστή (βλέπε Σχήμα 21).

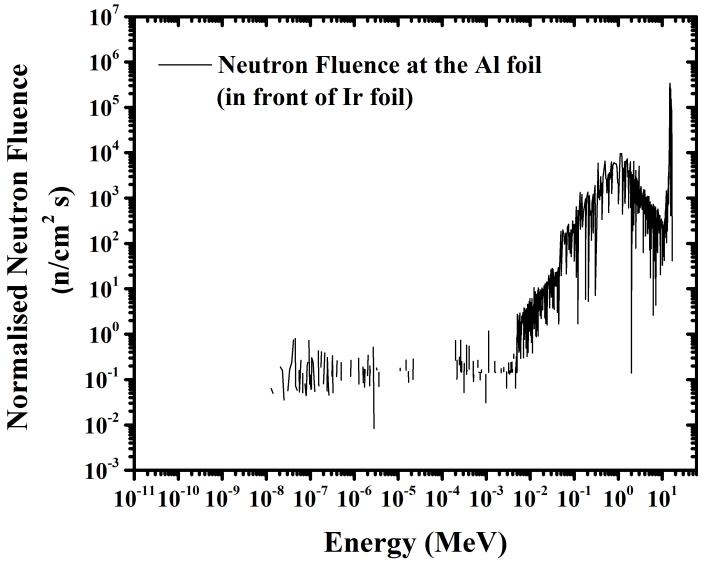

Σχήμα 21: Κανονικοποιημένη κατανομή της ροής των νετρονίων συναρτήσει της ενέργειας, σύμφωνα με την Εξ. 12, για την ακτινοβόληση στα 15.3 MeV.

Παρομοίως με το δεύτερο βήμα, ο αναμενόμενος ρυθμός ενεργοποίησης (expected reaction rate) για την αντίδραση ^{191}Ir(n,γ)^{192}Ir δίνεται από την σχέση:

$$RR_{\,expected}=\sum_{E_i}\sigma(E_i)\cdot\phi_{\,normalized}\left(E_i\right) \tag{13}$$

όπου $\sigma\left(E_i\right)$ είναι η ενεργός διατομή της αντίδρασης ^{191}Ir(n,γ)^{192}Ir σε κάθε ενεργειακό διάστημα (βλέπε Σχήμα 22).

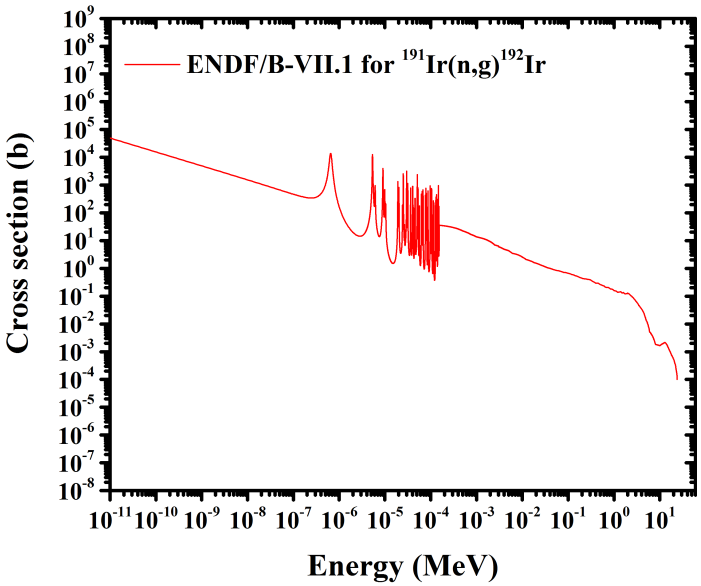

Σχήμα 22: Ενεργός διατομή της αντίδρασης ^{191}Ir(n,γ)^{192}Ir συναρτήσει της ενέργειας των νετρονίων. Η καμπύλη αξιολόγησης αντιστοιχεί στην βιβλιοθήκη ENDF/B.VII.1 [28].

Επομένως, σύμφωνα με την Εξ. 11, μπορεί να υπολογιστεί το $N_{\gamma\,correction}$, το οποίο αντιστοιχεί στον αριθμό των γεγονότων που πρέπει να αφαιρεθούν από τον συνολικό αριθμό γεγονότων στο φάσμα, προκειμένου να διορθωθεί η συνεισφορά των χαμηλοενεργειακών, παρασιτικών νετρονίων:

$$N_{\gamma\,correction} = N_{\gamma\,expected} = \frac{\varepsilon_\gamma \cdot I \cdot F \cdot D \cdot N_\tau \left(1 - e^{\lambda t_B}\right) \cdot RR_{expected}}{\lambda} \tag{14}$$

Όλα τα μεγέθη στην Εξ. 14 αντιστοιχούν σε αυτά της ανάλυσης των δεδομένων των τριών πιο ισχυρών ακτίνων-γ (316.5, 468.1 ανδ 308.5 keV) που εκπέμπονται κατά την αποδιέγερση του πυρήνα ^{192}Ir.

Έτσι, τα χρήσιμα γεγονότα για τον προσδιορισμό της ενεργού διατομής είναι τα ακόλουθα:

$$N_\gamma = N_{\gamma\,spectrum} - N_{\gamma\,correction} \tag{15}$$

Το σχετικό σφάλμα του $N_{\gamma\,correction}$ θεωρήθηκε ίδιο με το σχετικό σφάλμα του $N_{\gamma\,experimental}$ για την ακτίνα-γ στα 411.8 keV, ενώ η αβεβαιότητα του τελικού, διορθωμένου N_γ, βρέθηκε από την τετραγωνική άθροιση των δύο επιμέρους σφαλμάτων.

Οι τελικές, πειραματικές τιμές των ενεργών διατομών που προέκυψαν από το σταθμισμένο μέσο όρο δύο ή τριών πειραματικών τιμών (ανάλογα με τον αριθμό των ακτίνων-γ που αναλύθηκαν σε κάθε περίπτωση) παρουσιάζονται για όλες τις υπό μελέτη αντιδράσεις στον Πίνακα 6.

Πίνακας 6: Πειραματικές τιμές σταθμισμένου μέσου όρου ενεργών διατομών για τις έξι υπό μελέτη αντιδράσεις. Τα δεδομένα στις χαμηλές ενέργειες νετρονίων (10-11.3 MeV) για την ενεργό διατομή της αντίδρασης ^{193}Ir(n,2n) λήφθηκαν το 2005-2006, από τον Ν. Πατρώνη κ. ά, αλλά δεν συμπεριλήφθηκαν στην αναφορά [11]. Οι απαραίτητες διορθώσεις για την συνεισφορά των παρασιτικών νετρονίων πραγματοποιήθηκαν στα πλαίσια της παρούσας διατριβής, μέσω προσομοιώσεων με τον κώδικα MCNP5. Επιπλέον, όσον αφορά στις αντιδράσεις με χρήση στόχου Au, στις χαμηλές ενέργειες νετρονίων (10-11.3 MeV), τα αποτελέσματα δημοσιεύθηκαν το 2011 από τον Α. Τσιγγάνη κ. ά [12].

E_n	Σταθμισμένοι μέσοι όροι ενεργών διατομών (b)						
(MeV)	^{197}Au(n,2n)^{196}Au	^{197}Au(n,2n)^{196}Au^{m2}	^{197}Au(n,2n)^{196}Au^{m2} *	^{191}Ir(n,2n)^{190}Ir	^{191}Ir(n,2n)^{190}Ir^{m2}	^{191}Ir(n,3n)^{189}Ir	^{193}Ir(n,2n)^{192}Ir
10.0	-	-	-	-	-	-	1.290 ± 0.083
10.5	-	-	-	-	-	-	1.590 ± 0.100
11.0	-	-	-	-	-	-	1.931 ± 0.119
11.3	-	-	-	-	-	-	1.953 ± 0.120
15.3	1.995 ± 0.093	0.163 ± 0.009	0.172 ± 0.010	1.786 ± 0.076	0.179 ± 0.008	-	1.830 ± 0.076
17.1	1.772 ± 0.086	0.196 ± 0.012	0.212 ± 0.013	1.465 ± 0.072	0.203 ± 0.015	0.167 ± 0.043	1.390 ± 0.068
17.9	1.651 ± 0.080	0.213 ± 0.014	0.223 ± 0.015	1.291 ± 0.082	0.210 ± 0.012	-	-
18.9	1.394 ± 0.064	0.195 ± 0.013	0.204 ± 0.013	0.991 ± 0.052	0.178 ± 0.010	0.716 ± 0.179	0.769 ± 0.082
20.0	1.049 ± 0.091	0.169 ± 0.020	0.178 ± 0.013	0.731 ± 0.091	0.134 ± 0.013	-	-
20.9	0.716 ± 0.056	0.120 ± 0.013	0.126 ± 0.014	0.479 ± 0.037	0.086 ± 0.007	1.096 ± 0.198	0.270 ± 0.053

* Οι εντάσεις των ακτίνων-γ υιοθετήθηκαν από την αναφορά [38].

Θεωρητικοί Υπολογισμοί

Εκτός από τις πειραματικές μετρήσεις, στα πλαίσια της παρούσας διατριβής έγιναν θεωρητικοί υπολογισμοί ενεργών διατομών με χρήση των κωδίκων EMPIRE 3.2.2 [40, 41] και TALYS 1.8 [42, 43], τόσο για τις έξι υπό μελέτη αντιδράσεις, όσο και για άλλα κανάλια που αφορούν στους ίδιους πυρήνες-στόχους, όπως (n,elastic), (n,3n), (n,p), (n,α) και (n,total). Οι θεωρητικοί υπολογισμοί υλοποιήθηκαν σε ένα μεγάλο εύρος ενεγειών (έως 35 MeV) για τρείς διαφορετικούς πυρήνες-στόχους, τους ^{197}Au, ^{191}Ir και ^{193}Ir. Τρεις βασικοί μηχανισμοί αντιδράσεων λήφθηκαν υπόψη και στους δύο κώδικες, οι αντιδράσεις σύνθετου πυρήνα, οι αντιδράσεις προϊσορροπίας και οι άμεσες. Ο τελικός σκοπός δεν ήταν να γίνει σύγκριση μεταξύ των δύο κωδίκων, αλλά να βρεθεί ο βέλτιστος συνδυασμός παραμέτρων για κάθε κώδικα, ο οποίος να δίνει ικανοποιητικά αποτελέσματα σε σύγκριση με τα υπάρχοντα πειραματικά δεδομένα της κάθε αντίδρασης για διάφορα κανάλια εξόδου. Ιδιαίτερη προσοχή δόθηκε στις περιπτώσεις των ενεργών διατομών των ισομερών καταστάσεων.

Στον παρακάτω πίνακα (βλέπε Πίνακα 7) δίνονται οι βασικές εντολές που χρησιμοποιήθηκαν στα αρχεία εισόδου του κώδικα EMPIRE για τις αντιδράσεις των νετρονίων με τα τρία ισότοπα που μελετήθηκαν.

Πίνακας 7: Εντολές και τιμές που χρησιμοποιήθηκαν στο αρχείο εισόδου του κώδικα EMPIRE.

EMPIRE 3.2.2			
Εντολή	Τιμή για:		
	^{197}Au	^{191}Ir	^{193}Ir
LEVDEN	0	0	0
DIRECT	0	0	0
HRTW	3	3	3
GSTRFN	1	1	1
OMPOT (n)	401	401	401
OMPOT (p)	5405	5405	5405
OMPOT (α)	9600	9600	9600
PCROSS	2.2	2.99	2.0

Οι ενεργές διατομές των αντιδράσεων σύνθετου πυρήνα υπολογίστηκαν στα πλαίσια της θεωρίας Hauser-Feshbach [44]. Η προκαθορισμένη (default) επιλογή του κώδικα EMPIRE χρησιμοποιήθηκε για την περιγραφή της πυκνότητας των ενεργειακών καταστάσεων σύμφωνα με το Βελτιωμένο Γενικευμένο Πρότυπο Υπερρευστού (Enhanced Generalized Superfluid Model - EGSM [45]). Για να ληφθεί υπόψη η συσχέτιση του καναλιού εισόδου με τα κανάλια εξόδου στην ελαστική σκέδαση, εφαρμόσθηκε το μοντέλο των Hofmann, Richert, Tepel και Weidenmuller model (HRTW) για τις διορθώσεις του εύρους των διακυμάνσεων (width fluctuation corrections), για ενέργειες εισερχόμενων νετρονίων μέχρι 3 MeV. Όσον αφορά στην εκπομπή ακτίνων-γ, οι αντίστοιχες συναρτήσεις (γ-ray strength functions) περιγράφηκαν με τροποποιημένες Lorentzians (MLO1) με παραμέτρους διαθέσιμες στην βιβλιοθήκη δεδομένων RIPL-3 [46]. Οι παράμετροι του οπτικού δυναμικού για τα εξερχόμενα πρωτόνια υιοθετήθηκαν από την βιβλιοθήκη RIPL-3, με χρήση των παραμέτρων των A. J. Koning κ. ά [47], ενώ οι παράμετροι των V. Avrigeanu κ. ά [48] χρησιμοποιήθηκαν για τα εξερχόμενα σωματίδια α. Προκειμένου

να επιλεγεί το οπτικό δυναμικό για τα εξερχόμενα νετρόνια από την βιβλιοθήκη RIPL-3, όλα τα διαθέσιμα για κάθε ισότοπο δυναμικά δοκιμάσθηκαν και τελικά αυτό των D. Wilmore κ. ά [49] επιλέχθηκε ως το πιο κατάλληλο και για τα τρία ισότοπα. Επιπλέον, η συνεισφορά των αντιδράσεων προϊσορροπίας περιγράφηκε με το κλασικό μοντέλο των εξιτονίων [50, 51], μέσω της υπορουτίνας PCROSS [52] που είναι διαθέσιμη στον κώδικα EMPIRE. Στους παραπάνω υπολογισμούς, οι συντελεστές διάδοσης (transmission coefficients) υπολογίσθηκαν με χρήση υπορουτίνων οπτικών μοντέλων (κώδικας ECIS06 [53, 54]) που είναι διαθέσιμες στον κώδικα EMPIRE. Επίσης, πρέπει να σημειωθεί ότι χρησιμοποιήθηκαν σφαιρικά οπτικά δυναμικά.

Στον παρακάτω πίνακα (βλέπε Πίνακα 8) δίνονται οι βασικές εντολές που χρησιμοποιήθηκαν στα αρχεία εισόδου του κώδικα TALYS για τις αντιδράσεις των νετρονίων με τα τρία ισότοπα που μελετήθηκαν.

Πίνακας 8: Εντολές και τιμές που χρησιμοποιήθηκαν στο αρχείο εισόδου του κώδικα TALYS.

TALYS 1.8			
Εντολές	Τιμές για:		
	^{197}Au	^{191}Ir	^{193}Ir
ldmodel	3	3	3
alimit	79 198 16.827	77 192 16.4	77 194 20.6
alimit	79 197 16.736	77 191 16.3	77 193 20.0
alimit	79 196 16.645	77 190 16.1	77 192 20.2
alimit	79 195 16.554	77 189 16.1	-
spherical	n	n	n
widthfluc	3	3	3
widthmode	2	2	2
gammax	4	4	4
strength	1	1	1
jlmomp	n	n	n
alphaomp	6	6	6
preequilibrium	y	y	y
preeqmode	3	3	3
preeqspin	3	3	3
rspincut	1.5	0.7	0.7
spincutmodel	1	2	2
cstrip	α 2	α 2	α 2

Όσον αφορά στους θεωρητικούς υπολογισμούς με τον κώδικα TALYS, οι ενεργές διατομές των αντιδράσεων σύνθετου πυρήνα υπολογίσθηκαν και πάλι στα πλαίσια της θεωρίας Hauser-Feshbach [44], ενώ οι πυκνότητες ενεργειακών καταστάσεων περιγράφηκαν μέσω του Γενικευμένου Πρότυπου Υπερρευστού (Generalised Superfluid Model - GSM). Το εύρος της κατανομής των στροφορμών της πυκνότητας καταστάσεων (spin cut-off parameter, σ^2) περιγράφηκε είτε μέσω της σχέσης:

$$\sigma^2 = c\,\frac{\alpha}{\tilde{\alpha}}\sqrt{\frac{U}{\alpha}} \qquad \text{(spincutmodel 1)} \tag{16}$$

Είτε μέσω της σχέσης:

$$\sigma^2 = c\sqrt{\frac{U}{\alpha}} \qquad \text{(spincutmodel 2)} \tag{17}$$

όπου c είναι μία σταθερά, α είναι η παράμετρος πυκνότητας καταστάσεων, η οποία καθορίζεται είτε από πειραματικές πληροφορίες, είτε από ευρέως διαδεδομένες συστηματικές, $\tilde{\alpha}$ είναι η ασυμπτωτική παράμετρος πυκνότητας καταστάσεων, η οποία προκύπτει σε περίπτωση που δεν υπάρχουν φαινόμενα φλοιών ($\tilde{\alpha}$=α(E$\rightarrow\infty$)) και

$$U = E - \Delta \tag{18}$$

όπου E είναι η ενέργεια διέγερσης και Δ είναι μία εμπειρική παράμετρος που σχετίζεται με την ενέργεια σύζευξης και λαμβάνει υπόψη τα φαινόμενα περιττού-άρτιου αριθμού νουκλεονίων του πυρήνα. Επιπλέον, η παράμετρος σ^2 πολλαπλασιάστηκε με κατάλληλο παράγοντα ($0.7 \leq$ rspincut ≤ 1.5), ώστε να επιτυγχάνεται ικανοποιητική αναπαραγωγή των πειραματικών δεδομένων της ενεργού διατομής, ειδικά για τις περιπτώσεις των ισομερών καταστάσεων. Η ασυμπτωτική παράμετρος πυκνότητας καταστάσεων ($\tilde{\alpha}$) για τους εμπλεκόμενους σύνθετους πυρήνες που φαίνονται στον Πίνακα 8 δηλώθηκαν ξεχωριστά μέσω της παραμέτρου alimit, και οι τιμές υιοθετήθηκαν από τις αναφορές [55] και [46]. Διορθώσεις για το εύρος διακυμάνσεων (width fluctuation corrections) έγιναν μέσω του μοντέλου HRTW για νετρόνια ενέργειας μέχρι 3MeV. Όσον αφορά στην εκπομπή ακτίνων-γ, λήφθηκαν υπόψη μεταβάσεις με πολυπολικότητα έως 4 και χρησιμοποιήθηκαν κατάλληλες συναρτήσεις (strength functions) οι οποίες υπολογίστηκαν μικροσκοπικά από τον S. Goriely, σύμφωνα με το μοντέλο των Hartree-Fock-Bogolyubov που εξαρτάται από την θερμοκρασία. Για τα εξερχόμενα πρωτόνια και νετρόνια, χρησιμοποιήθηκε το οπτικό δυναμικό των Koning και Delaroche [47], ενώ για τα σωματίδια α υιοθετήθηκαν οι παράμετροι από τους Avrigeanu κ. ά [56]. Για τις αντιδράσεις προϊσορροπίας χρησιμοποιήθηκε το μοντέλο των εξιτονίων, ενώ η κατανομή των σπίν για τους παραγόμενους πυρήνες από αντιδράσεις προϊσορροπίας βασίστηκε στις πυκνότητες καταστάσεων σωματιδίου-οπής (particle-hole state densities). Για τις αντιδράσεις απογύμνωσης (stripping) και υφαρπαγής (pick-up) εξερχόμενων σωματιδίων α κατά την προϊσορροπία χρησιμοποιήθηκε ένας πολλαπλασιαστικός παράγοντας μέσω της εντολής cstrip α [57]. Όσον αφορά στις άμεσες αντιδράσεις, χρησιμοποιήθηκε η μέθοδος των συζευγμένων [58] καναλιών με οπτικό δυναμικό για παραμόρφωμένους πυρήνες. Οι συντελεστές διάδοσης υπολογίστηκαν μέσω του κώδικα ECIS06.

Τα αποτελέσματα των θεωρητικών υπολογισμών για όλες τις αντιδράσεις παρουσιάζονται στην επόμενη ενότητα, μαζί με τα υπάρχοντα πειραματικά δεδομένα, αλλά και με τα πειραματικά αποτελέσματα της παρούσας διατριβής.

Αποτελέσματα και Συμπεράσματα

Μετρήθηκαν οι ενεργές διατομές των αντιδράσεων ^{197}Au(n,2n)^{196}Au, ^{197}Au(n,2n)^{196}Au^{m2}, ^{191}Ir(n,2n)^{190}Ir$^{g+m1+0.086\,m2}$, ^{191}Ir(n,2n)^{196}Ir^{m2}, ^{191}Ir(n,3n)^{189}Ir και ^{193}Ir(n,2n)^{192}Ir, για έξι ενέργειες της δέσμης νετρονίων στο εύρος 15.3-20.9 MeV και τα αποτελέσματα παρουσιάζονται στα Σχήματα 23a-23f μαζί με τα ήδη υπάρχοντα δεδομένα στη βιβλιογραφία [9] και με την καμπύλη αξιολόγησης ENDF/B-VII.1 [28] (σε όποιες αντιδράσεις υπάρχει).

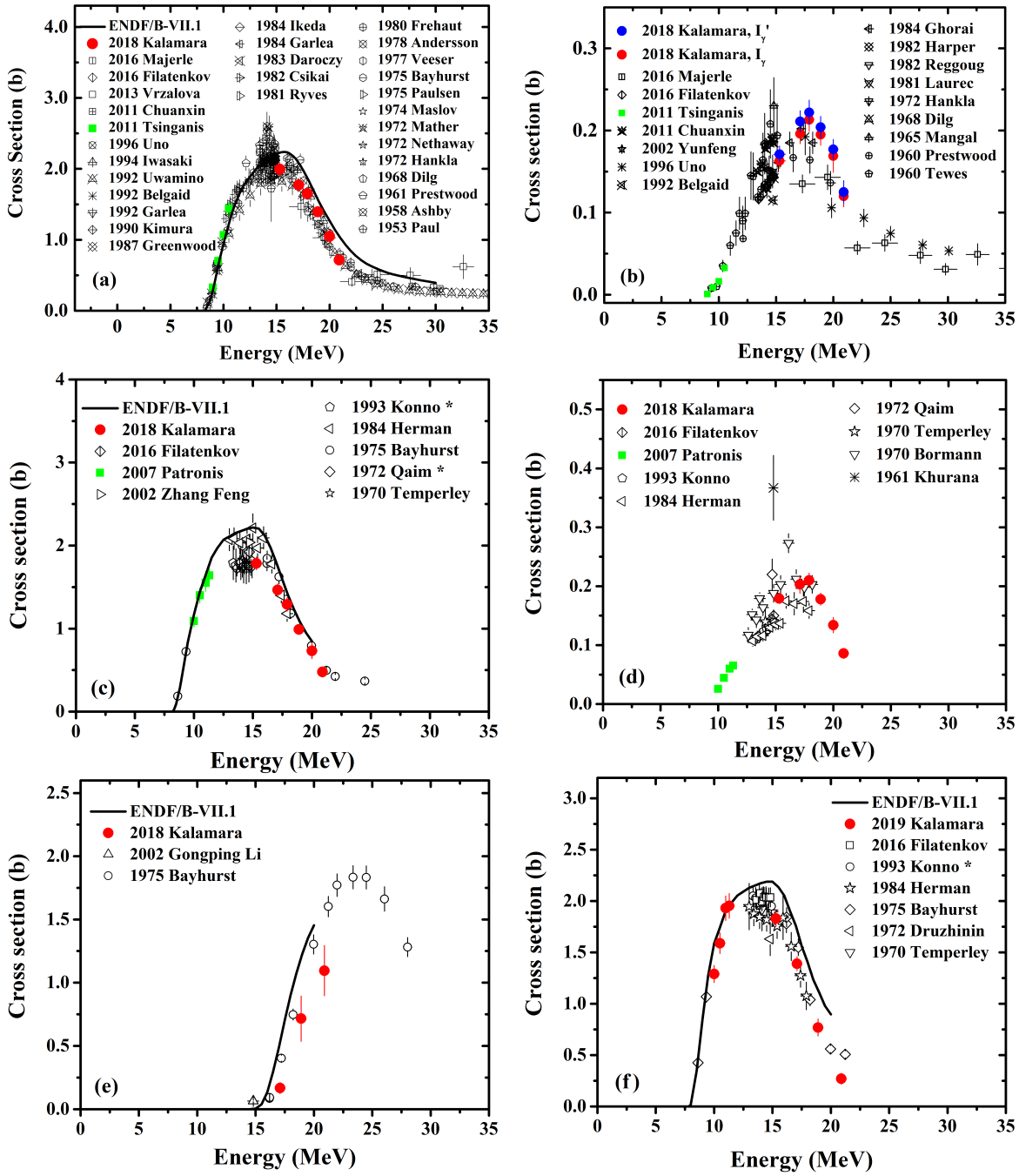

Σχήμα 23: Πειραματικά αποτελέσματα για τις ενεργές διατομές των έξι αντιδράσεων που μετρήθηκαν στα πλαίσια της παρούσας διατριβής, μαζί με προϋπάρχοντα πειραματικά δεδομένα [9] και την καμπύλη αξιολόγησης ENDF/B-VII.1 [28] (για όποιες αντιδράσεις υπάρχει): (a) ^{197}Au(n,2n)^{196}Au, (b) ^{197}Au(n,2n)^{196}Au^{m2}, (c) ^{191}Ir(n,2n)^{190}Ir$^{g+m1+0.086\,m2}$, (d) ^{191}Ir(n,2n)^{196}Ir^{m2}, (e) ^{191}Ir(n,3n)^{189}Ir και (f) ^{193}Ir(n,2n)^{192}Ir. Στο Σχήμα b τα κόκκινα σημεία έχουν προκύψει χρησιμοποιώντας τις τιμές των εντάσεων των ακτίνων-γ (I_γ) της αναφοράς [38], ενώ τα μπλε σημεία με τις τιμές ($I_\gamma{}'$) της αναφοράς [37]. Στα Σχήματα c και e τα δεδομένα με τον αστερίσκο αντιστοιχούν στην ολική ενεργό διατομή (n,2n) του κάθε καναλιού, ενώ τα υπόλοιπα στην ενεργό διατομή των σταθμών g+m1.

Τα πειραματικά αποτελέσματα για την ενεργό διατομή του αθροίσματος των ισομερών καταστάσεων και της βασικής (Σχήμα 23a) ακολουθούν τη γενική τάση των προγενέστερων πειραματικών σημείων σε όλο το ενεργειακό εύρος. Ειδικά για την περιοχή του πλατώ (∼14 MeV), το σημείο στα 15.3 MeV υποδεικνύει ότι η τιμή της ενεργού διατομής βρίσκεται μεταξύ των υψηλότερων και χαμηλότερων πειραματικών σημείων. Όσον αφορά στην ενεργό διατομή της μετασταθούς (Σχήμα 23b), το πειραματικό σημείο στα 15.3 MeV συμφωνεί με τους Ghorai κ. ά [14] και Tewes κ. ά [13] εντός των πειραματικών αβεβαιοτήτων. Τα υπόλοιπα σημεία, μεταξύ 17.1 και 20.9 MeV, βρίσκονται λίγο πιο ψηλά σε σχέση με τα προηγούμενα δεδομένα, ενώ το σημείο στα 20.9 MeV ακολουθεί την τάση των σημείων στα 19.5, 19.76 και 22.6 MeV των Majerle κ. ά [17], Prestwood κ. ά [16], και Uno κ. ά [15], αντίστοιχα. Οι τιμές των ενεργών διατομών που προέκυψαν χρησιμοποιώντας τις τιμές των εντάσεων των δύο πιο ισχυρών ακτίνων-γ (147.8 και 188.3 keV) από την αναφορά [38], βρίσκονται ελαφρώς πιο ψηλά από τα αποτελέσματα που υπολογίσθηκαν χρησιμοποιώντας τις αντίστοιχες εντάσεις της βιβλιοθήκης Lund [37]. Παρόλα αυτά, συμφωνούν μεταξύ τους εντός των πειραματικών αβεβαιοτήτων και υποδεικνύουν ότι το κεντροειδές της καμπύλης της ενεργού διατομής βρίσκεται περίπου στα 17 MeV, και όχι στα 15 MeV, όπως μπορούσε να θεωρηθεί με βάση τα παλαιότερα δεδομένα.

Όσον αφορά στην ενεργό διατομή της αντίδρασης ^{191}Ir(n,2n)^{190}Ir$^{g+m1+0.086\,m2}$, τα πειραματικά αποτελέσματα (Σχήμα 23c) ακολουθούν τη γενική τάση των προγενέστερων σημείων σε όλο το ενεργειακό εύρος. Ειδικά το σημείο στα 15.3 MeV, αποκαλύπτει ότι η τιμή της ενεργού διατομής στην περιοχή του πλατώ βρίσκεται κοντά στις κεντρικές τιμές των Filatenkov [19] κ. ά, Konno κ. ά [24] και Temperley κ. ά [20] και όχι τόσο κοντά στα σημεία των Herman κ. ά [21], Bayhurst κ. ά [18] και Qaim κ. ά [59] (παρόλο που κάποια σημεία του τελευταίου συμφωνούν με τα σημεία της παρούσας διατριβής). Έτσι, η τιμή της ενεργού διατομής στην περιοχή του πλατώ βρίσκεται πιο χαμηλά από την μέση τιμή που υποδεικνύεται από την καμπύλη αξιολόγησης ENDF/B-VII.1 στην περιοχή 11-18 MeV. Τα νέα σημεία για την ενεργό διατομή της μετασταθούς (Σχήμα 25d), δίνουν μεγαλύτερες τιμές σε σχέση με την πλειοψηφία των παλαιότερων δεδομένων, ενώ συμφωνούν με τα δεδομένα από τους Bormann κ. ά [23]. Επιπλέον, υποδεικνύουν έντονα ότι το κεντροειδές της καμπύλης της ενεργού διατομής βρίσκεται περίπου στα 17 MeV. Όσον αφορά στο κανάλι ^{191}Ir(n,3n) (Σχήμα 23e), λίγα πειραματικά σημεία υπάρχουν στην βιβλιογραφία [18, 60] και τα νέα δεδομένα από την παρούσα διατριβή παρουσίαζουν σημαντικές διαφορές με αυτά. Φαίνεται ότι τα δεδομένα των Bayhurst κ. ά [18] υπερεκτιμούν την ενεργό διατομή και ότι η τελευταία ξεκινά να αυξάνεται σε ενέργειες μεγαλύτερες σε σχέση με την καμπύλη αξιολόγησης ENDF/B-VII.1.

Η ενεργός διατομή της αντίδρασης ^{193}Ir(n,2n)^{192}Ir μετρήθηκε σε οκτώ ενέργειες δέσμης νετρονίων μεταξύ 10.0 και 20.9 MeV. Οι μετρήσεις στις υψηλότερες ενέργειες (15.3-20.9 MeV) υλοποιήθηκαν στα πλαίσια της παρούσας διατριβής, ενώ αυτές στις χαμηλότερες ενέργειες (10.0-11.3 MeV) έγιναν το 2005-2006 από τους N. Patronis κ. ά [11]. Από αυτήν την πειραματική καμπάνια, μόνο η αντίδραση ^{191}Ir(n,2n) αναλύθηκε, ενώ τα δεδομένα της αντίδρασης ^{193}Ir(n,2n) αναλύθηκαν στα πλαίσια της παρούσας διατριβής με ανανεωμένη μεθόδο και έγιναν οι απαραίτητες διορθώσεις για την συνεισφορά των χαμηλοενεργειακών, παρασιτικών νετρονίων στον αριθμό των γεγονότων, που είναι απαραίτητος για τον προσδιορισμό της ενεργού διατομής. Τα πειραματικά αποτελέσματα παρουσιάζονται στο Σχήμα 23f, μαζί με προϋπάρχοντα δεδομένα της βιβλιογραφίας [9] και την καμπύλη αξιολόγησης ENDF/B-VII.1 [28]. Τα νέα πειραματικά σημεία ακολουθούν τη γενική τάση των υπόλοιπων σημείων, τόσο στη χαμηλή,

όσο και στην υψηλή περιοχή ενεργειών. Μόνο το σημείο στα 20.9 MeV είναι χαμηλότερα σε σχέση με τα δεδομένα των Bayhurst κ. ά [18].

Τα αποτελέσματα των θεωρητικών υπολογισμών που έγιναν με τους κώδικες EMPIRE 3.2.2 και TALYS 1.8 για διάφορα κανάλια αντιδράσεων νετρονίων με τον πυρήνα ^{197}Au, παρουσιάζονται στα Σχήματα 24a-24g, μαζί με τα πειραματικά αποτελέσματα της παρούσας διατριβής και με προϋπάρχοντα δεδομένα της βιβλιογραφίας [9]. Όπως φαίνεται, και οι δύο κώδικες δίνουν μία αρκετά καλή αναπαραγωγή των πειραματικών δεδομένων των ενεργών διατομών για όλα τα κανάλια που μελετήθηκαν. Όσον αφορά στην ενεργό διατομή της μετασταθούς (Σχήμα 24b), και οι δύο κώδικες περιγράφουν πολύ καλά την τάση των πειραματικών σημείων και συμφωνούν με τα πειραματικά δεδομένα της παρούσας διατριβής στην θέση του μεγίστου της ενεργού διατομής που αναφέρθηκε παραπάνω. Σε αντίθεση με την αναφορά [12], δεν υπήρξε εμφανής ανάγκη να μειωθεί η ροπή αδράνειας (effective moment of inertia). Σε αυτό το σημείο, πρέπει να σημειωθεί ότι και οι δύο κώδικες έχουν βελτιωθεί σημαντικά τα τελευταία χρόνια. Εκτός από το γεγονός ότι αυτό μπορεί εύκολα να παρατηρηθεί συγκρίνοντας τα αποτελέσματα της παρούσας διατριβής για παράδειγμα, με αυτά που δημοσιεύθηκαν το 2011 από την ομάδα μας, από τους Tsinganis κ. ά [12], αναφέρεται ρητά και στην αναφορά [57] για το TALYS και στο εγχειρίδιο χρήσης του EMPIRE [61] (σελ.60). Έτσι, η διαχείριση των υψηλών στροφορμών στο μοντέλο EGSM του EMPIRE επηρεάζει αποτελεσματικά την κατανομή των σπίν για ενέργειες διέγερσης πάνω από την κρίσιμη, σε σχέση με το GSM, ενώ στον κώδικα TALYS, μία μικρή αύξηση της παραμέτρου αποκοπής των σπίν (spin cut-off parameter) μέσω της εντολής rspincut, ήταν αρκετή για να δώσει επιτυχή αναπαραγωγή της ενεργού διατομής της δεύτερης μετασταθούς. Όσον αφορά στην συνολική ενεργό διατομή της αντίδρασης (n,2n), και οι δύο καμπύλες είναι αποδεκτές, αλλά το TALYS για ενέργειες εισερχόμενων νετρονίων πάνω από 15 MeV φαίνεται να ευννοεί το κανάλι (n,3n) (Σχήμα 24c) σε βάρος του (n,2n) (Σχήμα 24b). Για τις ενεργές διατομές των αντιδράσεων με εξερχόμενα φορτισμένα σωματίδια (Σχήματα 24d και 24e), και οι δύο κώδικες δίνουν ικανοποιητικά αποτελέσματα παρόλο που υπάρχει σημαντική έλλειψη πειραματικών δεδομένων. Επιπλέον, τα αποτελέσματα για την ελαστική σκέδαση (Σχήμα 24f), και για την ολική ενεργό διατομή (Σχήμα 24g), παρουσιάζουν πολύ καλή συμφωνία με τα υπάρχοντα πειραματικά δεδομένα σε ένα μεγάλο εύρος ενεργειών.

Τα αποτελέσματα των θεωρητικών υπολογισμών της ενεργού διατομής για αντιδράσεις νετρονίων με τον πυρήνα ^{191}Ir παρουσιάζονται στα Σχήματα 25a-25f, μαζί με τα πειραματικά αποτελέσματα της παρούσας διατριβής και με προϋπάρχοντα δεδομένα της βιβλιογραφίας [9]. Η αναπαραγωγή της ενεργού διατομής για όλα τα κανάλια που μελετήθηκαν είναι αρκετά καλή. Όσον αφορά στην ενεργό διατομή της αντίδρασης ^{191}Ir(n,2n)^{190}Ir$^{g+m1+0.086\,m2}$ (Σχήμα 25a), και οι δύο καμπύλες είναι σε καλή συμφωνία με τα πειραματικά δεδομένα, ενώ το TALYS φαίνεται να υπερεκτιμά το κανάλι (n,3n) (Σχήμα 25c) και να υποτιμά το (n,2n). Πρέπει να σημειωθεί ότι η αναπαραγωγή της ενεργού διατομής της αντίδρασης ^{191}Ir(n,2n)^{190}Ir$^{g+m1+0.086\,m2}$ μπορούσε να επιτευχθεί με πολλούς συνδυασμούς οπτικών δυναμικών και μοντέλων πυκνότητας καταστάσεων και με τους δύο κώδικες. Ο ισχυρός περιορισμός στην επιλογή του τελικού συνδυασμού ήταν η ταυτόχρονη αναπαραγωγή των ενεργών διατομών των αντιδράσεων ^{191}Ir(n,2n)^{190}Ir$^{g+m1+0.086\,m2}$ και ^{191}Ir(n,2n)^{190}Ir^{m2}. Στην περίπτωση της δεύτερης μετασταθούς (Σχήμα 25b), και οι δύο κώδικες περιγράφουν πολύ καλά την τάση των πειραματικών σημείων και τη θέση του μεγίστου της ενεργού διατομής. Παρόλα αυτά, η καμπύλη του EMPIRE (μπλε) αναπαράγει ελαφρώς καλύτερα την ενεργό διατομή, σε σχέση με την καμπύλη του

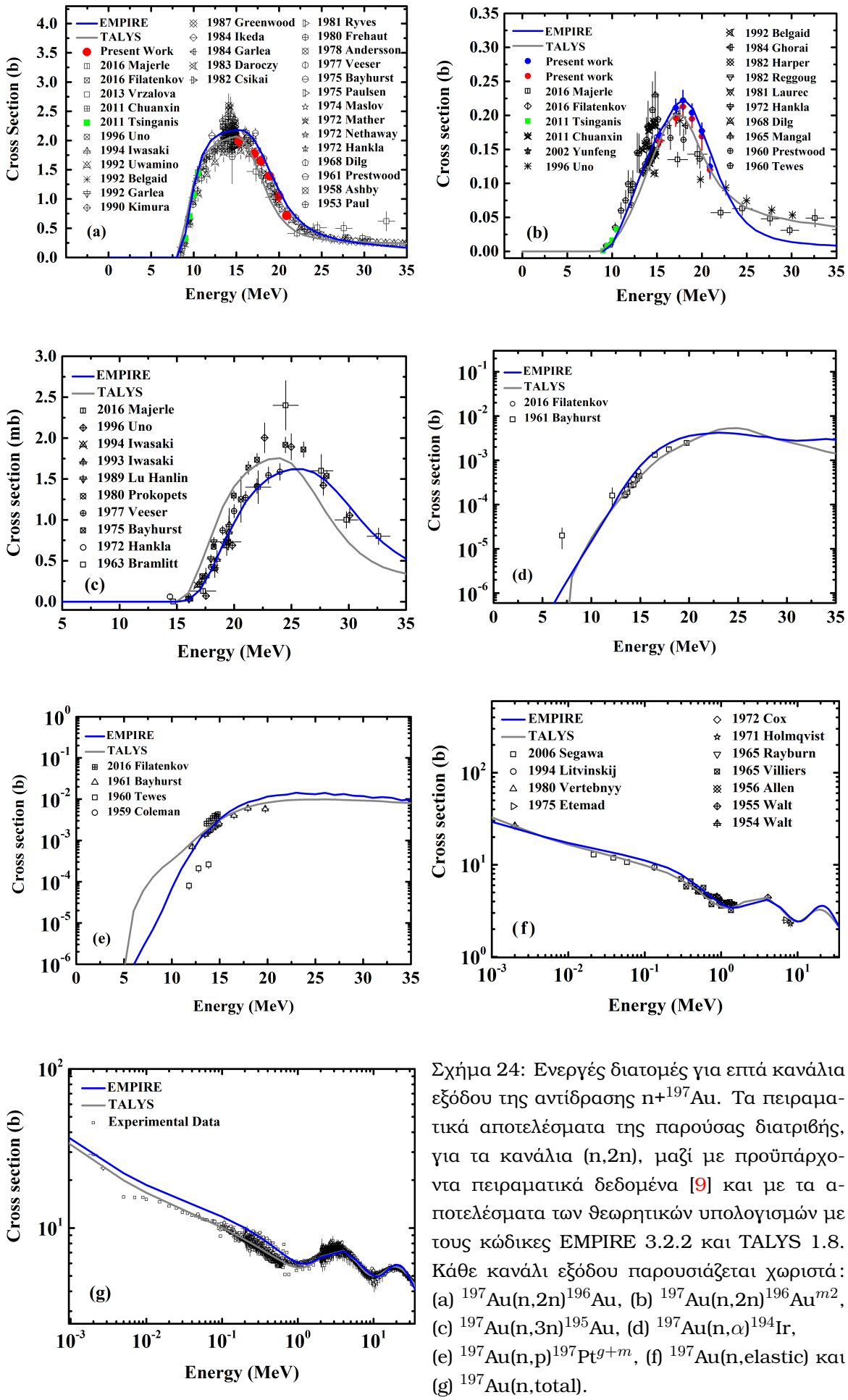

Σχήμα 24: Ενεργές διατομές για επτά κανάλια εξόδου της αντίδρασης n+^{197}Au. Τα πειραματικά αποτελέσματα της παρούσας διατριβής, για τα κανάλια (n,2n), μαζί με προϋπάρχοντα πειραματικά δεδομένα [9] και με τα αποτελέσματα των θεωρητικών υπολογισμών με τους κώδικες EMPIRE 3.2.2 και TALYS 1.8. Κάθε κανάλι εξόδου παρουσιάζεται χωριστά: (a) ^{197}Au(n,2n)^{196}Au, (b) ^{197}Au(n,2n)^{196}Au^{m2}, (c) ^{197}Au(n,3n)^{195}Au, (d) ^{197}Au(n,α)^{194}Ir, (e) ^{197}Au(n,p)^{197}Pt^{g+m}, (f) ^{197}Au(n,elastic) και (g) ^{197}Au(n,total).

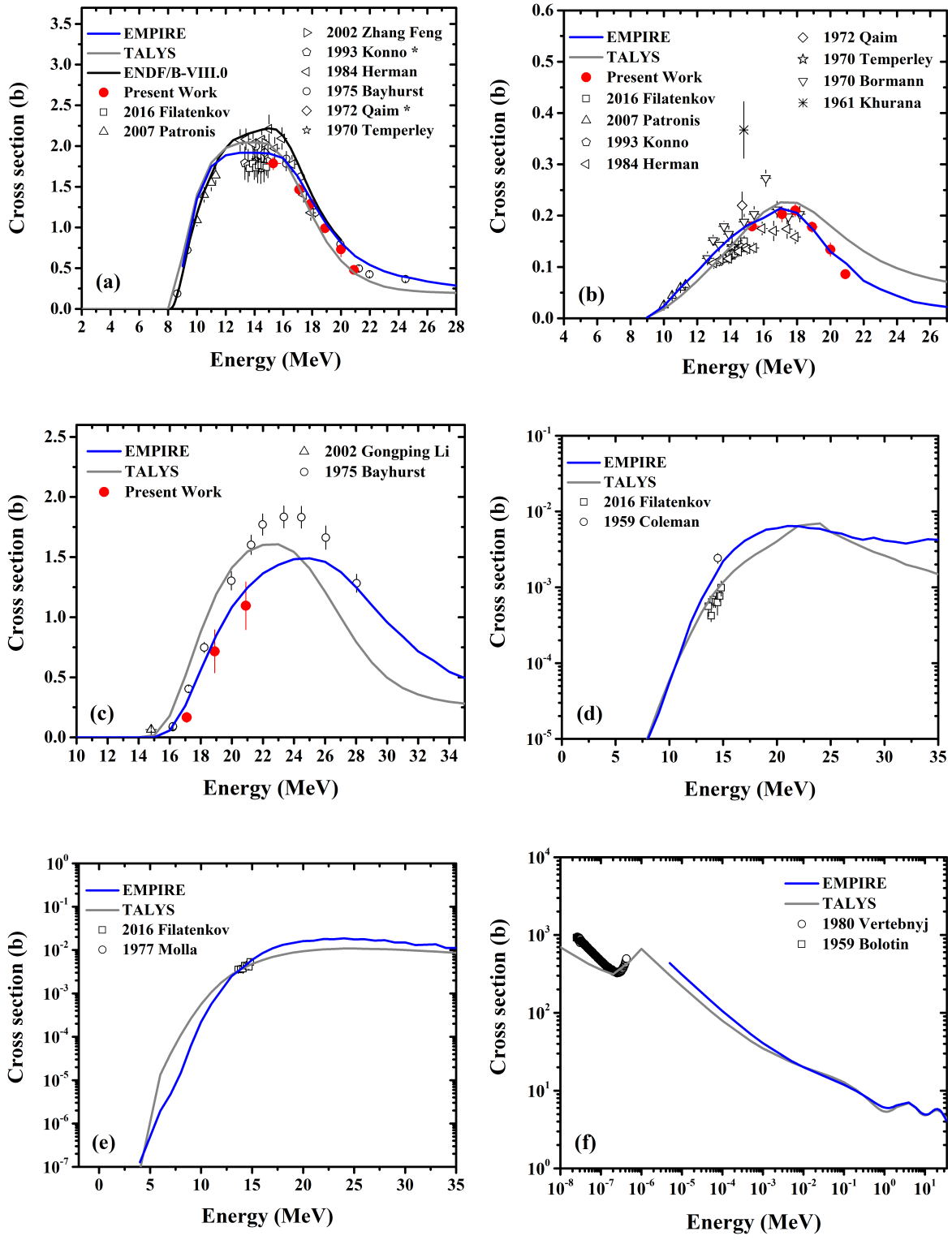

Σχήμα 25: Ενεργές διατομές για έξι κανάλια εξόδου της αντίδρασης n+^{191}Ir. Παρουσιάζονται τα πειραματικά αποτελέσματα της παρούσας διατριβής, για τα κανάλια (n,2n) και (n,3n), μαζί με προϋπάρχοντα πειραματικά δεδομένα [9] και με τα αποτελέσματα των θεωρητικών υπολογισμών με τους κώδικες EMPIRE 3.2.2 και TALYS 1.8. Κάθε κανάλι εξόδου παρουσιάζεται χωριστά: (a) ^{191}Ir(n,2n)^{190}Ir$^{g+m1+0.086\,m2}$, (b) ^{191}Ir(n,2n)^{196}Ir^{m2}, (c) ^{191}Ir(n,3n)^{189}Ir, (d) ^{191}Ir(n,α)^{188}Re,
(e) ^{191}Ir(n,p)^{191}Os και (f) ^{191}Ir(n,total). Στο Σχήμα 25a, τα δεδομένα με τον αστερίσκο αντιστιχούν στην ολική ενεργό διατομή του καναλιού (n, 2n), ενώ τα υπόλοιπα αντιστιχούν στην ενεργό διατομή του αθροίσματος g + m1.

TALYS (γκρι), τόσο στη χαμηλή (κοντά στο κατώφλι) περιοχή, όσο και στην υψηλή ενεργειακή περιοχή. Φαίνεται ότι αν η υπήρχε στον κώδικα TALYS η δυνατότητα ενός πολλαπλασιαστικού παράγοντα για την συνεισφορά των αντιδράσεων προϊσορροπίας, θα ήταν δυνατό αν γίνει μία καλύτερη περιγραφή της δεξιάς ουράς της καμπύλης της ενεργού διατομής. Πρέπει να σημειωθεί ότι η αναπαραγωγή της ενεργού διατομής γι αυτό το κανάλι μεμονωμένα, ήταν καλύτερη χωρίς να ληφθεί υπόψη η συνεισφορά των αντιδράσεων προϊσορροπίας (με τον κώδικα TALYS). Όμως αυτό το σενάριο δε θα μπορούσε να γίνει αποδεκτό, αφενός γιατί δεν είναι αναμενόμενο από φυσικής άποψης και αφετέρου γιατί υπήρχε ένας επιπλέον περιορισμός που τέθηκε από τον σκοπό να υπάρχει ταυτόχρονη αναπαραγωγή των δύο (n,2n) καναλιών και φαινόταν πως όταν βελτιώνονταν τα αποτελέσματα για την m2, χειροτέρευαν τα αποτελέσματα της ενεργού διατομής του αθροίσματος g+m1+0.086 m2.

Σε αυτό το σημείο, πρέπει να σημειωθεί ότι η ίδια συμπεριφορά όσον αφορά στην εκπομπή των νετρονίων παρατηρήθηκε στους θεωρητικούς υπολογισμούς που έγιναν με τους κώδικες EMPIRE 3.2.2 και TALYS 1.8, για τον γειτονικό πυρήνα ^{197}Au [62]. Επίσης, αξίζει να αναφερθεί ότι στους θεωρητικούς υπολογισμούς που έγιναν με τον κώδικα EMPIRE για την περιγραφή του συστήματος n+$^{197}_{79}$Au, επιλέχθηκαν οι ίδιες παράμετροι οπτικού δυναμικού (Wilmore κ. ά [49]) και ίδιο μοντέλο πυκνότητας καταστάσεων (EGSM) σε σχέση με αυτά που χρησιμοποιήθηκαν για την περιγραφή του συστήματος n+$^{191}_{77}$Ir [63], ως αυτά που δίνουν την πιο ικανοποιητική αναπαραγωγή της ενεργού διατομής όλων των υπό μελέτη καναλιών.

Όσον αφορά στο κανάλι (n,3n), (Σχήμα 25c) τα αποτελέσματα και των δύο κωδίκων υποεκτιμούν τα δεδομένα των Bayhurst κ. ά [18], αλλά σε σύγκριση με τα δεδομένα της παρούσας διατριβής, ιδιαίτερα τα αποτελέσματα του κώδικα EMPIRE, παρουσιάζουν πολύ καλή συμφωνία. Για τις ενεργές διατομές των αντιδράσεων με εξερχόμενα φορτισμένα σωματίδια (Σχήματα 25d και 25e), και οι δύο κώδικες αναπαράγουν ικανοποιητικά τις ενεργές διατομές, παρόλο που υπάρχει σημαντική έλλειψη πειραματικών δεδομένων. Ακόμα, τα αποτελέσματα και των δύο κωδίκων για την ολική ενεργό διατομή της αντίδρασης (Σχήμα 25f) συμφωνούν μεταξύ τους, αλλά σε αυτήν την περίπτωση υπάρχει σημαντική ανάγκη για πειραματικά δεδομένα για ενέργειες πάνω από 10^{-6} MeV. Υπάρχουν δεδομένα για την αντίδραση (n,total) για ένα μεγάλο ενεργειακό εύρος στην βιβλιογραφία, αλλά μόνο για την περίπτωση του φυσικού Ir και όχι για κάθε ισότοπο χωριστά [9, 64].

Επιπλέον, τα αποτελέσματα των θεωρητικών υπολογισμών για τις αντιδράσεις νετρονίων με τον πυρήνα ^{193}Ir παρουσιάζονται στα Σχήματα 26a-26d, μαζί με τα πειραματικά σημεία της παρούσας διατριβής και με υπάρχοντα δεδομένα της βιβλιογραφίας [9]. Όσον αφορά στην ενεργό διατομή της αντίδρασης (n,2n) (Σχήμα 26a), και οι δύο κώδικες αναπαράγουν πολύ καλά την τάση των πειραματικών δεδομένων και υποδεικνύουν ότι η τιμή της ενεργού διατομής στην περιοχή γύρω από τα 14 MeV, όπου υπάρχουν διάφορα δεδομένα [18–21, 24, 25], είναι κοντά στα χαμηλότερα σημεία των Herman κ. ά [21] και Temperley κ. ά [20]. Τα κανάλια (n,3n) και (n,elastic), για τον πυρήνα-στόχο ^{193}Ir, δεν παρουσιάζονται λόγω της έλλειψης δεδομένων στην βιβλιογραφία [9]. Για τις ενεργές διατομές των αντιδράσεων με εξερχόμενα φορτισμένα σωματίδια (Σχήματα 26b και 26c), και οι δύο κώδικες αναπαράγουν ικανοποιητικά την ενεργό διατομή, παρόλο που υπάρχει σημαντική έλλειψη δεδομένων. Επιπλέον, τα αποτελέσματα και των δύο κωδίκων για την ολική ενεργό διατομή της αντίδρασης (Σχήμα 26d) συμφωνούν μεταξύ τους, αλλά υπάρχει επείγουσα ανάγκη για νέα πειραματικά σημεία σε ενέργειες πάνω από 10^{-6} MeV.

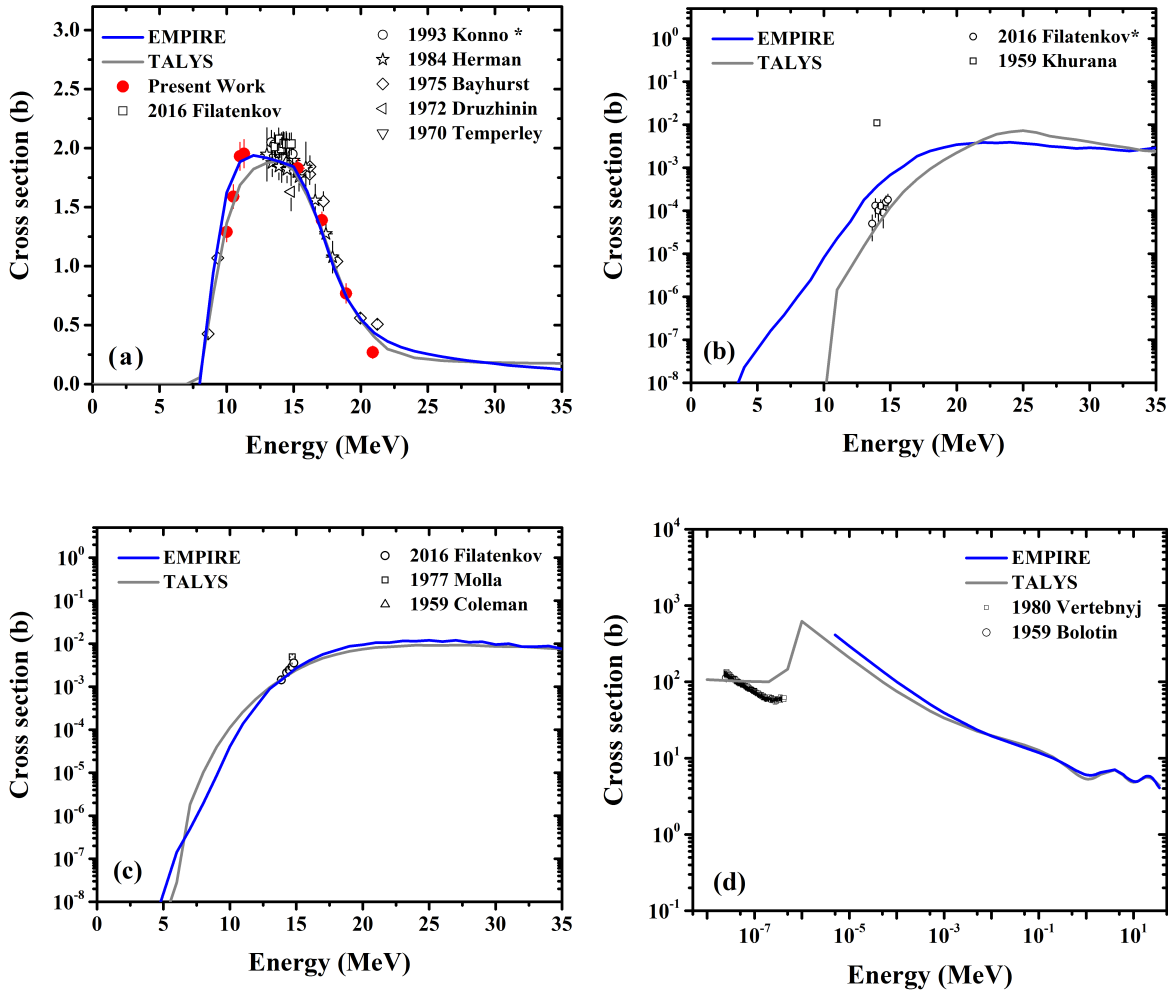

Σχήμα 26: Ενεργές διατομές για τέσσερα κανάλια εξόδου της αντίδρασης n+^{193}Ir. Παρουσιάζονται τα πειραματικά αποτελέσματα της παρούσας διατριβής για το κανάλι (n,2n), μαζί με προϋπάρχοντα πειραματικά δεδομένα [9] και με τα αποτελέσματα των θεωρητικών υπολογισμών με τους κώδικες EMPIRE 3.2.2 και TALYS 1.8. Κάθε κανάλι εξόδου παρουσιάζεται χωριστά:
(a) ^{193}Ir(n,2n)^{192}Ir, (b) ^{193}Ir(n,α)^{190}Re, (c) ^{193}Ir(n,p)^{193}Os and (d) ^{193}Ir(n,total). Στο Σχήμα 26a, τα δεδομένα με τον αστερίσκο αντιστοιχούν στην ολική ενεργό διατομή του καναλιού (n,2n), ενώ τα υπόλοιπα αντιστιχούν στην ενεργό διατομή του αθροίσματος g + m1. Αντιθέτως, στο Σχήμα 26b, τα δεδομένα με τον αστερίσκο αντιστοιχούν στην ενεργό διατομή της μετασταθούς στάθμης, ενώ τα υπόλοιπα σε αυτήν της βασικής κατάστασης.

Σύνοψη

Στα πλαίσια της παρούσας διδακτορικής διατριβής μετρήθηκαν οι ενεργές διατομές των εξής αντιδράσεων:

- ^{197}Au(n,2n)^{196}Au
- ^{197}Au(n,2n)^{196}Au^{m2}
- ^{191}Ir(n,2n)^{190}Ir
- ^{191}Ir(n,2n)^{190}Ir^{m2}
- ^{191}Ir(n,3n)^{189}Ir and
- ^{193}Ir(n,2n)^{192}Ir

σε έξι ενέργειες δέσμης νετρονίων, μεταξύ 15.3 και 20.9 MeV, ως προς την ενεργό διατομή της αντίδρασης ^{27}Al(n,α)^{24}Na. Οι μετρήσεις πραγματοποιήθηκαν στο εργαστήριο του επιταχυντή 5.5 MV Tandem T11/25 του ΕΚΕΦΕ ¨Δημόκριτος¨ στην Αθήνα, μέσω της μεθόδου ενεργοποίησης. Επιπλέον, πειραματικά δεδομένα που είχαν ληφθεί το 2005-2006 από τους N. Patronis κ. ά., με ενέργειες δέσμης νετρονίων στην περιοχή 10.0-11.3 MeV, αναλύθηκαν ειδικά για την ενεργό διατομή της αντίδρασης ^{193}Ir(n,2n)^{192}Ir. Προκειμένου να αναλυθούν αυτά τα δεδομένα σε όλο το ενεργειακό εύρος, μία πρόσφατα εφαρμοσμένη τεχνική χρησιμοποιήθηκε, λόγω του ότι ο πυρήνας που παράγεται από την αντίδραση ^{193}Ir(n,2n), ο ^{192}Ir, παράγεται και από την αντίδραση ^{191}Ir(n,γ), η οποία ενεργοποιείται από χαμηλοενεργειακά, παρασιτικά νετρόνια. Αυτή η μέθοδος διορθώνει τον αριθμό των γεγονότων που είναι απαραίτητος για τον προσδιορισμό της ενεργού διατομής, για την συνεισφορά από χαμηλοενεργειακά, παρασιτικά νετρόνια. Πιο συγκεκριμένα, γίνονται λεπτομερείς προσομοιώσεις για την ενεργειακή κατανομή της δέσμης των νετρονίων, με χρήση των κωδίκων NeuSDesc [34] και MCNP5 [36], και η τελευταία επιβεβαιώνεται μέσω της αντίδρασης ^{197}Au(n,γ). Επιπλέον, έγιναν θεωρητικοί υπολογισμοί των ενεργών διατομών, σε ένα μεγάλο ενεργειακό εύρος, με χρήση των κωδίκων EMPIRE 3.2.2 [40] και TALYS 1.8 [42], τόσο για τις αντιδράσεις που μετρήθηκαν, όσο και για άλλα κανάλια εξόδου που αφορούν στους ίδιους πυρήνες-στόχους.

Τα νέα πειραματικά σημεία για τις έξι αντιδράσεις που μετρήθηκαν και προαναφέρθηκαν, παρουσιάζονται στο Σχήμα 23. Οι τιμές των ενεργών διατομών των αντιδράσεων ^{197}Au(n,2n)^{196}Au (Σχήμα 23a) και ^{191}Ir(n,2n)^{190}Ir (Σχήμα 23c) ακολουθούν τη γενική τάση των προϋπάρχοντων στην βιβλιογραφία δεδομένων και ειδικά τα σημεία στα 15.3 MeV, δίνουν πληροφορία για την τιμή της ενεργού διατομής στο πλατώ, όπου υπάρχουν σημαντικές διαφορές μεταξύ των πειραματικών σημείων της βιβλιογραφίας. Όσον αφορά στα κανάλια που οι παραγόμενοι πυρήνες βρίσκονται σε ισομερείς καταστάσεις, τα ^{197}Au(n,2n)^{196}Au^{m2} (Σχήμα 23b) και ^{191}Ir(n,2n)^{190}Ir^{m2} (Σχήμα 23d), τα νέα πειραματικά σημεία αποκαλύπτουν τόσο το κεντροειδές της ενεργού διατομής, όσο και το σχήμα της. Τα νέα σημεία για την ενεργό διατομή της αντίδρασης ^{191}Ir(n,3n)^{189}Ir, που παρουσιάζονται στο Σχήμα 23e, έχουν σημαντικές διαφορές με τα υπάρχοντα στην βιβλιογραφία δεδομένα των Bayhurst κ. ά [18]. Επιπλέον, όσον αφορά στην ενεργό διατομή της αντίδρασης ^{193}Ir(n,2n)^{192}Ir, (Σχήμα 23f) τα νέα σημεία πάνω από τα 15 MeV συμφωνούν με τα παλαιότερα πειραματικά δεδομένα, ενώ τα σημεία στην περιοχή των

10 MeV δίνουν λογικές τιμές και γεμίζουν το κενό που υπήρχε σε εκείνη την ενεργειακή περιοχή της ενεργού διατομής. Εκτός από τα νέα δεδομένα, η τελευταία αντίδραση είχε ιδιαίτερο ενδιαφέρον διότι ήταν η ιδανική περίπτωση για να ελεγχθεί η πρόσφατα εφαρμοσμένη τεχνική που χρησιμοποιήθηκε για την διόρθωση της συνεισφοράς των χαμηλοενεργειακών νετρονίων στον αριθμό των γεγονότων, που είναι απαραίτητος για τον προσδιορισμό της ενεργού διατομής. Τα αποτελέσματα αυτής της μεθοδολογίας ήταν λογικά κι έτσι αυτή η τεχνική μπορεί να εφαρμοσθεί σε κάθε μέτρηση με μονοενεργεική δέσμη νετρονίων, σε εργαστήρια που δεν έχουν την δυνατότητα της μέτρησης του χρόνου πτήσης τους.

Τα αποτελέσματα των θεωρητικών υπολογισμών των ενεργών διατομών παρουσιάζονται στα Σχήματα 24, 25 και 26. Σε γενικές γραμμές, και οι δύο κώδικες (EMPIRE [40] και TALYS [42]) έδωσαν πολύ ικανοποιητικά αποτελέσματα και ειδικά στις περιπτώσεις των μετασταθών (Σχήματα 24b και 25b) φάνηκε ότι οι κώδικες έχουν βελτιωθεί τα τελευταία χρόνια. Τα αρχεία εισόδου που χρησιμοποιήθηκαν σε κάθε κώδικα για τις αντιδράσεις των νετρονίων στα ισότοπα ^{197}Au, ^{191}Ir και ^{193}Ir, ήταν σχεδόν ίδια (π.χ μοντέλο πυκνότητας καταστάσεων, οπτικό δυναμικό, μοντέλο αντιδράσεων προϊσορροπίας κτλ.). Παρόλο που αυτές οι ομοιότητες θα ήταν αναμενόμενες για γειτονικούς πυρήνες, η επιτυχής αναπαραγωγή των πειραματικών σημείων των ενεργών διατομών είναι μία ενθαρρυντική επιβεβαίωση για την αποτελεσματικότητα των θεωρητικών υπολογισμών σε αυτή την περιοχή μαζών.
Επιπλέον, θα ήταν ιδιαίτερα ενδιαφέρον για το μέλλον:

- Να γίνουν μετρήσεις ενεργών διατομών σε γειτονικούς πυρήνες-στόχους, όπως ^{187}Re, ^{192}Os, ^{198}Hg και ^{203}Tl.

- Να ελεγχθεί αν με τη χρήση των παραμέτρων που επιλέχθηκαν για τους θεωρητικούς υπολογισμούς της παρούσας διατριβής, θα μπορούσε να γίνει αναπαραγωγή των αντίστοιχων ενεργών διατομών των εμπλεκόμενων αντιδράσεων για γειτονικούς πυρήνες, με χρήση των κωδίκων EMPIRE και TALYS.

- Να γίνουν μετρήσεις ενεργοποίησης με ανιχνευτές που θα μετρούν την ενεργότητα την στιγμή της ακτινοβόλησης (in beam measurements), ώστε να μπορούν να μετρηθούν πυρήνες με μικρότερους χρόνους ημιζωής. Προκειμένου να γίνει κάτι τέτοιο, μια συστοιχία ανιχνευτών γερμανίου θα ήταν απαραίτητη, όπως η συστοιχία GEANIE στο εργαστήριο WNR, στο Los Alamos Neutron Science Center [65], ή όπως αυτήν της συνεργασίας AGATA [66].

- Να γίνουν μετρήσεις ενεργοποίησης με ταυτόχρονη μέτρηση του χρόνου πτήσης των νετρονίων (time of flight-TOF) στο ΕΚΕΦΕ ¨Δημόκριτος¨, μετά την αναβάθμιση του εργαστηρίου και να ελεγχθεί η χαμηλοενεργειακή περιοχή του φάσματος των νετρονίων. Για να επιτευχθεί κάτι τέτοιο, είναι απαραίτητη μία δέσμη νετρονίων που θα εκπέμπεται παλμικά, ώστε να είναι δυνατή η μέτρηση του χρόνου πτήσης των νετρονίων (start and stop). Πιθανώς η μέγιστη διαδρομή δεν θα μπορούσε να ξεπερνάει τα 10 m, αλλά αυτή η απόσταση είναι αρκετή για χαμηλοενεργειακά νετρόνια.

PhD thesis

Introduction

Accurate neutron induced reaction cross sections are of considerable importance for practical applications in nuclear technology, dosimetry, medicine and industry, as well as for fundamental research in Nuclear Physics and Astrophysics [1, 2].

Since the time of the discovery of the neutron [3], efforts have been made to understand the effects of neutron radiation in tissue and, eventually, to use neutrons for cancer treatment. In contrast to charged particle or photon irradiations which directly lead to the release of electrons, neutrons interact with the target nuclei and induce the emission of several different types of charged particles such as protons, alpha particles or heavier ions. Thus, a fundamental understanding of the neutron-nucleus interaction is necessary for dose calculations and treatment planning with the needed accuracy [4]. Hence, one part of the indispensability of dosimetry concerns the hospitals in which the neutron therapy is provided.

Another issue is that, as the years pass by, the need for the reprocessing of “high burnup" nuclear fuels containing plutonium and other higher actinides increases. The latter decay by spontaneous fission or produce neutrons via (α,n) reactions [5]. Therefore, the accurate determination of the neutron emission by nuclear waste is critical, for both the environment and the humans.

Especially (n,xn) threshold reactions on Au and Ir isotopes, which are under investigation in the present thesis, are proposed for high energy neutron dosimetry [6–8]. In order to determine the neutron fluence in neutron environments (i.e fusion reactor), the use of different radiochemical detectors and different nuclear reactions allows for a sampling of different energy regions of a neutron energy spectrum and for this purpose, accurate cross section data is needed. The passive method of neutron dosimetry which works by activating appropriate materials (i.e Au and Ir), which are also referred to as “activation detectors", has been proven to be the most sensitive one, concerning measuring instruments. For example, in designing personnel dosimeters, the “activation detectors" are considered the most appropriate supplement that produces a sensitive neutron dosimeter which can lower the dose detection limits. It should be noted that especially (n,2n), and generally (n,xn), reaction cross sections on Au are included in the NEA Nuclear Data High Priority Request List (HPRL),

since they are essential for improvement and validation of the evaluated data [67, 68].

Apart from the aforementioned technological applications of (n,xn) reactions on Au and Ir, there are more issues strictly related to the basic research in Nuclear Physics.

The study of neutron threshold reactions is of considerable importance for testing and improving nuclear model parameters, therefore accurate cross section experimental data is needed. More specifically, the residual nuclei of the (n,2n) reactions on ^{197}Au and ^{191}Ir present high-spin isomeric states. The cross sections of the latter provide important information for the study of the compound nucleus de-excitation mechanism, due to the fact that the population of isomeric states directly depends on the spin of the levels from which they are fed and on the spin distribution in the continuum. Moreover, concerning isomeric states reaction cross sections, the existing data points either present significant discrepancies, or they are absent. Therefore, the new data could give a boost to experimental applications, since they offer the possibility for an immediate and less time-consuming activation analysis, due to the shorter (compared to the ground state's) half-lives involved. Furthermore, the existence of accurate experimental data is of crucial importance for the evaluation of these reaction cross sections, since there are no evaluated data in the libraries, concerning the production of isomeric states.

Furthermore, the rapid evolution of computational codes and methods the last decade, allowed for another contribution in experimental physics. Through the use of current computational power, an analysis method, which could not be applied in the past, is implemented in order to determine the ^{193}Ir(n,2n)^{192}Ir reaction cross section, which is contaminated by the ^{191}Ir(n,γ)^{192}Ir one. This method corrects the yield that is used for the cross section determination for the contribution of low energy parasitic neutrons, by using updated evaluated data libraries and Monte Carlo simulations. This method provides a quite good estimation of the neutron energy distribution over the whole energy range (from 10^{-11} to tens of MeV) and can also be used in any measurement using a quasi-monoenergetic neutron beam, in facilities which do not possess Time-of-Flight experimental capabilities.

Literature Survey and New Measurements

The six reaction cross sections which were studied in the framework of the present thesis are the following:

- ^{197}Au(n,2n)^{196}Au
- ^{197}Au(n,2n)^{196}Au^{m2}
- ^{191}Ir(n,2n)^{190}Ir
- ^{191}Ir(n,2n)^{190}Ir^{m2}
- ^{191}Ir(n,3n)^{189}Ir
- ^{193}Ir(n,2n)^{192}Ir

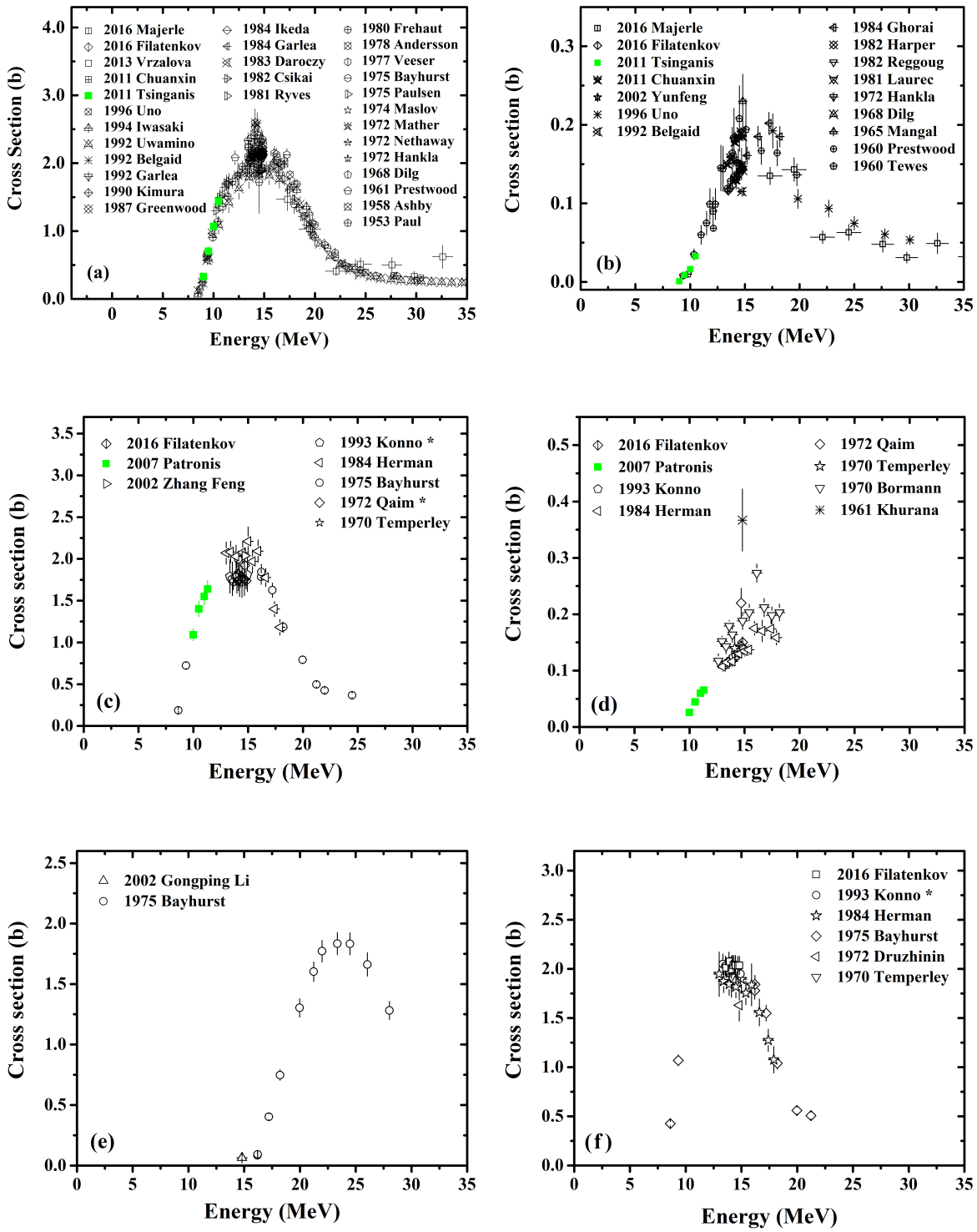

Figure 27: Existing datasets in literature [9] for the six reaction cross sections of interest in the framework of the present thesis:
(a)^{197}Au(n,2n)^{196}Au, (b)^{197}Au(n,2n)^{196}Au^{m2},
(c) ^{191}Ir(n,2n)^{190}Ir, (d) ^{191}Ir(n,2n)^{196}Ir^{m2},
(e) ^{191}Ir(n,3n)^{189}Ir and (f) ^{193}Ir(n,2n)^{192}Ir.
The green data points are previous measurements from our group [10], published in 2007 and 2011, by N. Patronis *et. al* [11] and A. Tsinganis *et. al* [12], respectively. The present work constitutes a continuation of the previous ones in order to determine the cross section at higher neutron energies.

The previously existing in literature datasets [9], for each one, are presented in Fig. 27. As can be seen in Fig. 27a, many cross section datasets [12, 15–19, 69–92] exist for the ground state of the residual nucleus of the ^{197}Au(n,2n) reaction, which present notable discrepancies in the plateau region, around 15 MeV. This is not the case for the second isomeric state of the ^{196}Au nucleus (Fig. 27b), especially at high neutron beam energies. Above 15 MeV only five datasets exist [13–17] and the corresponding data differ significantly with one another. Concerning the ^{191}Ir(n,2n)^{190}Ir reaction cross section for the sum of the ground and the first isomeric state (g+m1) (see Fig. 27c), six datasets exist [11, 18–22], which present few data points above 15 MeV. Going to an even worse case, for the cross section of the second metastable state of ^{190}Ir nucleus (Fig. 27d), although there exist two datasets [21, 23] in the energy range from 15 to 18 MeV, there are considerable differences among them, while at higher energies there is a complete lack of experimental data. Regarding the cross section of the ^{191}Ir(n,3n)^{189}Ir reaction (Fig. 27e), there are only two datasets over the whole energy range above threshold, which provide few data points. Last but not least, the ^{193}Ir(n,2n)^{192}Ir reaction cross section (Fig. 27f), for which six datasets [18–21, 24, 25] are available in literature, but the majority of the data points lies in the plateau region. For energies below 13 and above 16 MeV it seems that more experimental data is needed.

Therefore, the purpose of this work was to experimentally determine the cross section of the six aforementioned reaction cross sections at incident neutron beam energies ranging from 15 to 21 MeV. Additionally, in the framework of the present thesis, experimental data obtained in 2005 and 2006, using neutron beams ranging from 10 to 11.3 MeV were analyzed, especially for the cross section of the ^{193}Ir(n,2n)^{192}Ir reaction. The ^{191}Ir(n,2n) reaction cross section data obtained from the same irradiations were published in 2007 by N. Patronis *et. al* [11].

1

Measured Reactions and Activation Method

In this chapter the energy diagrams for all the studied reactions will be presented, along with the decay properties of the residual nuclei. Moreover, the basic formalism for the cross section determination by means of the activation technique will be given.

1.1 The n+^{197}Au system

When a high energy neutron, for example 20.8 MeV, impinges on a ^{197}Au nucleus, the compound nucleus ^{198}Au is produced in a highly excited state and the possible exit channels are presented in Fig. 1.1. In the present work the ^{197}Au(n,2n) reaction channel was studied,

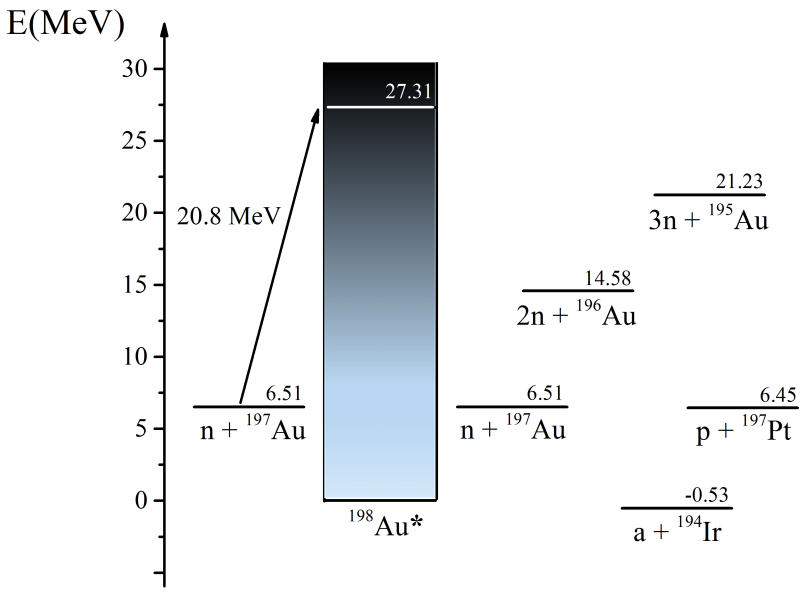

Figure 1.1: Energy diagram of the n+^{197}Au system. The atomic masses were adopted from the National Nuclear Data Center (NNDC) [93] and the calculations are described in detail in [33].

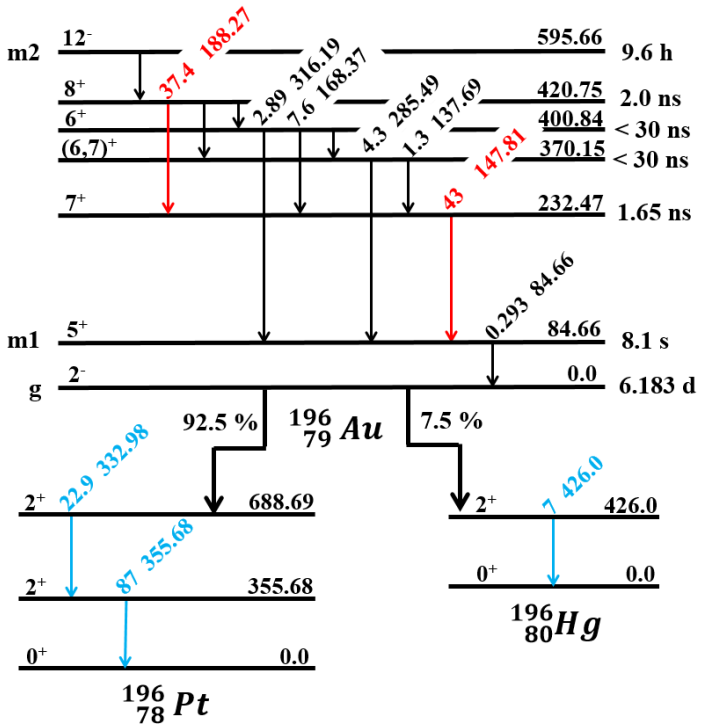

Figure 1.2: Simplified decay scheme for the de-excitation of the ground and isomeric states of the ^{196}Au nucleus. The intensities are obtained from the Lund/LBNL library [37] and all energies are given in keV.

in which the residual nucleus, namely the ^{196}Au, is unstable and decays by β^+ emission (92.5%) to ^{196}Pt and by β^- (7.5%) to ^{196}Hg (Fig. 1.2). The decay half-life of the ground state is 6.183 d and during its de-excitation several γ-rays are emitted, with the three most intense being 355.7, 333.0 and 426.0 keV. As shown in Fig. 1.2, evidently, by measuring them, the

$$^{197}Au(n,2n)^{196}Au^{g+m1+m2}$$

reaction cross section is determined, which includes the population of the ground, first and second isomeric states of ^{196}Au nucleus.

In addition, the nucleus can be produced in an excited state and populate one of the two isomeric states which lie at the excitation energies of 84.66 (m1) and 595.66 keV (m2), respectively. The former isomeric state decays with a relatively short half-life of 8.1 s, therefore it is not easy to measure it separately from the ground state, while the latter has a half-life of 9.6 h and thus it can be independently determined (with the energies of the two most intense γ-rays from its de-excitation being 147.8 and 188.3 keV).

At this point, it should be noted that the available intensities for the γ-rays of the ^{196}Au^{m2} metastable differ remarkably from one library to another ([37]- [39]) (see Table 1.1). In this respect, an effort on determining the correct intensities, guided by M. Majerle [94], was recently published [38]. Thus, in the present experimental cross section results for the ^{197}Au(n,2n)^{196}Au^{m2} reaction, intensity values obtained by the Lund/LBNL library [37] were adopted, as shown in Fig. 1.2, and cross section values obtained using the intensities of the work mentioned above [38] are also presented.

Table 1.1: γ-ray intensities for the de-excitation of $^{196}Au^{m2}$ residual nucleus [37–39].

Nucleus	γ-ray energy (keV)	γ-ray intensity (%) TOI [37]	NNDC [39]	Modified values [38]
$^{196}Au^{m2}$	147.81	43.0	43.5	43.0
	188.27	37.4	30.0	34.0
	168.37	7.6	7.8	5.9
	285.49	4.3	4.4	4.0
	316.19	2.89	3.00	2.7
	137.69	1.3	1.3	1.5

The decay properties of the daughter nuclei that were used for the cross section determination are presented in Table 1.2.

Table 1.2: Decay data used for the daughter nuclei.

Reaction	$T_{1/2}$	Eγ (keV)	Iγ (%)	Reference
^{197}Au(n,2n)$^{196}Au^{g+m1+m2}$	6.183 d	355.7	87.0	[37]
		333.0	22.9	[37]
		426.0	7.0	[37]
^{197}Au(n,2n)$^{196}Au^{m2}$	9.6 h	147.8	43.0	[37]
		188.3	37.4 & 34.0	[37] & [38]

1.2 The n+^{nat}Ir system

Natural iridium consists of two isotopes, namely the ^{191}Ir and the ^{193}Ir ones, with the latter being the most abundant (37.3 and 62.7 %, respectively). Due to the fact that natural Ir foils were used in the present measurements, it is useful to study the two Ir isotopes separately.

1.2.1 The n+^{191}Ir system

Similarly to section 1.1, when a 20.8 MeV neutron impinges on a ^{191}Ir nucleus, the compound nucleus ^{192}Ir is produced in a highly excited state and the possible exit channels are shown in Fig. 1.3. In the present work two of the open reaction channels were studied, namely the ^{191}Ir(n,2n) and ^{191}Ir(n,3n) ones.

The residual nucleus of the (n,2n) reaction, namely the^{190}Ir, is unstable and decays via electron capture (91.4%) and internal conversion (8.6%) to ^{190}Os (Fig. 1.4). The decay half-life of the ground state is 11.78 d and the de-excitation is accompanied by γ-ray emission with the energies of the three most intense γ-rays being 518.6, 558.0 and 569.3 keV. Due

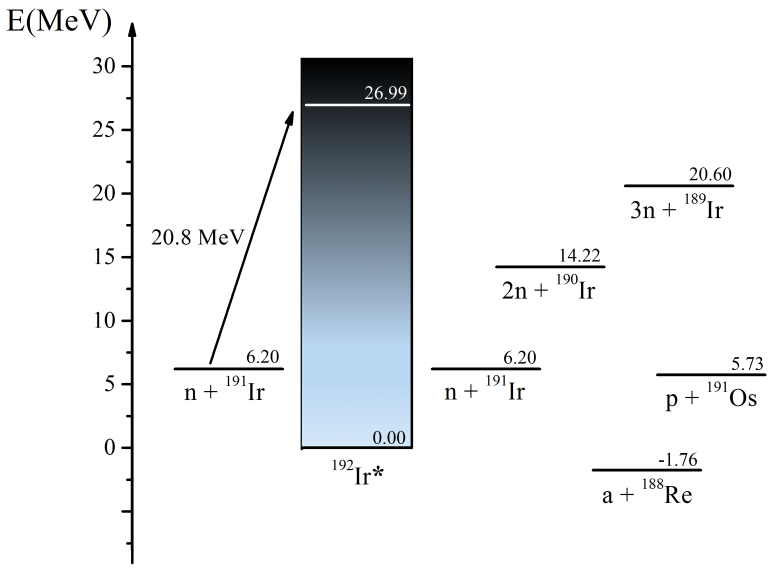

Figure 1.3: Energy diagram of the n+^{191}Ir system. The atomic masses were adopted from the National Nuclear Data Center (NNDC) [93] and the calculations are described in detail in [33].

to the fact that the 8.6% of the population of the m2 state decays to the ground state, the most appropriate summation to represent the experimental scenario in an activation measurement is given by the following expression [95]:

$$^{191}Ir(n,2n)^{190}Ir^{g+m1+0.086\,m2}$$

Thus, when measuring the 518.6, 558.0 and 569.3 keV γ-ray transitions, the population of the ground, first and a part of second isomeric states is included in the results.

Furthermore, the nucleus can be produced at an excited state and populate one of the two isomeric states at the excitation energies of 26.1 (m1) and 376.4 keV (m2), respectively. The former isomeric state decays with a half-life of 1.12 h by low energy γ-ray emission and due to the γ-ray high mass attenuation factor, its de-excitation can not be easily studied. The latter, having a half-life of 3.087 h, decays to ^{190}Os with a probability of 91.4% and can be independently determined by measuring the two most intense γ-rays (616.5 and 502.5 keV) emitted during its de-excitation.

The residual nucleus of the (n,3n) reaction on ^{191}Ir, namely ^{189}Ir, is unstable and decays by means of electron capture (100%) to ^{189}Os (Fig. 1.5) with a decay half-life 13.2 d. During its de-excitation several γ-rays are emitted and the most intense is the 245.1 keV one.

All the decay properties of the daughter nuclei that were used for the cross section determination are presented in Table 1.3.

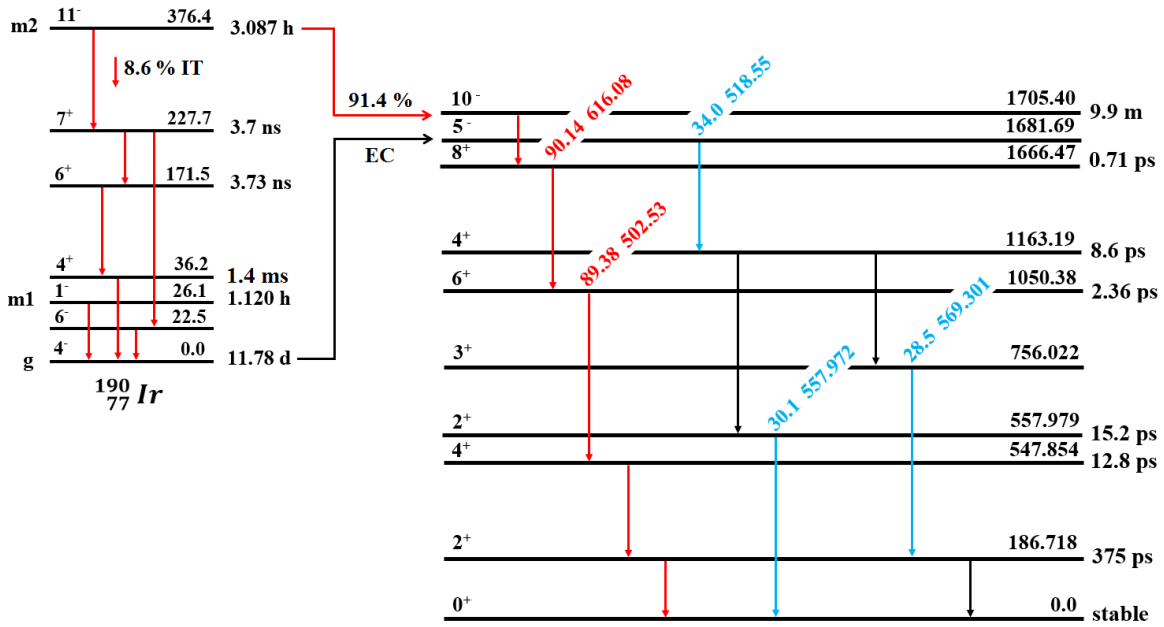

Figure 1.4: Simplified decay scheme for the de-excitation of the ground and isomeric states of the ^{190}Ir nucleus. The intensities are obtained from the NNDC Brookhaven National Laboratory library [39] and from refs. [95, 96]. All energies are presented in keV.

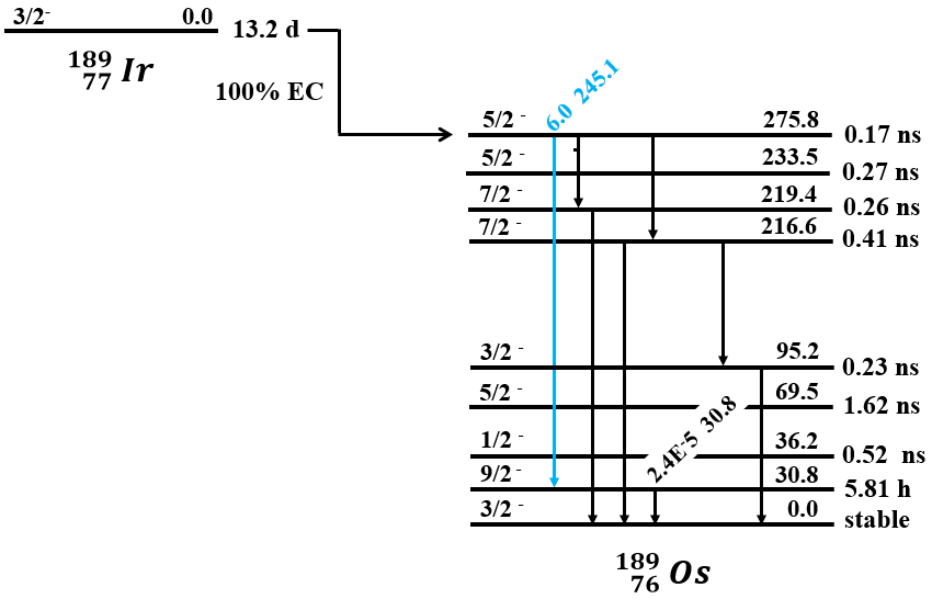

Figure 1.5: Simplified decay scheme for the de-excitation of the ^{189}Ir nucleus. The intensities are obtained from the NNDC Brookhaven National Laboratory library [39] and all energies are presented in keV.

Table 1.3: Decay data used for the daughter nuclei.

Reaction	$T_{1/2}$	Eγ (keV)	Iγ (%)	Reference
^{191}Ir(n,2n)^{190}Ir$^{g+m1+0.086\,m2}$	11.78 d	518.6	34.0	[39]
		558.0	30.1	[39]
		569.3	28.5	[39]
^{191}Ir(n,2n)^{190}Ir^{m2}	3.087 h	616.5	90.14	[39]
		502.5	89.38	[39]
^{191}Ir(n,3n)^{189}Ir	13.2 d	245.1	6.0	[39]

1.2.2 The n+^{193}Ir system

Concerning the neutron interaction on ^{193}Ir, the compound nucleus (^{194}Ir) is again produced in a highly excited state and the corresponding energy diagram is presented below (see Fig 1.6).

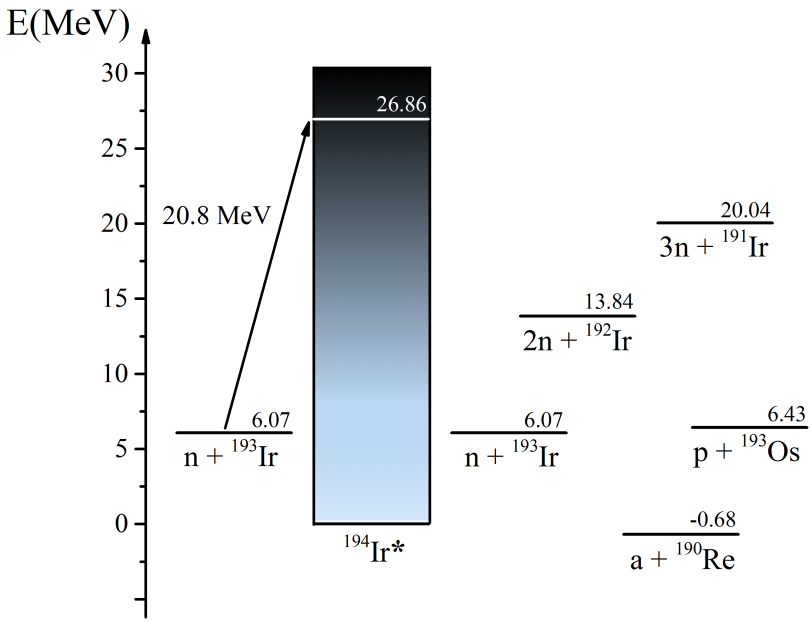

Figure 1.6: Energy diagram of the n+^{193}Ir system. The atomic masses were adopted from the National Nuclear Data Center (NNDC) [93] and the calculations are described in detail in [33].

In the present work the ^{193}Ir(n,2n) reaction channel was studied, in which the residual nucleus, namely the ^{192}Ir, is unstable and decays via electron capture (4.76%) to ^{192}Os and by β^- emission (95.24%) to ^{192}Pt (see Fig. 1.7). The decay half-life of the ground state is 73.829 d and the de-excitation is accompanied by γ-ray emission with the energies of

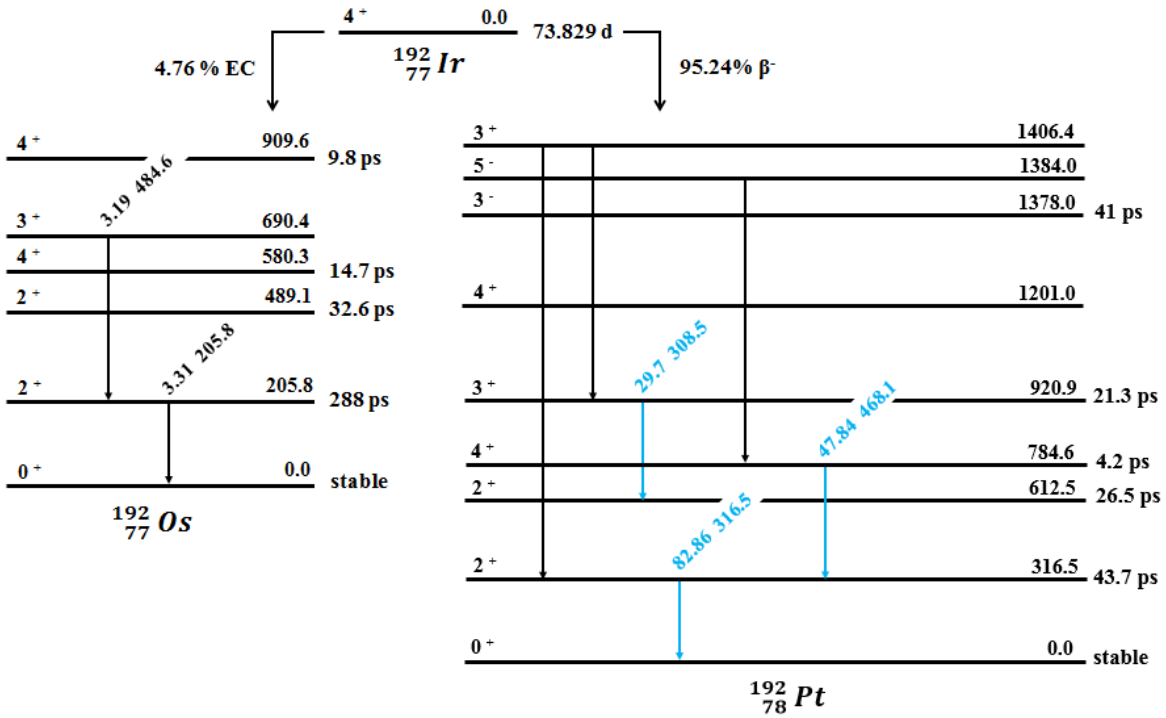

Figure 1.7: Simplified decay scheme for the de-excitation of the ^{192}Ir nucleus. The intensities are obtained from the NNDC Brookhaven National Laboratory library [39] and all energies are presented in keV.

the three most intense γ-rays being 316.5, 468.1 and 308.5 keV. Due to the fact that the γ-rays involved in the left brach in Fig. 1.7 have low intensities, only the γ-rays of the right branch were used. The decay properties of the daughter nucleus that were used for the cross section determination are presented in Table 1.4.

Table 1.4: Decay data used for the daughter nucleus.

Reaction	$T_{1/2}$	Eγ (keV)	Iγ (%)	Reference
^{193}Ir(n,2n)^{192}Ir	73.829 d	316.5	82.86	[39]
		468.1	47.84	[39]
		308.5	29.7	[39]

Another important issue concerning this reaction, is that the ^{192}Ir nucleus can also be produced by the ^{191}Ir(n,γ) reaction channel, which is open to low energy parasitic neutrons. In order to correct for this contribution, a recently applied analysis method was implemented and is described in 3.4.

1.3 Activation Method

The activation method is based on the measurement of radiation emitted during the decay of radioactive nuclei formed by irradiation of a material. When it comes to irradiations using neutron beams, the method is referred to as Neutron Activation Analysis (NAA) and it can be categorized according to whether γ-rays are measured during neutron irradiation (Prompt Gamma NAA - PGNAA) or at some time after the end of the irradiaton (Delayed Gamma NAA - DGNAA) (see Fig. 1.8). NAA is a very precise and non-destructive technique, mainly used to determine trace concentrations of elements in samples [97, 98] or to acquire information on the spatial distribution of a neutron field via neutron activation detectors [99]. In the present work, the DGNAA was implemented in order to determine the cross section of neutron induced reactions and the basic formulas are given below.

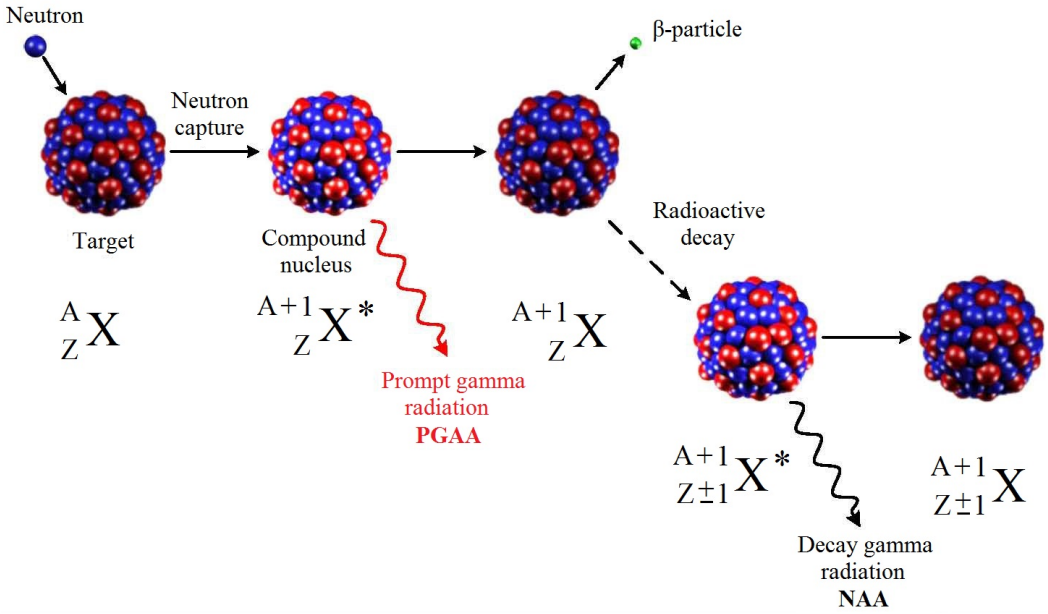

Figure 1.8: Schematic representation of the Neutron Activation Analysis (NAA) method [100].

When a projectile x impinges on a target nucleus X and a nuclear reaction (x+X $\rightarrow$ Y+y) with two products, namely the residual nucleus Y and the ejectile y, takes place, the production of the radioactive nuclei Y is described by:

$$\frac{dN}{dt} = \sigma \cdot f(t) \cdot N_\tau - \lambda \cdot N \tag{1.1}$$

where

σ: the cross section of the X(x,y)Y reaction

$f(t)$: the time dependent x beam flux impinging on the target

N_τ: the number of the X target nuclei

λ: the decay constant of the Y produced nuclei

N: the number of the Y produced nuclei

The general solution of the differential equation 1.1 is the following (see Appendix A for more details):

$$N(t) = \frac{\int e^{\lambda\, dt}\, \sigma\, N_\tau\, f(t) + C}{e^{\lambda\, dt}} \tag{1.2}$$

The total x beam flux impinging on the X target during the irradiation time t_B is:

$$\Phi = \int_0^{t_B} f(t)\, dt \tag{1.3}$$

Therefore, the number of the produced nuclei during the irradiation time t_B, can be written as:

$$N_p(t_B) = \sigma\, N_\tau\, \Phi\, \frac{\int_0^{t_B} e^{\lambda\, dt}\, f(t)\, dt}{\int_0^{t_B} f(t)\, dt}\, e^{-\lambda\, t_B} \tag{1.4}$$

where

$$f_c = \frac{\int_0^{t_B} e^{\lambda\, dt}\, f(t)\, dt}{\int_0^{t_B} f(t)\, dt}\, e^{-\lambda\, t_B} \tag{1.5}$$

is a correction factor for the produced nuclei which decayed during the irradiation. Thus, the number of the produced nuclei during the irradiation is given by the following expression:

$$N_p = \sigma\, N_\tau\, \Phi\, f_c \tag{1.6}$$

By using the 1.6 equation, three types of problems can be solved:

- Case 1: (Φ, N_τ) known $\xrightarrow{\text{find}}$ σ
- Case 2: (σ, N_τ) known $\xrightarrow{\text{find}}$ Φ
- Case 3: (Φ, σ) known $\xrightarrow{\text{find}}$ N_τ

Therefore, when measuring a reaction cross section with the activation method relative to a reference one, two of the aforementioned problems are solved (Case 1 and Case 2).

Step 1: Use the reference reaction (σ, N_τ known) to find $\Phi_{reference}$:

$$\Phi_{reference} = \frac{(N_p)_{reference}}{(\sigma\, N_\tau\, f_c)_{reference}} \tag{1.7}$$

Step 2: Find the beam flux ratio in reference and measured foil C_Φ (very close to 1, can also be assumed to be equal to 1):

$$C_\Phi = \frac{\Phi_{reference}}{\Phi_{measured}} \;\Rightarrow\; \Phi_{measured} = \frac{\Phi_{reference}}{C_\Phi} \tag{1.8}$$

Step 3: Find the measured cross section (Φ, N_τ known):

$$\sigma_{measured} = \frac{(N_p)_{measured}}{(N_\tau\, \Phi\, f_c)_{measured}} \tag{1.9}$$

By combining equations 1.7, 1.8 and 1.9, the measured cross section can be written as:

$$\sigma_{measured} = \sigma_{reference}\, \frac{(N_p)_{measured}}{(N_p)_{reference}}\, \frac{(N_\tau\, f_c)_{reference}}{(N_\tau\, f_c)_{measured}}\, C_\Phi \tag{1.10}$$

2

Experimental Part

In this chapter, all the available information on the experimental measurements (such as, neutron facility, parasitic neutrons, neutron monitoring, experimental setups and activation measurements) will be described in great detail.

2.1 Neutron Facility

The measurements were performed at the 5.5 MV Tandem T11/25 Accelerator Laboratory of NCSR "Demokritos" in Athens (see Fig. 2.1).

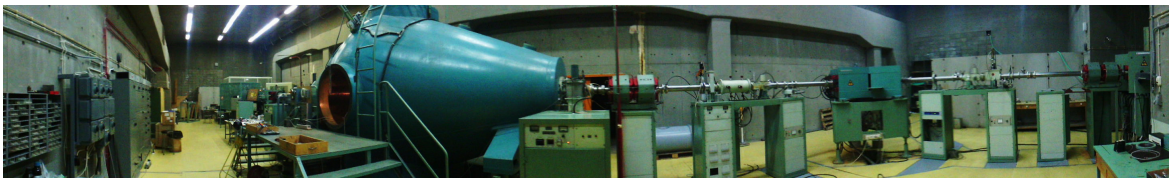

Figure 2.1: 5.5 MV Tandem T11/25 Accelerator of NCSR "Demokritos" in Athens [26].

The quasi-monoenergetic neutron beams were produced by means of the ^{3}H(d,n)^{4}He (D-T) reaction (see Fig. 2.2). The large positive Q-value (Q = 17.59 MeV) and the low atomic number make it possible to produce high yields of fast neutrons even at low incident deuteron energies [27].

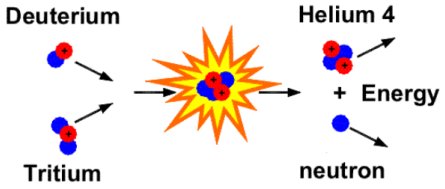

Figure 2.2: Schematic representation of the D-T reaction [101].

The cross section of the D-T reaction is shown in Fig. 2.3 over a wide energy range.

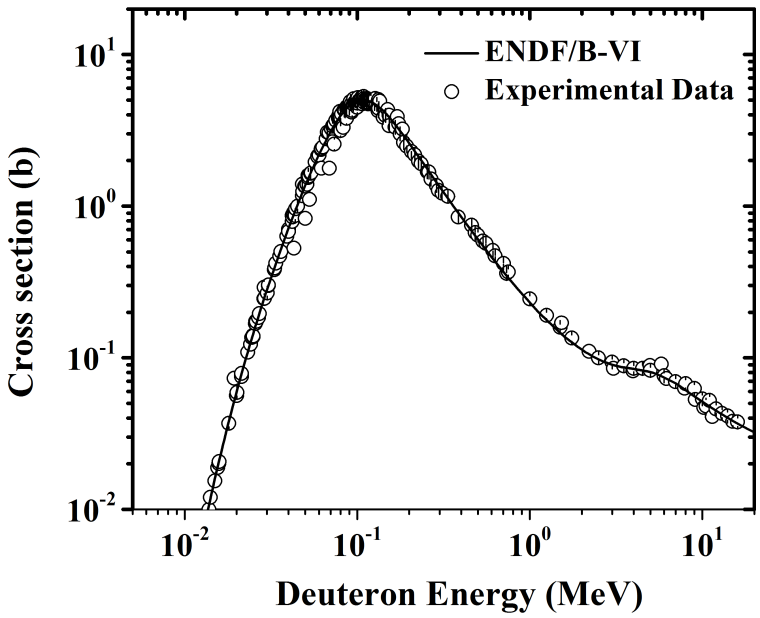

Figure 2.3: Experimental data and the ENDF/B-VI evaluation for the cross section of the ^{3}H(d,n)^{4}He (D-T) reaction relative to the deuteron beam energy [9, 28].

In the present measurements, the deuteron beam energies impinging on the T target varied between 1 and 4.3 MeV, whereas the cross section of the D-T reaction in this energy range is presented in Fig. 2.4.

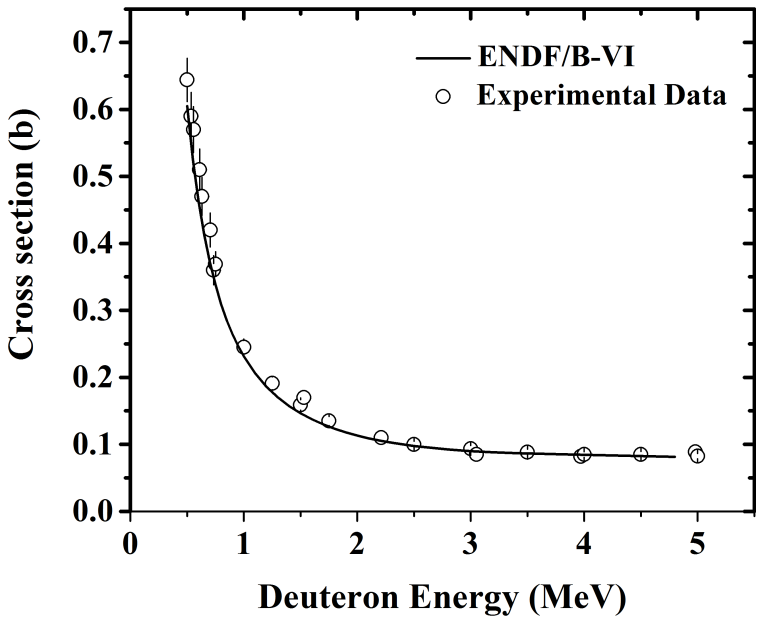

Figure 2.4: Experimental data and the ENDF/B-VI evaluation for the cross section of the ^{3}H(d,n)^{4}He (D-T) reaction relative to the deuteron beam energy, in the energy region of interest [9, 28].

The Tandem Accelerator transition is reduced for low energy beams, therefore in order to achieve a sufficient beam current at low beam energy irradiations, the deuteron beam

was accelerated at a higher energy and then passed through a 10 μm Mo foil placed in front of the tritium target, as shown in Fig. 2.5. In this way, the decelerated deuterons impinged on the T target with a higher probability to react with the target atoms, due to the higher D-T cross section at lower energies. This technique was implemented in two of the irradiations in order to send 1 and 1.5 MeV deuterons on the T target, instead of 2 and 2.5 MeV respectively. The uncertainty of the neutron energy in all cases (with and without Mo foils) was estimated by coupling the NeuSDesc [34] and MCNP5 [35] codes and the corresponding procedure and results are presented in section 2.4.2.

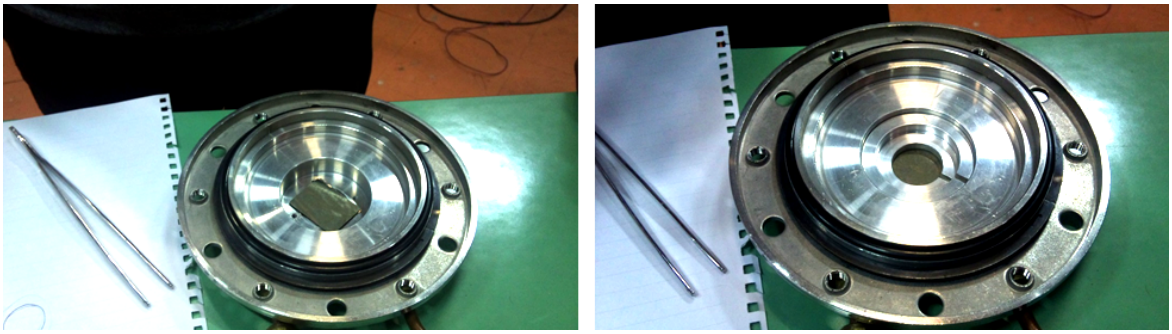

Figure 2.5: The placement of the 10 μm Mo foil in the flange of the T target.

Two solid Ti-tritiated targets consisting of a Ti-T layer on a 1 mm thick Cu backing, for good heat conduction, were used. The details for each one are presented in the following table (Table 2.1). More specifically, "Target 1" was placed in the flange so that the deuteron beam passes through a 10 μm Mo foil before hitting the T target, as shown in Fig. 2.5, and was used for the measurements at neutron energies between $\sim$ 15-17 MeV. For the higher neutron energies, "Target 2" was placed in the flange and no foils were used, since the deuteron beam from the accelerator had enough intensity to produce high neutron flux. Moreover, the TiT target assemblies were air cooled during all the irradiations.

Table 2.1: The information obtained from the construction company (SODERN [102]) for the two tritium targets used in the present work.

Name	Production Date	Mass (μm/cm^2)	T / Ti Ratio	Tritium Activity (GBq)
Target 1*	14 June 2007	2123.5	1.543	373.33
Target 2	15 January 2015	2305.0	1.530	400.00

* Target 1 was placed in the flange so that the deuteron beam passes through a 10 μm Mo foil before hitting the T target.

Figure 2.6: The placement of the T target in the flange. The process took place in an airtight isolation bag in an outdoor area due to the high T target activity and its high probability to adhere to air molecules.

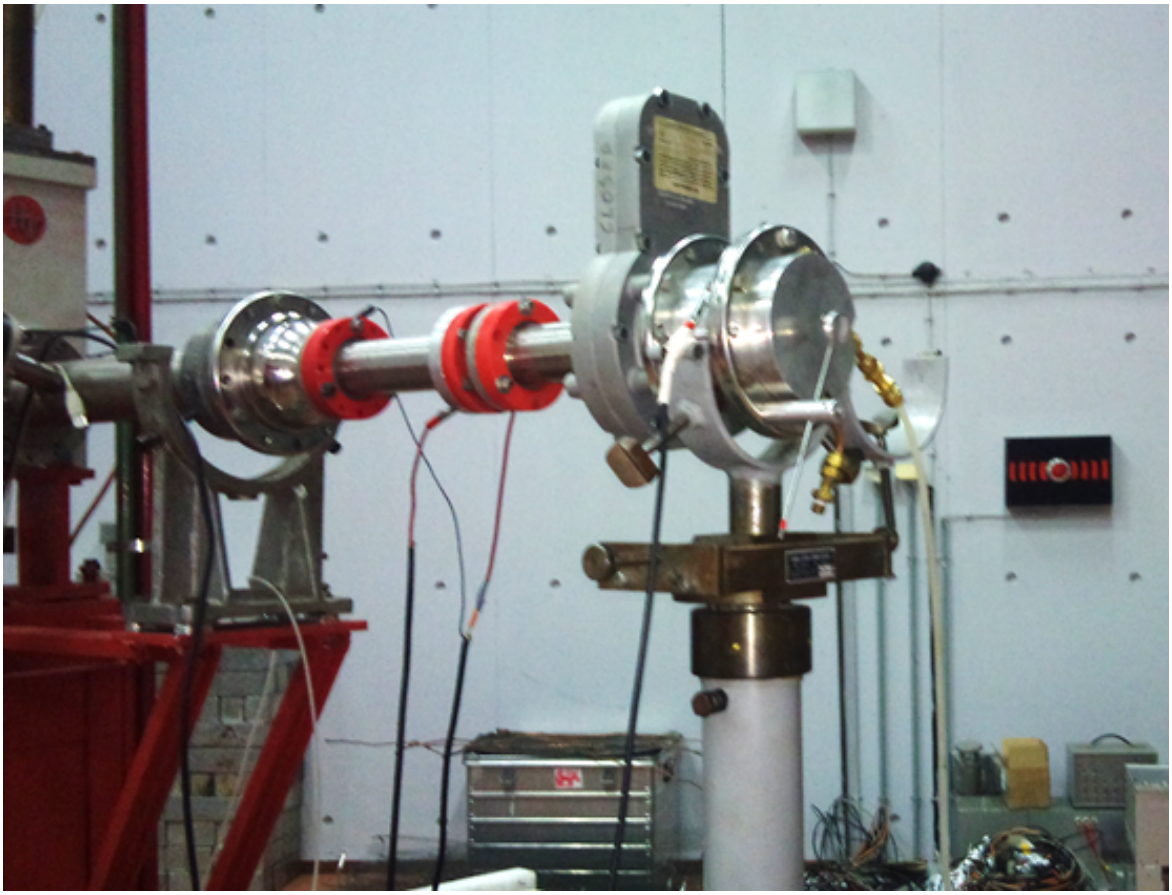

Figure 2.7: The end of the irradiation line in the experimental hall of the Tandem Acceletator Laboratory of NCSR "Demokritos".

2.2 Parasitic Neutrons

Monoenergetic neutrons can be produced by two-body reactions, however a practical source will not only produce these primary neutrons, but also "background" neutrons [29]. These neutrons can also be called "parasitic" and vary in energy from the thermal region up to a few MeVs [30].

Parasitic neutrons may stem from:

- Break-up

  For deuteron energies higher than 3.7 MeV, the break-up reaction cross sections rise significantly. Therefore, as the deuteron energy increases the ^{3}H(d,np)^{3}H, ^{3}H(d,2n)^{3}He, ^{3}H(d,nd)^{2}H, ^{3}H(d,2np)^{2}H and ^{3}H(d,3n)2p reactions gradually start to contribute to the neutron production [32].

- Target

  On the Ti-tritiated target, ^{12}C nuclei are abundant from the carbon built up process, due to the presence of C in the beam line and vacuum system. Therefore, secondary neutrons are produced by the ^{12}C(d,n)^{13}N reaction. Moreover, as shown in previous publications [2], ^{2}H beam is implanted in the tritium target resulting in background neutrons from the ^{2}H(d,n)^{4}He reaction [29, 30]. It should be noted that although in the case of gas targets the contribution from these background neutrons can relatively easily be determined via gas-in/gas-out measurements, for solid targets the task to perform a blank measurement using a non tritium containing dummy target is a somewhat more demanding task [27].

- Beam Line

  Neutron producing reactions can also be performed when the deuteron beam interacts with materials of beam pipes, collimators and other surroundings. For example, parasitic neutrons can be produced via the ^{16}O(d,n)^{17}F reaction, since ^{16}O nuclei are always present in the beam line due to oxidization processes [30].

- Room

  Due to the fact that the neutrons from the D-T reaction are emitted almost isotropically, there is a high room neutron background. For instance, in the experimental hall of the Tandem Acceletator Laboratory of NCSR "Demokritos", at ∼2 m distance from the neutron source, there are some water tanks in order to prevent neutrons from exiting the room. Apart from these, many objects and materials exist in the experimental area, leading to neutron scattering and thus in a low energy neutron tail in the spectrum.

The main reactions producing parasitic neutrons are presented in Table 2.2 along with their Q-values and energy thresholds.

Table 2.2: Main reactions producing parasitic neutrons along with their origin, energy thresholds and Q-values. All values were taken from the NNDC Q-value calculator [31].

Origin	Reaction	Threshold (MeV)	Primary Neutron Beam Energy (MeV) *	Q-value (MeV)
Target (Implantation)	^{2}H(d,n)^{4}He	0.000	-	3.269
Target (Built up)	^{12}C(d,n)^{13}N	0.328	14.960	-0.281
Beam Line (Oxidization)	^{16}O(d,n)^{17}F	1.829	17.710	-1.625
Break-up	^{3}H(d,np)^{3}H	3.710	20.304	-2.225
Break-up	^{3}H(d,2n)^{3}He	4.984	21.841	-2.988
Break-up	^{3}H(d,nd)^{2}H	10.435	-	-6.257
Break-up	^{3}H(d,2np)^{2}H	14.145	-	-8.482
Break-up	^{3}H(d,3n)2p **	17.876	-	-10.707

* The primary neutron beam energies were estimated by means of the NeuSDesc code for the "Target 2" (see Table 2.1), therefore there is no estimation above 10 MeV deuteron beam energy.
** The energy threshold and the Q-value for this reaction were adopted from ref. [32].

2.3 Neutron Monitoring

In order to record the neutron beam fluctuations, a BF_3 detector (see Fig. 2.8) was placed at a distance of ~3 m from the neutron source.

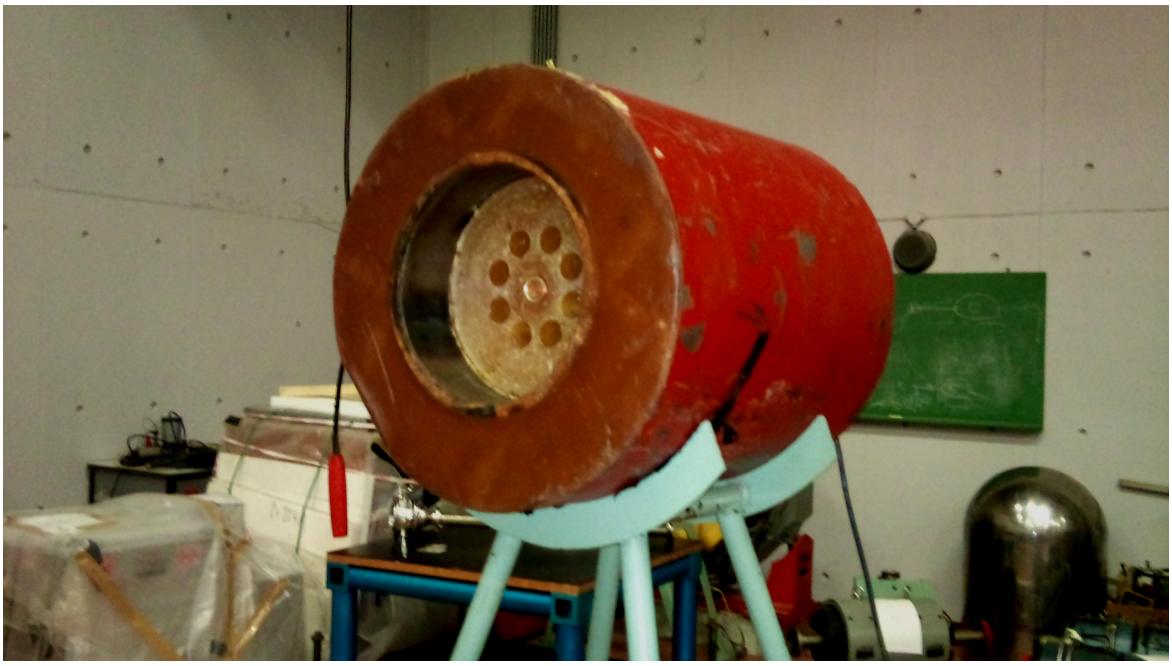

Figure 2.8: BF_3 detector used for monitoring the neutron beam fluctuations during the irradiations.

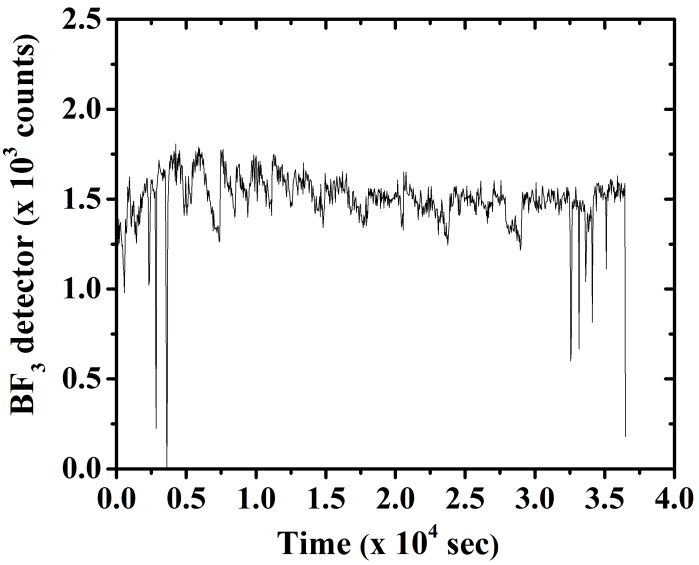

Figure 2.9: Neutron beam fluctuations for the irradiation at 20.0 MeV neutron beam energy. The irradiation lasted for 36480 sec and the BF_3 detector data were stored every 40 s.

This detector is a proportional counter which employs the following reactions:

^{10}B(n,α)^{7}Li	Q = 2.792 MeV	(6%)
^{10}B(n,α)^{7}Li*	Q = 2.310 MeV	(94%)

while the produced nuclei (^{7}Li and ^{4}He) are detected by losing energy in the gas of the detector. The aforementioned reactions present high cross section values for low energy neutrons, while the opposite (low cross sections) holds for high energy neutrons. In this respect, the BF_3 detector was placed inside a paraffin cylinder, so that the neutrons lose a part of their energy by successive collisions.

The BF_3 data were stored at regular time intervals by means of a multichannel scaler and then the obtained information on the beam instabilities (see Fig. 2.9) was used in the off-line analysis to correct for the produced nuclei which decayed during the irradiation (factor f_c). More specifically, the regular time intervals are denoted as dt in Eq. 3.3, while the collected counts during this period are defined by the factor $f(t)$.

The BF_3 detector acts only as a neutron counter, which means that it can not provide any information neither for the neutron energy, nor for the number of the neutrons. The absolute neutron flux of the main energy peak in the neutron spectrum is determined via reference reactions, while in the framework of the present thesis, a recently applied analysis method was used in order to qualitatively and quantitatively estimate the low energy parasitic neutrons (see section 3.4).

2.4 Irradiations

Six irradiations were performed at the neutron facility of the Tandem Acceletator Laboratory of NCSR "Demokritos". The date on which the measurements were performed, the TiT target used, the typical beam current, the deuteron energy, the neutron energy and the duration of each irradiation are presented in Table 2.3.

Table 2.3: Experimental details concerning the irradiations.

Date of measurement	Name of TiT target	E_d (MeV)	E_n (MeV)	I (μA)	Irradiation time (h)
April 2013	Target 1	$2.0 \xrightarrow[\text{Mo}]{10\mu m} 1.0$	15.3 ± 0.5	1.5	26.1
April 2013	Target 1	$2.5 \xrightarrow[\text{Mo}]{10\mu m} 1.5$	17.1 ± 0.3	1.0	96.1
January 2017	Target 2	2.0	17.9 ± 0.3	0.3	9.7
January 2017	Target 2	2.7	18.9 ± 0.3	0.5	27.8
March 2015	Target 2	3.5	20.0 ± 0.2	0.2	10.1
March 2015	Target 2	4.3	20.9 ± 0.2	0.3	32.4

As shown in Table 2.3, the uncertainty of the lowest neutron energy (15.3 MeV) is larger than of the rest. This can be attributed not only to the existence of the Mo foils before the TiT target, but also to the low deuteron energy, since the lower the latter, the higher the energy loss in the assembly materials. This is also verified by the uncertainties of the higher neutron energies (i.e 20.0 and 20.9 MeV) which are even smaller, since the deuterons with higher energies do not lose that much energy in the TiT target. The uncertainies of all the neutron energies were estimated by coupling the NeuSDesc [34] and MCNP5 [35] codes and the corresponding procedure and results are presented in section 2.4.2.

2.4.1 Experimental setup

The experimental setups for each of the six irradiations are presented in Fig. 2.10. In each case, high purity Al, Au and Ir foils (0.4-0.5 mm in thickness and 13-14 mm in diameter) were included in the target assembly, while the measured samples were placed near the reference ones in order to accurately determine the neutron flux. Moreover, during the irradiations performed in the framework of the present thesis, some more samples were also placed in the experimental setups (Am, Hf and Er targets, see Fig. 2.10), but the corresponding data belongs to other separate projects. Furthermore, in order to study various energy regions of the neutron spectrum, several reactions with different thresholds were used (see Table 2.4). In this table, the threshold of the measured reactions are also presented.

Table 2.4: Half-lives, γ-ray energies, intensities of the most intense γ-rays and reaction thresholds for both measured and reference reactions.

Reaction	$T_{1/2}$	E_γ (keV)	I_γ (%)	$E_{threshold}$ (MeV)	$E_{threshold}$* (MeV)
Measured reactions					
^{197}Au(n,2n)^{196}Au	6.183 d	355.7	87.0	8.11	8.25
^{191}Ir(n,2n)^{190}Ir	11.78 d	518.6	34.0	8.07	8.20
^{191}Ir(n,3n)^{189}Ir	13.2 d	245.1	6.0	14.48	15.00
^{193}Ir(n,2n)^{192}Ir	73.829 d	316.5	82.86	7.81	8.00
Reference reactions					
^{27}Al(n,α)^{24}Na	14.9590 h	1368.6	100	3.25	6.75
^{93}Nb(n,2n)^{92}Nb^m	10.15 d	934.5	99.15	8.93	9.09
^{197}Au(n,γ)^{198}Au	2.6941 d	411.8	95.62	0.0	0.0
^{115}In(n,inl)^{115}In^m	4.486 h	336.2	45.9	0.0	0.5

* This column corresponds to the neutron energies above which the reactions have sufficient cross setions values to give high reaction rates.

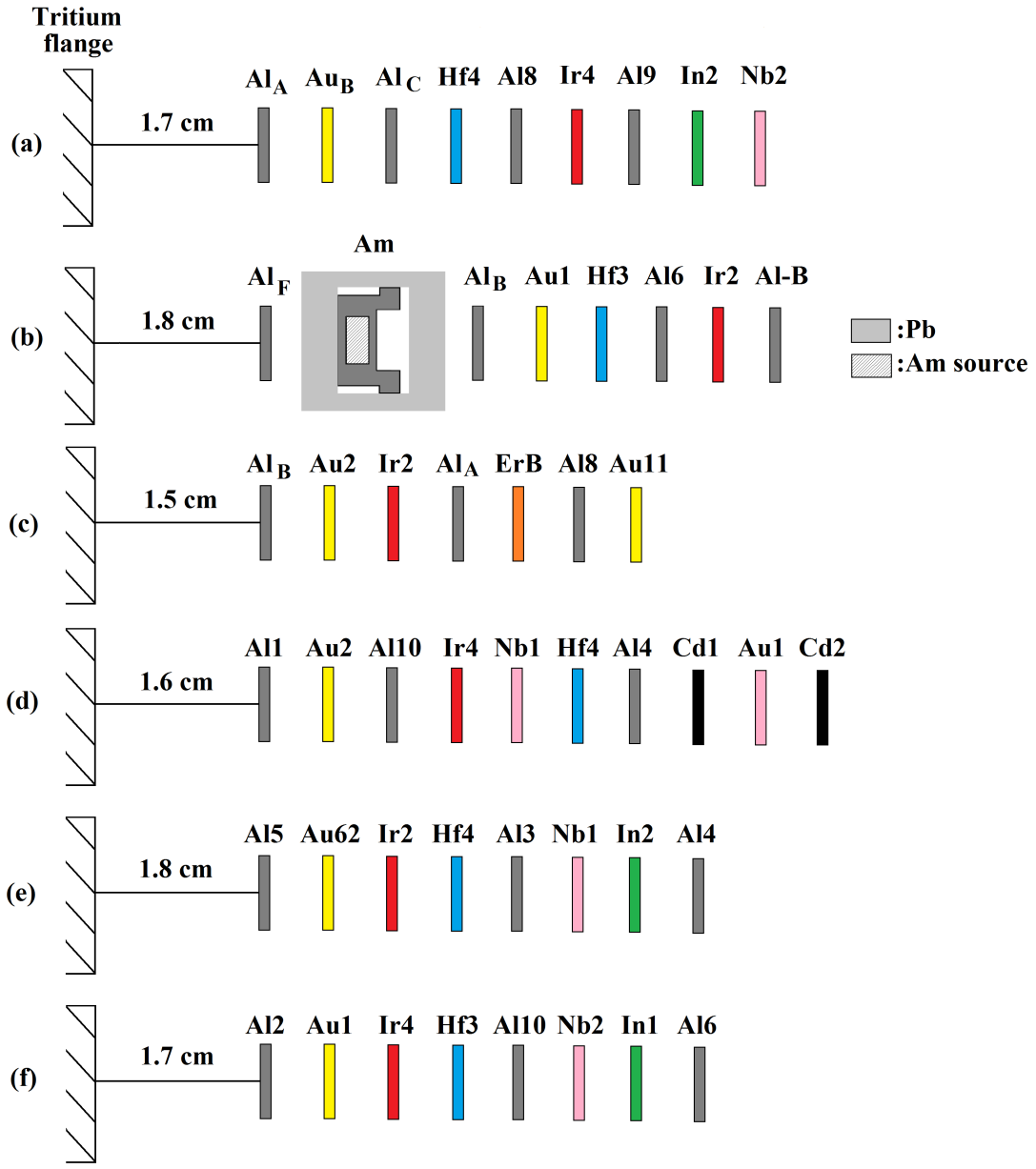

Figure 2.10: Schematic representation of the experimental setups for the irradiations at: (a) 15.3 MeV, (b) 17.1 MeV, (c) 17.9 MeV, (d) 18.9 MeV, (e) 20.0 MeV and (f) 20.9 MeV neutron beam energies, respectively.

It should be noted that there is no gap between the successive foils, but they are presented in this way (in Fig. 2.10) for clarity. Moreover, the Cd1 and Cd2 foils in Fig. 2.10d, were placed in the front and back side of the Au1 one as low energy neutron absorbers.

In addition, as shown in Fig. 2.10, all the samples were placed at a distance of ∼2 cm from the Ti-tritiated target, taking into account the 2 mm Al flange window and the 1 mm Cu backing of the T target. In this way, the angular acceptance of the samples is limited to ±19° where the neutron beam can practically be considered as monoenergetic (concerning the main peak of the neutron beam and ignoring the parasitic neutron tail) (see Fig. 2.11).

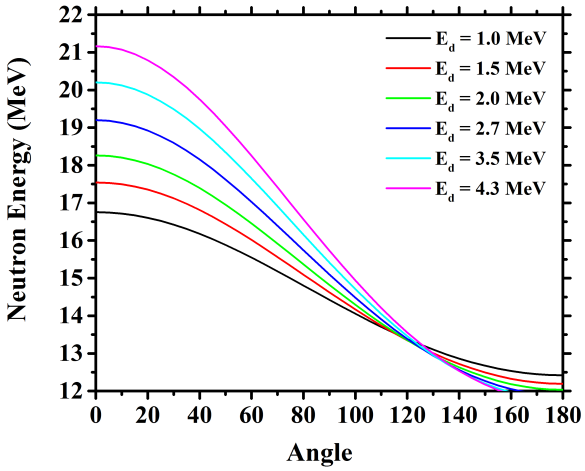

Figure 2.11: The neutron energy with respect to the angle, for each irradiation, according to the D-T reaction kinematics.

In Figs. 2.12(a) and 2.12(b), photographs taken before the beginning of the irradiations (mentioned also in Figs. 2.10(a) and 2.10(b)) are presented, for 15.3 and 17.1 MeV neutron beam energies, respectively.

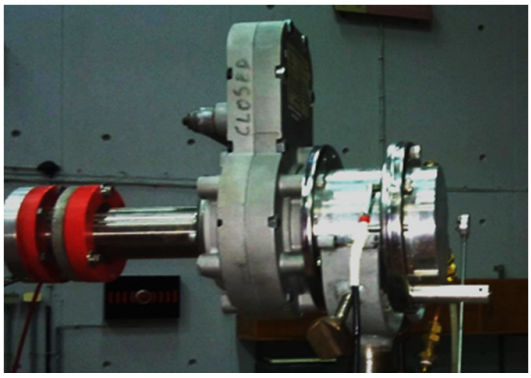

(a) Irradiation with 15.3 MeV neutrons.

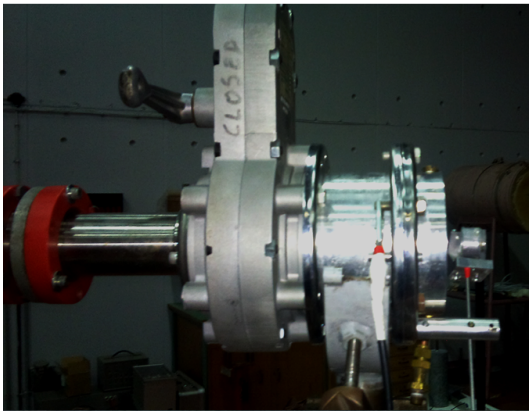

(b) Irradiation with 17.1 MeV neutrons.

Figure 2.12: Photographs taken before the beginning of the irradiations.

2.4.2 Neutron Energy and Neutron Flux

The study of neutron energy spectra generated by deuterons on the Ti-tritiated target was carried out using the NeuSDesc (Neutron Source Description) code, developed at IRMM [34]. The program takes into consideration the energy loss, energy spread and angular straggling of the deuterons in the target assembly through the Monte Carlo simulation program SRIM-2008 and calculates average neutron energies, fluences and resolutions [103]. A typical NeuSDesc input includes the deuteron energy (E_d), the Ti-tritiated target details (Ti thickness and T/Ti ratio), the entrance foil along with its thickness, the neutron emission angle, the mean deuteron beam current during the irradiation, the detector radius in which the neutron fluence is determined and the distance from the Ti-tritiated target. Moreover, the NeuSDesc program includes the option of creating an MCNP [35] file containing the description of the neutron field (sdef -source definition- card) at an arbitrary surface in space. An example of the input parameters used in NeuSDesc to produce the sdef card for the irradiation at 20.9 MeV is shown in Fig. 2.13.

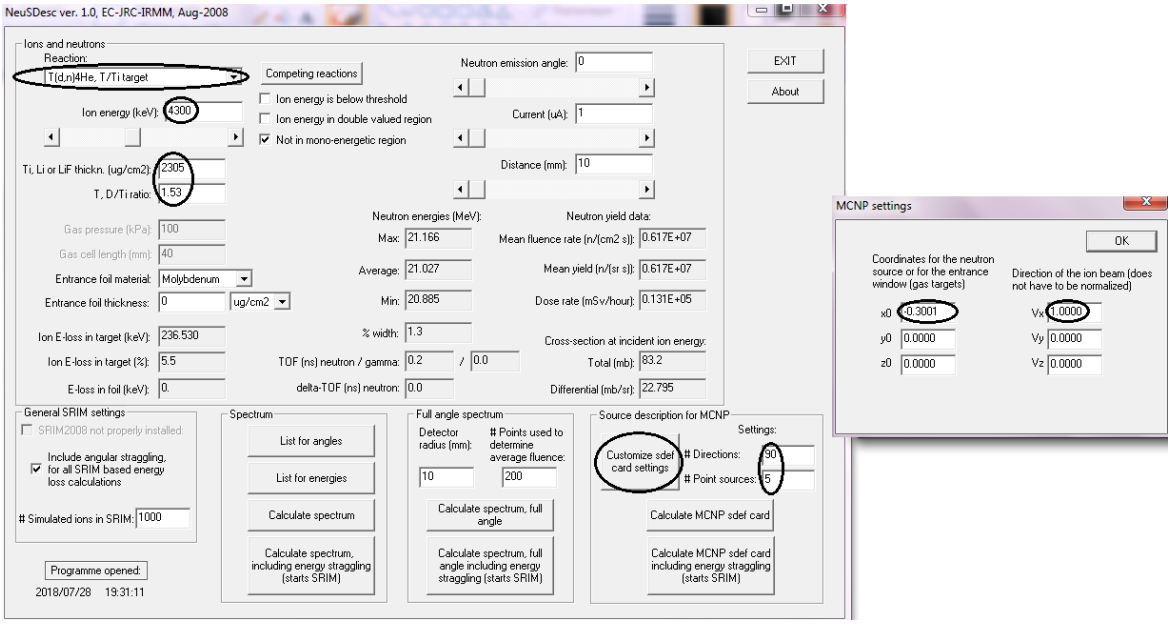

Figure 2.13: NeuSDesc interface. In this figure the input parameters of interest have been marked and tuned so as to produce the neutron source description card (sdef card) for the irradiation at 20.9 MeV. The MCNP settings depend on the description of the irradiation setup in MCNP5.

The NeuSDesc output file (sdef card)[1] was used for Monte Carlo simulations by means of the MCNP5 [36] code to investigate the neutron fluence in the successive foils, by taking into account the detailed geometry of the experimental setup for each irradiation (Fig. 2.10). Therefore, the neutron beam energies along with their uncertainties that were presented in Table 2.3, were determined by coupling the NeuSDesc and MCNP5 codes, by using (in the NeuSDesc code) the input parameters shown in Fig. 2.14.

[1]It should be noted that the produced sdef card is a text file which has a size of ∼8000 lines, therefore it has not been included in any of the appendices concerning MCNP5 simulations.

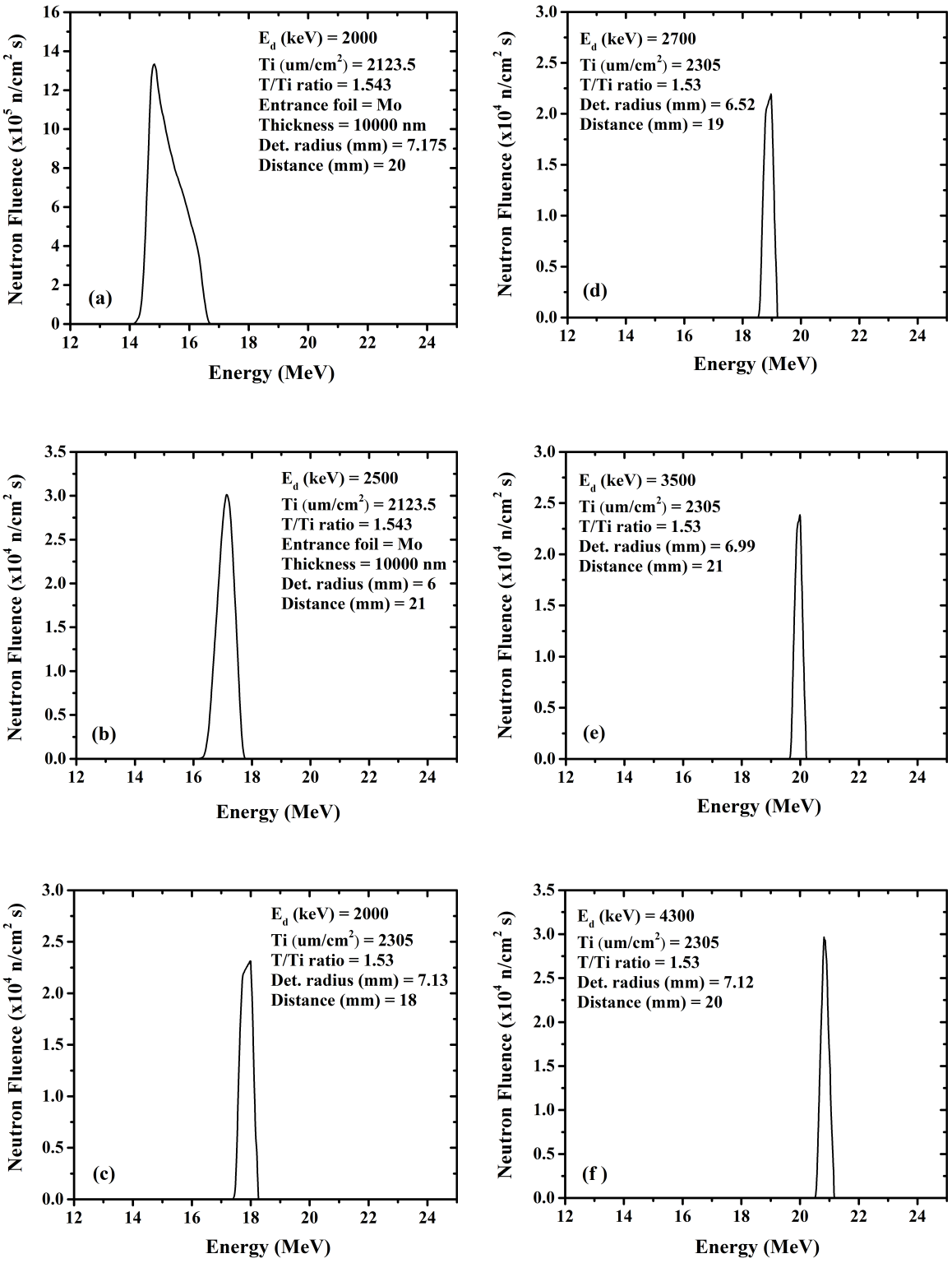

Figure 2.14: The main peak of the neutron energy spectra for the irradiations at (a) (15.3 ± 0.5) MeV, (b) (17.1 ± 0.3) MeV, (c) (17.9 ± 0.3) MeV, (d) (18.9 ± 0.3) MeV, (e) (20.0 ± 0.2) MeV and (f) (20.9 ± 0.2) MeV neutron beam energies, according to the NeuSDesc code [34]. The mean neutron beam energy and its error for the six irradiations were estimated by means of these subfigures. The input parameters used in the NeuSDesc code are also presented, except for the neutron emission angle and the typical deuteron beam current, which were assumed to be 0° and 1 μA respectively, in all cases. The detector radius was considered as the radius of the first (with respect to the neutron source) Al foil and the distance from the Ti-tritiated target is taken from Fig. 2.10 increased by 3 mm, which correspond to the Cu backing (1 mm) and the Al flange window (2 mm) thicknesses.

For example, the end of the irradiation line along with the experimental setup for the irradiation at 18.9 MeV neutron beam energy (see Fig. 2.10d) were simulated using the MCNP5 code as shown in Fig. 2.15.

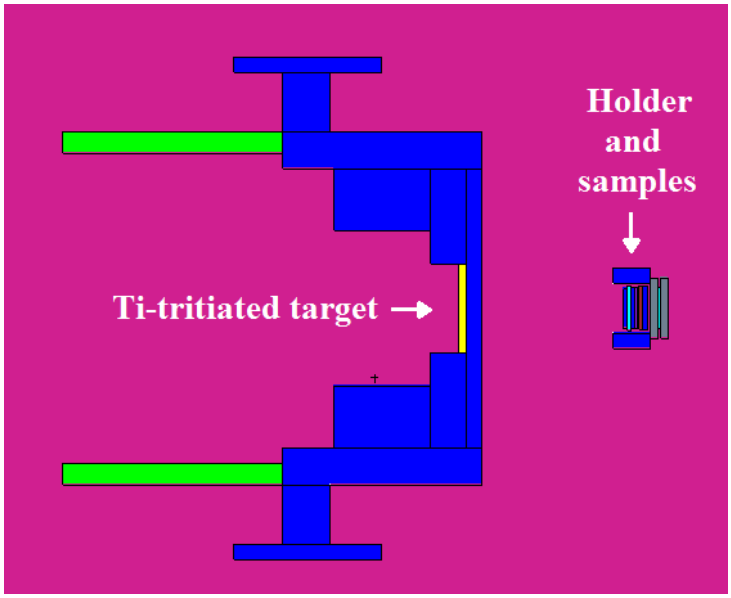

Figure 2.15: Simulated geometry of the irradiation setup at 18.9 MeV neutron beam energy. The figure is obtained from the Visual Editor of the MCNP5 code. The three last foils (see also Fig. 2.10d, Cd1, Au1 and Cd2) are placed behind the holder with the other foils.

The results of the simulations reproduced very well the experimental fluences for all the irradiations and both simulated and experimental fluences are presented in Fig. 2.16. The input files of the MCNP5 code for each irradiation are given in Appendix B. In some of the simulations the distance of the first Al foil (with respect to the neutron source) from the tritium flange was increased, compared to the value shown in Fig. 2.10, in order to achieve the best agreement between experiment and simulation. This modification concerning simulations is quite fair for two reasons. Firstly, the distances mentioned in Fig. 2.10 may not be so accurately measured and secondly, this modification does not affect the NeuSDesc calculations concerning the neutron beam energy and its uncertainty (Fig. 2.14).

From the subfigures (2.16a-2.16f), the necessary quantities for the determination of the measured reaction cross sections are the following two:

- The experimental neutron fluences in the reference foils placed in front (with respect to the neutron source) of the measured ones, either Au or Ir (factor $\Phi_{reference}$, Eq. 1.7).
- The ratio of the neutron fluences in reference and measured foils (factor C_{Φ}, Eq. 1.10).

These quantities lead to the determination of the neutron fluence in the samples of interest, either Au or Ir (factor $\Phi_{measured}$, Eq. 1.8). As it was mentioned above, there is a good agreement between the experimental and simulated neutron fluences of the reference foils and this indicates that the simulations are successful and can be trusted for the estimation of the neutron fluence.

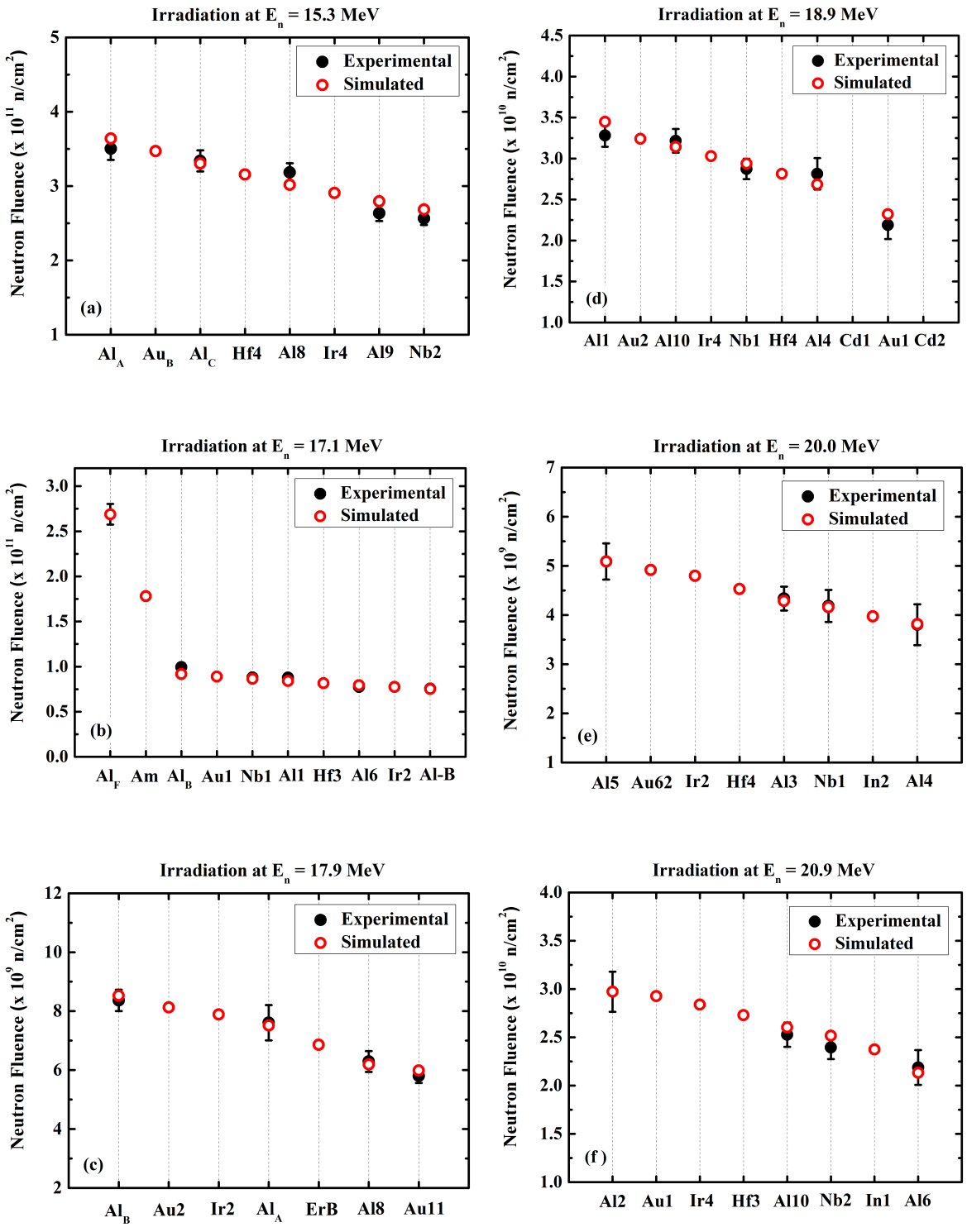

Figure 2.16: Experimental neutron fluences in the reference foils along with the simulated ones, obtained by means of the MCNP5 code, for the irradiations at (a) (15.3 ± 0.5) MeV, (b) (17.1 ± 0.3) MeV, (c) (17.9 ± 0.3) MeV, (d) (18.9 ± 0.3) MeV, (e) (20.0 ± 0.2) MeV and (f) (20.9 ± 0.2) MeV neutron beam energies. The distances of the first Al foil from the Ti-tritiated target in the simulated geometries are (a) 2.0 cm, (b) 2.0 cm, (c) 2.0 cm, (d) 1.9 cm, (e) 1.8 cm and (f) 1.7 cm, respectively. In Fig. 2.16d, the simulated flux was not estimated for the Cd1 and Cd2 foils, since they were placed in the front and back side of the Au1 one as low energy neutron absorbers.

2.5 Measurements

After the end of the irradiations, the induced activity on the Au, Ir and reference foils was measured using high purity germanium detectors (HPGe) of 100%, 80%, 56% and 16% relative efficiency. The activity measurements of all samples were carried out at a distance

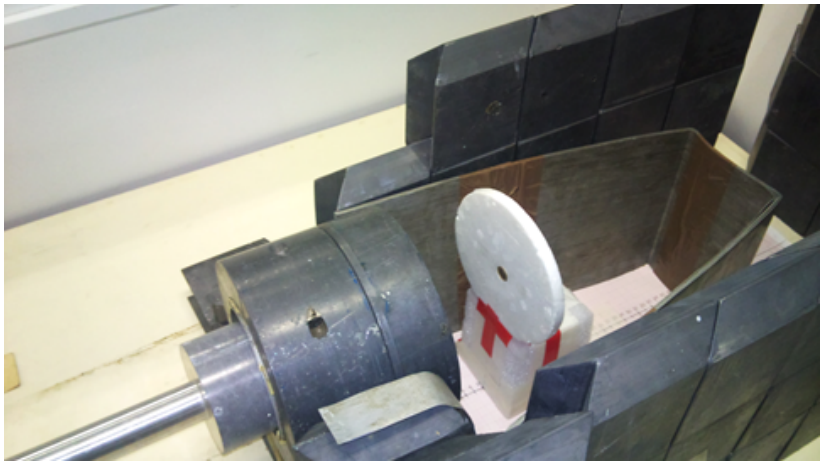

Figure 2.17: The 100% relative efficiency HPGe which is properly shielded to reduce the contribution of natural radioactivity.

of 10 cm from the detector window, thus there was no need for significant pile-up or true coincidence summing effect corrections. At the same distance, a ^{152}Eu point source was placed in order to determine the absolute efficiency of each detector. In Fig. 2.18, a typical spectrum of a ^{152}Eu point source is presented, obtained with a HPGe detector of 100% relative efficiency.

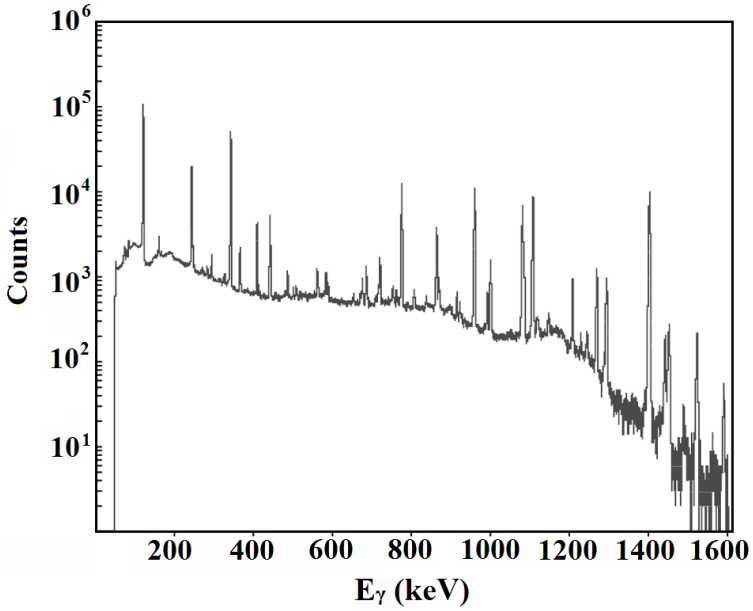

Figure 2.18: γ-ray spectrum of a ^{152}Eu point source obtained with a HPGe detector of 100% relative efficiency. The acquisition time was 49 min.

The absolute efficiency curve with respect to the γ-ray energy, obtained from the analysis of the spectrum shown in Fig. 2.18, for the detector shown in Fig. 2.17, is presented in Fig. 2.19.

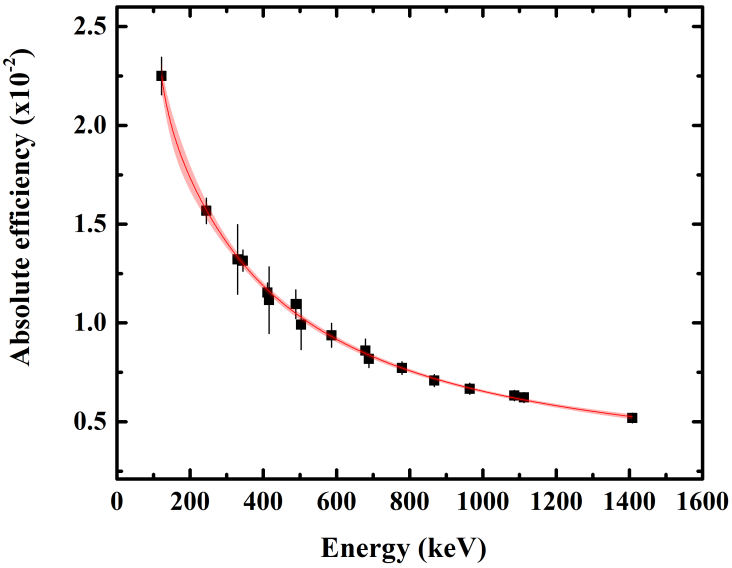

Figure 2.19: The absolute efficiency with respect to the γ-ray energy for the 100% relative efficiency HPGe detector shown in Fig. 2.17. The red hatched region denotes the confidence bands at a 95% level.

Moreover, a typical spectrum obtained after the end of the irradiation is presented in Fig. 2.20. In the following sections, other figures of spectra focused on the energy region of interest, in each case, will be given. All the γ-ray spectra were analyzed by using the SPECTRW program [104] developed by C. A. Kalfas.

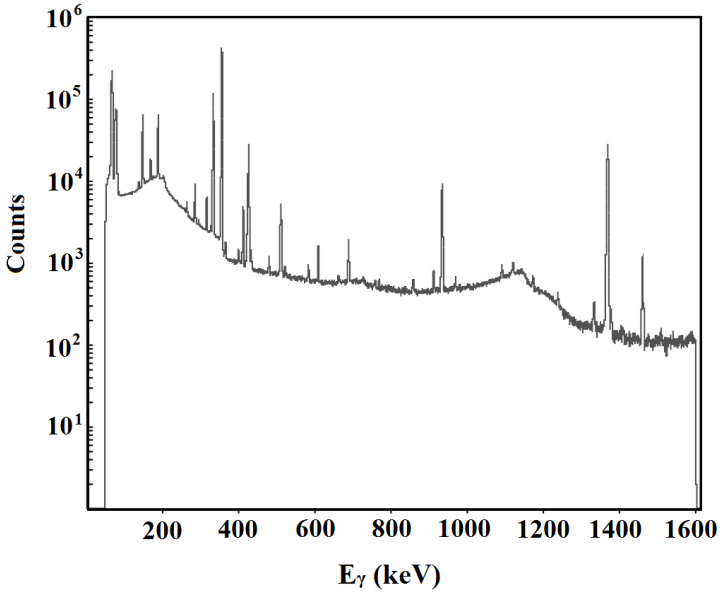

Figure 2.20: γ-ray spectrum after the end of the irradiation at 15.3 MeV, obtained with a HPGe detector of 100% relative efficiency. The acquisition time was 19 h.

2.5.1 ^{196}Au Measurements

For the population of the second isomeric state (m2) of ^{196}Au nucleus (see Fig. 1.2 and Table 1.2), the measurements began ∼1 h after the end of the irradiations and the corresponding cross sections were derived from the two most intense γ-rays (147.8 and 188.3 keV) emitted during the de-excitation of the ^{196}Au^{m2} nucleus [17] (see Fig. 2.21). In this way, the cross section for this state was independently determined.

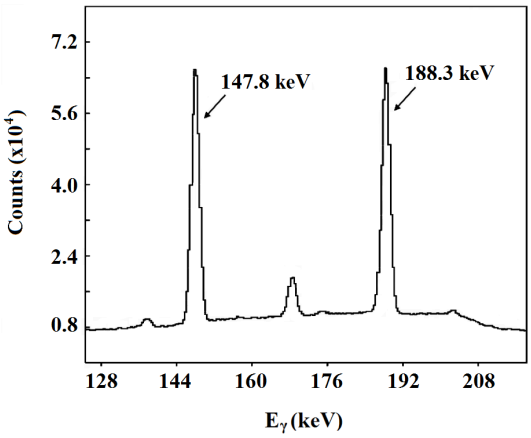

Figure 2.21: Off-beam γ-ray energy spectrum observed after the neutron irradiation at 15.3 MeV. γ-ray transitions from the decay of the second isomeric state (m2) of ^{196}Au nucleus have been marked. The acquisition time was 19 h.

Apart from the measurements mentioned above, Au spectra were also taken ∼2 d after the irradiations in order to obtain the cross section of the ground state, after the second metastable state ($T_{1/2}$ = 9.6 h) had fully decayed to the ground one. These cross section values were obtained as the weighted average using the integral of the 355.7, 333.0, and 426.0 keV γ-ray peaks (see Fig. 2.22). As shown in Fig. 1.2, the population of the ground, first, and second isomeric states was evidently included in the results (g+m1+m2) (see also Appendix D).

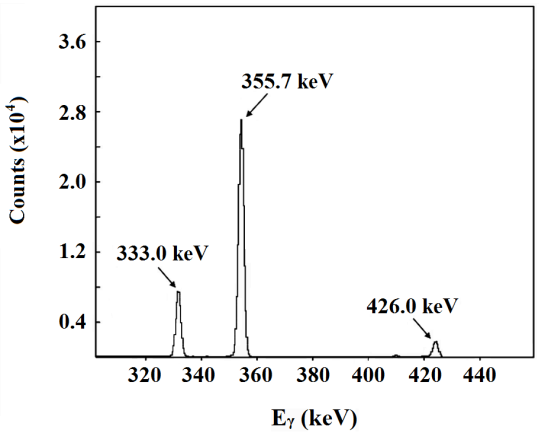

Figure 2.22: Off-beam γ-ray energy spectrum observed after the neutron irradiation at 15.3 MeV. γ-ray transitions from the decay of the ground plus both isomeric states (g+m1+m2) of ^{196}Au nucleus have been marked. The duration of this measurement was 19 h.

2.5.2 ^{190}Ir, ^{189}Ir and ^{192}Ir Measurements

Similarly to ^{196}Au^{m2} measurements, for the population of the second isomeric state (m2) of the ^{190}Ir nucleus (see Fig. 1.4 and Table 1.3), the measurements began ∼1 h after the end of the irradiations and the corresponding cross sections were independently determined through the two most intense γ-rays (616.5 and 518.55 keV) emitted during the de-excitation of the ^{190}Ir^{m2} nucleus (see Fig. 2.23).

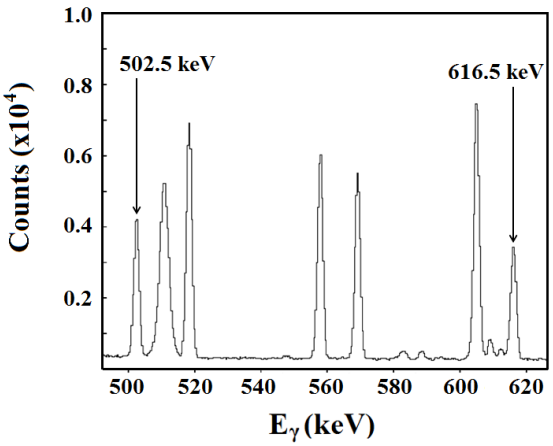

Figure 2.23: Off-beam γ-ray energy spectrum observed after the neutron irradiation at 15.3 MeV. γ-ray transitions from the decay of the second isomeric state (m2) of ^{190}Ir nucleus have been marked. The acquisition time was 10 h.

Apart from the aforementioned measurements, Ir spectra were also taken ∼2 d after the irradiations in order to obtain the cross section of the ground state, when the second metastable state ($T_{1/2}$=3.087 h) had fully decayed to the ground one. These cross section values were deduced as the weighted average using the integral of the 518.55, 557.95 and 569.30 keV γ-ray peaks and, as mentioned in section 1.2.1, correspond to the sum of the population of (g+m1+0.086 m2) levels.

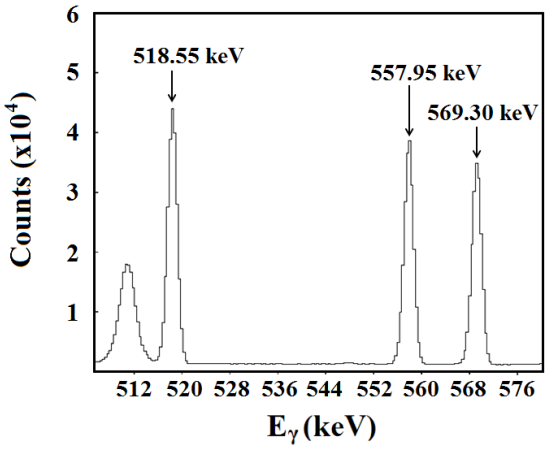

Figure 2.24: Off-beam γ-ray energy spectrum observed after the neutron irradiation at 15.3 MeV. γ-ray transitions from the decay of the ground plus both isomeric states (g+m1+0.086 m2) of ^{190}Ir nucleus have been marked. The duration of this measurement was 72 h.

Regarding the determination of the ^{191}Ir(n,3n) reaction cross section, due to the ^{189}Ir nucleus half-life of 13.2 d (see Fig. 1.5 and Table 1.3), it was crucial to analyze spectra with the longest available duration, in order to collect more counts in the γ-ray peak of interest. The latter was the one emitted at 245.1 keV and a typical spectrum is presented in Fig. 2.25.

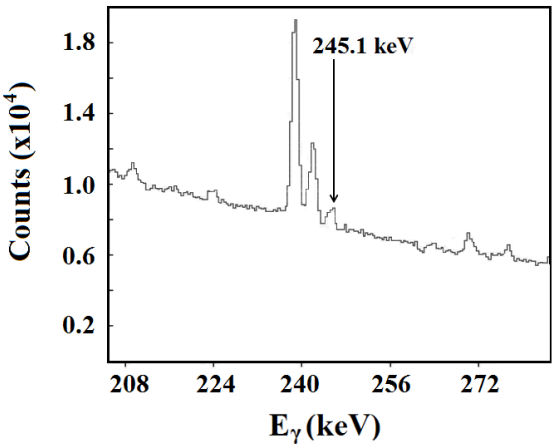

Figure 2.25: Off-beam γ-ray energy spectrum observed after the neutron irradiation at 20.9 MeV. The 245.1 keV γ-ray from the decay of the ground state of ^{189}Ir nucleus has been marked. The acquisition time was 56 h.

Concerning the ^{193}Ir(n,2n) reaction cross section, the population of the ground state of the ^{192}Ir nucleus (see Fig. 1.7 and Table 1.4) was measured using the same spectra used for the determination of the ^{191}Ir(n,2n)^{190}Ir$^{g+m1+m2}$ one, due to the longer acquisition times involved. These cross section values were obtained as the weighted average using the integral of the 316.5, 468.1, and 308.5 keV γ-ray peaks (see Fig. 2.26). However, the ^{192}Ir

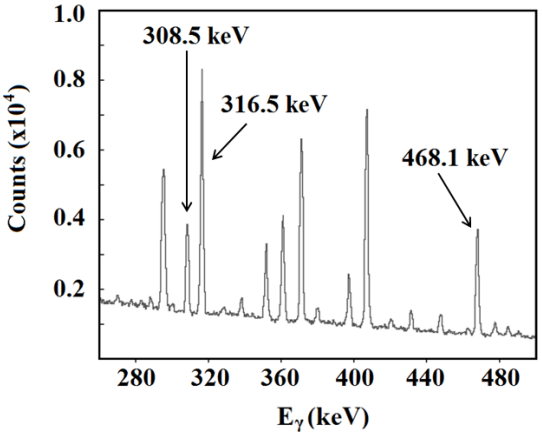

Figure 2.26: Off-beam γ-ray energy spectrum observed after the neutron irradiation at 17.1 MeV. γ-ray transitions from the decay of the ground state of ^{192}Ir nucleus have been marked. The duration of this measurement was 54 h.

nucleus is also produced by the ^{191}Ir(n,γ) reaction, which is always present and open to low energy parasitic neutrons. Therefore, a recently applied method was implemented, in order to account and correct for this contribution (see section 3.4).

3

Data Analysis

3.1 Cross Sections

As mentioned in chapter 1, Eq. 1.10, the experimental cross sections for the six measured reaction channels were determined using the following expression:

$$\sigma_{measured} = \sigma_{reference} \cdot \frac{N_{\gamma_{measured}}}{N_{\gamma_{reference}}} \cdot \frac{(\varepsilon_\gamma \cdot I_\gamma \cdot F \cdot D \cdot f_c \cdot N_\tau)\, reference}{(\varepsilon_\gamma \cdot I_\gamma \cdot F \cdot D \cdot f_c \cdot N_\tau)\, measured} \cdot C_\Phi \tag{3.1}$$

where N_γ is the integral of the γ-ray peak in the spectrum obtained with the HPGe detector, ε_γ is the absolute efficiency of the detector at the corresponding energy, I_γ is the γ-ray intensity and F is a factor estimated via Monte Carlo simulations using the MCNP5 code, in order to correct for the γ-ray self-absorption effects in the sample. An additional correction factor, named D, was necessary for the counting collection,

$$D = e^{-\lambda \cdot t_1} - e^{-\lambda \cdot t_2} \tag{3.2}$$

where t_1 and t_2 are time intervals from the end of the irradiation to the beginning and termination of the measurement with each HPGe detector, respectively (see also Appendix A.1) and λ is the decay constant of the residual nucleus. The fluctuations in the beam flux and the produced nuclei which decayed during irradiation were taken into account by means of the f_c factor (see also section 2.3 and Appendix A).

$$f_c = \frac{\int_0^{t_B} e^{\lambda t}\, f(t)\, dt}{\int_0^{t_B} f(t)\, dt}\, e^{-\lambda\, t_B} \tag{3.3}$$

where f(t) is the beam flux in arbitrary units as given by the BF_3 counter over specific time intervals (dt) and t_B is the irradiation time. Moreover, the number of the target nuclei, N_τ, was determined via the target mass (m) corrected for the abundance of each isotope ($Abund$), the atomic mass A and the Avogadro's number by means of the relation:

$$N_\tau = N_A\, \frac{m \cdot Abund}{A} \tag{3.4}$$

The factor C_Φ, which corresponds to the neutron flux ratio in reference and measured foils (Eq. 1.8):

$$C_\Phi = \frac{\Phi_{reference}}{\Phi_{measured}} \tag{3.5}$$

was estimated within good agreement both experimentally and with Monte Carlo simulations implementing the MCNP5 [36] code (see section 2.4.2 and Fig. 2.16). Furthermore, the cross section values for the ^{27}Al(n,α)^{24}Na reference reaction ($\sigma_{reference}$) were adopted from the IRDFF 1.05 library [28] using the available in the ENDF website cross section interpolation button at a single energy, for the six energies of interest. The decay data of the reference and measured targets are summarized in Table 3.1.

Table 3.1: Decay data used for the daughter nuclei.

Reaction	$T_{1/2}$	Eγ (keV)	Iγ (%)	Reference
^{197}Au(n,2n)^{196}Au$^{g+m1+m2}$	6.183 d	355.7	87.0	[37]
		333.0	22.9	[37]
		426.0	7.0	[37]
^{197}Au(n,2n)^{196}Au^{m2}	9.6 h	147.8	43.0	[37]
		188.3	37.4 & 34.0	[37] & [38]
^{191}Ir(n,2n)^{190}Ir$^{g+m1+0.086\,m2}$	11.78 d	518.6	34.0	[39]
		558.0	30.1	[39]
		569.3	28.5	[39]
^{191}Ir(n,2n)^{190}Ir^{m2}	3.087 h	616.5	90.14	[39]
		502.5	89.38	[39]
^{191}Ir(n,3n)^{189}Ir	13.2 d	245.1	6.0	[39]
^{193}Ir(n,2n)^{192}Ir	73.829 d	316.5	82.86	[39]
		468.1	47.84	[39]
		308.5	29.7	[39]
^{27}Al(n,α)^{24}Na	14.959 h	1368.6	100	[37]

The values of all the aforementioned factors involved in Eq. 3.1 along with the cross sections obtained from each γ-ray of interest for the six studied reactions are presented analytically in Tables 3.2-3.7 for the six neutron beam energies.

Table 3.2: Experimental cross section values for the ^{197}Au(n,2n)^{196}Au reaction at each neutron energy. The values of all the factors involved in Eq. 3.1 are also given.

E_n	σ_{Au}	Reference (Al)								Measured (Au)							Flux Ratio
(MeV)	(b)	σ	N_γ	ε_γ	I_γ	F	D	f_c	N_τ	N_γ	ε_γ	I_γ	F	D	f_c	N_τ	C_Φ
Multiply x		-	10^3	10^{-3}	10^{-2}	10^{-2}	10^{-1}	10^{-1}	10^{21}	10^3	10^{-2}	10^{-2}	10^{-2}	10^{-1}	10^{-1}	10^{21}	-
Cross sections obtained via the analysis of the 355.7 keV γ-ray peak.																	
15.3	2.075	0.104	392.0	5.4	100	99.6	7.4	5.6	4.92	1572.7	1.3	87.0	88.3	0.5	9.4	4.62	1.025
17.1	1.913	0.075	3.4	5.1	100	99.6	1.1	2.2	3.73	134.3	0.6	87.0	91.4	0.9	8.1	2.08	1.062
17.9	1.652	0.063	9.0	5.2	100	99.7	8.3	8.1	4.92	86.1	1.3	87.0	87.8	1.5	9.8	4.62	1.020
18.9	1.396	0.050	11.4	5.2	100	99.6	5.8	5.7	4.07	296.3	1.3	87.0	88.6	1.6	9.4	4.39	1.010
20.0	1.024	0.038	4.8	8.7	100	99.6	8.0	8.0	4.49	12.9	2.2	87.0	91.4	0.8	9.8	2.00	1.035
20.9	0.710	0.031	17.1	8.7	100	99.6	8.2	5.4	4.81	57.5	2.2	87.0	91.2	0.8	9.3	2.08	1.015
Cross sections obtained via the analysis of the 333.0 keV γ-ray peak.																	
15.3	2.094	0.104	392.0	5.4	100	99.6	7.4	5.6	4.92	428.1	1.3	22.9	87.0	0.5	9.4	4.62	1.025
17.1	1.989	0.075	3.4	5.1	100	99.6	1.1	2.2	3.73	38.0	0.7	22.9	90.4	0.9	8.1	2.08	1.062
17.9	1.723	0.063	9.0	5.2	100	99.7	8.3	8.1	4.92	24.2	1.3	22.9	86.3	1.5	9.8	4.62	1.020
18.9	1.418	0.050	11.4	5.2	100	99.6	5.8	5.7	4.07	81.4	1.3	22.9	87.3	1.6	9.4	4.39	1.010
20.0	1.171	0.038	4.8	8.7	100	99.6	8.0	8.0	4.49	4.0	2.3	22.9	90.4	0.8	9.8	2.00	1.035
20.9	0.724	0.031	17.1	8.7	100	99.6	8.2	5.4	4.81	15.9	2.3	22.9	90.1	0.8	9.3	2.08	1.015
*Cross sections obtained via the analysis of the 426.0 keV γ-ray peak.																	
15.3	1.896	0.104	392.0	5.4	100	99.6	7.4	5.6	4.92	107.0	1.1	7.0	91.2	0.5	9.4	4.62	1.025
17.1	1.721	0.075	3.4	5.1	100	99.6	1.1	2.2	3.73	8.8	0.6	7.0	93.6	0.9	8.1	2.08	1.062
17.9	1.550	0.063	9.0	5.2	100	99.7	8.3	8.1	4.92	6.0	1.1	7.0	90.8	1.5	9.8	4.62	1.020
18.9	1.372	0.050	11.4	5.2	100	99.6	5.8	5.7	4.07	21.6	1.1	7.0	91.5	1.6	9.4	4.39	1.010
20.9	0.715	0.031	17.1	8.7	100	99.6	8.2	5.4	4.81	4.3	1.9	7.0	93.4	0.8	9.3	2.08	1.015

* The cross section value obtained from the 426.0 keV γ-line, at 20.0 MeV incident neutron energy, was excluded due to the low counting statistics.

Table 3.3: Experimental cross section values for the ^{197}Au(n,2n)^{196}Au^{m2} reaction at each neutron energy. The values of all the factors involved in Eq. 3.1 are also given. In the first two blocks of the table the intensity values were adopted by the Lund/LBNL library [37], while in the third one were taken from the Ref. [38].

E_n	σ_{Au}	Reference (Al)								Measured (Au)							Flux Ratio
(MeV)	(b)	σ	N_γ	ε_γ	I_γ	F	D	f_c	N_τ	N_γ	ε_γ	I_γ	F	D	f_c	N_τ	C_Φ
Multiply x		-	10^3	10^{-3}	10^{-2}	10^{-2}	10^{-1}	10^{-1}	10^{21}	10^3	10^{-2}	10^{-2}	10^{-2}	10^{-1}	10^{-1}	10^{21}	-
Cross sections obtained via the analysis of the 147.8 keV γ-ray peak.																	
15.3	0.171	0.104	392.0	5.4	100	99.6	7.4	5.6	4.92	306.0	2.0	43.0	44.4	7.0	4.2	4.62	1.025
17.1	0.218	0.075	3.4	5.1	100	99.6	1.1	2.2	3.73	8.7	1.0	43.0	54.3	6.4	1.4	2.08	1.062
17.9	0.218	0.063	9.0	5.2	100	99.7	8.3	8.1	4.92	19.0	2.0	43.0	42.5	8.8	7.2	4.62	1.020
18.9	0.203	0.050	11.4	5.2	100	99.6	5.8	5.7	4.07	34.8	2.0	43.0	45.3	7.0	4.4	4.39	1.010
20.0	0.177	0.038	4.8	8.7	100	99.6	8.0	8.0	4.49	6.5	3.5	43.0	54.1	6.4	7.1	2.00	1.035
20.9	0.124	0.031	17.1	8.7	100	99.6	8.2	5.4	4.81	16.8	3.5	43.0	53.4	6.6	4.1	2.08	1.015
Cross sections obtained via the analysis of the 188.3 keV γ-ray peak.																	
15.3	0.156	0.104	392.0	5.4	100	99.6	7.4	5.6	4.92	300.6	1.8	37.4	61.9	7.0	4.2	4.62	1.025
17.1	0.188	0.075	3.4	5.1	100	99.6	1.1	2.2	3.73	7.8	1.0	37.4	70.3	6.4	1.4	2.08	1.062
17.9	0.208	0.063	9.0	5.2	100	99.7	8.3	8.1	4.92	17.5	1.8	37.4	60.3	7.7	7.2	4.62	1.020
18.9	0.188	0.050	11.4	5.2	100	99.6	5.8	5.7	4.07	34.6	1.8	37.4	62.6	7.0	4.4	4.39	1.010
20.0	0.162	0.038	4.8	8.7	100	99.6	8.0	8.0	4.49	5.9	3.1	37.4	70.2	6.4	7.1	2.00	1.035
20.9	0.116	0.031	17.1	8.7	100	99.6	8.2	5.4	4.81	15.7	3.1	37.4	69.6	6.6	4.1	2.08	1.015
Cross sections obtained via the analysis of the 188.3 keV γ-ray peak. Intensity by Ref. [38] adopted.																	
15.3	0.171	0.104	392.0	5.4	100	99.6	7.4	5.6	4.92	300.6	1.8	34.0	61.9	7.0	4.2	4.62	1.025
17.1	0.205	0.075	3.4	5.1	100	99.6	1.1	2.2	3.73	7.8	1.0	34.0	70.3	6.4	1.4	2.08	1.062
17.9	0.227	0.063	9.0	5.2	100	99.7	8.3	8.1	4.92	17.5	1.8	34.0	60.3	7.7	7.2	4.62	1.020
18.9	0.205	0.050	11.4	5.2	100	99.6	5.8	5.7	4.07	34.6	1.8	34.0	62.6	7.0	4.4	4.39	1.010
20.0	0.177	0.038	4.8	8.7	100	99.6	8.0	8.0	4.49	5.9	3.1	34.0	70.2	6.4	7.1	2.00	1.035
20.9	0.127	0.031	17.1	8.7	100	99.6	8.2	5.4	4.81	15.7	3.1	34.0	69.6	6.6	4.1	2.08	1.015

Table 3.4: Experimental cross section values for the ^{191}Ir(n,2n)^{190}Ir reaction at each neutron energy. The values of all the factors involved in Eq. 4.40 are also given.

E_n	σ_{Ir}	Reference (Al)								Measured (Ir)							Flux Ratio
(MeV)	(b)	σ	N_γ	ε_γ	I_γ	F	D	f_c	N_τ	N_γ	ε_γ	I_γ	F	D	f_c	N_τ	C_Φ
Multiply x		-	10^3	10^{-3}	10^{-2}	10^{-2}	10^{-1}	10^{-1}	10^{21}	10^3	10^{-3}	10^{-2}	10^{-2}	10^{-1}	10^{-1}	10^{20}	-
Cross sections obtained via the analysis of the 518.6 keV γ-ray peak.																	
15.3	1.775	0.104	88.6	2.4	100	99.6	4.7	5.6	4.29	220.2	9.6	34.0	95.4	1.6	9.7	9.08	1.095
17.1	1.491	0.075	2.2	1.9	100	99.7	2.3	2.2	4.05	32.5	9.6	34.0	94.6	1.2	8.9	8.87	1.000
17.9	1.227	0.063	9.0	5.2	100	99.7	8.3	8.1	4.92	3.6	9.9	34.0	95.7	1.3	9.9	8.86	1.060
18.9	1.004	0.050	9.7	4.6	100	99.6	5.8	5.7	4.04	10.2	9.9	34.0	94.6	1.2	9.7	9.05	1.062
20.0	0.762	0.038	4.8	8.7	100	99.6	8.0	8.0	4.49	1.2	16.9	34.0	95.4	0.7	9.9	8.88	1.061
20.9	0.484	0.031	17.1	8.7	100	99.6	8.2	5.4	4.81	3.3	8.9	34.0	94.4	1.0	9.6	9.07	1.047
Cross sections obtained via the analysis of the 558.0 keV γ-ray peak.																	
15.3	1.780	0.104	88.6	2.4	100	99.6	4.7	5.6	4.29	86.4	9.2	30.1	95.7	0.7	9.7	9.08	1.095
17.1	1.421	0.075	2.2	1.9	100	99.7	2.3	2.2	4.05	15.9	9.2	30.1	95.0	0.7	8.9	8.87	1.000
17.9	1.398	0.063	9.0	5.2	100	99.7	8.3	8.1	4.92	3.4	9.4	30.1	95.7	1.3	9.9	8.86	1.060
18.9	0.980	0.050	9.7	4.6	100	99.6	5.8	5.7	4.04	8.5	9.4	30.1	95.8	1.2	9.7	9.05	1.062
20.0	0.777	0.038	4.8	8.7	100	99.6	8.0	8.0	4.49	1.0	16.0	30.1	95.7	0.7	9.9	8.88	1.061
20.9	0.467	0.031	17.1	8.7	100	99.6	8.2	5.4	4.81	2.7	8.4	30.1	94.8	1.0	9.6	9.07	1.047
Cross sections obtained via the analysis of the 569.3 keV γ-ray peak.																	
15.3	1.809	0.104	88.6	2.4	100	99.6	4.7	5.6	4.29	177.7	9.0	28.5	95.9	1.6	9.7	9.08	1.095
17.1	1.537	0.075	2.2	1.9	100	99.7	2.3	2.2	4.05	26.6	9.0	28.5	95.2	1.2	8.9	8.87	1.000
17.9	1.287	0.063	9.0	5.2	100	99.7	8.3	8.1	4.92	3.0	9.3	28.5	95.9	1.3	9.9	8.86	1.060
18.9	0.992	0.050	9.7	4.6	100	99.6	5.8	5.7	4.04	8.1	9.3	28.5	95.9	1.2	9.7	9.05	1.062
20.0	0.666	0.038	4.8	8.7	100	99.6	8.0	8.0	4.49	0.8	15.8	28.5	95.6	0.7	9.9	8.88	1.061
20.9	0.488	0.031	17.1	8.7	100	99.6	8.2	5.4	4.81	2.6	8.3	28.5	94.7	1.0	9.6	9.07	1.047

Table 3.5: Experimental cross section values for the ^{191}Ir(n,2n)^{190}Ir^{m2} and ^{191}Ir(n,3n)^{189}Ir reactions at each neutron energy. The values of all the factors involved in Eq. 3.1 are also given.

E_n	σ_{Ir}	Reference (Al)								Measured (Ir)							Flux Ratio
(MeV)	(b)	σ	N_γ	ε_γ	I_γ	F	D	f_c	N_τ	N_γ	ε_γ	I_γ	F	D	f_c	N_τ	C_Φ
Multiply x		-	10^3	10^{-3}	10^{-2}	10^{-2}	10^{-1}	10^{-1}	10^{21}	10^3	10^{-3}	10^{-2}	10^{-2}	10^{-1}	10^{-1}	10^{20}	-
Cross sections for the ^{191}Ir(n,2n)^{190}Ir^{m2} reaction, obtained via the analysis of the 616.5 keV γ-ray peak.																	
15.3	0.176	0.104	88.6	2.4	100	99.6	4.7	5.6	4.29	17.0	8.6	90.14	96.2	3.3	1.5	9.08	1.095
17.1	0.196	0.075	2.2	1.9	100	99.7	2.3	2.2	4.05	0.5	8.6	90.14	95.6	1.1	0.4	8.87	1.000
17.9	0.211	0.063	9.0	5.2	100	99.7	8.3	8.1	4.92	4.0	8.8	90.14	96.2	8.5	4.1	8.86	1.060
18.9	0.182	0.050	9.7	4.6	100	99.6	5.8	5.7	4.04	4.6	8.8	90.14	96.4	7.2	1.7	9.05	1.062
20.0	0.131	0.038	4.8	8.7	100	99.6	8.0	8.0	4.49	2.2	15.0	90.14	96.2	7.6	3.9	8.88	1.061
20.9	0.084	0.031	17.1	8.7	100	99.6	8.2	5.4	4.81	3.5	15.0	90.14	95.5	7.8	1.6	9.07	1.047
Cross sections for the ^{191}Ir(n,2n)^{190}Ir^{m2} reaction, obtained via the analysis of the 502.5 keV γ-ray peak.																	
15.3	0.182	0.104	88.6	2.4	100	99.6	4.7	5.6	4.29	19.7	9.8	89.38	95.1	3.3	1.5	9.08	1.095
17.1	0.210	0.075	2.2	1.9	100	99.7	2.3	2.2	4.05	0.6	9.8	89.38	94.2	1.1	0.4	8.87	1.000
17.9	0.208	0.063	9.0	5.2	100	99.7	8.3	8.1	4.92	4.4	10.1	89.38	95.1	8.5	4.1	8.86	1.060
18.9	0.172	0.050	9.7	4.6	100	99.6	5.8	5.7	4.04	4.9	10.1	89.38	95.1	7.2	1.7	9.05	1.062
20.0	0.138	0.038	4.8	8.7	100	99.6	8.0	8.0	4.49	2.5	17.2	89.38	95.0	7.6	3.9	8.88	1.061
20.9	0.089	0.031	17.1	8.7	100	99.6	8.2	5.4	4.81	4.1	17.2	89.38	94.0	7.8	1.6	9.07	1.047
Cross sections for the ^{191}Ir(n,3n)^{189}Ir reaction, obtained via the analysis of the 245.1 keV γ-ray peak.																	
17.1	0.167	0.075	2.2	1.9	100	99.7	2.3	2.2	4.05	0.8	15.4	6.0	80.0	1.0	9.0	8.87	1.000
18.9	0.716	0.050	9.7	4.6	100	99.6	5.8	5.7	4.04	1.7	15.6	6.0	83.0	1.1	9.7	9.05	1.062
20.9	1.096	0.031	17.1	8.7	100	99.6	8.2	5.4	4.81	4.0	27.0	6.0	79.5	1.1	9.7	9.07	1.047

Table 3.6: Experimental cross section values for the ^{193}Ir(n,2n)^{192}Ir reaction at each neutron energy. The values of all the factors involved in Eq. 3.1 are also given.

E_n	σ_{Ir}		Reference (Al)							Measured (Ir)							Flux Ratio
(MeV)	(b)	σ	N_γ	ε_γ	I_γ	F	D	f_c	N_τ	N_γ	ε_γ	I_γ	F	D	f_c	N_τ	C_Φ
Multiply x		-	10^3	10^{-3}	10^{-2}	10^{-2}	10^{-2}	10^{-1}	10^{21}	10^5	10^{-2}	10^{-2}	10^{-2}	10^{-2}	10^{-1}	10^{21}	-
Cross sections obtained via the analysis of the 316.5 keV γ-ray peak.																	
15.3	1.841	0.104	88.6	2.4	100	99.6	4.7	5.6	4.29	2.209	1.3	82.86	89.5	2.8	9.9	1.53	1.095
17.1	1.412	0.075	2.2	1.9	100	99.7	2.3	2.2	4.05	0.318	1.3	82.86	87.8	2.1	9.8	1.49	1.000
18.9	0.740	0.050	9.7	4.6	100	99.6	5.8	5.7	4.04	0.086	1.4	82.86	89.8	2.5	9.9	1.52	1.062
20.9	0.273	0.031	17.1	8.7	100	99.6	8.2	5.4	4.81	0.020	1.3	82.86	87.5	1.9	9.9	1.52	1.047
Cross sections obtained via the analysis of the 468.1 keV γ-ray peak.																	
15.3	1.817	0.104	88.6	2.4	100	99.6	4.7	5.6	4.29	1.032	1.0	47.84	94.5	2.8	9.9	1.53	1.095
17.1	1.365	0.075	2.2	1.9	100	99.7	2.3	2.2	4.05	0.147	1.0	47.84	93.5	2.1	9.8	1.49	1.000
18.9	0.773	0.050	9.7	4.6	100	99.6	5.8	5.7	4.04	0.043	1.1	47.84	94.6	2.5	9.9	1.52	1.062
20.9	0.265	0.031	17.1	8.7	100	99.6	8.2	5.4	4.81	0.009	1.0	47.84	93.3	1.9	9.9	1.52	1.047
Cross sections obtained via the analysis of the 308.5 keV γ-ray peak.																	
15.3	1.834	0.104	88.6	2.4	100	99.6	4.7	5.6	4.29	0.796	1.4	29.7	88.8	2.8	9.9	1.53	1.095
17.1	1.397	0.075	2.2	1.9	100	99.7	2.3	2.2	4.05	0.114	1.4	29.7	87.1	2.1	9.8	1.49	1.000
18.9	0.810	0.050	9.7	4.6	100	99.6	5.8	5.7	4.04	0.034	1.4	29.7	89.1	2.5	9.9	1.52	1.062
20.9	0.274	0.031	17.1	8.7	100	99.6	8.2	5.4	4.81	0.007	1.3	29.7	86.7	1.9	9.9	1.52	1.047

Table 3.7: Experimental cross section values for the ^{193}Ir(n,2n)^{192}Ir reaction at low neutron beam energies along with the values of all the factors involved in Eq. 3.1. The data were obtained in 2005-2006 and were analyzed by N. Patronis, while the corrections for the low energy parasitic neutrons contribution were performed based on the MCNP5 simulations presented in Appendix E.

E_n	σ_{Ir}	Reference (Al)								Measured (Ir)							Flux Ratio
(MeV)	(b)	σ	N_γ	ε_γ	I_γ	F	D	f_c	N_τ	N_γ	ε_γ	I_γ	F	D	f_c	N_τ	C_Φ
Multiply x		-	10^3	10^{-3}	10^{-2}	10^{-2}	10^{-2}	10^{-1}	10^{21}	10^5	10^{-3}	10^{-2}	10^{-2}	10^{-2}	10^{-2}	10^{21}	-
Cross sections obtained via the analysis of the 316.5 keV γ-ray peak.																	
10.0	1.315	0.091	1.8	2.9	100	99.6	1.8	8.5	4.10	1.829	8.5	82.86	84.5	0.7	99.9	3.09	1.040
10.5	1.607	0.099	1.9	2.9	100	99.6	1.9	7.9	4.06	4.953	8.5	82.86	84.5	1.6	99.8	2.97	1.027
11.0	1.951	0.106	2.3	2.8	100	99.6	1.7	8.1	4.06	2.785	8.3	82.86	84.5	0.6	99.8	2.97	1.023
11.3	2.037	0.109	2.4	2.8	100	99.6	1.7	8.2	4.10	3.315	8.3	82.86	84.5	0.6	99.8	3.09	1.024
Cross sections obtained via the analysis of the 468.1 keV γ-ray peak.																	
10.0	1.279	0.091	1.8	2.9	100	99.6	1.8	8.5	4.10	0.842	6.4	47.84	91.8	0.7	99.9	3.09	1.040
10.5	1.578	0.099	1.9	2.9	100	99.6	1.9	7.9	4.06	2.301	6.4	47.84	91.8	1.6	99.8	2.97	1.027
11.0	1.893	0.106	2.3	2.8	100	99.6	1.7	8.1	4.06	1.280	6.3	47.84	91.8	0.6	99.8	2.97	1.023
11.3	1.896	0.109	2.4	2.8	100	99.6	1.7	8.2	4.10	1.462	6.3	47.84	91.8	0.6	99.8	3.09	1.024
Cross sections obtained via the analysis of the 308.5 keV γ-ray peak.																	
10.0	1.282	0.091	1.8	2.9	100	99.6	1.8	8.5	4.10	0.649	8.7	29.7	84.2	0.7	99.9	3.09	1.040
10.5	1.591	0.099	1.9	2.9	100	99.6	1.9	7.9	4.06	1.784	8.7	29.7	84.2	1.6	99.8	2.97	1.027
11.0	1.972	0.106	2.3	2.8	100	99.6	1.7	8.1	4.06	1.023	8.5	29.7	84.2	0.6	99.8	2.97	1.023
11.3	1.971	0.109	2.4	2.8	100	99.6	1.7	8.2	4.10	1.166	8.5	29.7	84.2	0.6	99.8	3.09	1.024

3.2 Uncertainties

An overview of the uncertainties of all the main quantities used for the cross section determination is given in Table 3.8. As shown in the latter, the most dominant uncertainty is that of the counting statistics in the measured foils, which can be attributed either to the low cross section values (in the case of the ^{191}Ir(n,3n) reaction), or to the significant contamination from other reaction (in the case of the ^{193}Ir(n,2n)). In addition, the uncertainty of the detector efficiency is large enough in some cases, since it varies from 2 to 11%, depending on the fit of the experimental absolute efficiency data (by using an IAEA function, see Appendix C, Eq. C.9) and on the energy region. These uncertainties were estimated through the confidence bands of the fitting curve at a level of 95%. Furthermore, in the total uncertainty, the one of the neutron integrated fluence is included and it is also important, since it corresponds to the 4-7%. The uncertainty of the reference reaction cross section was assumed in all cases 3%, while the one of the counting statistics of reference foils could be assumed negligible (1-2%).

Table 3.8: Compilation of uncertainties.

Quantity	Uncertainty (%)
Neutron energy	1-3
Neutron integrated fluence	4-7
Counting statistics for reference foils	1-2
Counting statistics for measured foils	1-38
Detector efficiency	2-11
Reference reaction cross section	3
Measured reaction cross section (Total uncertainty)	5-39

In more detail, all the factors involved in Eq. 3.1 were considered uncorrelated. Therefore, the most significant partial uncertainties, namely those which correspond to $\sigma_{reference}$, $N_{\gamma_{measured}}$, $N_{\gamma_{reference}}$, $\varepsilon_{\gamma_{measured}}$, $\varepsilon_{\gamma_{reference}}$, $N_{\tau\ measured}$ and $N_{\tau\ reference}$ factors, were summed up quadratically in order to obtain the total one. The uncertainties are also presented analytically in Tables 3.9-3.13, for each reaction separately.

As mentioned explicitly in Ref. [105], a detailed list of all the uncertainty components, their value and a specification of existing correlations is the recommended way to present uncertainties rather than constructing a covariance matrix evaluated by the experimenter. This is the reason why the uncertainties are presented in this way (Tables 3.9-3.13), while the correlations between the measurements were taken into account in the next step of analysis (see section 3.3).

Table 3.9: The ^{197}Au(n,2n)^{196}Au cross sections obtained from each γ-ray (mentioned also in Table 3.2) along with the total uncertainties (in %) and the uncertainties for the most significant contributions in Eq. 3.1 at each neutron energy.

E_n	Cross section	Uncertainties (%)							
(MeV)	(b)	Total	$(N_\gamma)_{Au}$	$(N_\gamma)_{Al}$	$(N_\tau)_{Au}$	$(N_\tau)_{Al}$	$(\varepsilon_\gamma)_{Au}$	$(\varepsilon_\gamma)_{Al}$	σ_{Al}
For the cross sections obtained via the analysis of the 355.7 keV γ-ray peak.									
15.3	2.075	4.8	0.1	1.5	0.07	0.45	2.1	2.7	3
17.1	1.913	5.0	1.6	1.5	0.15	0.60	1.6	2.9	3
17.9	1.652	5.3	1.7	1.6	0.07	0.45	2.7	2.7	3
18.9	1.396	5.0	0.2	1.1	0.07	0.55	2.7	2.7	3
20.0	1.024	9.0	2.4	2.1	0.15	0.50	4.8	6.2	3
20.9	0.710	8.7	1.7	0.9	0.15	0.46	4.5	6.2	3
For the cross sections obtained via the analysis of the 333.0 keV γ-ray peak.									
15.3	2.094	4.8	0.2	1.5	0.07	0.45	2.1	2.7	3
17.1	1.989	4.8	0.6	1.5	0.15	0.60	1.6	2.9	3
17.9	1.723	5.3	1.4	1.6	0.07	0.45	2.6	2.7	3
18.9	1.418	5.0	0.6	1.1	0.07	0.55	2.6	2.7	3
20.0	1.171	10.8	6.3	2.1	0.15	0.50	4.9	6.2	3
20.9	0.724	8.8	1.9	0.9	0.15	0.46	4.6	6.2	3
*For the cross sections obtained via the analysis of the 426.0 keV γ-ray peak.									
15.3	1.896	5.1	1.6	1.5	0.07	0.45	2.2	2.7	3
17.1	1.721	5.0	1.4	1.5	0.15	0.60	1.8	2.9	3
17.9	1.550	6.6	4.2	1.6	0.07	0.45	2.5	2.7	3
18.9	1.372	5.2	1.4	1.1	0.07	0.55	2.5	2.7	3
20.9	0.715	9.8	4.7	0.9	0.15	0.46	4.3	6.2	3

* The cross section value obtained from the 426.0 keV γ-line, at 20.0 MeV incident neutron energy, was excluded due to the low counting statistics.

Table 3.10: The ^{197}Au(n,2n)^{196}Au^{m2} cross sections obtained from each γ-ray (mentioned also in Table 3.3) along with the total uncertainties (in %) and the uncertainties for the most significant contributions in Eq. 3.1 at each neutron energy.

E_n	Cross section	Uncertainties (%)							
(MeV)	(b)	Total	$(N_\gamma)_{Au}$	$(N_\gamma)_{Al}$	$(N_\tau)_{Au}$	$(N_\tau)_{Al}$	$(\varepsilon_\gamma)_{Au}$	$(\varepsilon_\gamma)_{Al}$	σ_{Al}
For the cross sections obtained via the analysis of the 147.8 keV γ-ray peak.									
15.3	0.171	6.5	0.3	1.5	0.07	0.45	4.8	2.7	3
17.1	0.218	6.3	2.3	1.5	0.15	0.60	3.7	2.9	3
17.9	0.218	7.8	2.8	1.6	0.07	0.45	5.9	2.7	3
18.9	0.203	7.4	1.4	1.1	0.07	0.55	5.9	2.7	3
20.0	0.177	14.3	6.2	2.1	0.15	0.50	10.7	6.2	3
20.9	0.124	13.1	2.7	0.9	0.15	0.46	10.7	6.2	3
For the cross sections obtained via the analysis of the 188.3 keV γ-ray peak.									
15.3	0.156	6.6	0.4	1.5	0.07	0.45	4.9	2.7	3
17.1	0.188	6.7	3.2	1.5	0.15	0.60	3.8	2.9	3
17.9	0.208	8.1	3.0	1.6	0.07	0.45	6.2	2.7	3
18.9	0.188	7.8	2.3	1.1	0.07	0.55	6.2	2.7	3
20.0	0.162	15.0	6.8	2.1	0.15	0.50	11.2	6.2	3
20.9	0.116	13.6	3.2	0.9	0.15	0.46	11.2	6.2	3
For the cross sections obtained via the analysis of the 188.3 keV γ-ray peak. Intensity by Ref. [38] adopted.									
15.3	0.171	6.6	0.4	1.5	0.07	0.45	4.9	2.7	3
17.1	0.205	6.7	3.2	1.5	0.15	0.60	3.8	2.9	3
17.9	0.227	8.1	3.0	1.6	0.07	0.45	6.2	2.7	3
18.9	0.205	7.8	2.3	1.1	0.07	0.55	6.2	2.7	3
20.0	0.177	15.0	6.8	2.1	0.15	0.50	11.2	6.2	3
20.9	0.127	13.6	3.2	0.9	0.15	0.46	11.2	6.2	3

Table 3.11: The ^{191}Ir(n,2n)^{190}Ir$^{g+m1+0.086\,m2}$ cross sections obtained from each γ-ray (mentioned also in Table 3.4) along with the total uncertainties (in %) and the uncertainties for the most significant contributions in Eq. 3.1 at each neutron energy.

E_n	Cross section	Uncertainties (%)							
(MeV)	(b)	Total	$(N_\gamma)_{Ir}$	$(N_\gamma)_{Al}$	$(N_\tau)_{Ir}$	$(N_\tau)_{Al}$	$(\varepsilon_\gamma)_{Ir}$	$(\varepsilon_\gamma)_{Al}$	σ_{Al}
For the cross sections obtained via the analysis of the 518.6 keV γ-ray peak.									
15.3	1.775	4.8	1.6	0.3	0.1	0.5	2.6	2.3	3
17.1	1.491	5.5	1.8	2.3	0.1	0.6	2.6	2.4	3
17.9	1.227	8.5	6.7	1.6	0.1	0.5	2.9	2.7	3
18.9	1.004	6.4	3.4	1.2	0.1	0.6	2.9	3.1	3
20.0	0.762	19.5	17.2	2.1	0.1	0.5	5.4	6.2	3
20.9	0.484	8.6	4.0	0.9	0.1	0.5	3.0	6.2	3
For the cross sections obtained via the analysis of the 558.0 keV γ-ray peak.									
15.3	1.780	4.9	1.6	0.3	0.1	0.5	2.6	2.3	3
17.1	1.421	5.3	1.1	2.3	0.1	0.6	2.6	2.4	3
17.9	1.398	8.7	7.0	1.6	0.1	0.5	2.9	2.7	3
18.9	0.980	6.2	3.1	1.2	0.1	0.6	2.9	3.1	3
20.0	0.777	17.5	15.0	2.1	0.1	0.5	5.4	6.2	3
20.9	0.467	9.0	4.9	0.9	0.1	0.5	3.0	6.2	3
For the cross sections obtained via the analysis of the 569.3 keV γ-ray peak.									
15.3	1.809	4.9	1.6	0.3	0.1	0.5	2.6	2.3	3
17.1	1.537	5.3	0.9	2.3	0.1	0.6	2.6	2.4	3
17.9	1.287	9.7	8.1	1.6	0.1	0.5	2.9	2.7	3
18.9	0.992	6.3	3.4	1.2	0.1	0.6	2.9	3.1	3
20.0	0.666	19.7	17.5	2.1	0.1	0.5	5.4	6.2	3
20.9	0.488	8.9	4.6	0.9	0.1	0.5	3.0	6.2	3

Table 3.12: The ^{191}Ir(n,2n)^{190}Ir^{m2} and ^{191}Ir(n,3n)^{189}Ir cross sections obtained from each γ-ray (mentioned also in Table 3.5) along with the total uncertainties (in %) and the uncertainties for the most significant contributions in Eq. 3.1 at each neutron energy.

E_n	Cross section	Uncertainties (%)							
(MeV)	(b)	Total	$(N_\gamma)_{Ir}$	$(N_\gamma)_{Al}$	$(N_\tau)_{Ir}$	$(N_\tau)_{Al}$	$(\varepsilon_\gamma)_{Ir}$	$(\varepsilon_\gamma)_{Al}$	σ_{Al}
For ^{191}Ir(n,2n)^{190}Ir^{m2} cross section obtained via the analysis of the 616.5 keV γ-ray peak.									
15.3	0.176	4.9	1.8	0.3	0.1	0.5	2.5	2.3	3
17.1	0.196	9.9	8.5	2.3	0.1	0.6	2.5	2.4	3
17.9	0.211	6.7	4.3	1.6	0.1	0.5	2.8	2.7	3
18.9	0.182	5.8	2.4	1.2	0.1	0.6	2.8	3.1	3
20.0	0.131	11.3	7.0	2.1	0.1	0.5	5.3	6.2	3
20.9	0.084	9.4	3.4	0.9	0.1	0.5	5.3	6.2	3
For ^{191}Ir(n,2n)^{190}Ir^{m2} cross section obtained via the analysis of the 502.5 keV γ-ray peak.									
15.3	0.182	4.9	1.8	0.3	0.1	0.5	2.6	2.3	3
17.1	0.210	8.9	7.2	2.3	0.1	0.6	2.6	2.4	3
17.9	0.208	7.2	5.0	1.6	0.1	0.5	2.9	2.7	3
18.9	0.172	6.5	3.7	1.2	0.1	0.6	2.9	3.1	3
20.0	0.138	11.2	6.7	2.1	0.1	0.5	5.3	6.2	3
20.9	0.089	9.6	3.9	0.9	0.1	0.5	5.3	6.2	3
For ^{191}Ir(n,3n)^{189}Ir cross section obtained via the analysis of the 245.1 keV γ-ray peak.									
17.1	0.167	25.7	25.0	2.3	0.1	0.6	3.6	2.4	3
18.9	0.716	25.0	24.2	1.2	0.1	0.6	4.3	3.1	3
20.9	1.095	18.1	14.8	0.9	0.1	0.5	7.8	6.2	3

Table 3.13: The ^{193}Ir(n,2n)^{192}Ir cross sections obtained from each γ-ray (mentioned also in Tables 3.6 and 3.7) along with the total uncertainties (in %) and the uncertainties for the most significant contributions in Eq. 3.1 at each neutron energy. The data at lower neutron energies (10-11.3 MeV) were obtained in 2005-2006, by N. Patronis et al. but they were not included in Ref. [11], while the corrections for the low energy parasitic neutrons contribution were performed based on the MCNP5 simulations presented in Appendix E.

E_n	Cross section	Uncertainties (%)							
(MeV)	(b)	Total	$(N_\gamma)_{Ir}$	$(N_\gamma)_{Al}$	$(N_\tau)_{Ir}$	$(N_\tau)_{Al}$	$(\varepsilon_\gamma)_{Ir}$	$(\varepsilon_\gamma)_{Al}$	σ_{Al}
For the cross sections obtained via the analysis of the 316.5 keV γ-ray peak.									
10.0	1.315	8.3	2.3	2.4	0.3	0.5	4.0	4.0	3.0
10.5	1.607	8.2	1.6	2.3	0.3	0.6	4.0	4.0	3.0
11.0	1.951	8.2	1.6	2.1	0.3	0.6	4.0	4.0	3.0
11.3	2.037	8.1	1.5	2.0	0.3	0.5	4.0	4.0	3.0
15.3	1.841	4.5	0.3	0.3	0.1	0.5	2.1	2.3	3
17.1	1.412	5.2	1.0	2.3	0.1	0.6	2.4	2.4	3
18.9	0.740	16.6	15.7	1.2	0.1	0.6	2.8	3.1	3
20.9	0.273	29.0	28.0	0.9	0.1	0.5	2.8	6.2	3
For the cross sections obtained via the analysis of the 468.1 keV γ-ray peak.									
10.0	1.279	8.0	2.5	2.4	0.3	0.5	4.0	4.0	3.0
10.5	1.578	7.7	1.7	2.3	0.3	0.6	4.0	4.0	3.0
11.0	1.893	7.7	1.8	2.1	0.3	0.6	4.0	4.0	3.0
11.3	1.896	7.7	1.8	2.0	0.3	0.5	4.0	4.0	3.0
15.3	1.817	4.6	0.5	0.3	0.1	0.5	2.1	2.3	3
17.1	1.365	5.4	1.6	2.3	0.1	0.6	2.5	2.4	3
18.9	0.773	16.7	15.9	1.2	0.1	0.6	2.8	3.1	3
20.9	0.265	31.9	31.0	0.9	0.1	0.5	2.9	6.2	3
For the cross sections obtained via the analysis of the 308.5 keV γ-ray peak.									
10.0	1.282	8.4	2.9	2.4	0.3	0.5	4.0	4.0	3.0
10.5	1.591	8.1	1.8	2.3	0.3	0.6	4.0	4.0	3.0
11.0	1.972	8.1	2.0	2.1	0.3	0.6	4.0	4.0	3.0
11.3	1.971	8.1	2.0	2.0	0.3	0.5	4.0	4.0	3.0
15.3	1.834	4.6	0.7	0.3	0.1	0.5	2.2	2.3	3
17.1	1.397	5.6	2.2	2.3	0.1	0.6	2.5	2.4	3
18.9	0.810	18.7	17.9	1.2	0.1	0.6	2.9	3.1	3
20.9	0.274	38.9	38.2	0.9	0.1	0.5	2.9	6.2	3

3.3 Weighted Average Cross Sections

The final experimental cross section results for each reaction were deduced using the weighted average cross sections obtained either by two or by three cross section values, depending on the number of the analyzed γ-ray peaks in each case (see Table 3.14).

Table 3.14: Number of analyzed γ-ray peaks for each measured reaction.

Reaction	Analyzed γ-rays peaks in keV		
^{197}Au(n,2n)^{196}Au$^{g+m1+m2}$	355.7	333.0	426.0
^{197}Au(n,2n)^{196}Au^{m2}	147.8	188.3	
^{191}Ir(n,2n)^{190}Ir$^{g+m1+0.086\,m2}$	518.6	558.0	569.3
^{191}Ir(n,2n)^{190}Ir^{m2}	616.5	502.5	
* ^{191}Ir(n,3n)^{189}Ir	245.1		
^{193}Ir(n,2n)^{192}Ir	316.5	468.1	308.5

* Concerning this reaction, it was not necessary to determine the weighted average value, since the cross sections were deduced only by the analysis of one γ-ray peak.

Let's assume the case in which two cross section values exist, for example:
$\sigma_1 = \left(\sigma_{ref_1}, (N_\gamma)_{meas_1}, (N_\gamma)_{ref_1}, (\varepsilon_\gamma)_{meas_1}, (\varepsilon_\gamma)_{ref_1}, (N_\tau)_{meas_1}, (N_\tau)_{ref_1}\right)$
$\sigma_2 = \left(\sigma_{ref_2}, (N_\gamma)_{meas_2}, (N_\gamma)_{ref_2}, (\varepsilon_\gamma)_{meas_2}, (\varepsilon_\gamma)_{ref_2}, (N_\tau)_{meas_1}, (N_\tau)_{ref_2}\right)$
As it was mentioned in section 3.2, in each parenthesis all the parameters were considered uncorrelated. Therefore, horizontally there is no correlation. However, the vertical correlations between the two cross section measurements were taken into account by determining the weighted average and its uncertainty according to Eqs. (27) reported in Ref. [106], which are the following:

$$\bar{\sigma} = \frac{(\delta\sigma_2{}^2 - V_{12})\,\sigma_1 + (\delta\sigma_1{}^2 - V_{12})\,\sigma_2}{\delta\sigma_1{}^2 + \delta\sigma_2{}^2 - 2V_{12}} \tag{3.6}$$

$$\delta\sigma = \sqrt{\frac{\delta\sigma_1{}^2\,\delta\sigma_2{}^2 - V_{12}{}^2}{\delta\sigma_1{}^2 + \delta\sigma_2{}^2 - 2V_{12}}} \tag{3.7}$$

where $\sigma_1 \pm \delta\sigma_1$ is the cross section obtained by the analysis of the first γ-ray peak along with its uncertainty, $\sigma_2 \pm \delta\sigma_2$ is the cross section obtained by the analysis of the second γ-ray peak along with its uncertainty and V_{12} is the covariance of σ_1 and σ_2 values:

$$V_{12} = cov(\sigma_1, \sigma_2)$$

The covariance of σ_1 and σ_2 values can be written as:

$$\begin{aligned} V_{12} = & \left(\frac{\theta\sigma}{\theta\sigma_{ref}}\right)_1 cov(\sigma_{ref_1}, \sigma_{ref_2}) \left(\frac{\theta\sigma}{\theta\sigma_{ref}}\right)_2 + \\ & + \left(\frac{\theta\sigma}{\theta(N_\gamma)_{meas}}\right)_1 cov((N_\gamma)_{meas_1}, (N_\gamma)_{meas_2}) \left(\frac{\theta\sigma}{\theta(N_\gamma)_{meas}}\right)_2 + \\ & + \left(\frac{\theta\sigma}{\theta(N_\gamma)_{ref}}\right)_1 cov((N_\gamma)_{ref_1}, (N_\gamma)_{ref_2}) \left(\frac{\theta\sigma}{\theta(N_\gamma)_{ref}}\right)_2 + \\ & + \left(\frac{\theta\sigma}{\theta(\varepsilon_\gamma)_{meas}}\right)_1 cov((\varepsilon_\gamma)_{meas_1}, (\varepsilon_\gamma)_{meas_2}) \left(\frac{\theta\sigma}{\theta(\varepsilon_\gamma)_{meas}}\right)_2 + \\ & + \left(\frac{\theta\sigma}{\theta(\varepsilon_\gamma)_{ref}}\right)_1 cov((\varepsilon_\gamma)_{ref_1}, (\varepsilon_\gamma)_{ref_2}) \left(\frac{\theta\sigma}{\theta(\varepsilon_\gamma)_{ref}}\right)_2 + \\ & + \left(\frac{\theta\sigma}{\theta(N_\tau)_{meas}}\right)_1 cov((N_\tau)_{meas_1}, (N_\tau)_{meas_2}) \left(\frac{\theta\sigma}{\theta(N_\tau)_{meas}}\right)_2 + \\ & + \left(\frac{\theta\sigma}{\theta(N_\tau)_{ref}}\right)_1 cov((N_\tau)_{ref_1}, (N_\tau)_{ref_2}) \left(\frac{\theta\sigma}{\theta(N_\tau)_{ref}}\right)_2 \end{aligned} \tag{3.8}$$

The detailed operations for the determination of the V_{12} factor are given in Appendix C.

For the cases in which three cross section values exist, for example:
$\sigma_1 = \left(\sigma_{ref_1}, (N_\gamma)_{meas_1}, (N_\gamma)_{ref_1}, (\varepsilon_\gamma)_{meas_1}, (\varepsilon_\gamma)_{ref_1}, (N_\tau)_{meas_1}, (N_\tau)_{ref_1}\right)$
$\sigma_2 = \left(\sigma_{ref_2}, (N_\gamma)_{meas_2}, (N_\gamma)_{ref_2}, (\varepsilon_\gamma)_{meas_2}, (\varepsilon_\gamma)_{ref_2}, (N_\tau)_{meas_2}, (N_\tau)_{ref_2}\right)$
$\sigma_3 = \left(\sigma_{ref_3}, (N_\gamma)_{meas_3}, (N_\gamma)_{ref_3}, (\varepsilon_\gamma)_{meas_3}, (\varepsilon_\gamma)_{ref_3}, (N_\tau)_{meas_3}, (N_\tau)_{ref_3}\right)$

the formalism mentioned in Appendix 2 of Ref. [105] was adopted, which is served better by using operations between matrices (see Appendix D). According to this formalism, the weighted average cross section and its uncertainty are given by the following expressions:

$$\bar{\sigma} = w_1 \cdot \sigma_1 + w_2 \cdot \sigma_2 + w_3 \cdot \sigma_3 \tag{3.9}$$

$$\begin{aligned} \delta\sigma^2 = & \; w_1 \left(w_1 V_{11} + w_2 V_{21} + w_3 V_{31}\right) + \\ & + w_2 \left(w_1 V_{12} + w_2 V_{22} + w_3 V_{32}\right) + \\ & + w_3 \left(w_1 V_{13} + w_2 V_{23} + w_3 V_{33}\right) \end{aligned} \tag{3.10}$$

where the covariances V_{ij} are determined as presented in Eq. 3.8 for i=1 and j=2 and w_i are the weights, which in general form can be written as:

$$w_i = \frac{\sum\limits_j V_{ji}^{-1}}{\sum\limits_k \sum\limits_l V_{kl}^{-1}} \tag{3.11}$$

For example, the weight for $i = 1$, is given by the following expression:

$$\begin{aligned} w_1 = & \frac{\left(V_{22}V_{33} - {V_{23}}^2\right) + \left(V_{23}V_{31} - V_{33}V_{12}\right) + \left(V_{12}V_{23} - V_{13}V_{22}\right)}{\left(V_{22}V_{33} - {V_{23}}^2\right) + \left(V_{11}V_{33} - {V_{13}}^2\right) + \left(V_{11}V_{22} - {V_{12}}^2\right) + } \\ & + 2\left(V_{13}V_{23} - V_{33}V_{12}\right) + 2\left(V_{12}V_{23} - V_{22}V_{13}\right) + 2\left(V_{13}V_{21} - V_{23}V_{11}\right) \end{aligned} \tag{3.12}$$

The detailed operations for the determination of all the weights and uncertainties are given in Appendix D.

The weighted average cross sections for each of the six reactions are presented in Table 3.15.

Table 3.15: Experimental weighted average cross section values for the six measured reactions. The new data points at lower neutron energies (10-11.3 MeV) for the ^{193}Ir(n,2n) reaction cross section were obtained in 2005-2006, by N. Patronis et al. but they were not included in Ref. [11]. The necessary corrections for the low energy parasitic neutrons contribution were performed based on the MCNP5 simulations presented in Appendix E. Moreover, concerning neutron induced reactions on Au, in the 10-11.3 MeV energy region, the results were published in 2011, by A. Tsinganis et al. [12].

E_n	Weighted Average Cross Section (b)						
(MeV)	^{197}Au(n,2n)^{196}Au	^{197}Au(n,2n)^{196}Au^{m2}	^{197}Au(n,2n)^{196}Au^{m2} *	^{191}Ir(n,2n)^{190}Ir	^{191}Ir(n,2n)^{190}Ir^{m2}	^{191}Ir(n,3n)^{189}Ir	^{193}Ir(n,2n)^{192}Ir
10.0	-	-	-	-	-	-	1.290 ± 0.083
10.5	-	-	-	-	-	-	1.590 ± 0.100
11.0	-	-	-	-	-	-	1.931 ± 0.119
11.3	-	-	-	-	-	-	1.953 ± 0.120
15.3	1.995 ± 0.093	0.163 ± 0.009	0.172 ± 0.010	1.786 ± 0.076	0.179 ± 0.008	-	1.830 ± 0.076
17.1	1.772 ± 0.086	0.196 ± 0.012	0.212 ± 0.013	1.465 ± 0.072	0.203 ± 0.015	0.167 ± 0.043	1.390 ± 0.068
17.9	1.651 ± 0.080	0.213 ± 0.014	0.223 ± 0.015	1.291 ± 0.082	0.210 ± 0.012	-	-
18.9	1.394 ± 0.064	0.195 ± 0.013	0.204 ± 0.013	0.991 ± 0.052	0.178 ± 0.010	0.716 ± 0.179	0.769 ± 0.082
20.0	1.049 ± 0.091	0.169 ± 0.020	0.178 ± 0.013	0.731 ± 0.091	0.134 ± 0.013	-	-
20.9	0.716 ± 0.056	0.120 ± 0.013	0.126 ± 0.014	0.479 ± 0.037	0.086 ± 0.007	1.096 ± 0.198	0.270 ± 0.053

* The intensities of the γ-rays were adopted by Ref. [38] (see Table 1.1).

3.4 Correction for Low Energy Parasitic Neutrons

In the framework of the present thesis, through the use of current computational power and updated evaluated data libraries, a recently applied analysis method was implemented for the determination of the ^{193}Ir(n,2n)^{192}Ir reaction cross section which is contaminated by the ^{191}Ir(n,γ)^{192}Ir one and it will be presented step by step in this section. Due to the fact that the ^{191}Ir(n,γ)^{192}Ir reaction is activated by low energy parasitic neutrons, there is a strong need for both qualitative and quantitative estimation of the low energy neutron tail. However, once this correction is made, the ^{193}Ir(n,2n)^{192}Ir reaction cross section can be accurately determined, since it is a threshold reaction (see Table 2.4) and is not affected by the low energy tail of parasitic neutrons. At this point, it should be mentioned that the parasitic neutrons may come from break-up reactions, from the TiT target itself, from reactions with materials of the beam-line and from scattering in the materials of the room (see section 2.2 for more details).

3.4.1 MCNP5 simulations

The method is based on simulations of the irradiation setups by means of the MCNP5 code [35, 36]. Although these setups were also simulated as mentioned in section 2.4.2, in order to determine the main neutron peak energy and the effect of solid angle in the neutron flux for each target foil, those simulations were not capable of solving the problem of the low energy neutron tail. Therefore, more simulations were performed, in which the experimental setups were described in great detail, implementing a very low neutron energy cut-off (10^{-11}MeV) and were executed for much longer ($\sim$ 11 d per run) for better statistics (an order of magnitude higher number of simulated particles - nps=10^9).

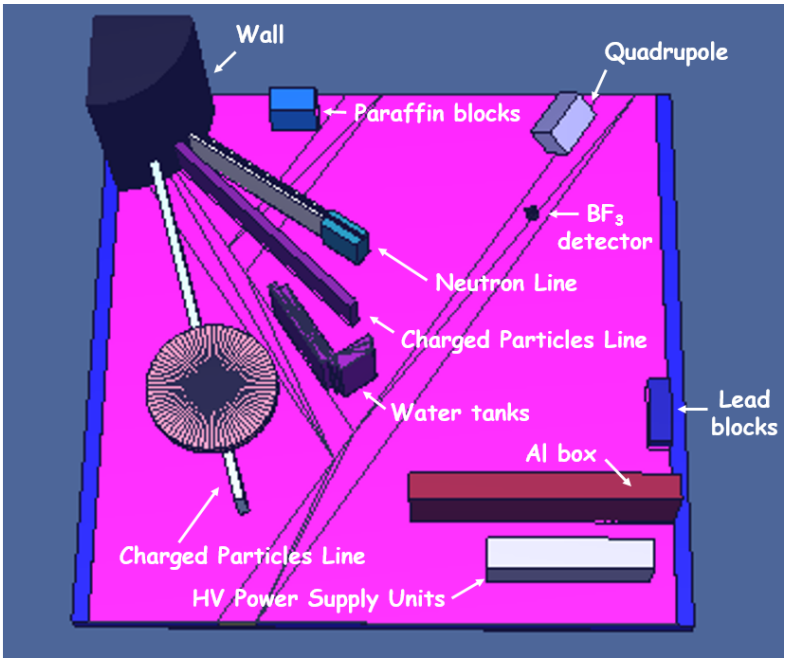

Figure 3.1: 3D-figure representing the overview of the experimental hall of the Tandem Acceletator Laboratory of NCSR "Demokritos", as described in MCNP5.

More specifically, the geometry of the whole experimental hall of the Tandem Acceletator Laboratory of NCSR "Demokritos" was introduced in the MCNP5 input file (see Fig. 3.1-3.7). The walls and the ceiling of the room have been excluded from the following figures, but they were included in the input file. All the information on the materials and dimensions of the objects described in simulation was adopted from Ref. [107].

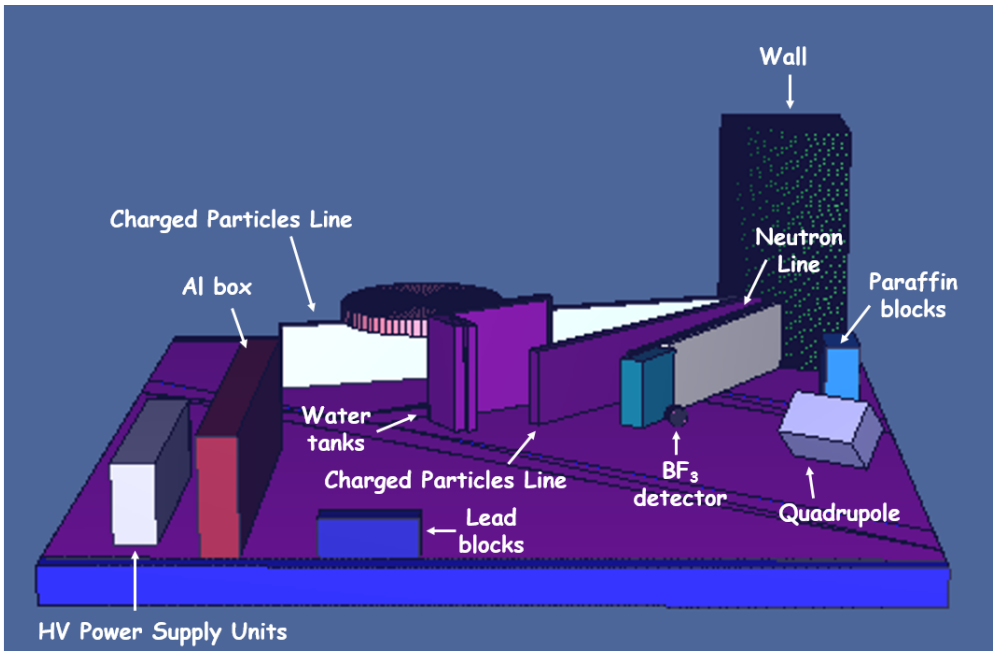

Figure 3.2: 3D-figure representing the experimental hall of the Tandem Acceletator Laboratory of NCSR "Demokritos" from another point of view.

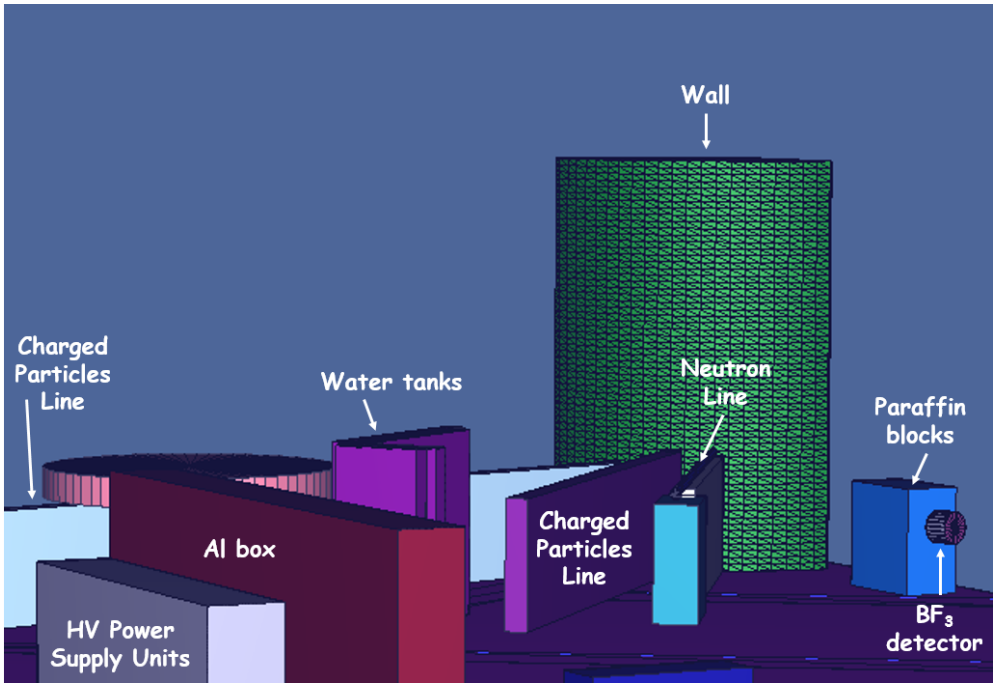

Figure 3.3: 3D-figure representing the experimental hall of the Tandem Acceletator Laboratory of NCSR "Demokritos" from another point of view.

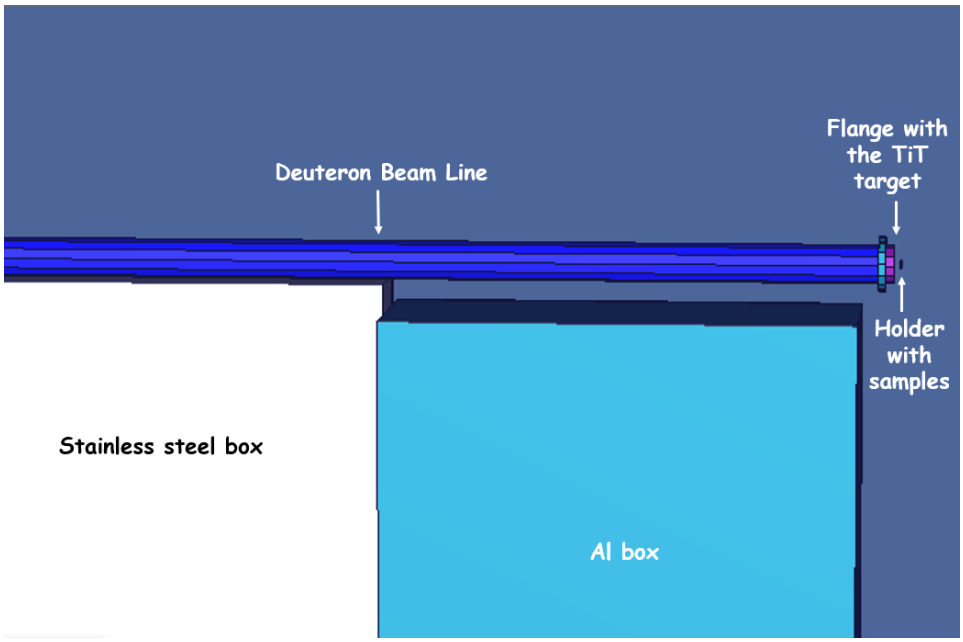

Figure 3.4: 3D-figure representing the irradiation line for the cases that the D-T reaction was used for the neutron production (irradiations at neutron beam energies ranging from 15.3-20.9 MeV).

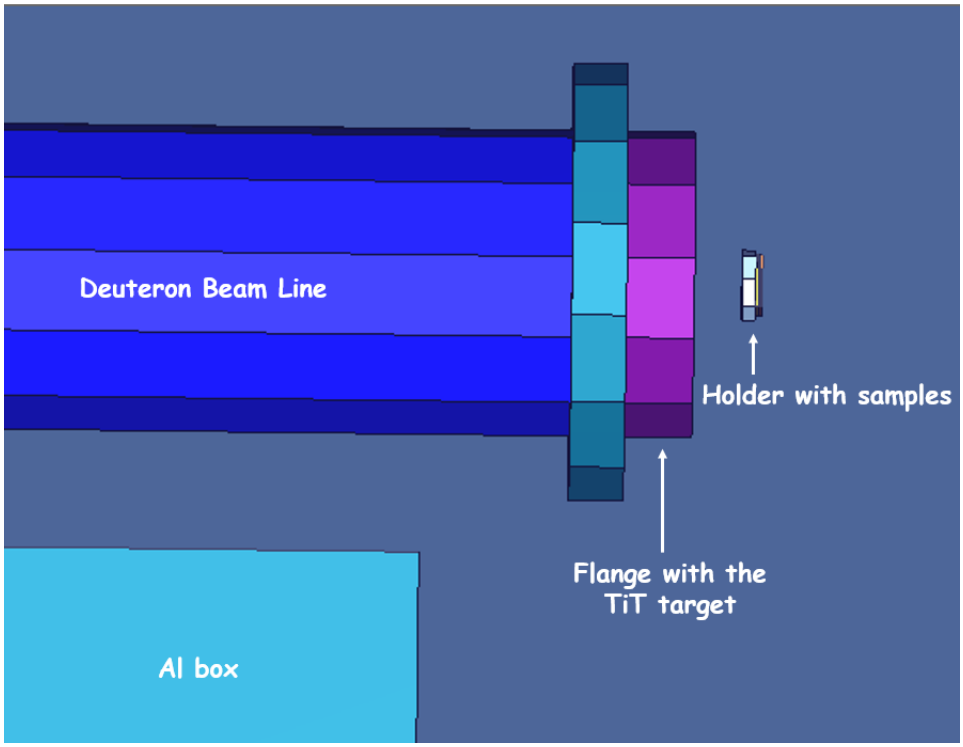

Figure 3.5: 3D-figure representing the end of the neutron production line, the flange with the TiT target and the holder along with the irradiated samples.

The input file of the MCNP5 code including the full geometry of the room for the cases that the solid Ti-T target was used for the neutron production is given in Appendix E.

Concerning the measurements performed in 2005 and 2006 at lower neutron beam energies (10-11.3 MeV), by Patronis *et. al* [11], there is a slight difference in the geometry description. Instead of the Ti-T target, a deuterium gas target was used in order to produce neutrons at lower energies. The gas cell geometry, as described in MCNP5 code, is presented in Figs. 3.6 and 3.7.

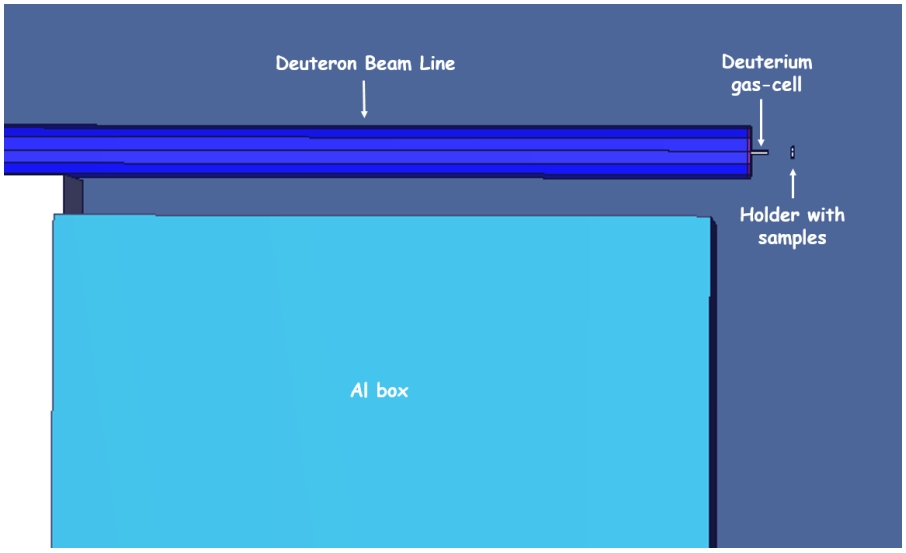

Figure 3.6: 3D-figure representing the irradiation line for the cases that the D-D reaction was used for the neutron production (irradiations at neutron beam energies ranging from 10-11.3 MeV).

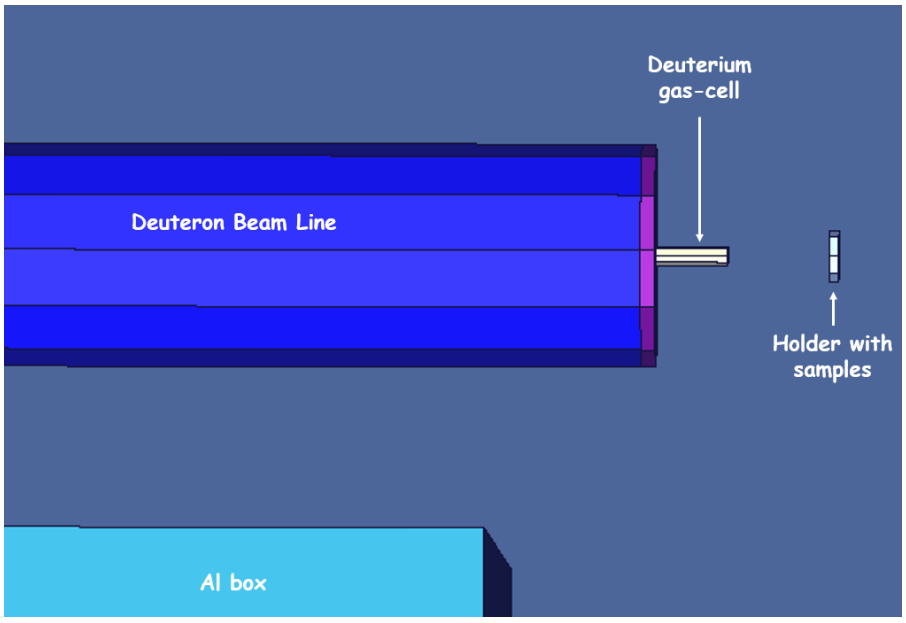

Figure 3.7: 3D-figure representing the end of the irradiation line, the deuterium filled gas cell and the holder along with the irradiated samples.

The input file of the MCNP5 code including the full geometry of the room for the cases that the deuterium gas cell was used for the neutron production is given in Appendix E.

3.4.2 Validation with ^{197}Au(n,γ) reaction

Once the MCNP5 simulations are completed, the shape of the neutron flux distribution is known and is presented in Fig. 3.8.

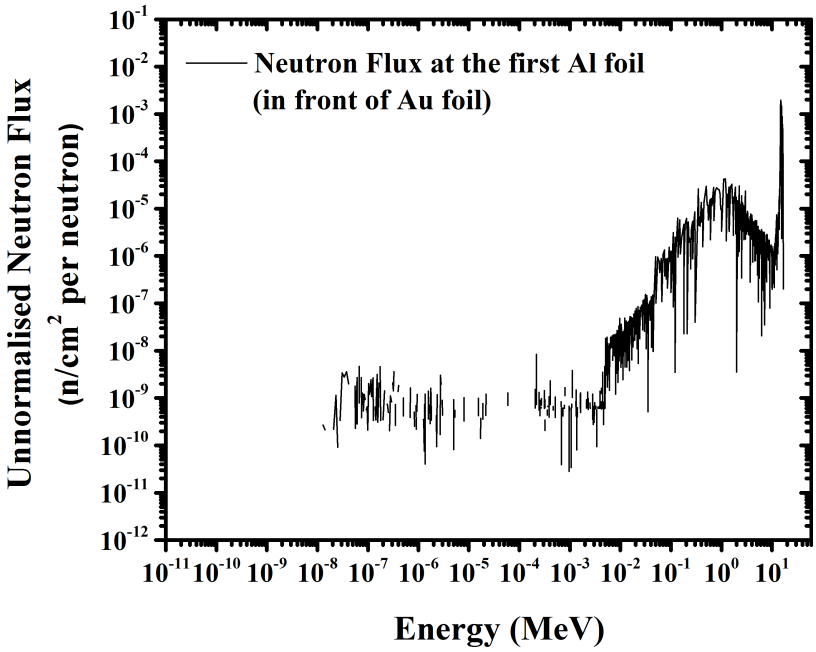

Figure 3.8: Neutron flux distribution with respect to neutron energy obtained from simulation using the MCNP5 code for the irradiation at 15.3 MeV. The neutron flux was scored at the Al foil, which was placed in front of the Au one and this is the actual flux hitting the Au foil.

However, this distribution (Fig. 3.8) has to be normalized in order to comply with the experiment. The normalization was based on the ^{197}Au(n,γ)^{198}Au reaction, which is sensitive to the low energy neutron tail, due to the following reasons:

- It is a non threshold reaction ($E_{threshold} = 0$ MeV), therefore it can be activated by the low energy neutron tail.
- Its cross section is orders of magnitude higher for low energy neutrons and decreases significantly above 1 MeV (see Fig. 3.9). The latter means that a low energy neutron (10^{-11}-10^{-1} MeV) has a very significant contribution compared to the high energy one in the ^{197}Au(n,γ)^{198}Au reaction yield.

Therefore, the neutron flux distribution was normalized according to the following expression:

$$\phi_{normalized}(E_i)\left(\frac{n}{cm^2\,s}\right) = \frac{\phi^{Au}_{experimental}\left(\frac{n}{cm^2\,s}\right)\cdot\phi_{mcnp}(E_i)}{\sum_{E_i=8MeV}^{30}\phi_{mcnp}(E_i)}\cdot Scale\,Factor \qquad (3.13)$$

where $\phi^{Au}_{experimental}\left(\frac{n}{cm^2\,s}\right)$ is the experimentally determined neutron fluence which impinged on the Au foil during the irradiation and $\phi_{mcnp}(E_i)$ is the unnormalized neutron

flux obtained from the MCNP5 simulation. As a first approximation, the ratio in Eq. 3.13 normalizes the neutron flux obtained from the MCNP5 simulation to the neutron flux which impinged on the Au foil during the irradiation.

The initial value of "$Scale\ Factor$" is 1 and exists in Eq. 3.13 in order to correct for parasitic neutrons that have not been taken into account in the simulation, such as neutrons from (d,n) reactions on the materials of the beam line and neutrons from the D(d,n) reaction on the implanted D nuclei in the TiT target (see also section 2.2).

By using the $\phi_{normalized}(E_i)$, the expected reaction rate (RR) is determined according to equation:

$$RR_{expected} = \sum_{E_i} \sigma(E_i) \cdot \phi_{normalized}(E_i) \tag{3.14}$$

where $\sigma(E_i)$ is the cross section of the ^{197}Au(n,γ)^{198}Au reaction at each energy bin (see Fig. 3.9). It should be noted that the energy binning of the ENDF/B-VII.1 library [28] was adopted.

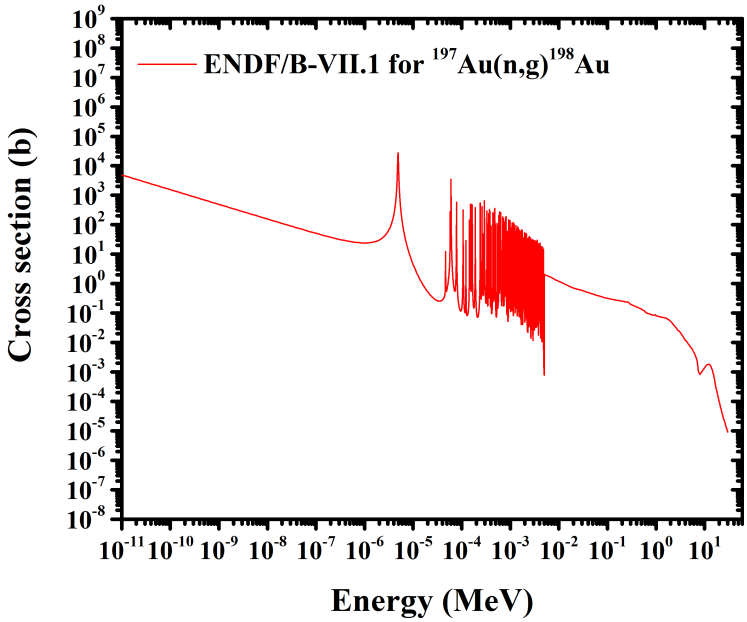

Figure 3.9: Cross section of the ^{197}Au(n,γ)^{198}Au reaction with respect to neutron energy. The evaluated data are adopted from ENDF/B.VII.1 library [28].

The reaction rate is also experimentally given by the following expression:

$$RR_{experimental} = \frac{\lambda \cdot N_p}{N_\tau\ (1 - e^{\lambda t_B})} \tag{3.15}$$

where N_p is the number of the produced nuclei during the irradiation and is given by the relation:

$$N_p = \frac{N_\gamma}{\varepsilon_\gamma \cdot I \cdot F \cdot D} \tag{3.16}$$

the remaining symbols have been explained in section 3.1.

By combining Eqs. 3.15 and 3.16, the number of the γ-ray peak integral, N_γ, can be written as:

$$N_\gamma = \frac{\varepsilon_\gamma \cdot I \cdot F \cdot D \cdot N_\tau \left(1 - e^{\lambda t_B}\right) \cdot RR_{experimental}}{\lambda} \tag{3.17}$$

while the expected number of γ-rays, $N_{\gamma\,expected}$, using the simulated neutron flux is:

$$N_{\gamma\,expected} = \frac{\varepsilon_\gamma \cdot I \cdot F \cdot D \cdot N_\tau \left(1 - e^{\lambda t_B}\right) \cdot RR_{expected}}{\lambda} \tag{3.18}$$

All the quantities in Eq. 3.18 were substituted by those referring to the analysis of the 411.8 keV γ-ray emitted during the de-excitation of the ^{198}Au nucleus and the final value of the $Scale\,Factor$ was chosen in such a way that the 411.8 keV γ-ray peak integral be reproduced within its experimental error. Thus, the final purpose is to match the $N_{\gamma\,expected}$ with the $N_{\gamma\,experimental}$ for the 411.8 keV γ-ray peak. In other words, Eq. 3.18 is the "key" of this method because it leads to the determination of the $Scale\,Factor$ of Eq. 3.13.

The values of the $Scale\,Factor$ for the six neutron beam energies (15.3-20.9 MeV) are presented in Table 3.16 and Fig. 3.10. Only in four of these measurements the γ-rays emitted during the de-excitation of the ^{192}Ir nucleus gave reasonable statistics to allow for the cross section determination, but since the 411.8 keV γ-ray peak emitted during the de-excitation of the ^{198}Au nucleus was present in every measurement, the $Scale\,Factor$ was determined for all the irradiations.

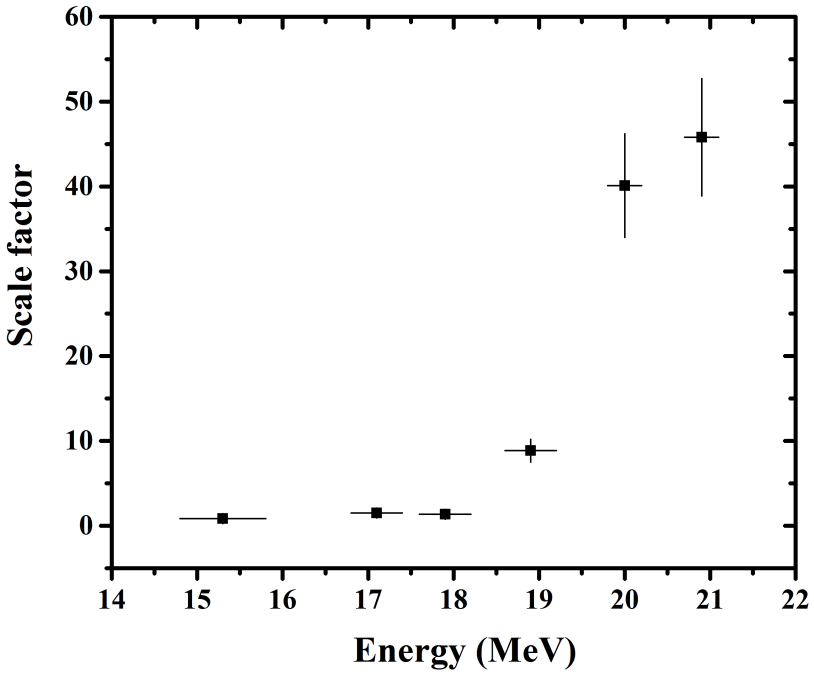

Figure 3.10: The $Scale\,Factor$ (mentioned in Eq. 3.13) with respect to the neutron beam energy for the irradiations performed by means of the D-T reaction. In each energy the $Scale\,Factor$ was adjusted so as the $N_{\gamma\,expected}$ in Eq. 3.18 reproduces the integral of the 411.8 keV γ-ray peak emitted during the de-excitation of the ^{198}Au nucleus.

As shown in Fig. 3.10, in the energy region below 18 MeV, the $Scale\,Factor$ is close to 1, meaning that the parasitic neutrons are well described by the simulations. On the contrary,

above 18.9 MeV, the *Scale Factor* increases rapidly, indicating that parasitic neutrons, which are not taken into account in the simulations, become important. These neutrons are expected to be produced from the following reactions: ^{2}H(d,n)^{4}He (E_{thr}= 0.0 MeV), ^{12}C(d,n)^{13}N (E_{thr}= 0.3 MeV), ^{16}O(d,n)^{17}F (E_{thr}= 1.8 MeV) and ^{3}H(d,np)^{3}H (E_{thr}= 3.7 MeV), which were also mentioned in section 2.2 (see Table 2.2). Obviously, it is not only the threshold reaction that matters, but also the corresponding cross section shape.

Concerning the irradiations at lower neutron beam energies (10.0-11.3 MeV), the corresponding factors are presented in Table 3.16 and Fig. 3.11.

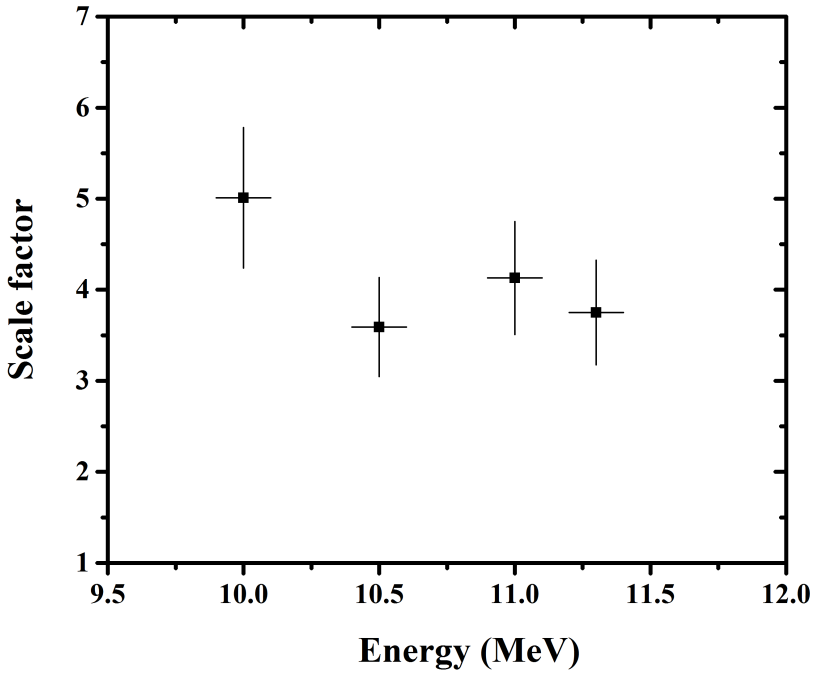

Figure 3.11: The *Scale Factor* (mentioned in Eq. 3.13) with respect to the neutron beam energy for the irradiations performed by means of the D-D reaction. In each energy the *Scale Factor* was adjusted so as the $N_{\gamma\,expected}$ in Eq. 3.18 reproduces the integral of the 411.8 keV γ-ray peak emitted during the de-excitation of the ^{198}Au nucleus.

In these cases, where the neutrons are produced by means of the ^{2}H(d,n)^{3}He reaction, the situation is much more complicated. There are many reactions that produce parasitic neutrons, especially at deuteron energies above 4 MeV [32]. Therefore, in the present irradiations (performed in 2005-2006 by N. Patronis *et al.* [11]), in which all the deuteron beam energies were above 7 MeV, the basic reactions that may produce parasitic neutrons are the following: ^{2}H(d,pn)^{2}H (E_{thr}= 4.45 MeV), ^{2}H(d,2n)^{2}He (E_{thr}= 8.9 MeV), ^{nat}Mo(d,n) (E > 4 MeV) and ^{nat}Mo(d,2n) (E > 4 MeV). Thus, the *Scale Factor* values presented in Fig. 3.11 for neutron energies above 10 MeV should be expected. The unexpected point is the one at 10 MeV which is much higher than the others. This could be attributed to a different deuteron beam alignment and therefore, it could lead the deuterons to enter the gas cell slightly off-centered. However, even this was the case, the threshold reactions which were studied in the past are not affected from the low energy parasitic neutrons.

Table 3.16: The $Scale\,Factor$ of Eq. 3.13 for each irradiation adjusted so as the $N_{\gamma\,expected}$ reproduces the integral of the 411.8 keV γ-ray peak emitted during the de-excitation of the ^{198}Au nucleus within its experimental error.

Neutron Production Reaction	E_n (MeV)	$Scale\,Factor$
^{2}H(d,n)^{3}He (D-D)	10.0 ± 0.1	5.01
	10.5 ± 0.1	3.59
	11.0 ± 0.1	4.13
	11.3 ± 0.1	3.75
^{3}H(d,n)^{4}He (D-T)	15.3 ± 0.5	0.85
	17.1 ± 0.3	1.52
	17.9 ± 0.3	1.35
	18.9 ± 0.3	8.85
	20.0 ± 0.2	40.1
	20.9 ± 0.2	45.8

As shown in Table 3.16, the $Scale\,Factor$ value at E_n=15.3 MeV is 0.85 (<1). The latter means that the $RR_{expected}$ is higher than the $RR_{experimental}$ and this is not expected, since the simulation misses some parasitic neutron producing reactions. Therefore, this 15%, which is due to the uncertainty of the simulated neutron flux, was assumed to be the main uncertainty of this method. The relative error of the $N_{\gamma\,experimental}$ for the 411.8 keV γ-ray peak was also taken into account, but that did not exceed the 4%. The final uncertainty of this method was estimated by the quadratic summation of the two aforementioned uncertainties. In Figs. 3.10 and 3.11, the same uncertainty (15-19%) is abusively used for the presentation of the energy dependence of the $Scale\,Factor$ (abusively, due to the fact that the uncertainty actually corresponds to the simulated neutron flux).

The experimentally determined $Scale\,Factor$ values were then used in order to make the appropriate corrections for the determination of the ^{193}Ir(n,2n)^{192}Ir reaction cross section, which is contaminated by the ^{191}Ir(n,γ)^{192}Ir one, as presented in the following section.

3.4.3 Contribution of ^{191}Ir(n,γ) reaction

Similarly, in order to determine the neutron fluence distribution in the Ir foil, the normalization was carried out according to the following equation:

$$\phi_{normalized}\left(E_i\right)\left(\frac{n}{cm^2\,s}\right)=\frac{\phi^{Ir}_{experimental}\left(\frac{n}{cm^2\,s}\right)\cdot\phi_{mcnp}\left(E_i\right)}{\sum_{E_i=8MeV}^{30}\phi_{mcnp}\left(E_i\right)}\cdot Scale\,Factor \tag{3.19}$$

where $\phi^{Ir}_{experimental}\left(\frac{n}{cm^2\,s}\right)$ is the experimentally determined neutron fluence which impinged on the Ir foil during the irradiation and $\phi_{mcnp}\left(E_i\right)$ is the unnormalized neutron flux obtained from the MCNP5 simulation. The values of the "$Scale\,Factor$" for each irradiation are presented in Figs. 3.10 and 3.11 and were chosen in such a way that the $N_{\gamma\,experimental}$ for the 411.8 keV γ-ray peak emitted during the de-excitation of the ^{198}Au nucleus was reproduced within its experimental error.

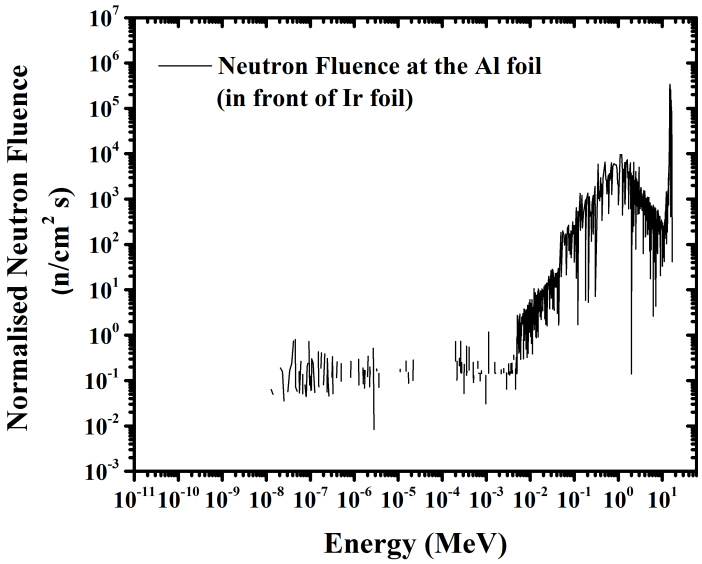

Figure 3.12: Normalized neutron fluence distribution with respect to the neutron energy obtained from Eq. 3.19 for the irradiation at 15.3 MeV.

Since the neutron flux distribution is known, the expected reaction rate for the ^{191}Ir(n,γ)^{192}Ir is determined according to the equation:

$$RR_{expected} = \sum_{E_i} \sigma(E_i) \cdot \phi_{normalized}(E_i) \tag{3.20}$$

where $\sigma(E_i)$ is the cross section of the ^{191}Ir(n,γ)^{192}Ir reaction at each energy bin (see Fig. 3.13).

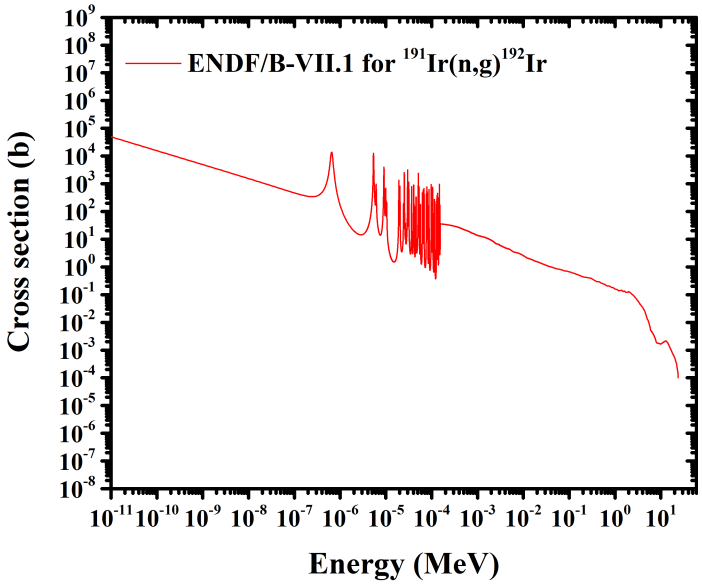

Figure 3.13: Cross section of the ^{191}Ir(n,γ)^{192}Ir reaction with respect to neutron energy. The evaluated data are adopted from ENDF/B.VII.1 library [28].

Then, according to Eq. 3.18, one can estimate the $N_{\gamma\,correction}$, which is the number of

counts that have to be subtracted from the total counts in the spectrum, in order to correct for the contribution of low energy parasitic neutrons:

$$N_{\gamma\,correction} = N_{\gamma\,expected} = \frac{\varepsilon_\gamma \cdot I \cdot F \cdot D \cdot N_\tau \left(1 - e^{\lambda t_B}\right) \cdot RR_{expected}}{\lambda} \tag{3.21}$$

All the quantities in Eq. 3.21 were substituted by those referring to the analysis of the three most intense γ-rays (316.5, 468.1 and 308.5 keV) emitted during the de-excitation of the ^{192}Ir nucleus.

Therefore, the useful counts for the cross section determination are given as:

$$N_\gamma = N_{\gamma\,spectrum} - N_{\gamma\,correction} \tag{3.22}$$

The relative error of the $N_{\gamma\,correction}$ was assumed to be the same to the relative error of the $N_{\gamma\,experimental}$ for the 411.8 keV γ-ray peak, while the uncertainty of the final, corrected N_γ was assumed to be the quadratical summing of the two individual errors.

The results are presented in Tables 3.17 and 3.18 for each irradiation and for each γ-ray separately.

Table 3.17: The $N_{\gamma\,spectrum}$, $N_{\gamma\,correction}$ and N_γ for the three most intense γ-rays (316.5, 468.1 and 308.5 keV) emitted during the de-excitation of the ^{192}Ir nucleus for the irradiations at neutron beam energies between 10 and 11.3 MeV.

E_n (MeV)	E_γ (keV)	$N_{\gamma\,spectrum}$	$N_{\gamma\,correction}$	N_γ	$\frac{N_{\gamma\,correction}}{N_{\gamma\,spectrum}}$ (%)
10.0 ± 0.1	316.5	20809 ± 170	2517 ± 387	18290 ± 423	12
	468.1	9606 ± 111	1173 ± 183	8433 ± 214	12
	308.5	7406 ± 123	920 ± 141	6486 ± 187	12
10.5 ± 0.1	316.5	54241 ± 276	4717 ± 715	49524 ± 766	9
	468.1	25243 ± 180	2196 ± 338	23047 ± 383	9
	308.5	19557 ± 195	1723 ± 260	17834 ± 325	9
11.0 ± 0.1	316.5	30474 ± 211	2629 ± 395	27845 ± 448	9
	468.1	14045 ± 141	1246 ± 187	12799 ± 234	9
	308.5	11187 ± 152	956 ± 144	10231 ± 209	9
11.3 ± 0.1	316.5	36105 ± 227	2959 ± 454	33146 ± 507	8
	468.1	16019 ± 146	1402 ± 215	14617 ± 260	9
	308.5	12734 ± 160	1076 ± 165	11658 ± 230	8

As shown in Table 3.17, the correction is $\sim$ 10% in all cases and follows the same behavior to the *Scale Factor* shown in Fig. 3.11, as expected, since in this energy region there are many reactions that produce parasitic neutrons.

Table 3.18: The $N_{\gamma\,spectrum}$, $N_{\gamma\,correction}$ and N_{γ} for the three most intense γ-rays (316.5, 468.1 and 308.5 keV) emitted during the de-excitation of the ^{192}Ir nucleus for the irradiations at neutron beam energies between 15.3 and 20.9 MeV.

E_n (MeV)	E_γ (keV)	$N_{\gamma\,spectrum}$	$N_{\gamma\,correction}$	N_{γ}	$\frac{N_{\gamma\,correction}}{N_{\gamma\,spectrum}}$ (%)
15.3 ± 0.5	316.5	222500 ± 700	1613 ± 243	220887 ± 741	1
	468.1	104000 ± 500	764 ± 115	103236 ± 513	1
	308.5	80200 ± 550	583 ± 88	79617 ± 557	1
17.1 ± 0.3	316.5	32730 ± 300	902 ± 139	31828 ± 330	3
	468.1	15140 ± 230	431 ± 66	14709 ± 239	3
	308.5	11700 ± 250	326 ± 50	11374 ± 255	3
18.9 ± 0.3	316.5	16900 ± 460	8343 ± 1262	8557 ± 1343	49
	468.1	8230 ± 310	3972 ± 601	4258 ± 676	48
	308.5	6400 ± 400	3015 ± 456	3385 ± 607	47
20.9 ± 0.2	316.5	5300 ± 250	3305 ± 499	1995 ± 558	62
	468.1	2540 ± 130	1638 ± 247	902 ± 279	64
	308.5	1920 ± 210	1195 ± 180	725 ± 277	62

As shown in Table 3.18, the correction varies from 1% at lower energies, to ∼60% at the higher ones. As it was also mentioned in section 3.4.2, the contribution of the parasitic neutrons becomes important with increasing energy and that is consistent with the $Scale\,Factor$ shown in Fig. 3.10, as expected.

The corrected numbers of counts, N_γ, shown in the fifth column of Tables 3.17 and 3.18, were used to deduce the cross section of the ^{193}Ir(n,2n)^{192}Ir reaction by means of Eq. 3.1.

The experimentally deduced cross section values for all the studied reactions, in the framework of the present thesis, are presented in chapter 5, along with the cross section theoretical calculations that will be discussed in the next chapter.

4

Theoretical Calculations

In this chapter a brief historical retrospection of statistical models of nuclear decay processes will be presented, focusing on the mechanisms that are relative to the subject of the present thesis. Therefore, special attention will be given to the Hauser-Feshbach theory in the frame of which the cross section theoretical calculations have been carried out using two nuclear reaction model codes, namely the EMPIRE 3.2.2 [40] and TALYS 1.8 [42]. Moreover, the optimum input for both codes will be described for the three interactions of interest, namely the n + ^{197}Au, the n + ^{191}Ir and the n + ^{193}Ir ones.

4.1 Historical Elements

- In 1936, N. Bohr pointed out that when a high speed particle α collides with a heavy nucleus A, a compound system of remarkable stability (compound nucleus C) is formed [108, 109]. He made a hypothesis, widely known as "the Bohr assumption", in which the mode of disintegration of the compound system (B+β) depends only on its energy, angular momentum and parity, but not on the specific way in which it has been produced [110].

$$\alpha + A \longrightarrow C^* \longrightarrow B + \beta$$

- At the time of Bohr's work, the first statistical theory of compound nuclear decay came in the scene by V. Weisskopf [111, 112]. According to his theoretical context, the kinetic energy of the emitted particles β is of the same form as the spectrum of particles evaporated from an ideal fluid and that is the reason why this theory is also known as the Weisskopf evaporation theory. It constitutes a quantitative implementation of the Bohr hypothesis and is based on the inverse reaction β + B $\longrightarrow C^*$. Some of the approximations considered in this formulation is that the nucleus B is a stationary heavy mass and its excitation energy is usually ignored. When the former restriction was removed, the Weisskopf's model was improved and lead to the reciprocity theorem which can be summarised in the following relation:

$$\frac{\sigma_{\alpha\beta}}{\kappa_\beta^2} = \frac{\sigma_{\beta\alpha}}{\kappa_\alpha^2} \tag{4.1}$$

where $\sigma_{\alpha\beta}$ is the cross section of the forward reaction $\sigma_{\alpha+A\longrightarrow C^*\longrightarrow B+\beta}$, $\sigma_{\beta\alpha}$ the cross section of the inverse reaction $\sigma_{\beta+B\longrightarrow C^*\longrightarrow A+\alpha}$, κ_α the wave number in channel α and κ_β the wave number in channel β. Another approximation of this formulation is that there is no a priori inclusion of the angular momentum. The latter was the main drawback of this theory, since the densities of nuclear states are strongly angular momentum dependent and perhaps the reason why this theory was superseded by the quantum mechanical Hauser-Feshbach one [110].

- In 1949, S. Fernbach, R. Serber and T. B. Taylor proposed the so-called optical model, a model of elastic scattering, according to which a nucleon incident on a nucleus may be elastically scattered or it may be absorbed, just like it happens in optics with the scattering of light by a refracting and absorbing sphere [113].

- The experimental verification of the Bohr's independence hypothesis came in 1950 by S. N. Ghoshal [114], who used different entrance channels p + ^{63}Cu and α + ^{60}Ni to form the compound nucleus ^{64}Zn.

- In 1952, a new class of "fast" nuclear reactions was established, referred as direct ones. Such reactions happen when the product of the interaction have a high probability to escape and seemed that Bohr hadn't considered this point [115, 116].

- In the same year (1952), W. Hauser and H. Feshbach proposed their theory [44] which is similar to the V. Weisskopf's one but provides a proper quantum mechanical treatment of angular momentum [110]. The optical model is considered as a part of this model structure and the latter will be described in more detail in section 4.3.1.

- At about the same time (1954) the quantum mechanical version of the optical model was developed and this formulation ended up (among others) to the respective/corresponding relation for the transmission coefficients, which constitute an essential ingredient of the Hauser-Feshbach theory and represent the probability that a given partial wave (l-wave) is absorbed by the target nucleus [117].

- In 1966, another theory was proposed by J. J. Griffin, referred to as the exciton model, in order to describe the effect of producing incomplete "compound" nuclei. Following this effect, more statistical theories were developed in order to describe the same phenomenon by C. K. Cline and M. Blann [118, 119], G. D Harp, J. M. Miller and B. J. Berne [120] and Fabrici *et al.* [121]. More details on pre-equilibrium emission will be given in sections 4.2.2 and 4.3.3.

- In the early 1970s the availability of heavy ion beams was increased, thus the interest in the topic of fusion grew rapidly. Fusion is defined as the process in which a compound nucleus composed of the sum of the projectile and target nucleons is formed. The essential physics can be understood by considering the model proposed in 1975 by D. Glas and U. Mosel [122].

4.2 Basic reaction mechanisms

The basic nuclear reaction mechanisms that one can distinguish are the following three: direct, compound and pre-compound ones. These reaction processes can be subdivided according to time scales or, equivalently, to the number of intranuclear collisions taking place before emission. Moreover, each mechanism preferentially excites certain parts of the nuclear level spectrum and is characterized by different types of angular distributions. The overall situation is presented in Fig. 4.1, where the associated angular distributions show a gradual transition to isotropy for decreasing outgoing energies [123].

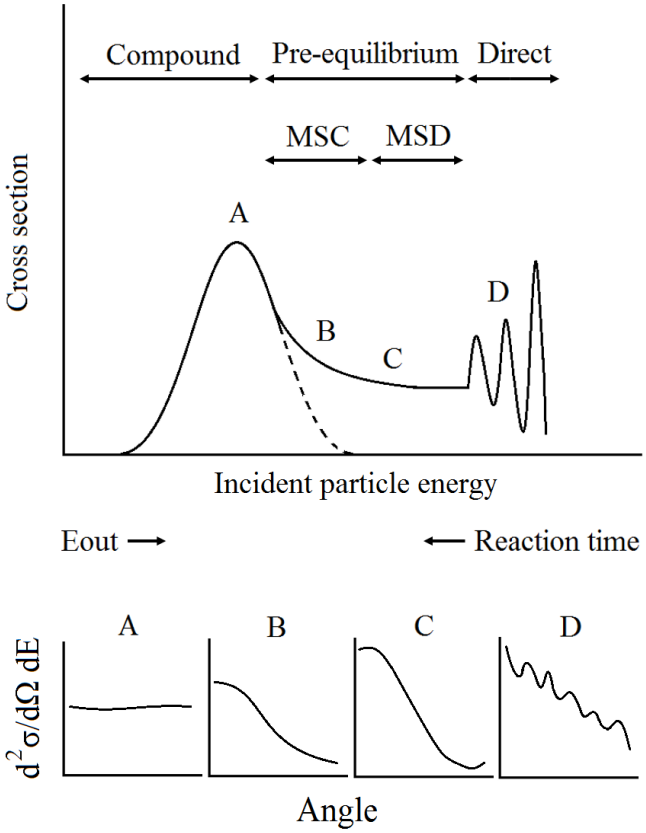

Figure 4.1: Typical energy spectrum of a reaction A(α,β)B with an incident energy of several tens of MeV. The MSC and MSD processes are described in subsection 4.2.2.

4.2.1 Compound nucleus reactions

Compound nucleus is an intermediate state after the absorption of an incident particle, but before the emission of the outgoing one. In more detail, when an incident particle enters a target nucleus, it has a high probability of interacting with one of the target's nucleons, possibly through a simple scattering. The recoils (nucleon and incident particle) can each make successive collisions with other nucleons and after several such interactions, the incident energy is shared among many of the nucleons of the combined system of projectile and target until the equilibrium is reached. The escape from a compound nucleus

is a statistical phenomenon, since the more random collisions occur, the more high is the probability for a single nucleon to gain sufficient energy to overcome the nuclear potential, similar to the mechanism with which molecules evaporate from the surface of a drop of liquid [124, 125].
This intermediate state is called compound nucleus (C^*) and can be symbolized using the following expression, which was also mentioned in section 4.1:

$$\alpha + A \longrightarrow C^* \longrightarrow B + \beta$$

The energy diagram of this reaction process is presented in Fig. 4.2.

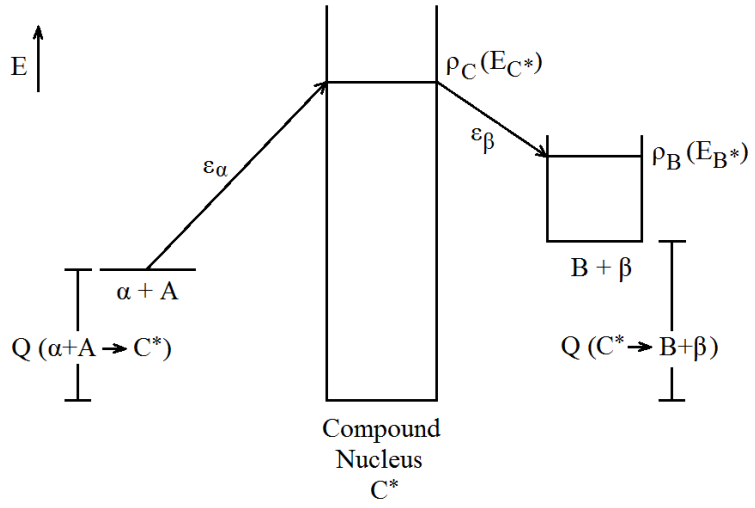

Figure 4.2: Schematic representation of the $\alpha + A \longrightarrow B + \beta$ via the formation of the compound nucleus C*. $\rho_C(E)$ is the nuclear level density of the compound nucleus at the excitation energy E_{C*} and the same holds for the residual nucleus, with symbols $\rho_B(E)$ and E_{B*}, respectively. ε_α and ε_β are the kinetic energies of α and β nuclei, respectively, in the center of mass system.

Some of the characteristics of the compound nucleus reactions will be described below [124, 126]:

- According to Bohr's assumption (see also section 4.1) *the relative probability of a decay into any specific set of final products is independent of the means of formation of the compound nucleus.*

- The compound nucleus excitation energy (E_{C^*}) is given by the binding energy (Q) and the available kinetic energy in the center of mass system. Thus,

$$E_{C^*} = Q + \frac{E_{\alpha\,lab}\, m_A}{(m_\alpha + m_A)} = Q + \varepsilon_\alpha$$

  where $E_{\alpha\,lab}$ is the bombarding energy in the lab system.

- Due to the fact that in such reactions the incident energy has to be distributed and reconcentrated, additional time is necessary for the decay of a compound nucleus and this time is of the order of 10^{-16}-10^{-18} s.

- This model works best for low incident energies, where the incident projectile has a small chance of escaping from the nucleus.

- The exit channel with neutron emission is much more favoured than the charged particle ones (p, α), as the latter have to overcome the Coulomb barrier.

- In contrast to direct reactions, the products of compound nucleus reactions do not present an angular distribution. The reason for this, is because the interactions among the nucleons are random, thus the outgoing particles are expected to be emitted isotropically.

4.2.2 Pre-equilibrium reactions

Pre-compound or pre-equilibrium reactions constitute an intermediate state between the one-step direct processes, which involve few degrees of freedom and the compound nucleus reactions in which the projectile energy is divided between all the nucleons of the compound nucleus. In some cases, these processes make dominant contributions to the cross sections of reactions initiated by neutrons of 10-20 MeV [127, 128].

The quantum-mechanical approach of these reactions is the multistep theory, in which it is assumed that the interaction between the incident nucleon and the target nucleus takes place in a number of stages of increasing complexity. The projectile enters the nucleus and collides with a nucleon, producing a two-particle one-hole excitation. The secondary particles can themselves interact, producing three-particle two-hole excitations and so on. At each stage there is a finite probability that the reaction proceeds to the next stage, returns to a previous stage or goes directly to the continuum. The latter possibility corresponds to pre-equilibrium reactions [128]. A distinction is made for them, in the theory of H. Feshbach *et.al.* [129], between multistep compound and multistep direct reactions.

- Multistep Compound (MSC)
  In a multistep compound reaction all the particles remain bound during the equilibration cascade. The phases of the matrix elements (J, parity etc.) which are required in order to specify a channel, are assumed to be random so that no interference terms remain after averaging. Thus, the energy averaged cross sections are symmetric about 90°.

- Multistep Direct (MSD)
  A multistep direct reaction occurs as the incident energy increases and is more likely that one particle remains in the continuum and therefore retains a strong memory of the original direction of the projectile. In this case, there is constructive interference between matrix elements involving the same change in the momentum of the particle in the continuum and so the cross sections are forward peaked.

4.2.3 Direct reactions

The direct reactions are defined to be those processes which connect the initial and final states in a nuclear reaction without formation of an intermediate compound system [127]. They occur very rapidly, in a time of the order of 10^{-22}s, while the incident particle interacts primarily at the surface of the target nucleus. Such reactions are also called peripheral processes and are most likely to involve one nucleon or very few valence nucleons near the surface of the target nucleus. Their contribution is important at higher nucleon energies, where the de Broglie wavelength of the nucleon becomes small enough to "see" individual nucleons (20 MeV $\longleftrightarrow$ 1 fm, whereas 1 MeV $\longleftrightarrow$ 4 fm). For incident nucleon energies above 10 MeV, the low lying, discrete states of the residual nucleus are almost completely excited by direct reaction processes, as shown in Fig. 4.3.

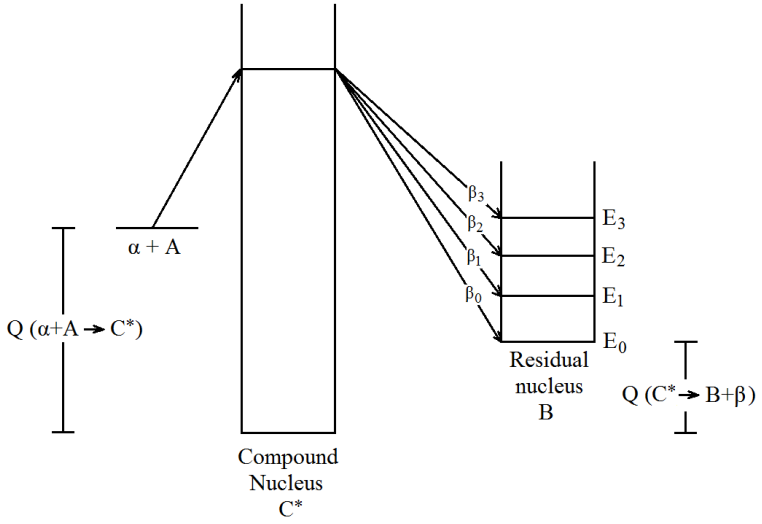

Figure 4.3: Schematic representation of the way that the low-lying states of the residual nucleus B can be excited in a direct reaction $\alpha + A \longrightarrow B + \beta$. The compound nucleus C^* is not formed in this case but is drawn in the sketch because is widely used as an energy reference for Q-value calculations.

An easy way to distinguish a direct reaction from a compound nucleus one is the sharply forward peaked angular distribution of the outgoing particles, which has a markedly oscillatory behaviour, as shown in Fig. 4.1 [123, 124]. This oscillatory shape enables the determination of the spin and parity of the residual nucleus.

The following processes can occur via the direct mechanism [127, 130]:

- Elastic scattering
  The simplest direct interaction between an incident particle and a target nucleus, when the particle's direction of motion and state of polarization is changed, without loss of energy. For example, (n,n), (p,p), (α, α), etc.

- Inelastic scattering
  Occurs when a projectile interacts with a nucleus and gives some of its energy, rais-

ing it to an excited state. This generally alters the direction of motion and state of polarization of the projectile. Such reactions are (n,n'), (p,p'), (α, α'), etc.

- Transfer reactions
  - Stripping
    A nucleon from the incident particle is transferred to an unfilled state of the residual (target) nucleus, as happens in reactions like (d,p), (d,n), (t,d), etc.
  - Pick-up
    A nucleon from a filled or partly filled state of the target nucleus is removed and transferred to the emitted particle. Such reactions are the (p,d), (n,d), (d,t), etc.
- Knock-out reactions
  The incident particle may collide with a nucleon or group of nucleons in the target nucleus and knock it out. If the incident particle is captured, the reaction is observed as inelastic scattering or nucleon transfer, and if it escapes, it is a reaction with three particles in the final state. For example, (d,p), (d,dp), (n,np), (p,pn), (p,2p), (n,2n), etc.
- Charge-exchange reactions
  The emitted particle has the same mass as the projectile, so that the net effect is the transfer of charge like in the following reactions (n,p), (p,n), (t,^{3}He), (^{3}He,t), etc.
- Break-up reactions
  In the Coulomb field, at few MeV incident energy, a composite particle may undergo a break-up into its constituents. The simplest example is a (d,pn) reaction. The break-up may take place in the Coulomb field specially when the target nucleus has high Z, without the neutron being captured. This is known as Coulomb breakup. At higher energies (of the order of 100 MeV or more) the break-up may occur in the nuclear field. In this process, the proton and neutron may be emitted on the opposite side and the target nucleus may be left in the ground state or raised to an excited state. These processes are known as elastic and inelastic break-up respectively [126].

4.3 Basic theoretical models for nuclear reactions

4.3.1 The optical model

The optical model is a simple model which was used in order to describe the elastic scattering in the presence of absorbing effects. The calculation resembles that of light incident on a somewhat opaque glass sphere [32, 109, 124, 127, 131]. The scattering is represented in terms of a complex potential U(r):

$$U(r) = V(r) + iW(r) \tag{4.2}$$

where the real part V(r) describes the nuclear interaction of scattering between target and projectile and the imaginary part W(r) is responsible for the absorption. The standard optical

model potential may be written in the form [131]:

$$\begin{aligned} U(r,E) = &- V_V(r,E) && \text{a real volume term,} \\ &- iW_V(r,E) && \text{an imaginary volume term,} \\ &- iW_D(r,E) && \text{an imaginary surface term,} \\ &+ V_{SO}(r,E)\cdot\mathbf{l}\cdot\sigma && \text{a real spin-orbit term,} \\ &+ iW_{SO}(r,E)\cdot\mathbf{l}\cdot\sigma && \text{an imaginary spin-orbit term,} \\ &+ V_C(r) && \text{a Coulomb term,} \end{aligned} \tag{4.3}$$

where E is the lab energy of the incident particle in MeV. All components can be separated in energy-dependent well depths and energy-independent radial parts f, namely

$$V_V(r,E) = V_V(E) f(r, R_V, \alpha_V) \tag{4.4}$$

$$W_V(r,E) = W_V(E) f(r, R_V, \alpha_V) \tag{4.5}$$

$$W_D(r,E) = -4\alpha_D W_D(E) \frac{d}{dr} f(r, R_D, \alpha_D) \tag{4.6}$$

$$V_{SO}(r,E) = V_{SO}(E) \left(\frac{\hbar}{m_\pi c}\right)^2 \frac{1}{r}\frac{d}{dr} f(r, R_{SO}, \alpha_{SO}) \tag{4.7}$$

$$W_{SO}(r,E) = W_{SO}(E) \left(\frac{\hbar}{m_\pi c}\right)^2 \times \frac{1}{r}\frac{d}{dr} f(r, R_{SO}, \alpha_{SO}) \tag{4.8}$$

Using the relations 4.4 - 4.8, Eq. 4.3 becomes:

$$\begin{aligned} U(r,E) = V_C(r) &- V_V(E) f(r, R_V, \alpha_V) \\ &- i\left(W_V(E) f(r, R_V, \alpha_V) - 4\alpha_D W_D(E) \frac{d}{dr} f(r, R_D, \alpha_D)\right) \\ &+ V_{SO}(E) \left(\frac{\hbar}{m_\pi c}\right)^2 \frac{1}{r}\frac{d}{dr} f(r, R_{SO}, \alpha_{SO})\cdot\mathbf{l}\cdot\sigma \\ &+ iW_{SO}(E) \left(\frac{\hbar}{m_\pi c}\right)^2 \times \frac{1}{r}\frac{d}{dr} f(r, R_{SO}, \alpha_{SO})\cdot\mathbf{l}\cdot\sigma \end{aligned} \tag{4.9}$$

The form factor f(r, R_i, α_i) is a Woods-Saxon shape:

$$f(r, R_i, \alpha_i) = \frac{1}{1 + e^{(r-R_i)/\alpha_i}} \tag{4.10}$$

where the geometry parameters are the radius R_i=r_i $A^{1/3}$, with A being the atomic mass number, and α_i the diffuseness parameters. The Coulomb term V_C for charged particles is given by the following relation:

$$V_C(r) = \begin{cases} \dfrac{Zze^2}{2R_C}\left(3 - \dfrac{r^2}{R_C^2}\right), for \quad r \le R_C \\ \dfrac{Zze^2}{r}, for \quad r \ge R_C \end{cases} \tag{4.11}$$

with Z(z) the charge of the projectile, and R_C = $r_C A^{1/3}$ the Coulomb radius.

The solutions of the Schrodinger equation that describe sufficiently the elastic scattering and the absorption of the projectiles have the following form:

$$\psi_{r\longrightarrow\infty} = e^{ikz} + \frac{e^{ikr}}{r} f(\theta) \tag{4.12}$$

where the first term is the incident wave (i.e the incident neutron beam) and the second one a scattered spherical wave. f(θ) is the scattering width, while $k = \sqrt{2mE}/\hbar$ the wave number. From this wavefunction, the scattering differential cross section is:

$$\frac{d\sigma}{d\Omega}(\theta) = |f(\theta)|^2 \tag{4.13}$$

In the case of uncharged and spinless particles, where Coulomb and spin-orbit terms do not exist, the scattering width can be determined by means of the partial wave analysis. By using the dividing variables method, the solutions of the Schrodinger equation can be written in the form:

$$\psi(r,\theta) = R(r)\, Y_m^l(\theta,\phi)$$

where $Y_m^l(\theta,\phi)$ are the spherical harmonics. Since there is axial symmetry ($U = U(r,\theta)$), only the m=0 spherical harmonics terms contribute, therefore Y_m^l can be expressed as:

$$Y_l^0(\theta) = \frac{\sqrt{2l+1}}{4\pi} P_l(cos(\theta))$$

By expanding the asymptotic form of the wavefunction 4.12 for the scattered wave, using Legendre polynomials, the wavefunction becomes:

$$\psi(r,\theta) = \sum_{l=0}^{\infty} \frac{u_l(r)}{r} P_l(cos\theta) \tag{4.14}$$

and the scattering amplitude can be written as:

$$f(\theta) = \sum_{l=0}^{\infty} (2l+1)\, f_l P_l(cos\theta) \tag{4.15}$$

The Schrodinger equation for the radial part of the wavefunction $u_l(r)/r$ is the following:

$$\frac{d^2u_l(r)}{dr^2} + \frac{2m}{\hbar^2}(E - V(r))\, u_l(r) - \frac{l(l+1)}{r^2} u_l(r) = 0 \tag{4.16}$$

while its solution has the form:

$$\frac{u_l(r)}{r} \propto \frac{1}{kr} e^{i\left(kr - \frac{1}{2}l\pi + \delta_l\right)} \propto -S_l \frac{e^{ikr}}{kr} \tag{4.17}$$

where δ_l is the phase shift and is determined from the boundary conditions in the limit of the potential range in order to have a smooth transition from the asymptotic limit to the nucleus interior and $S_l = e^{2i\delta_l}$ is the partial scattering matrix. It can be proved that the scattering amplitude can be written as:

$$f(\theta) = \frac{1}{2ik} \sum_{l=0}^{\infty} (2l+1)(e^{2i\delta_l} - 1) P_l(cos\theta) \tag{4.18}$$

By integrating Eq. 4.13 over all angles and combining it with Eq. 4.18, the scattering cross section is given by this expression:

$$\sigma_{scattering} = \frac{4\pi}{k^2}\sum_{l=0}^{\infty}(2l+1)|1-e^{2i\delta_l}|^2 \quad \Rightarrow$$
$$\Rightarrow \quad \sigma_{scattering} = \frac{4\pi}{k^2}\sum_{l=0}^{\infty}(2l+1)|1-S_l|^2 \tag{4.19}$$

while the absorption one by the following relation:

$$\sigma_{absorption} = \frac{\pi}{k^2}\sum_{l=0}^{\infty}(2l+1)\left(1-|e^{2i\delta_l}|^2\right) \quad \Rightarrow$$
$$\Rightarrow \quad \sigma_{absorption} = \frac{\pi}{k^2}\sum_{l=0}^{\infty}(2l+1)\left(1-|S_l|^2\right) \quad \Rightarrow$$
$$\Rightarrow \quad \sigma_{absorption} = \frac{\pi}{k^2}\sum_{l=0}^{\infty}(2l+1)\ T_l \tag{4.20}$$

which defines the transmission coefficient as:

$$T_l = 1-|S_l|^2 \tag{4.21}$$

The transmission coefficients constitute an essential ingredient of the Hauser-Feshbach theory, which will be described in section 4.3.2.

The optical model is particularly important for the study of the direct (fast) contribution. Although the latter was not that crucial for the present work, it was worthy to briefly mention the basic knowledge about it (see the subsection 4.2.3).

4.3.2 The Hauser-Feshbach theory

The Hauser-Feshbach theory [44] describes reactions which proceed via the formation of a compound nucleus. In order to present this model [109, 132], it is convenient to begin with the Bohr hypothesis which was mentioned in section 4.1 and can be summarized in the following expression:

$$\sigma(\alpha+A\longrightarrow B+\beta)=\sigma(\alpha+A\longrightarrow C^*)P(C^*\longrightarrow B+\beta) \quad \Rightarrow \quad \sigma_{\alpha\beta}=\sigma_\alpha P_\beta \tag{4.22}$$

where σ_α is the cross section for the formation of the compound nucleus and P_β is the probability for the compound nucleus decay to channel β. Then, the new independence hypothesis can be expressed for an arbitrary entrance channel using the transmission coefficients, T_l, as:

$$\sigma_{\alpha\beta}(l)=\left[\frac{\pi}{k_\alpha^2}(2l+1)T_l(\varepsilon_\alpha)\right]P_\beta(l) \tag{4.23}$$

While for the inverse reaction involving the same partial wave and the same compound nucleus excitation energy can be written as:

$$\sigma_{\beta\alpha}(l)=\left[\frac{\pi}{k_\beta^2}(2l+1)T_l(\varepsilon_\beta)\right]P_\alpha(l) \tag{4.24}$$

By dividing Eq. 4.23 with 4.24 and assuming that the reciprocity theorem (Eq. 4.1) can be applied to partial cross sections, the following expression is obtained:

$$\frac{P_\alpha(l)}{T_l(\varepsilon_\alpha)} = \frac{P_\beta(l)}{T_l(\varepsilon_\beta)} \quad \Rightarrow \quad \frac{P_\alpha(l)}{P_\beta(l)} = \frac{T_l(\varepsilon_\alpha)}{T_l(\varepsilon_\beta)} \tag{4.25}$$

This equation states that the ratio of probabilities of decay from the compound nucleus for any pair of channels is equal to the ratio of the corresponding transmission coefficients. Therefore, for any decay channel β, the probability of decay will be:

$$P_\beta(l) = \frac{T_l(\varepsilon_\beta)}{\sum_\gamma T_{\gamma,l}} \tag{4.26}$$

where the sum in the denominator represents all accessible exit channels γ. In Eq. 4.26, the energy ε_β is fixed by the excitation energy of the compound nucleus (E^*_C) and that of the final state in the residual nucleus (for instance $\varepsilon_\beta + E^*_B = E^*_C + Q_{C\to\beta+B}$).
If the excitation energy of the residual nucleus E^*_B belongs to the continuum, then it can be considered that there are $\Omega_B(E^*_B)$ states at this excitation energy. Moreover, in a small energy range ΔE, over which ε_β can be considered as constant, the number of states can be expressed as a function of the nuclear level density $\rho_B(E^*_B)$, as $\Omega_B(E^*_B) = \rho_B(E^*_B)\,\Delta E$. Similarly, for all accessible exit channels, γ, will be $\Omega_\Gamma(E^*_\Gamma) = \rho_\Gamma(E^*_\Gamma)\,\Delta E$. Thus, the decay probability to any one of these states can be written as:

$$P_\beta(l) = \frac{T_l(\varepsilon_\beta)\,\Omega_B(E^*_B)}{\sum_\gamma T_{\gamma,l}\,\Omega_\Gamma(E^*_\Gamma)} \quad \Rightarrow \quad P_\beta(l) = \frac{T_l(\varepsilon_\beta)\,\rho_B(E^*_B)}{\sum_\gamma T_{\gamma,l}\,\rho_\Gamma(E^*_\Gamma)} \tag{4.27}$$

Eq. 4.27 combined with the 4.23 one, leads to the basic form of the Hauser-Feshbach formalism for spinless particles, which follows:

$$\sigma_{\alpha\beta}(l) = \frac{\pi}{k^2_\alpha}(2l+1)\frac{T_l(\varepsilon_\alpha)\,T_l(\varepsilon_\beta)\,\rho_B(E^*_B)}{\sum_\gamma T_{\gamma,l}\,\rho_\Gamma(E^*_\Gamma)} \tag{4.28}$$

If the interacting particles have spin, the expression for the cross section must include spin weighting factors. Suppose that the spins and angular momenta for the reaction A(α, β)B are defined as follows:

$$\begin{array}{ccccccc} \alpha & + & A & \longrightarrow & C^* & \longrightarrow & B + \beta \\ & & & l & & l' & \\ s & & S & & J & & S' \quad s' \\ j = s + S & & & & & & j' = s' + S' \end{array}$$

The spin of the incident particle, s, and the one of the target nucleus, S, combine to give the channel spin j, which in turn combines with the orbital angular momentum l to give the total compound nucleus angular momentum J, and similarly for the exit channel. In order to obtain an expression for the cross section for particles with angular momentum, Eq. 4.28 must be averaged over all the allowed spin combinations in the incident channel and summed over those in the outgoing channel. The probability that the spins s and S combine to give a particular j is:

$$P(j) = \frac{2j+1}{(2s+1)(2S+1)} \tag{4.29}$$

and the probability of j combining with l to give J is likewise:

$$P(J) = \frac{2J+1}{(2j+1)(2l+1)} \tag{4.30}$$

Therefore, if the transmission coefficients depend only on orbital angular momenta, the partial cross section to final states of angular momentum S' in the nucleus B can be written as:

$$\sigma_{\alpha\beta}(J,S') = \frac{\pi}{k_\alpha^2}\,\frac{(2J+1)}{(2s+1)(2S+1)}\,\frac{\sum\limits_{l,j,l',j'} T_l(\varepsilon_\alpha)\,T_{l'}(\varepsilon_\beta)\,\rho_B(E_B^*,S')}{\sum\limits_{\gamma,l'',j''} T_{\gamma,l''}\,\rho_\Gamma(E_\Gamma^*)} \tag{4.31}$$

where the unprimed symbols represent quantities associated with the entrance channel α and primed symbols for the exit channel β. All the summations are made subject to the appropriate vector coupling relations. These are symbolised by the triangular relation Δ (abc), which means that when angular momenta **a** and **b** are coupled to give **c**, they must satisfy the relation $|a-b| < c < (a+b)$. Thus, the following triangular relations hold:

$$\begin{aligned} |S-s| &< \ \ j\ \ < (S+s) \\ |J-j| &< \ \ l\ \ < (J+j) \\ |j-l| &< \ \ J\ \ < (j+l) \end{aligned} \qquad\qquad \begin{aligned} |S'-s'| &< \ \ j'\ \ < (S'+s') \\ |J-j'| &< \ \ l'\ \ < (J+j') \\ |j'-l'| &< \ \ J'\ \ < (j'+l') \end{aligned}$$

The denominator is a summation over all possible exit channels that are allowed with respect to the conservation of energy principle and to the angular momentum selection rules [127].

4.3.3 The exciton model

Concerning pre-equilibrium reactions, apart from the multistep theories which were briefly mentioned in section 4.2.2, the simplest one is that of Griffin's [50,51] and is usually referred to as the exciton model. According to the latter, the incoming projectile initially interacts with the target nucleus and gives rise to a single particle state above the Fermi surface, while a hole is left below. Two examples involving a two particle - one hole (2p-1h) state and a three particle - two holes (3p-2h) state are shown in Fig. 4.4. The total number of excited particles, p, and holes h which occupy single particle states above and below Fermi energy, respectively, is referred to as the number of excitons $n = p + h$ [32, 109, 127, 132].

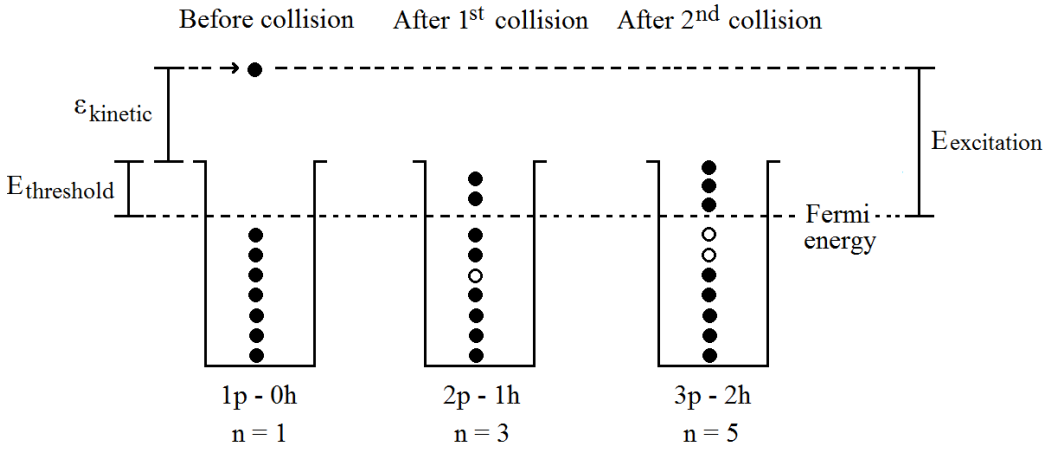

Figure 4.4: Schematic representation of the excitation of a nucleus in states characterized by an increasing exciton number. All particles are bound to the potential well and these processes lead to a fully equilibrated residual nucleus [109].

Such successive interactions lead to an intra-nuclear cascade, which through a sequence of states characterized by an increasing exciton number and more degrees of freedom, ends up to the equilibrium. The processes of increasing exciton number meet selection rules concerning the possible variation of the number of excitons (n), the number of particles (p) and the number of holes (h), which are the following:

$$\Delta n = 0, \pm 2, \qquad \Delta p = 0, \pm 1, \qquad \Delta h = 0, \pm 1 \tag{4.32}$$

If a particle has such a high energy as to exceed the effective energy threshold for emission, it escapes the nucleus (for a neutron is the separation energy, - Q-value, while for proton is the separation energy plus the Coulomb barrier). Thus, at each stage of the aforementioned equilibrium process, there is a competition between two decay modes:

- The decay by exciton-exciton interactions to more complex configurations (internal transitions).
- The decay by emission of particles into the continuum.

The two most important assumptions of this theory are the following:

- All the states having the same particle-hole configuration and the same total energy and parity are equiprobable.
- All the decay modes are equiprobable.

Another Griffin's assumption was that the most dominant decay mode was the internal conversion $\Delta n = +2$. All the probable internal conversions were taken into account later by the evoluted model by Cline and Blann [118, 119].

According to Griffin's model [50], the transition rate of a nucleus in a typical n-exciton state to other states with $n' = n$ or $n' = n \pm 2$ excitons is given by the Fermi's Gold Rule:

$$\lambda_{n \to n'} = \frac{2\pi}{\hbar} |M|^2 \rho_{n'}(E) \quad \Rightarrow \quad \lambda_{ph \to p'h'} = \frac{2\pi}{\hbar} |M|^2 \rho_{p'h'}(E) \tag{4.33}$$

where $|M|^2$ is the average squared matrix element for the $n \rightarrow n'$ transition, which is assumed to be energy-independent and $\rho_{p'h'}(E)$ the density of p' particle and h' hole states at excitation energy E which is given by the expression [133, 134]:

$$\rho_{p'h'}(E) = \frac{g(gE - A_{p'h'})^{p'+h'-1}}{p'!\ h'!\ (p'+h'-1)!} \tag{4.34}$$

$$A_{p'h'} = \frac{1}{4}(p'^2 + h'^2 + p' - 3h') \tag{4.35}$$

where g is the density of single-particle states in the equispacing model. The quantity $A_{p'h'}$ contains the effects of the Pauli exclusion principle and Eq. 4.34 reduces to the Ericson particle-hole state density if one sets $A_{p'h'} = 0$ [133].

The probability of finding the nucleus with excitation energy E at time t in a configuration by $n = p + h$ excitons is called the occupation probability and is symbolized as $P(n, E, t)$. It satisfies the following relation [118]:

$$\begin{aligned}\frac{dP(n,E,t)}{dt} &= P(n-2,E,t)\,\lambda_{n-2,n}(E) \\ &+ P(n+2,E,t)\,\lambda_{n+2,n}(E) \\ &- P(n,E,t)\,\{\lambda_{n,n+2}(E) + \lambda_{n,n-2} + \lambda_{n,c}(E)\}\end{aligned} \tag{4.36}$$

which integrated over time gives:

$$\begin{aligned}-P(n,E,0) &= t_{n-2}(E)\,\lambda_{n-2,n}(E) \\ &+ t_{n+2}(E)\,\lambda_{n+2,n}(E) \\ &- t_n(E)\,\{\lambda_{n,n+2}(E) + \lambda_{n,n-2} + \lambda_{n,c}(E)\}\end{aligned} \tag{4.37}$$

where $\lambda_{n,c}(E)$ is the total decay rate for emission to the continuum of whatever particle with whatever energy and t_n is the mean lifetime of an n-exciton state. The former can be written as:

$$\lambda_{n,c}(E) = \sum_{c'} \int_0^{E_{c',max}} \lambda_{n,c}(E, \varepsilon_{c'})\, d\varepsilon_{c'} \tag{4.38}$$

where $\varepsilon_c = \varepsilon - B$ is the energy of the particle reduced by its binding energy in the nucleus and the latter is given by the relation below:

$$t_n = \int_0^{t_{eq}} P(n,E,t)dt \tag{4.39}$$

where t_{eq} is the equilibration time necessary to reach a state of statistical equilibrium.

Once the value of $P(n, E, t)$ at $t = 0$ is given (usually it is $P(n, E, t) = \delta_{n,n_0}$), the set of equations 4.36 and 4.37 can be solved.

The cross section for emission of particles in channel c is calculated by the following expression:

$$\sigma_c(E, \varepsilon_c)\, d\varepsilon_c = \sigma_R \int_0^{t_{eq}} \sum_{n,\Delta n=2} P(n,E,t)\, \lambda_{n,c}(E, \varepsilon_c)\, dt\, d\varepsilon_c \tag{4.40}$$

where σ_R is the reaction cross section for the incident channel.

4.4 Nuclear level density models

The nuclear level densities constitute a crucial component of the cross section in the Hauser-Feshbach theory (see Eq. 4.28 and 4.31), therefore the basic relations for the models that were finally chosen for the theoretical calculations with EMPIRE 3.2.2 and TALYS 1.8 codes will be presented in this section. The available models in each code are summarized in Table 4.1.

EMPIRE 3.2.2	
Keyword & Value	Nuclear Level Density Model
LEVDEN 0	Enhanced Generalized Superfluid Model (EGSM)
LEVDEN 1	Generalized Superfluid Model (GSM)
LEVDEN 2	Gilbert-Cameron Model (GCM)
LEVDEN 3	Hartree-Fock-Bogoliubov (microscopic) (HFBM)
TALYS 1.8	
Keyword & Value	Nuclear Level Density Model
ldmodel 1	Constant Temperature (CTM) & Fermi Gas Model (FGM)
ldmodel 2	Back-shifted Fermi Gas Model (BFM)
ldmodel 3	Generalized Superfluid Model (GSM)
ldmodel 4	Goriely (microscopic)
ldmodel 5	Hilaire (microscopic)
ldmodel 6	Hartree-Fock-Bogoliubov & Gogny force (microscopic)

Table 4.1: Nuclear level density models available in EMPIRE 3.2.2 and TALYS 1.8 codes along with the corresponding keywords and values for each code.

4.4.1 The Fermi Gas Model

The Fermi Gas Model (FGM) [135], although it can not be applied by using a specific value of the keywords presented in Table 4.1, it should be presented, since it is implemented simultaneously with other models in both codes.

It is based on the assumption that the single particle states which construct the excited levels of the nucleus are equally spaced and in fact, holds for non-interacting nucleons in the absence of collective levels [136]. The Fermi gas level density (under the assumption that the projections of the total angular momentum are randomly coupled) can be written as:

$$\rho_F(E,J,\Pi) = \frac{1}{2}\,\frac{2J+1}{2\sqrt{2\pi}\sigma^3}\; exp\left[-\frac{\left(J+\frac{1}{2}\right)^2}{2\sigma^2}\right]\,\frac{\sqrt{\pi}}{12}\,\frac{exp\left[2\sqrt{\alpha U}\right]}{\alpha^{1/4}\,U^{5/4}} \tag{4.41}$$

where the first factor $\frac{1}{2}$ represents the equiparity distribution, α is the level density param-

eter, σ is the square root of the spin cut-off parameter (both parameters will be discussed in the subsections 4.4.1.1 and 4.4.1.2) and U is the effective excitation energy which is equal to:

$$U = E - \Delta \tag{4.42}$$

where Δ is an empirical parameter related to the pairing energy which is included to account for the known odd-even effects in nuclei. It is more convenient to discuss about Δ for each specific level density model separately in the corresponding section.

The Fermi gas spin distribution is given by the following expression:

$$R_F(E,J) = \frac{2J+1}{2\sigma^2}\, exp\left[-\frac{\left(J+\frac{1}{2}\right)^2}{2\sigma^2}\right] \tag{4.43}$$

By summing Eq. 4.41 over all spins and parities the total Fermi gas level density becomes:

$$\rho_F^{tot}(E) = \frac{1}{\sqrt{2\pi}\sigma}\,\frac{\sqrt{\pi}}{12}\,\frac{exp\left[2\sqrt{\alpha U}\right]}{\alpha^{1/4}\,U^{5/4}} \tag{4.44}$$

and also can be written as:

$$\rho_F^{tot}(E) = \frac{1}{\sqrt{2\pi}\sigma}\,\frac{e^S}{\sqrt{D}} \tag{4.45}$$

where S is the entropy given by the relation:

$$S = 2\alpha t \tag{4.46}$$

D is the determinant:

$$D = \frac{144}{\pi}\,\alpha^3\,t^5 \tag{4.47}$$

and t the thermodynamic temperature:

$$t = \sqrt{\frac{U}{\alpha}} \tag{4.48}$$

4.4.1.1 The level density parameter α

The first formula suggested for the level density parameter α lead to a nuclide-specific constant value independent of energy [136]. Later, Ignatyuk *et. al.* [137] recognized that energy-dependent shell effects should be effectively included through an energy-dependent expression for α, which was assumed to be the following:

$$\alpha = \alpha(E) = \tilde{\alpha}\left(1 + \delta W\,\frac{1 - exp[-\gamma U]}{U}\right) \tag{4.49}$$

where $\tilde{\alpha}$ is the asymptotic level density parameter one would obtain in the absence of any shell effects ($\tilde{\alpha}$=α(E$\rightarrow\infty$)), or in the absence of shell correction energy ($\delta W = 0$) and is given by the form:

$$\tilde{\alpha} = \alpha A + \beta A^{2/3} \tag{4.50}$$

where A is the mass number. The shell correction energy δW is defined as:

$$\delta W(MeV) = M(MeV) - M_{LDM}(MeV) \tag{4.51}$$

where M is the nucleus mass and M_{LDM} the nucleus mass according to the spherical liquid-drop model (see Ref. [136] for details). The damping parameter γ determines how rapidly $\alpha(E)$ approaches $\tilde{\alpha}$ and can be written as:

$$\gamma = \frac{\gamma_1}{A^{1/3}} \tag{4.52}$$

In Eqs. 4.50 and 4.52, α, β and γ_1 are global parameters that need to be determined to give the best average level density description over a whole range of nuclides.

For low excitation energies ($E \leq \Delta$) the limiting value of Eq. 4.49 is given by its first order Taylor expansion:

$$\lim_{U\to 0} \alpha(E) = \tilde{\alpha}\,[1 + \gamma\,\delta W] \tag{4.53}$$

4.4.1.2 The spin cut-off parameter (σ^2)

The spin cut-off parameter σ^2 represents the width of the angular momentum distribution of the level density. The observation that a nucleus possesses collective rotational energy that can not be used to excite the individual nucleons leads to the general expression for the continuum:

$$\sigma^2 = \sigma_F^2(E) = I_0 \frac{\alpha}{\tilde{\alpha}} t \tag{4.54}$$

where the undeformed moment of inertia of the nucleus I_0 is defined by its radius $R = 1.2A^{1/3}$ and the neutron mass in amu m_0 by the relation:

$$I_0 = \frac{(2/5)\, m_0\, R^2\, A}{(\hbar c)^2} \tag{4.55}$$

and t is the thermodynamic temperature. It can be proved (see Ref. [136]) that the spin cut-off parameter can be found using the following expression:

$$\sigma_F^2(E) = 0.01389 \frac{A^{5/3}}{\tilde{\alpha}} \sqrt{\alpha U} \tag{4.56}$$

An alternative method to determine the spin cut-off parameter, which is needed in case of low excitation energies ($E \leq \Delta$) where Eq. 4.56 is not defined, is obtained from the spins of the low-lying discrete levels as follows:

$$\sigma_d^2 = \frac{1}{3 \sum_{i=N_L}^{N_U} (2J_i + 1)} \sum_{i=N_L}^{N_U} J_i(J_i+1)\,(2J_i+1) \tag{4.57}$$

where J_i is the spin of discrete level i and σ_d^2 is the discrete spin cut-off parameter in the energy range from a lower discrete level N_L, with energy E_L, to an upper level N_U, with energy E_U, where the total level density agrees well with the discrete level sequence.

4.4.2 Generalised Superfluid Model (TALYS 1.8, ldmodel 3)

The phenomenological version of the Generalised Superfluid Model (GSM) [138, 139] is characterized by a phase transition from a superfluid behavior at low energy, to a high energy region which is described by the Fermi Gas Model (FGM) [136]. It automatically provides a constant temperature-like behavior at low energies, under the so-called critical energy U_c, where pairing correlations strongly influence the level density. The superconductive pairing correlations are taken into account according to the Bardeen-Cooper-Schrieffer theory [140]. Therefore, the GSM level density has two forms: one below and one above the critical energy U_c [136].

- For $U' < U_c$,

  Where U' is the effective excitation energy defined as:

$$U' = E + \chi\Delta_0 + \delta \tag{4.58}$$

  where

$$\chi = \begin{cases} 2, & \text{for odd-odd,} \\ 1, & \text{for odd,} \\ 0, & \text{for even-even,} \end{cases} \tag{4.59}$$

  and δ is an adjustable shift parameter to obtain the best description of experimental data per nucleus. The following thermodynamical expressions hold:

$$U_c = \alpha_c\, T_c^2 + E_{cond} \tag{4.60}$$

  where α_c is the critical level density parameter, T_c is the critical temperature and E_{cond} the condensation energy, which can be written as:

$$\alpha_c = \tilde{\alpha}\left[1 + \delta W\,\frac{1 - exp\left(-\gamma\,\alpha_c\,T_c^2\right)}{\alpha_c\,T_c^2}\right] \tag{4.61}$$

$$T_c = 0.567\,\Delta_0 \tag{4.62}$$

$$E_{cond} = \frac{3}{2\pi^2}\,\alpha_c\,\Delta_0^2 \tag{4.63}$$

  where the pairing correlation function is given by:

$$\Delta_0 = \frac{12}{\sqrt{A}} \tag{4.64}$$

Some useful relations for the determination of the level density are also the following:

$$S_c = 2\,\alpha_c\,T_c \tag{4.65}$$

$$D_c = \frac{144}{\pi}\,\alpha_c^3\,T_c^5 \tag{4.66}$$

$$\sigma_c^2 = 0.01389\,A^{5/3}\,\frac{\alpha_c}{\tilde{\alpha}}\,T_c \tag{4.67}$$

where S_c is the critical entropy, D_c is the critical determinant and σ_c^2 the critical spin cut-off parameter.

According to the superfluid Equation Of State (EOS) [138] the temperature T can be written as:

$$T = 2\,T_c\,\phi\,\left[ln\,\frac{1+\phi}{1-\phi}\right]^{-1} \tag{4.68}$$

where

$$\phi^2 = 1 - \frac{U'}{U_c} \tag{4.69}$$

The entropy S can be written as:

$$S = S_c\,\frac{T_c}{T}\,(1-\phi^2) \quad \Rightarrow \quad S = S_c\,\frac{T_c}{T}\,\frac{U'}{U_c} \tag{4.70}$$

the determinant D as:

$$D = D_c\,(1-\phi^2)\,(1+\phi^2)^2 \quad \Rightarrow \quad D = D_c\,\frac{U'}{U_c}\,\left(2 - \frac{U'}{U_c}\right) \tag{4.71}$$

and the spin cut-off parameter σ^2 as:

$$\sigma^2 = \sigma_c^2\,(1-\phi^2) \quad \Rightarrow \quad \sigma^2 = \sigma_c^2\,\frac{U'}{U_c} \tag{4.72}$$

For $U' \leq U_c$, the total level density is given by:

$$\rho_{GSM}^{tot}(E) = \frac{1}{\sqrt{2\pi}\sigma}\,\frac{e^S}{\sqrt{D}} \tag{4.73}$$

with all ingredients given by Eqs. 4.70-4.72. Similar, the level density is:

$$\rho_{GSM}(E,J,\Pi) = \frac{1}{2}\,R_F(E,J)\,\rho_{GSM}^{tot}(E) \tag{4.74}$$

- For $U' \geq U_c$,

The FGM applies, with a different energy shift. The effective excitation energy U' is defined as:

$$U' = E - \Delta^{GSM} \tag{4.75}$$

where

$$\Delta^{GSM} = E_{cond} - \chi\Delta_0 - \delta \tag{4.76}$$

The spin cut-off parameter in the high energy region reads Eq. 4.54, which combined with Eq. 4.48, gives:

$$\sigma^2 = I_0 \frac{\alpha}{\tilde{\alpha}} \sqrt{\frac{U}{\alpha}} \tag{4.77}$$

The level density is given by:

$$\rho_{GSM}(E, J, \Pi) = \frac{1}{2} R_F(E, J)\ \rho^{tot}_{GSM}(E) \tag{4.78}$$

where

$$\rho^{tot}_{GSM}(E) = \rho^{tot}_{F}(E) = \frac{1}{\sqrt{2\pi}\sigma} \frac{\sqrt{\pi}}{12} \frac{exp\left[2\sqrt{\alpha U}\right]}{\alpha^{1/4}\, U^{5/4}} \tag{4.79}$$

and $R_F(E, J)$ is given by Eq. 4.43.

At the matching energy ($E = U_c - \chi\Delta_0 - \delta$) the two prescriptions match so that the total level density is perfectly continuous.

In fact, the term "general" in the GSM was originally added to denote the inclusion of explicit collective enhancement factors on top of an intrinsic level density $\rho^{tot}_{GSM,int}(E)$ as follows:

$$\rho^{tot}_{GSM} = K_{rot}(E)\, K_{vib}(E)\, \rho^{tot}_{GSM,int}(E) \tag{4.80}$$

where $K_{rot}(E)$ and $K_{vib}(E)$ are the rotational and vibrational enhancement factors respectively. For more details on these factors, see Ref. [42].

4.4.3 Enhanced Generalised Superfluid Model (EMPIRE 3.2.2, LEVDEN 0)

The Enhanced Generalized Superfluid Model (EGSM), which is also referred as "Empire Global Specific Model", uses the superfluid model below critical excitation energy (U_c) and the Fermi gas model above, as GSM does. The enhancement compared to GSM, as the latter is implemented in EMPIRE code (LEVDEN 1), relates to the spin distribution above critical excitation energy, where the FGM is used, and it includes a more accurate treatment of high angular momenta [61].

More specifically, the spin dependence in GSM is treated as a separate factor characterized by a spin cut-off parameter (σ^2), whereas in EGSM the rotational energy is subtracted from the intrinsic excitation energy. The collective enhancement of the level density is achieved using the non-adiabatic form of nuclear rotation, therefore it considers the shape of nucleus in a dynamical situation. In other words, the rotational enhancement depends on the shape of the nucleus. The deformation is inserted in the level density formulas through the moment of inertia and through the level density parameter α, which increases with increasing surface of the nucleus [61].

In the EMPIRE formalism (see Ref. [61]), the similar to Eq. 4.80 relation for the GSM level density with rotational and vibrational enhancements included in an adiabatic mode, is the following:

$$\rho(E,J,\Pi) = \rho_{qp}(E,J,\Pi)\ K_{rot}\,Q_{rot}\,K_{vib}\,Q_{vib} \tag{4.81}$$

where K_{rot}, K_{vib} are the rotational and vibrational enhancement factors, respectively, Q_{rot}, Q_{vib} are their damping with increasing energy and ρ_{qp} is the quasi-particle level density which can be written as:

$$\rho_{qp}(E,J,\Pi) = \frac{1}{2}\,\frac{(2J+1)}{\sqrt{8\pi\sigma^3}}\,exp\left[-\frac{(J+1/2)^2}{2\sigma^2}\right]\frac{e^S}{\sqrt{D}} \tag{4.82}$$

The effective excitation energy in EGSM is defined as:

$$U' = E + \chi\Delta_0 \tag{4.83}$$

where

$$\chi = \begin{cases} 2, & \text{for odd-odd,} \\ 1, & \text{for odd,} \\ 0, & \text{for even-even,} \end{cases} \tag{4.84}$$

and $\Delta_0 = 12\sqrt{A}$.

- For $U' < U_c$,

  The nuclear level density is given by Eq. 4.81.

- For $U' > U_c$,

  An energy shift equal to the condensation energy is introduced:

$$U^* = U - E_{cond} \tag{4.85}$$

  Assuming that the prolate nuclei rotate along the axis perpendicular to the symmetry axis, the level density can be expressed as:

$$\begin{aligned}\rho(E,J,\Pi) =& \frac{1}{16\sqrt{6\pi}}\left(\frac{\hbar^2}{I_\parallel}\right)^{1/2}\alpha^{-1/4}\sum_{K=-J}^{J}\left(U^* - \frac{\hbar^2K^2}{2I_{eff}}\right)^{-5/4} \\ & exp\left[2\left[\alpha\left(U^* - \frac{\hbar^2K^2}{2I_{eff}}\right)\right]^{1/2}\right]Q_{rot}\,K_{vib}\,Q_{vib}\end{aligned} \tag{4.86}$$

  And similarly assuming that the oblate nuclei rotate parallel to the symmetry axis, the level density is:

$$\begin{aligned}\rho(E,J,\Pi) =& \frac{1}{16\sqrt{6\pi}}\left(\frac{\hbar^2}{I_\parallel}\right)^{1/2}\alpha^{-1/4} \\ & \sum_{K=-J}^{J}\left(U^* - \frac{\hbar^2[J(J+1)-K^2]}{2\mid I_{eff}\mid}\right)^{-5/4} \\ & exp\left[2\left[\alpha\left(U^* - \frac{\hbar^2[J(J+1)-K^2]}{2\mid I_{eff}\mid}\right)\right]^{1/2}\right]Q_{rot}\,K_{vib}\,Q_{vib}\end{aligned} \tag{4.87}$$

The summation over the projection of angular momentum, K, accounts for the rotational enhancement, while I_{eff} is the effective moment of inertia. The latter is given as a function of the parallel and perpendicular moments of inertia and can be written as:

$$\frac{1}{I_{eff}} = \frac{1}{I_{\parallel}} - \frac{1}{I_{\perp}} \tag{4.88}$$

In the limit of $J >> K$, Eqs. 4.86 and 4.87 are equivalent to:

$$\rho(E, J, \Pi) = \frac{1}{2} \frac{(2J+1)}{\sqrt{8\pi\sigma^3}} exp\left[-\frac{(J+1/2)^2}{2\sigma^2}\right] \frac{e^S}{\sqrt{D}} K_{rot}\, Q_{rot}\, K_{vib}\, Q_{vib} \tag{4.89}$$

For more details on the rotational and vibrational enhancements, see Ref. [61].

4.5 Theoretical Calculations using the EMPIRE and TALYS codes

In this section, the input parameters that were chosen in order to reproduce the cross section curves by means of the EMPIRE 3.2.2 [40] and TALYS 1.8 [42] codes will be described in detail, not only for the (n,2n) measured reactions, but also for additional reaction channels involving the same target nucleus, such as the (n,elastic), (n,3n), (n,p), (n,α) and (n,total) ones. However, the figures with the theoretical calculations results will be given in the next chapter 5, along with the new experimental data points.

4.5.1 Neutron induced reactions on ^{197}Au

The ^{197}Au(n,2n) reaction leads to the formation of two levels of the residual nucleus ^{196}Au, which present large spin difference (isomeric state, m2 (J^{π} : 12^{-}) and ground state g (J^{π} : 2^{-})). Due to the existence of the high spin second metastable, is a powerful tool for obtaining information on the structure of the involved nuclei and thus constitutes an open field of study [12, 57, 141]. Above 15 MeV the contribution of preequilibrium emission becomes important and the (n,3n) competing reaction channel opens. Thus, the simultaneous reproduction of the isomeric cross section along with other channels sets a significant constraint, rendering theoretical calculations quite sensitive to the choice of specific nuclear model parameters such as the level density (α) and the spin cut-off (σ^2) ones.

Theoretical cross section calculations were carried out in the incident neutron energy range between 0.001 and 35 MeV, using the nuclear reaction model codes EMPIRE 3.2.2 [40, 41] and TALYS 1.8 [42, 43]. In principle in both codes the three basic reaction mechanisms, namely the compound nucleus, pre-equilibrium emission and direct reaction ones are taken into account. The final goal was not to compare the two codes with one another (i.e. by using the same input parameters), but rather to determine the optimum combination of nuclear model parameters for each code, which yields the most satisfactory results compared to all the available existing experimental datasets for seven reaction channels, namely for the (n,elastic), (n,2n)$_{g+m1+m2}$, (n,2n)$_{m2}$, (n,3n), (n,p), (n,α) and (n,total) ones. Special attention was devoted to reproduce the cross section of the isomeric production.

Concerning theoretical calculations with the EMPIRE code, compound nucleus reaction cross sections were calculated in the framework of the Hauser-Feshbach theory [44]. The default level density formulation of EMPIRE was used, which is based on the Enhanced Generalized Superfluid Model (EGSM) [45]. The enhancement compared to the standard GSM corresponds to a more accurate treatment of high angular momenta that affect the spin distribution above the critical excitation energy, where the Fermi Gas model is implemented in both the GSM and EGSM [61]. To account for the correlation between the incident and exit channels in elastic scattering, width fluctuation corrections were activated implementing the Hofmann, Richert, Tepel and Weidenmuller model (HRTW) [142] up to an incident neutron energy of 3 MeV. Concerning the γ-ray emission, γ-ray strength functions were described via modified Lorentzians (MLO1) [143] with parameters available in the RIPL-3 database [46]. The optical model parameters for the outgoing protons were taken from RIPL-3 using the data by A. J. Koning et. al. [47], while parameters obtained by V. Avrigeanu et. al. [48] were used for the outgoing alphas. In order to choose from RIPL-3 the most suitable neutron optical model (OM) potential, several tests using different OM potentials [49, 144–151] were carried out (see Ref. [62]) and finally, the one of D. Wilmore et. al. [49] was chosen as the most appropriate. The contribution of pre-equilibrium emission effects was imported in the calculations by implementing the classical approach of the exciton model [50, 51] by means of the PCROSS module [52] of the EMPIRE code. In the above calculations, the transmission coefficients were calculated by implementing optical model routines via the ECIS06 code [53, 54]. It should be noted that in the calculations the direct reaction channels were suppressed and spherical optical model calculations were performed. The basic keywords used in the input file of the EMPIRE code are summarized in Table 4.2.

Table 4.2: Basic keywords and the corresponding values used in the input file of the EMPIRE 3.2.2 code in order to reproduce the cross sections of neutron induced reactions on ^{197}Au.

EMPIRE 3.2.2 for ^{197}Au	
Keyword	Value
LEVDEN	0
DIRECT	0
HRTW	3
GSTRFN	1
OMPOT (n)	401
OMPOT (p)	5405
OMPOT (α)	9600
PCROSS	2.2

Regarding theoretical calculations with the TALYS code, compound nucleus reaction cross sections were calculated according to the Hauser-Feshbach theory. Continuous excitation spectra of the nuclei at equilibrium deformation were described with level densities from the Generalised Superfluid Model (GSM). The width of the angular momentum distribution of the level density (spin cut-off parameter, σ^2) is given by the following expression:

$$\sigma^2 = c\,\frac{\alpha}{\tilde{\alpha}}\sqrt{\frac{U}{\alpha}} \tag{4.90}$$

where c is a constant, α is the level density parameter determined either by experimental information or by global systematics, $\tilde{\alpha}$ is the asymptotic level density parameter one would obtain in the absence of any shell effects ($\tilde{\alpha}$=α(E$\rightarrow\infty$)) and

$$U = E - \Delta \tag{4.91}$$

where E is the excitation energy, Δ is an empirical parameter related to the pairing energy which is included to account for the known odd-even effects in nuclei. In order to fairly reproduce the cross section of the second isomeric state the spin cut-off parameter was multiplied by a factor of 1.5 (default value 1, see Table 4.3). Moreover, the asymptotic level density parameters ($\tilde{\alpha}$) for the ^{198}Au, ^{197}Au, ^{196}Au and ^{195}Au nuclei were explicitly declared and the values were taken from literature [55] as mentioned in [12]. Additional width fluctuation corrections were included for neutrons up to 3 MeV using the HRTW model. Regarding γ emission, transitions with a multipolarity up to 4 were taken into account with strength functions calculated microscopically by S. Goriely according to the Hartree-Fock-Bogolyubov temperature dependent model. For outgoing neutrons and protons, the global optical model parameters by Koning and Delaroche were used [47], whereas for alphas the parameters by Avrigeanu et. al [56] were adopted. Concerning pre-equilibrium de-excitation, the exciton model was assumed and the transition rates between exciton states were approached numerically with optical model collision probability. Furthermore, the spin distribution for the pre-equilibrium population of the residual nuclei was chosen to be based on the particle-hole state densities and an additional adjustment was made for the stripping and pick-up pre-equilibrium processes for α particle emission [57]. As far as the direct reactions are concerned, no spherical OMP calculations were enforced, thus meaning that the coupled-channels method [58] was implemented using a deformed optical model potential. The transmission coefficients were calculated again by means of the ECIS06 code. In any case the direct reaction mechanism contribution to the cross section did not exceed 8% over the studied energy range, above the E$_{threshold}$ of the (n,2n) reaction. The basic keywords used in the input file of the TALYS code are shown in Table 4.3.

4.5.2 Neutron induced reactions on ^{191}Ir

The ^{191}Ir(n,2n) reaction leads to the population of two levels of the residual nucleus ^{190}Ir, which present large spin differences (isomeric state, m2 (J^{π} : 11^{-}) and ground state g (J^{π} : 4^{-})). Due to the existence of the former (m2), the theoretical study of this reaction is a powerful tool for obtaining information on the structure of the involved nuclei and therefore constitutes an open field of study [57]. Above 15 MeV, apart from the energetically allowable (n,3n) competing reaction channel, an additional contribution to the cross section arises from the pre-equilibrium emission. As was also mentioned in the previous section, the simultaneous reproduction of the isomeric cross section along with other channels, sets a significant constraint, rendering theoretical calculations quite sensitive to the choice of specific nuclear model parameters such as the level density (α) and the spin cut-off (σ^2) ones.

Theoretical cross section calculations were performed for incident neutron energies ranging from 10^{-8} to 35 MeV, by means of the EMPIRE 3.2.2 [40, 41] and TALYS 1.8 [42, 43]

Table 4.3: Basic keywords and the corresponding values used in the input file of the TALYS 1.8 code in order to reproduce the cross sections of neutron induced reactions on ^{197}Au.

TALYS 1.8 for ^{197}Au	
Keyword	Value
ldmodel	3
alimit	79 198 16.827
alimit	79 197 16.736
alimit	79 196 16.645
alimit	79 195 16.554
spherical	n
widthfluc	3
widthmode	2
gammax	4
strength	1
jlmomp	n
alphaomp	6
preequilibrium	y
preeqmode	3
preeqspin	3
rspincut	1.5
spincutmodel	1
cstrip	α 2

codes. Similarly to the theoretical calulations of the previous section, the purpose was to determine the optimum combination of nuclear model parameters for each code and to achieve a good reproduction of the cross section for the three measured reaction channels ((n,2n)$_{g+m1+0.086\,m2}$, (n,2n)$_{m2}$ and (n,3n)) and for three more: (n,p), (n,α) and (n,total). In both codes, the compound nucleus reaction cross sections were calculated in the framework of the Hauser-Feshbach theory [44].

The basic keywords used in the input file of the EMPIRE code are presented in Table 4.4. The description of the compound nucleus level densities was made by using the formalism of the Enhanced Generalized Superfluid Model (EGSM) [45], while the transmission coefficients were calculated by implementing optical model routines via the ECIS06 code [53, 54]. Regarding direct reaction channels, spherical optical model calculations were performed and in order to account for the correlation between the incident and exit channels in elastic scattering, width fluctuation corrections were activated implementing the Hofmann, Richert, Tepel and Weidenmuller model (HRTW) [142] up to an incident neutron energy of 3 MeV. Gamma emission, which is important for nuclear de-excitation in the low energy range, was described by using Modified Lorentzian (MLO1) γ-ray strength functions by V. A. Plujko [143], with parameters available in the RIPL-3 database [46]. All the available in RIPL-3 neutron optical model potentials [49, 146, 149–159] were tested, but the one introduced by D. Wilmore *et al.* [49] was finally chosen, for yielding the most satisfying results on the simultaneous reproduction of the ^{191}Ir(n,2n)^{190}Ir$^{g+m1+0.086\,m2}$ and ^{191}Ir(n,2n)^{190}Ir^{m2} reaction cross sections. It should be noted that this optical model potential [49], is the one

that was also chosen for yielding the best reproduction of the ^{197}Au(n,2n)^{196}Au$^{g+m1+m2}$ and ^{197}Au(n,2n)^{196}Au^{m2} reaction cross sections.

Table 4.4: Basic keywords and the corresponding values used in the input file of the EMPIRE 3.2.2 code in order to reproduce the cross sections of neutron induced reactions on ^{191}Ir.

EMPIRE 3.2.2 for ^{191}Ir	
Keyword	Value
LEVDEN	0
DIRECT	0
HRTW	3
GSTRFN	1
OMPOT (n)	401
OMPOT (p)	5405
OMPOT (α)	9600
PCROSS	2.99

Concerning the optical model parameters for the outgoing protons, the data by A. J. Koning *et al.* [149] were adopted, while parameters obtained by V. Avrigeanu *et al.* [48] were used for the outgoing alphas. Furthermore, the classical exciton model [50, 51] was implemented by means of the PCROSS code [52], which is included in EMPIRE, to account for the pre-equilibrium emission mechanism.

The basic keywords used in the input file of the TALYS code are presented in Table 4.5, and as shown in Table 4.3, they are the same to those used in the case of the ^{197}Au target nucleus. The nuclear level densities were described according to the Generalised Superfluid Model (GSM), whereas the asymptotic level density parameters ($\tilde{\alpha}$) for the ^{192}Ir, ^{191}Ir, ^{190}Ir and ^{189}Ir nuclei were explicitly declared in order to take the values from literature [55] as mentioned in [11].

Furthermore, direct inelastic scattering was treated by the Distorted Wave Born Approximation (DWBA) [160], whereas width fluctuation corrections were included for neutrons up to 3 MeV using again the Hofmann-Richert-Tepel-Weidenmuller (HRTW) model. Gamma-ray transitions with a multipolarity up to 4 were taken into account with strength functions calculated by the Kopecky-Uhl generalised Lorentzian model. Regarding the optical model potential for outgoing neutrons, the default option of TALYS was used, implementing the global parameterization of Koning and Delaroche [149], while for α-particles the parameters by Avrigeanu et al. [56] were adopted. Concerning pre-equilibrium emission, the exciton model was assumed and the transition rates between exciton states were approached numerically with the optical model for collision probability. In order to fairly reproduce the cross section of the second isomeric state the spin distribution for the pre-equilibrium population of the residual nuclei was chosen to be based on the particle-hole state densities and the spin cut-off parameter was multiplied by a factor of 0.7. Moreover, the spin cut-off parameter for the ground state level densities was described by means of the following model:

$$\sigma^2 = c\sqrt{\frac{U}{\alpha}} \tag{4.92}$$

Table 4.5: Basic keywords and the corresponding values used in the input file of the TALYS 1.8 code in order to reproduce the cross sections of neutron induced reactions on ^{191}Ir.

TALYS for ^{191}Ir	
Keyword	Value
ldmodel	3
alimit	77 192 16.4
alimit	77 191 16.3
alimit	77 190 16.2
alimit	77 189 16.1
spherical	n
widthfluc	3
widthmode	2
gammax	4
strength	1
jlmomp	n
alphaomp	6
preequilibrium	y
preeqmode	3
preeqspin	3
rspincut	0.7
spincutmodel	2
cstrip	α 2

where c is a constant, α is the level density parameter determined either by experimental information or by global systematics and U is the excitation energy given by Eq. 4.91. In addition, for the stripping and pick-up pre-equilibrium processes of outgoing α particles a scale factor of 2 was used [57].

4.5.3 Neutron induced reactions on ^{193}Ir

Due to the fact that the ^{193}Ir nucleus does not present any long-lived isomeric state, the interest in theoretical calculations of neutron induced reactions on ^{193}Ir was focused in trying to reproduce the involved cross sections by using the same parameters to those used in the neighboring isotopes ^{191}Ir and ^{197}Au.

Theoretical cross section calculations were performed for incident neutron energies ranging from 10^{-8} to 35 MeV, by means of the EMPIRE 3.2.2 [40, 41] and TALYS 1.8 [42, 43] codes. In both codes, the compound nucleus reaction cross sections were calculated in the framework of the Hauser-Feshbach theory [44].

The basic keywords used in the input file of the EMPIRE code are presented in Table 4.6. The description of the compound nucleus level densities was made by using the formalism of the Enhanced Generalized Superfluid Model (EGSM) [45], while the transmission coefficients were calculated by implementing optical model routines via the ECIS06

code [53, 54]. Concerning direct reaction channels, spherical optical model calculations were performed and additional width fluctuation corrections were activated implementing the Hofmann, Richert, Tepel and Weidenmuller model (HRTW) [142] up to an incident neutron energy of 3 MeV. Gamma emission was described by using Modified Lorentzian (MLO1) γ-ray strength functions by V. A. Plujko [143], with parameters available in the RIPL-3 database [46]. Regarding the optical model parameters for the outgoing protons, the data by A. J. Koning *et al.* [149] were adopted, while parameters obtained by V. Avrigeanu *et al.* [48] were used for the outgoing alphas. Furthermore, all the available in RIPL-3 neutron optical model potentials [49, 146, 149–153, 156–159] were tested. Although the (n,2n) channel was reproduced fairly well by many of them, such as the one introduced by A. Koning and J. P. Delaroche [149], by R. L. Walter and P. P. Guss [159], by M. B. Chadwick and A. C Hayes [157] and by D. Wilmore *et al.* [49], the latter was chosen to be presented in the framework of trying to reproduce all the studied reactions by using the same input parameters in each code. In order to account for the pre-equilibrium emission mechanism, the classical exciton model [50, 51] was implemented by means of the PCROSS code [52]. Apart from the (n,2n) reaction channel, the aforementioned parameterization also gave satisfactory results for the (n,p), (n,α) and (n,total) ones.

Table 4.6: Basic keywords and the corresponding values used in the input file of the EMPIRE 3.2.2 code in order to reproduce the cross sections of neutron induced reactions on ^{193}Ir.

EMPIRE 3.2.2 for ^{193}Ir	
Keyword	Value
LEVDEN	0
DIRECT	0
HRTW	3
GSTRFN	1
OMPOT (n)	401
OMPOT (p)	5405
OMPOT (α)	9600
PCROSS	2.0

The basic keywords used in the input file of the TALYS code are presented in Table 4.7. The nuclear level densities were described according to the Generalised Superfluid Model (GSM), whereas the asymptotic level density parameters ($\tilde{a}$) for the ^{194}Ir, ^{193}Ir and ^{192}Ir nuclei were explicitly declared in order to take the values from literature [46].

Moreover, direct inelastic scattering was treated by Distorted Wave Born Approximation (DWBA) [160], whereas width fluctuation corrections were included for neutrons up to 3 MeV using again the Hofmann-Richert-Tepel-Weidenmuller (HRTW) model. Gamma-ray transitions with a multipolarity up to 4 were taken into account with strength functions calculated by the Kopecky-Uhl generalised Lorentzian model. Concerning the optical model potential for outgoing neutrons, the default option of TALYS was used, implementing the global parameterization of Koning and Delaroche [149], while for α-particles the parameters by Avrigeanu et al. [56] were adopted. Concerning pre-equilibrium emission, the exciton model was assumed and the transition rates between exciton states were approached numerically

Table 4.7: Basic keywords and the corresponding values used in the input file of the TALYS 1.8 code in order to reproduce the cross sections of neutron induced reactions on ^{193}Ir.

TALYS for ^{193}Ir	
Keyword	Value
ldmodel	3
alimit	77 194 20.6
alimit	77 193 20.0
alimit	77 192 20.2
spherical	n
widthfluc	3
widthmode	2
gammax	4
strength	1
jlmomp	n
alphaomp	6
preequilibrium	y
preeqmode	3
preeqspin	3
rspincut	0.7
spincutmodel	2
cstrip	α 2

with the optical model for collision probability. Similarly to the theoretical calculations described in the previous section for the ^{191}Ir nucleus, the pre-equilibrium population of the residual nuclei was chosen to be based on the particle-hole state densities, the spin cut-off parameter was multiplied by a factor of 0.7, the spin cut-off parameter for the ground state level densities was described by Eq. 4.92 and for the stripping and pick-up pre-equilibrium processes of outgoing α particles, a scale factor of 2 was used [57].

The results of the theoretical calculations for all the reactions will be presented in the following chapter, along with the experimental data both from the present work and the literature.

5

Results and Conclusions

In this chapter, the final experimental data mentioned in Table 3.15 will be presented in Figs. 5.1, 5.2, 5.4, 5.5, 5.6 and 5.8, along with previously existing in literature experimental data [9] and the ENDF/B-VII.1 evaluation [28] (in the cases that it exists). Moreover, the cross section theoretical calculations results, not only for the measured reaction channels, but also for several competing ones, will be given in Figs. 5.3, 5.7 and 5.9 along with previously existing in literature experimental data [9] and the new data points of the present work.

5.1 Cross sections for neutron induced reactions on ^{197}Au

The ^{197}Au(n,2n)^{196}Au and ^{197}Au(n,2n)^{196}Au^{m2} reaction cross sections were measured at six incident neutron energies covering the range from 15.3 to 20.9 MeV and the results are presented in Figs. 5.1 and 5.2, respectively. The experimental results for the sum of the ground and isomeric states (Fig. 5.1) follow the general trend indicated by previous data points over the whole energy range. Especially for the cross section on the plateau region ($\sim$14 MeV) the point at 15.3 MeV reveals that the plateau value lies in between the highest and the lowest existing experimental points. Regarding the cross section of the second metastable (Fig. 5.2), the point at 15.3 MeV agrees with Ghorai *et al.* [14] and Tewes *et al.* [13] within experimental uncertainties. The other ones, ranging from 17.1 to 20.0 MeV, stand a bit higher than those reported in previous datasets, while the point at 20.9 MeV follows the trend of the points at 19.5, 19.76 and 22.6 MeV by Majerle *et al.* [17], Prestwood *et al.* [16] and Uno *et al.* [15], respectively. The cross section values obtained using the modified intensities [38] for the two most intense γ-rays (147.8 and 188.3 keV) are slightly higher than the ones determined using the values from the Lund library [37]. However, they agree within their experimental uncertainties and in both cases indicate that the centroid of the cross section curve is formed at $\sim$ 17 MeV and not at 15 MeV as one would deduce based on previously existing data points.

The results obtained from the EMPIRE 3.2.2 and TALYS 1.8 codes are presented in Fig. 5.3, along with the data points of this work and already existing experimental datasets from literature [9]. The theoretical calculations from both codes reproduce fairly well all

the studied reaction channels. For the cross section of the total (n,2n) reaction (Fig. 5.3a), both curves are acceptable, but TALYS probably for incident neutron energies above 15 MeV seems to slightly favor the (n,3n) channel (Fig. 5.3c) over the (n,2n) one.

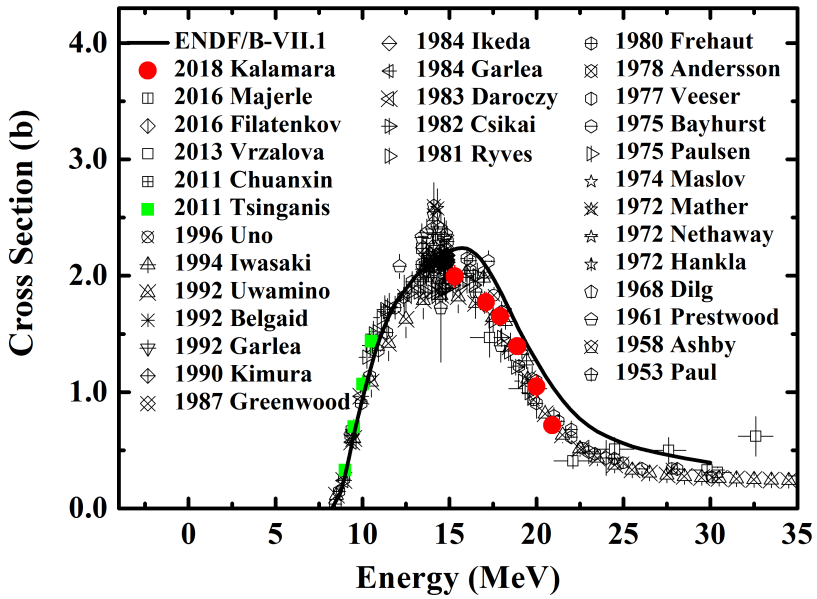

Figure 5.1: Experimental results of the present work, along with previously existing data in literature [9] and the ENDF/B-VII.1 evaluation [28] (solid curve) for the cross section of the ^{197}Au(n,2n)^{196}Au reaction.

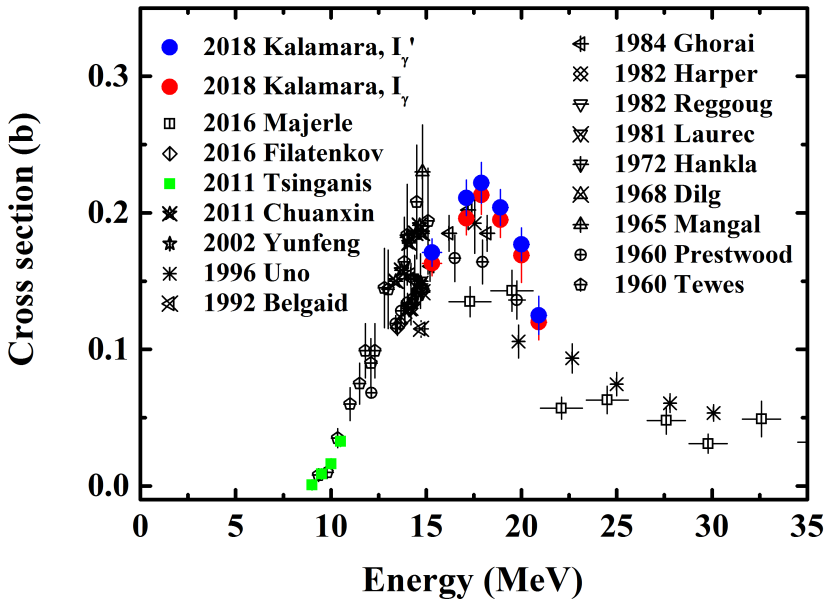

Figure 5.2: Experimental results of the present work, along with previously existing data in literature [9] for the cross section of the ^{197}Au(n,2n)^{196}Au^{m2} reaction. The red points correspond to the values of the third column of Table 3.15, with γ-ray intensities (I$_\gamma$) obtained from Ref. [37], while the blue ones are the results presented in the fourth column of Table 3.15, using the intensities (I$_\gamma$ ′) of Ref. [38] (see Table 1.1).

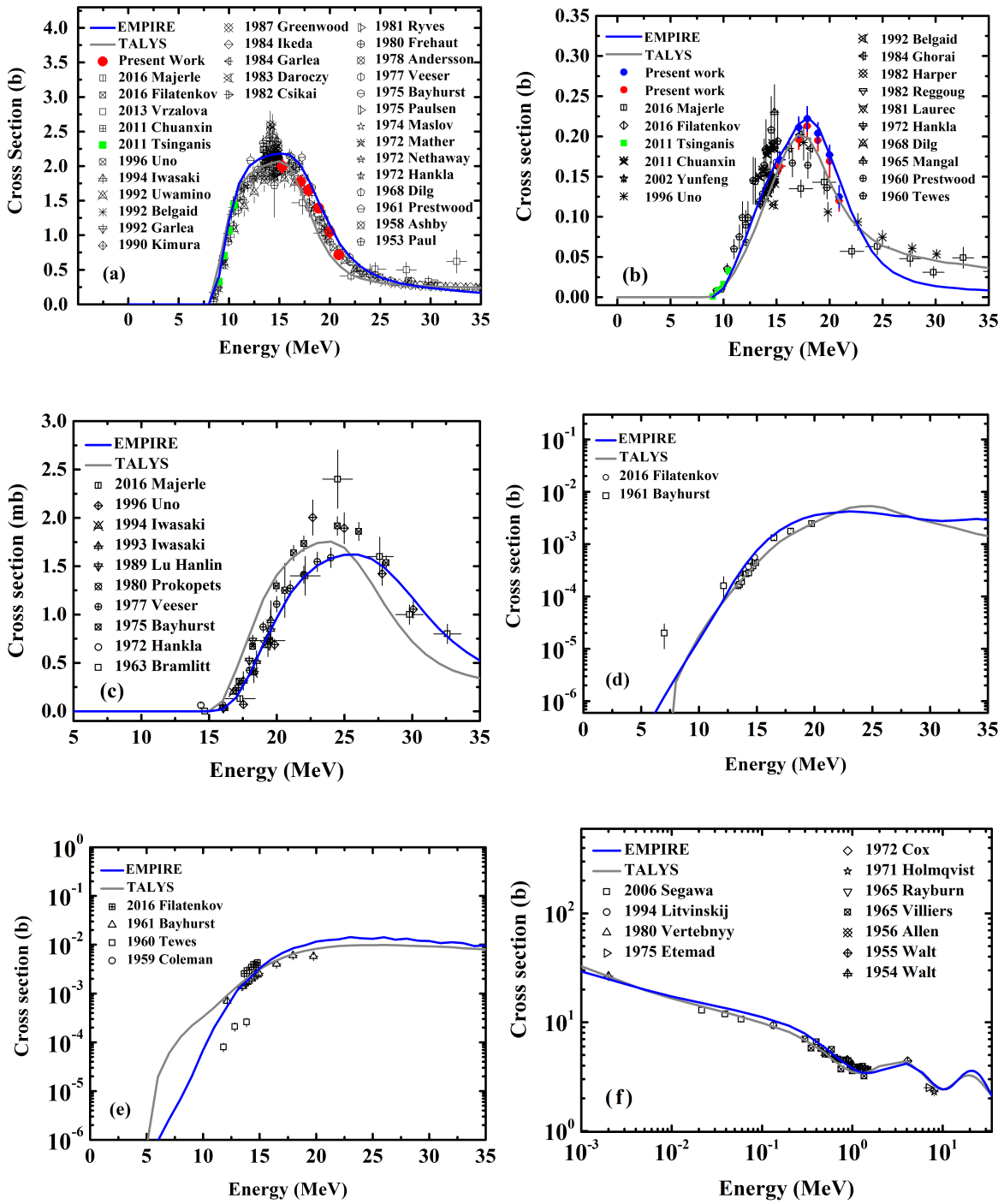

Figure 5.3: Cross section of seven reaction channels for the n+^{197}Au interaction. The experimental results of this work for the (n,2n) channels are presented along with existing data in literature [9] and theoretical calculations obtained with EMPIRE 3.2.2 and TALYS 1.8 codes. Each reaction channel is shown separately:
(a) ^{197}Au(n,2n)^{196}Au,
(b) ^{197}Au(n,2n)^{196}Au^{m2},
(c) ^{197}Au(n,3n)^{195}Au, (d) ^{197}Au(n,α)^{194}Ir,
(e) ^{197}Au(n,p)^{197}Pt^{g+m},
(f) ^{197}Au(n,elastic) and (g) ^{197}Au(n,total).

Regarding the cross section of the second metastable (Fig. 5.3b), both codes seem to describe very well the trend of experimental data and agree with the ones obtained in the present work on the position of the cross section maximum that was mentioned above. In contrast with a previous work from our group, published in 2011 by Tsinganis *et al.* [12], there was no prominent need to reduce the effective moment of inertia. At this point, it should be pointed out that both codes have been considerably improved over the last years. Apart from the fact that this can be easily noticed when comparing the present results with previous ones, i.e Ref. [12], it is also explicitly mentioned in the manual of EMPIRE 3.2 [61] (p.60). Thus, the high angular momenta treatment in the EGSM in EMPIRE code affects more efficiently the spin distribution above the critical excitation energy, as compared to the GSM, while in TALYS, a small increase of the spin cut-off parameter via the "Rspincut" keyword, was sufficient to successfully reproduce the cross section of the second isomeric state.

As far as charged particle reaction cross sections are concerned (Figs. 5.3d and 5.3e), both codes yield satisfactory results although there is a certain lack of experimental data (see Fig. 5.3e). Moreover, results for the elastic (Fig. 5.3f) and total reaction channels (Fig. 5.3g) also exhibit a very good agreement with existing data over a wide energy range.

5.2 Cross sections for neutron induced reactions on ^{191}Ir

The cross section of the ^{191}Ir(n,2n) reaction for two experimental channels, resulting in the ^{190}Ir$^{g+m1+0.086\,m2}$ and ^{190}Ir^{m2} residual nuclei respectively, as well as the ^{191}Ir(n,3n) reaction cross section were measured at incident neutron beam energies ranging from 15.3 to 20.9 MeV and the results are presented in Figs. 5.4, 5.5 and 5.6, respectively.

The experimental results for the cross section of the ^{191}Ir(n,2n)^{190}Ir$^{g+m1+0.086\,m2}$ reaction (Fig. 5.4) follow the general trend pointed out by previous data points over the whole energy range. Especially the new experimental data point at 15.3 MeV reveals that the cross section plateau lies near the lowest experimental data existing in literature, meaning close to the central values given by Filatenkov *et al.* [19], Konno *et al.* [24] and Temperley *et al.* [20] and not so close to the central values obtained by Herman *et al.* [21], Bayhurst *et al.* [18] and Qaim *et al.* [59] (although some points of the latter datasets agree within errors with the present ones). Therefore, the cross section plateau also lies much lower than the mean value indicated by the ENDF/B-VII.1 evaluation for the 11-18 MeV energy region. Regarding the cross section of the second metastable state (Fig. 5.5), the new data points result in a higher cross section compared to the majority of the previously existing datasets, while they agree only with the data introduced by Bormann *et al.* [23]. Moreover, they strongly indicate that the centroid of the cross section curve is formed at $\sim$ 17 MeV. Concerning the ^{191}Ir(n,3n) reaction channel (Fig. 5.6), only few measurements exist in literature [18, 60] and the new points present significant discrepancies with them. It seems that the cross section is overestimated by the data of Bayhurst *et al.* [18] and furthermore, it seems that the cross section curve starts to increase at slightly higher energies compared to ENFB/VII.1 evaluation.

The cross section theoretical calculation results obtained from EMPIRE 3.2.2 and TALYS

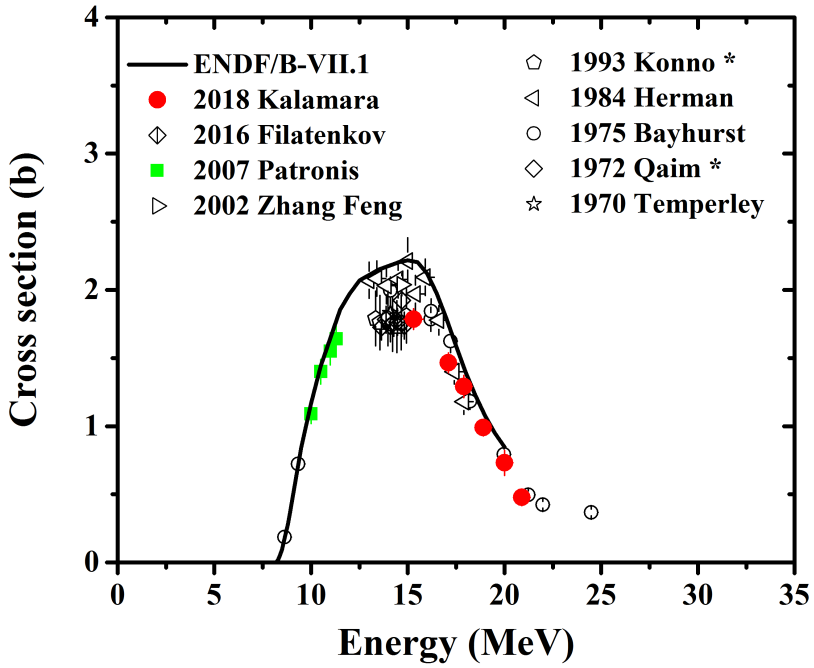

Figure 5.4: Experimental results of the present work, along with previously existing data in literature [9] and the ENDF/B-VII.1 evaluation [28] (solid curve) for the cross section of the ^{191}Ir(n,2n)^{190}Ir$^{g+m1+0.086\,m2}$ reaction. The datasets with an asterisk in the end correspond to the total (n,2n) channel cross section, while the rest correspond to g+m1 cross section values.

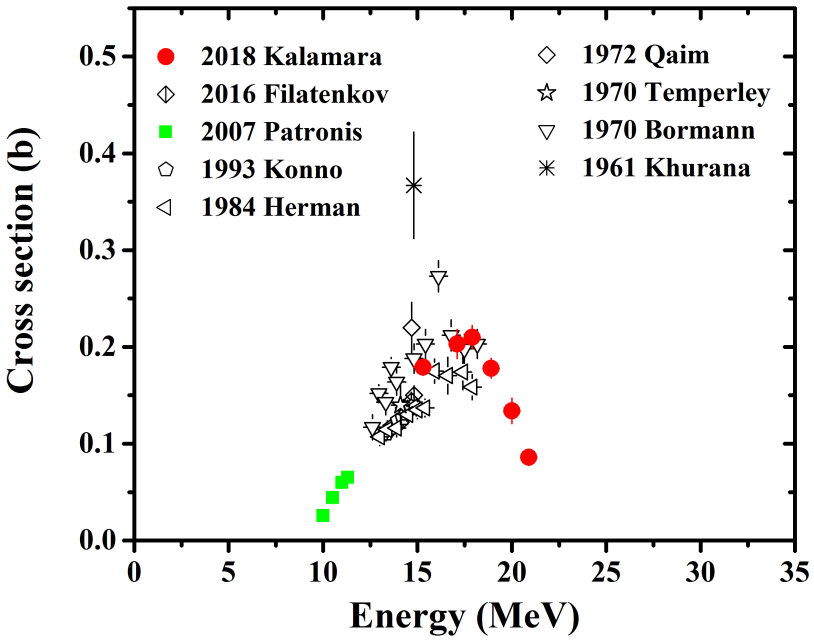

Figure 5.5: Experimental results of the present work, along with previously existing data in literature [9] for the cross section of the ^{191}Ir(n,2n)^{190}Ir^{m2} reaction.

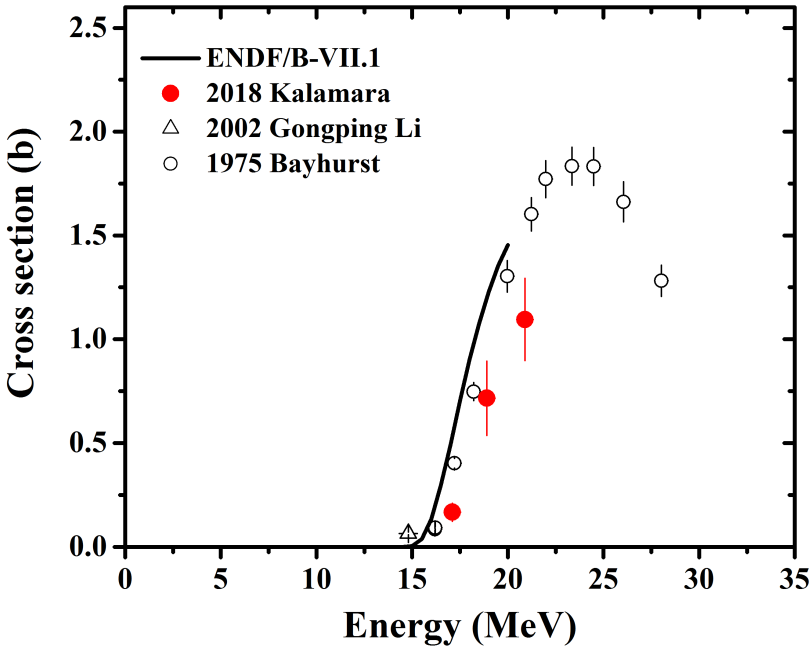

Figure 5.6: Experimental results of the present work, along with previously existing data in literature [9] and the ENDF/B-VII.1 evaluation [28] (solid curve) for the cross section of the ^{191}Ir(n,3n)^{189}Ir reaction.

1.8 codes are presented in Fig. 5.7 along with the data points of the present work and already existing experimental datasets in literature [9]. The reproduction of the cross section is quite good for all the studied reaction channels. More specifically, regarding the cross section of the ^{191}Ir(n,2n)^{190}Ir$^{g+m1+0.086\,m2}$ reaction channel (Fig. 5.7a), both curves are in very good agreement with experimental data, while TALYS for neutron energies above 15 MeV, seems to slightly favor the (n,3n) channel (Fig. 5.7c) over the (n,2n) one. In the case of the second isomeric state (Fig. 5.7b), both codes seem to describe well the trend of experimental data and the position of the cross section maximum. However, the EMPIRE (blue) curve reproduces the cross section slightly better than TALYS (grey) curve in both low (near threshold) and high energy regions. It seems that if there was the flexibility of a multiplication factor in the pre-equilibrium mechanism contribution in the TALYS code, it would be possible to describe much better the right tail of the cross section curve. It should be noted that the reproduction of this reaction channel alone, was better without taking into account the contribution of pre-equilibrium emission (when using the TALYS code). But this scenario could not be accepted, firstly because it is not physically expected and secondly because there was an additional constraint introduced by the simultaneous description of the two measured (n,2n) channels and it seemed that when the result for the m2 level improved, the result for the cross section of the sum of the levels (g+m1+0.086 m2) presented increased deviations. It should be noted that the ^{191}Ir(n,2n)^{190}Ir$^{g+m1+0.086\,m2}$ cross section data could be well reproduced by many combinations of optical and level density models using both codes. The strong constraint for the selection of the final combination of the parameters turned out to be the simultaneous reproduction of the cross sections for both ground and second isomeric states.

At this point it should be mentioned that the same behavior concerning the neutron

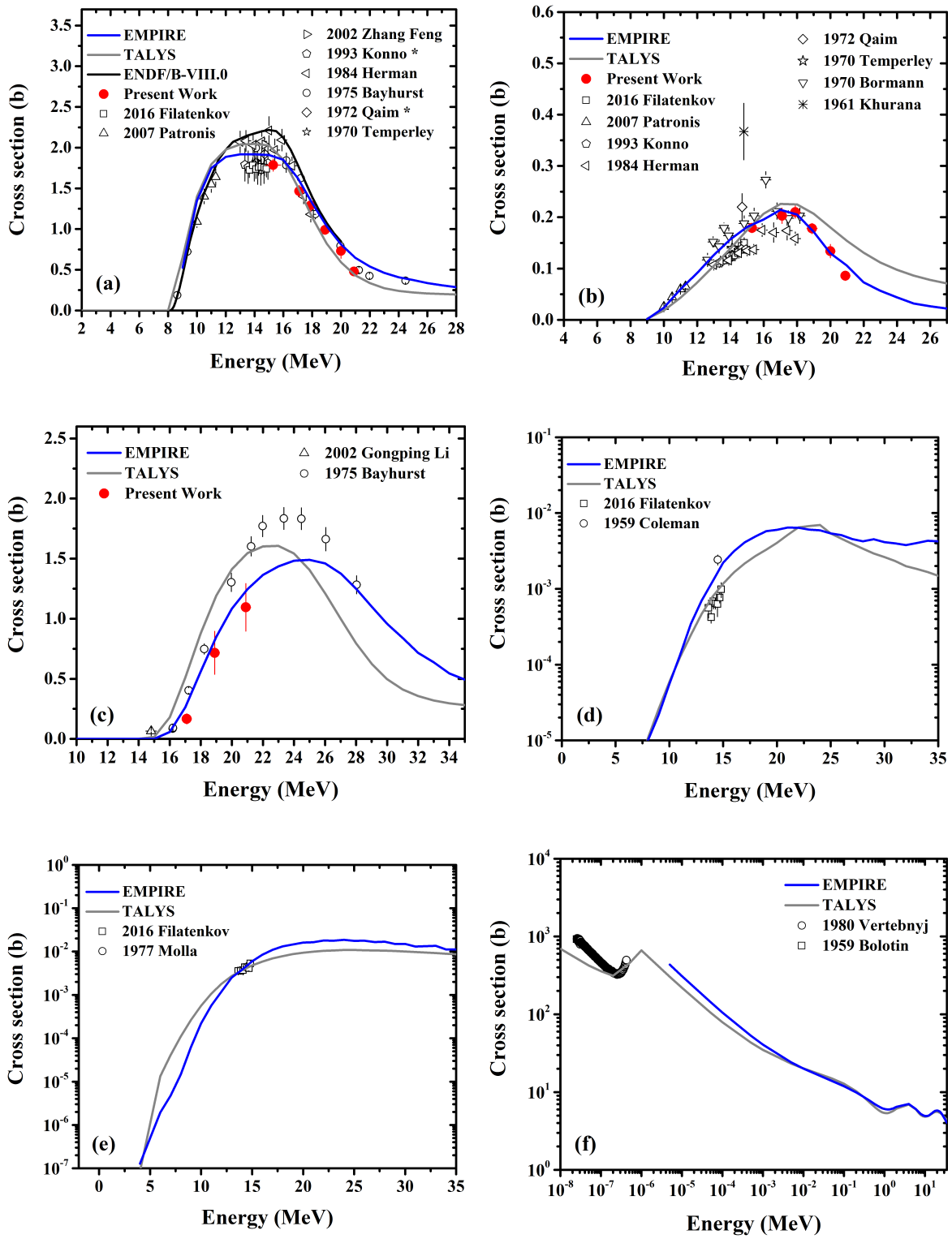

Figure 5.7: Cross section of six reaction channels for the n+^{191}Ir interaction. The experimental results of this work for the (n,2n) channels are presented along with existing data in literature [9] and theoretical calculations obtained with EMPIRE 3.2.2 and TALYS 1.8 codes. Each reaction channel is shown separately:
(a) ^{191}Ir(n,2n)^{190}Ir$^{g+m1+0.086\,m2}$, (b) ^{191}Ir(n,2n)^{196}Ir^{m2}, (c) ^{191}Ir(n,3n)^{189}Ir, (d) ^{191}Ir(n,α)^{188}Re, (e) ^{191}Ir(n,p)^{191}Os and (f) ^{191}Ir(n,total). In Fig. 5.7a, the datasets with an asterisk in the end correspond to the total (n,2n) channel cross section, while the rest correspond to g + m1 cross section values.

evaporation was observed when cross section theoretical calculations were carried out by using the EMPIRE 3.2.2 and TALYS 1.8 codes for the interaction of neutrons with the neighboring ^{197}Au nucleus [62] (see section 5.1). It is also worth mentioning that in those cross section theoretical calculations performed with the EMPIRE code for the n+$^{197}_{79}$Au system, the same optical model parameters (Wilmore *et al.* [49]) and EGSM level densities to those used for the n+$^{191}_{77}$Ir system [63] were chosen for yielding the most satisfactory results.

Concerning the (n,3n) reaction channel (Fig. 5.7c), the results obtained from both codes seem to underestimate the cross section compared to the data by Bayhurst *et al.* [18], but compared to the present work, especially the results of EMPIRE code present a very good agreement.

Furthermore, concerning the charged particle reaction channels (see Figs. 5.7d, 5.7e), both codes seem to reproduce in a quite satisfactory manner the cross sections, although there is a certain lack of experimental data. In addition, results of both codes for the total reaction cross section (Fig. 5.7f) agree well with each other, but for this case there is a certain need for experimental cross section measurements for energies above 10^{-6} MeV. Cross section data for the (n,total) reaction over a wide energy range exist in literature but only for the case of natural Ir and not for each isotope separately [9, 64].

5.3 Cross sections for neutron induced reactions on ^{193}Ir

The ^{193}Ir(n,2n)^{192}Ir reaction cross section was measured at eight incident neutron beam energies covering the range between 10.0 and 20.9 MeV.

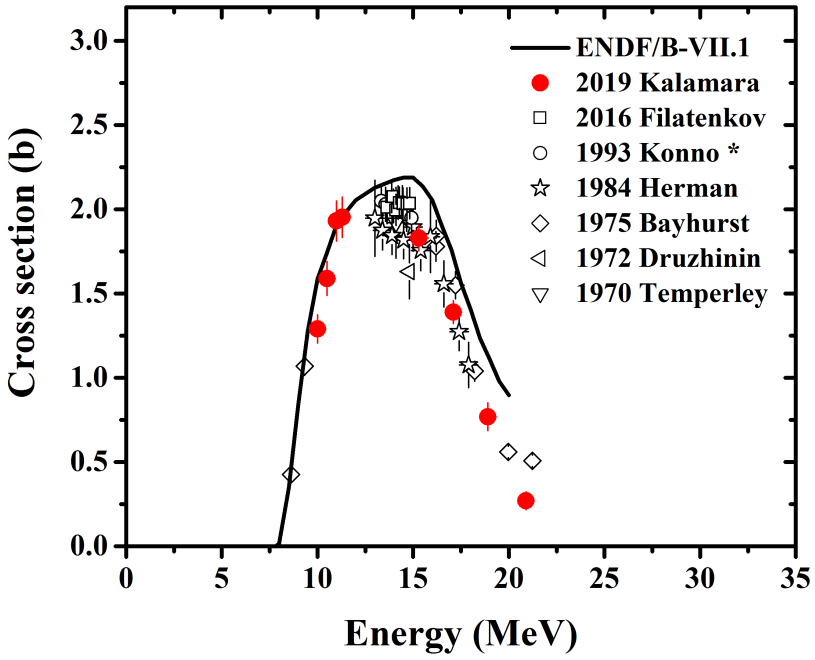

Figure 5.8: Experimental results of the present work, along with previously existing data in literature [9] and the ENDF/B-VII.1 evaluation [28] (solid curve) for the cross section of the ^{193}Ir(n,2n)^{192}Ir reaction.

The measurements at higher energies (15.3-20.9 MeV) were performed in the framework of the present thesis, while those at lower ones (10-11.3 MeV) were carried out in 2005 and 2006 by N. Patronis *et al.* [11]. From this experimental campaign, only the ^{191}Ir(n,2n) reaction was analyzed and published [11], while the ^{193}Ir(n,2n) data were currently treated with the necessary corrections for the contribution of low energy parasitic neutrons in the yield, according to the methodology mentioned in section 3.4. The experimental results are presented in Fig. 5.8, along with previously existing in literature [9] datasets and the ENDF/B-VII.1 evaluation [28]. The new data points follow the general trend indicated by previous datasets in both low and high energy regions. Only the point at 20.9 MeV gives a lower cross section value compared to the data by Bayhurst *et. al* [18].

The results obtained from the EMPIRE 3.2.2 and TALYS 1.8 codes are presented in Fig. 5.9, along with the data points of this work and already existing experimental datasets from literature [9]. Regarding the cross section of the (n,2n) reaction (Fig. 5.9a), both curves reproduce very well the trend of experimental data and also indicate that the cross section value around 14 MeV, where several datasets exist [18–21, 24, 25], lies near the lowest data points by Herman *et. al* [21] and Temperley *et. al* [20]. The (n,3n) and (n,elastic) channels of the neutron interaction on ^{193}Ir are not presented, due to the absence of experimental data in literature [9].

As far as charged particle reaction cross sections are concerned (Figs. 5.9b and 5.9c), both codes yield satisfactory results although there is a certain lack of experimental data. Moreover, results obtained from both codes for the total reaction channel (Fig. 5.9d) agree well with each other, however there is an urgent need for experimental cross section measurements for energies above 10^{-6} MeV.

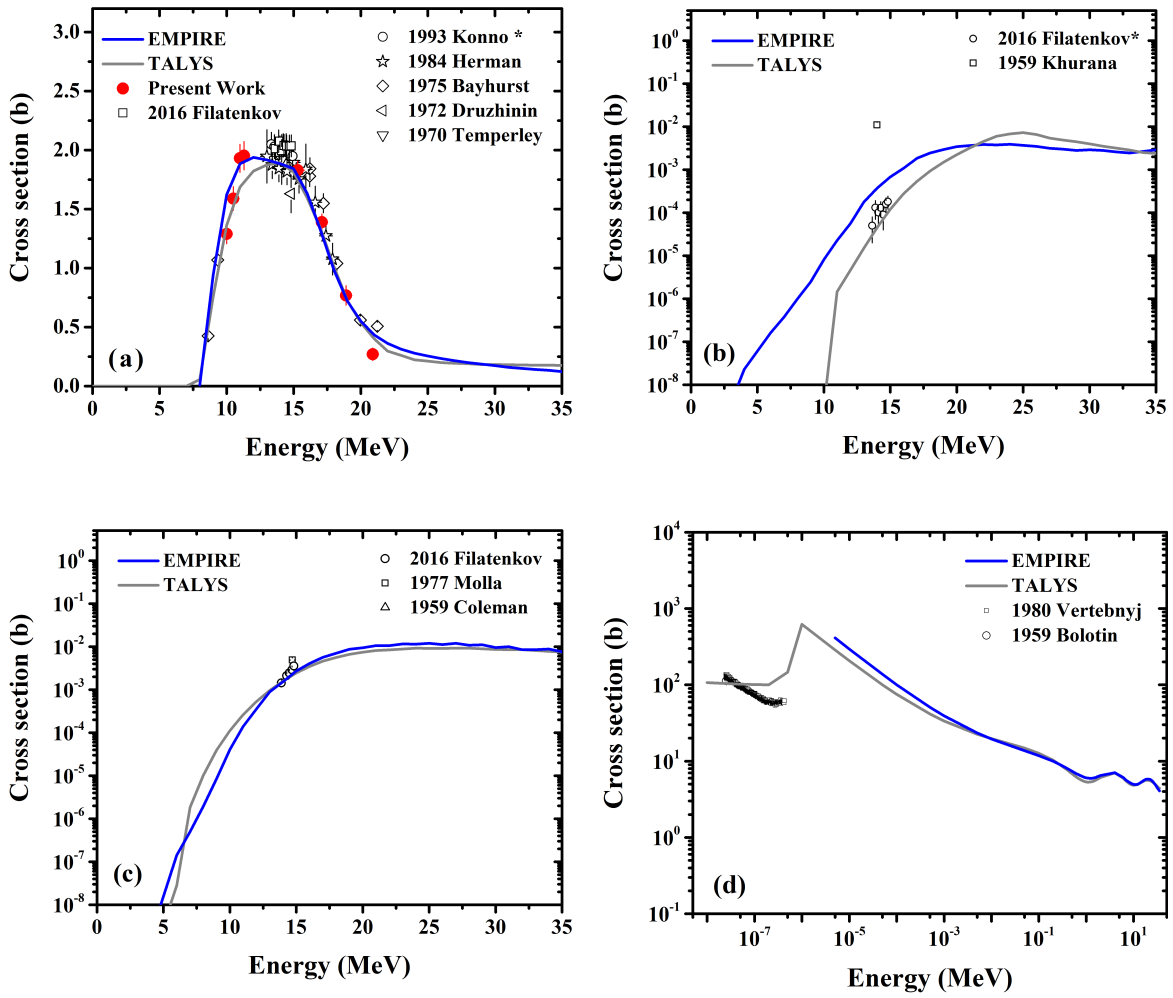

Figure 5.9: Cross section of four reaction channels for the n+^{193}Ir interaction. The experimental results of this work for the (n,2n) channel are presented along with existing data in literature [9] and theoretical calculations obtained with EMPIRE 3.2.2 and TALYS 1.8 codes. Each reaction channel is shown separately: (a) ^{193}Ir(n,2n)^{192}Ir, (b) ^{193}Ir(n,α)^{190}Re, (c) ^{193}Ir(n,p)^{193}Os and (d) ^{193}Ir(n,total). In Fig. 5.9a, the dataset with the asterisk in the end correspond to the total (n, 2n) channel cross section, while the rest corresponds to g + m1 cross section values. In contrary, in Fig. 5.9b, the dataset with the asterisk in the end corresponds to the cross section of the metastable state, while the other to the cross section of the ground.

5.4 Summary and Discussion

In the framework of the present thesis, the:

- ^{197}Au(n,2n)^{196}Au
- ^{197}Au(n,2n)^{196}Au^{m2}
- ^{191}Ir(n,2n)^{190}Ir
- ^{191}Ir(n,2n)^{190}Ir^{m2}
- ^{191}Ir(n,3n)^{189}Ir and
- ^{193}Ir(n,2n)^{192}Ir

reaction cross sections were measured at six incident neutron beam energies ranging from 15.3 to 20.9 MeV, relative to the ^{27}Al(n,α)^{24}Na and ^{93}Nb(n,2n)^{92}Nb^{m} reference reaction ones. The new measurements were performed at the 5.5 MV Tandem T11/25 Accelerator Laboratory of NCSR “Demokritos" in Athens, by means of the activation technique. Additionally, experimental data obtained in 2005 and 2006, by N. Patronis *et. al*, by using neutron beams in the 10-11.3 MeV energy range were analyzed, especially for the determination of the ^{193}Ir(n,2n)^{192}Ir reaction cross section. In order to analyze the data obtained for the latter reaction over the whole energy range, a recently developed methodology was implemented (see section 3.4), due to the fact that the residual nucleus of the ^{193}Ir(n,2n) reaction, namely the ^{192}Ir, is also produced by the ^{191}Ir(n,γ) one, which is activated by low energy parasitic neutrons. This method corrects the yield that is used for the cross section determination for the contribution of low energy parasitic neutrons. More specifically, it is performed by using detailed simulations for the energy distribution of the produced neutrons, by coupling the NeuSDesc [34] and MCNP5 [36] codes and it has been verified experimentally through the ^{197}Au(n,γ) reaction. Furthermore, cross section theoretical calculations were carried out over a wide energy range, by means of the EMPIRE 3.2.2 [40] and TALYS 1.8 [42] codes, not only for the measured reaction channels, but also for several additional ones involving the same target nuclei.

The new data points for the six aforementioned measured reactions are presented in Figs. 5.1, 5.2, 5.4, 5.5, 5.6 and 5.8. The cross section values for the ^{197}Au(n,2n)^{196}Au (Fig. 5.1) and ^{191}Ir(n,2n)^{190}Ir (Fig. 5.4) reaction channels follow the general trend of previously existing datasets and especially the data points at 15.3 MeV provide information on the plateau cross section value, where the existing data present significant discrepancies. Regarding the reaction channels in which the residual nuclei are produced in isomeric states, namely the ^{197}Au(n,2n)^{196}Au^{m2} (Fig. 5.2) and ^{191}Ir(n,2n)^{190}Ir^{m2} (5.5) ones, the new data points clearly reveal the centroid of the cross section curve and its shape. The new data for the ^{191}Ir(n,3n)^{189}Ir (Fig. 5.6) reaction cross section present significant discrepancies with the previously existing data introduced by Bayhurst *et al.* [18]. Concerning the ^{193}Ir(n,2n)^{192}Ir reaction cross section (Fig. 5.8), the new data above 15 MeV agree with previously existing datasets, while the results around 10 MeV give reasonable cross section values and fill the gap that existed in literature [9] in this energy region. Apart from the new data points,

the last reaction was the perfect test-case for the recently applied methodology (section 3.4) which was implemented in order to correct for the contribution of low energy parasitic neutrons. The results proved that this methodology works quite well and it can be used in any measurement with quasi-monoenergetic neutron beams, in facilities which do not possess Time-of-Flight experimental capabilities.

The cross section theoretical calculations results are presented in Figs. 5.3, 5.7 and 5.9. In general terms, both EMPIRE [40] and TALYS [42] codes gave quite satisfying results and especially the reproduction of the isomeric states cross sections (Fig. 5.3b and 5.7b) showed that they have been improved over the last years. The input files used in each code in order to reproduce cross sections of neutron induced reactions on ^{197}Au and ^{191}Ir and ^{193}Ir target nuclei were almost the same (i.e level density models, optical models, pre-equilibrium reaction models etc.) Although these similarities in the theoretical parameterization would be expected for neighboring nuclei, it is still an encouraging confirmation of how successfully the theoretical models can reproduce the experimental results in this mass region.

Moreover, it would be really interesting for the future:

- To perform new cross section measurements using other neighboring nuclei as targets, such as ^{187}Re, ^{192}Os, ^{198}Hg and ^{203}Tl.
- To check if the same parameterization used in the present work could also reproduce the involved reaction cross sections in the neighboring nuclei, by means of the EMPIRE and TALYS codes.
- To perform in beam activation measurements, so that residual nuclei with shorter half-lives (prompt gammas) could also be measured. In order to achieve this, an array consisting of several HPGe detectors would be needed, i.e the GEANIE array at the WNR facility at the Los Alamos Neutron Science Center [65] or the detector array of the AGATA collaboration [66].
- To perform TOF measurements at NCSR “Demokritos", once the facility is upgraded, and to check the low energy region of the neutron spectrum. To achieve this, a pulsed neutron beam would be necessary, in order to be able to measure the time of flight of the neutrons. Probably the flight path could not be larger than 10 m, but this is quite enough for the low neutron energy region.

List of Relevant Publications

Publications in Peer Reviewed Journals (7):

1. "^{191}Ir(n,2n) and ^{191}Ir(n,3n) reaction cross sections in the 15-21 MeV energy range", A. Kalamara, R. Vlastou, M. Kokkoris, S. Chasapoglou, A. Stamatopoulos, N. Patronis, M. Serris, A. Lagoyannis and S. Harissopulos, Physical Review C 98, 034607 (2018).

2. "^{197}Au(n,2n) reaction cross section in the 15-21 MeV energy range", A. Kalamara, R. Vlastou, M. Kokkoris, N. G. Nicolis, N. Patronis, M. Serris, V. Michalopoulou, A. Stamatopoulos, A. Lagoyannis and S. Harissopulos, Physical Review C 97, 034615 (2018).

3. "The intensities of γ-rays from the decay of ^{196m2}Au", M. Majerle, M. Stefanik, J. Kameník, E. Šimečková, D. Vénos, A. Kalamara and R. Vlastou, Applied Radiation and Isotopes 141 (2018) 5-9.

4. "Measurement of the ^{234}U(n,f) cross-section with quasi-monoenergetic beams in the keV and MeV range using a Micromegas detector assembly", A. Stamatopoulos, A. Kanellakopoulos, A. Kalamara, M. Diakaki, A. Tsinganis, M. Kokkoris, V. Michalopoulou, M. Axiotis, A. Lagoyiannis and R. Vlastou, Eur. Phys. J. A (2018) 54:7

5. "The (n,2n) reaction for the lightest stable erbium isotope ^{162}Er from reaction threshold up to 19 MeV", E. Georgali, Z. Eleme, N. Patronis, X. Aslanoglou, M. Axiotis, M. Diakaki, V. Foteinou, S. Harissopulos, A. Kalamara, M. Kokkoris, A. Lagoyannis, N. G. Nicolis, G. Provatas, A. Stamatopoulos, S. Stoulos, A. Tsinganis, E. Vagena, R. Vlastou and S. M. Vogiatzi, Physical Review C 98, 014622 (2018).

6. "An alternative methodology for high counting-loss corrections in neutron time-of-flight measurements", A.Stamatopoulos, M.Diakaki, A.Tsinganis, , F.Gunsing, L.Tassan-Got, M. Kokkoris, A. Kalamara, P. Žugec, N.Patronis, M.Sabate-Gilarte, R.Vlastou, The n_TOF collaboration, Nuclear Instruments and Methods in Physics A 913, 40-47 (2018).

7. "Investigation of the ^{241}Am(n,2n)^{240}Am cross section",A. Kalamara, R. Vlastou, M. Kokkoris, M. Diakaki, A. Tsinganis, N. Patronis, M. Axiotis, A. Lagoyannis, Physical Review C 93, 014610 (2016).

Publications in International Conference Proceedings (6):

1. "Cross section of the ^{197}Au(n,2n)^{196}Au reaction", A. Kalamara, R. Vlastou, M. Kokkoris, M. Diakaki, M. Serris, N. Patronis, M. Axiotis, A. Lagoyannis, International Conference on Nuclear Data for Science and Technology, 11-16.9.2016, Bruges, Belgium, EPJ Web of Conferences 146, No. 11048 (2017).

2. "Neutron-induced fission cross-section measurement of ^{234}U with (quasi-monoenergetic beams in the keV and MeV range using Micromegas detectors", A. Tsinganis, M. Kokkoris, R. Vlastou, A. Kalamara, A. Stamatopoulos, A. Kanellakopoulos, A. Lagoyannis, M. Axiotis, International Conference on Nuclear Data for Science and Technology, 11-16.9.2016, Bruges, Belgium, EPJ Web of Conferences 146, No. 04035 (2017).

3. "Study of (n,2n) reaction on ^{191,193}Ir isotopes and isomeric cross section ratios", R. Vlastou, A. Kalamara, M. Kokkoris, N. Patronis, M. Serris, M. Georgoulakis, S. Hassapoglou, K. Kobothanasis, M. Axiotis, A. Lagoyannis, International Conference on Nuclear Data for Science and Technology, 11-16.9.2016, Bruges, Belgium, EPJ Web of Conferences 146, No. 11013 (2017).

4. "Measurement of the ^{236}U(n,f) cross section with the micromegas detector", M. Diakaki, A. Kalamara, M. Kokkoris, G. Marangouli, A. Tsinganis, A. Panagiotopoulos, R. Vlastou, E. Berthoumieux, A. Lagoyannis, M. Axiotis, N. Patronis, XXXIV Mazurian Lakes Conference on Physics Frontiers in Nuclear Physics, 6-13.9.2015, Piaski, Poland, Acta Physica Polonica B 47 (2016).

5. "Neutron induced reactions with the 17 MeV facility at the Athens tandem accelerator NCSR "Demokritos"", R. Vlastou, A. Kalamara, M. Serris, M. Diakaki, M.Kokkoris, V. Paneta, M. Axiotis, A. Lagoyannis, The 23^{rd} International Conference on the Application of Accelerators in Research and Industry, CAARI 2014 , Physics Procedia 66 (2015) 425.

6. "New measurements of the ^{241}Am(n,2n)^{240}Am cross sectio", A. Kalamara, M. Diakaki, R. Vlastou, M. Kokkoris, N. Nikolis, A. Tsinganis, S. Ashley, M. Axiotis, A. Lagoyannis, Nuclear Data Sheets 119 (2014).

Appendices

A

Activation Method

As mentioned in section 1.3, when a projectile x impinges on a target nucleus X and a nuclear reaction (x+X $\rightarrow$ Y+y) with two products, namely the residual nucleus Y and the ejectile y, takes place, the production of the radioactive nuclei Y is described by:

$$\frac{dN}{dt} = \sigma \cdot f(t) \cdot N_\tau - \lambda \cdot N \tag{AA.1}$$

where

σ: the cross section of the X(x,y)Y reaction

$f(t)$: the time dependent x beam flux impinging on the target

N_τ: the number of the X target nuclei

N: the number of the Y produced nuclei

In equation AA.1 the first term describes the production of Y nuclei, while the second one their decay. Therefore, as would be expected, the production of the Y nuclei is a competition between creation and decay. In this Appendix, the solution of the above mentioned differential equation will be described in detail:

$$\begin{aligned}
\frac{dN}{dt} &= \sigma \cdot f(t) \cdot N_\tau - \lambda \cdot N \xrightarrow{\cdot e^{\lambda t}} \\
\Rightarrow \frac{dN}{dt} e^{\lambda t} &= \sigma \cdot f(t) \cdot N_\tau \cdot e^{\lambda t} - \lambda \cdot N \cdot e^{\lambda t} \Rightarrow \\
\Rightarrow \frac{dN}{dt} e^{\lambda t} + \lambda \cdot N \cdot e^{\lambda t} &= \sigma \cdot f(t) \cdot N_\tau \cdot e^{\lambda t} \Rightarrow \\
\Rightarrow \frac{dN}{dt} e^{\lambda t} + N \frac{de^{\lambda t}}{dt} &= \sigma \cdot f(t) \cdot N_\tau \cdot e^{\lambda t} \Rightarrow \\
\Rightarrow \frac{d(N \cdot e^{\lambda t})}{dt} &= \sigma \cdot f(t) \cdot N_\tau \cdot e^{\lambda t} \Rightarrow \\
\Rightarrow \int \frac{d(N \cdot e^{\lambda t})}{dt} dt &= \int \sigma \cdot f(t) \cdot N_\tau \cdot e^{\lambda t} dt \Rightarrow \\
\Rightarrow N(t)\, e^{\lambda t} &= \int \sigma \cdot f(t) \cdot N_\tau \cdot e^{\lambda t} dt + C
\end{aligned} \tag{AA.2}$$

For an irradiation that lasts for t_B and starts at t=0 (where N=0 and C=0), equation AA.2 becomes:

$$
\begin{aligned}
N(t_B) &= \frac{\sigma \cdot N_\tau \cdot \int_0^{t_B} e^{\lambda t} f(t)\, dt}{e^{\lambda (t_B - 0)}} \Rightarrow \\
\Rightarrow\ N(t_B) &= \sigma \cdot N_\tau \left(\int_0^{t_B} e^{\lambda t} f(t)\, dt \right) e^{-\lambda t_B} \Rightarrow \\
\Rightarrow\ N(t_B) &= \sigma \cdot N_\tau \left(\int_0^{t_B} e^{\lambda t} f(t)\, dt \right) e^{-\lambda t_B} \frac{\int_0^{t_B} f(t)\, dt}{\int_0^{t_B} f(t)\, dt} \Rightarrow \\
\Rightarrow\ N(t_B) &= \sigma \cdot N_\tau \left(\int_0^{t_B} f(t)\, dt \right) e^{-\lambda t_B} \frac{\int_0^{t_B} e^{\lambda t} f(t)\, dt}{\int_0^{t_B} f(t)\, dt} \xrightarrow{Equation\ 1.3 \rightarrow \Phi = \int_0^{t_B} f(t)\, dt} \\
\Rightarrow\ N(t_B) &= \sigma \cdot N_\tau \cdot \Phi \quad \frac{\int_0^{t_B} e^{\lambda t} f(t)\, dt}{\int_0^{t_B} f(t)\, dt} e^{-\lambda t_B} \xrightarrow{Equation\ 3.3 \rightarrow f_c = \frac{\int_0^{t_B} e^{\lambda\, dt} f(t)\, dt}{\int_0^{t_B} f(t)\, dt} e^{-\lambda\, t_B}} \\
\Rightarrow\ N(t_B) &= \sigma \cdot N_\tau \cdot \Phi \cdot f_c
\end{aligned}
\tag{AA.3}
$$

This is the main equation (Eq. 1.6) of section 1.3.

The aforementioned formalism is accurate for almost all the studied reactions. However, in the cases in which the second metastable (m2) decays to the ground one (i.e in the case of ^{196}Au, see Fig. 1.2), it has to be adjusted in order to describe this process. It should be noted that the ground along with the first isomeric state are assumed to be one state. Therefore, it is:

$$
\frac{dN}{dt} = \sigma \cdot f(t) \cdot N_\tau - \lambda \cdot N + p \cdot \lambda_m \cdot N_m \tag{AA.4}
$$

where

p: is the branching ratio for the decay of metastable to ground

By multiplying Eq. AA.4 with $e^{\lambda t}$, it becomes:

$$
\begin{aligned}
\frac{dN}{dt} e^{\lambda t} &= \sigma \cdot f(t) \cdot N_\tau \cdot e^{\lambda t} - \lambda \cdot N \cdot e^{\lambda t} + p \cdot \lambda_m \cdot N_m \cdot e^{\lambda t} \Rightarrow \\
\Rightarrow \frac{dN}{dt} e^{\lambda t} + \lambda \cdot N \cdot e^{\lambda t} &= \sigma \cdot f(t) \cdot N_\tau \cdot e^{\lambda t} + p \cdot \lambda_m \cdot N_m \cdot e^{\lambda t} \Rightarrow \\
\Rightarrow \frac{d(N \cdot e^{\lambda t})}{dt} &= \sigma \cdot f(t) \cdot N_\tau \cdot e^{\lambda t} + p \cdot \lambda_m \cdot N_m \cdot e^{\lambda t} \Rightarrow \\
\Rightarrow \int_0^{t_B} \frac{d(N \cdot e^{\lambda t})}{dt}\, dt &= \int_0^{t_B} \left[\sigma \cdot f(t) \cdot N_\tau \cdot e^{\lambda t} + p \cdot \lambda_m \cdot N_m \cdot e^{\lambda t} \right] dt + C
\end{aligned}
\tag{AA.5}
$$

For an irradiation that lasts for t_B and starts at t=0 (where N=0 and C=0), equation AA.5 becomes:

$$
N(t_B)\, e^{\lambda t_B} = \int_0^{t_B} \left[\sigma \cdot f(t) \cdot N_\tau + p \cdot \lambda_m \cdot N_m \right] \cdot e^{\lambda t}\, dt \tag{AA.6}
$$

In addition, it is:

$$N_m = \sigma_m \cdot N_\tau \left(\int_0^{t_B} f(t)\, e^{\lambda_m t}\, dt \right) \cdot e^{-\lambda_m t_B} \tag{AA.7}$$

By combining Eqs. AA.6 and AA.7, it is:

$$\begin{aligned}
N(t_B)\, e^{\lambda t_B} &= \int_0^{t_B} \left[\sigma \cdot f(t) \cdot N_\tau + p \cdot \lambda_m \cdot \sigma_m \cdot N_\tau \left(\int_0^{t_B} f(t)\, e^{\lambda_m t}\, dt \right) \cdot e^{-\lambda_m t_B} \right] \cdot e^{\lambda t}\, dt \;\Rightarrow \\
\Rightarrow\; N(t_B)\, e^{\lambda t_B} &= N_\tau \left[\int_0^{t_B} \left[\sigma \cdot f(t) + p \cdot \lambda_m \cdot \sigma_m \cdot e^{-\lambda_m t_B} \left(\int_0^{t_B} f(t)\, e^{\lambda_m t} dt \right) \right] \cdot e^{\lambda t}\, dt \right] \;\Rightarrow \\
\Rightarrow\; N(t_B) &= N_\tau \cdot e^{-\lambda t_B} \left[\int_0^{t_B} \left[\sigma \cdot f(t) + p \cdot \lambda_m \cdot \sigma_m \cdot e^{-\lambda_m t_B} \left(\int_0^{t_B} f(t)\, e^{\lambda_m t} dt \right) \right] \cdot e^{\lambda t}\, dt \right] \;\Rightarrow \\
\Rightarrow\; N(t_B) &= N_\tau \cdot e^{-\lambda t_B} \int_0^{t_B} \sigma \cdot f(t)\, e^{\lambda t}\, dt + \\
&\quad + N_\tau \cdot e^{-\lambda t_B} \int_0^{t_B} p \cdot \lambda_m \cdot \sigma_m \cdot e^{-\lambda_m t_B} \left(\int_0^{t_B} f(t)\, e^{\lambda_m t}\, dt \right) e^{\lambda t}\, dt \;\Rightarrow \\
\Rightarrow\; N(t_B) &= \sigma \cdot N_\tau \cdot e^{-\lambda t_B} \int_0^{t_B} f(t)\, e^{\lambda t}\, dt + \\
&\quad + p \cdot \lambda_m \cdot \sigma_m \cdot N_\tau \cdot e^{-\lambda t_B} \int_0^{t_B} e^{-\lambda_m t_B} \left(\int_0^{t_B} f(t)\, e^{\lambda_m t}\, dt \right) e^{\lambda t}\, dt \;\Rightarrow \\
\Rightarrow\; N(t_B) &= \sigma \cdot N_\tau \cdot \int_0^{t_B} f(t)\, dt \cdot \frac{\int_0^{t_B} f(t)\, e^{\lambda t}\, dt}{\int_0^{t_B} f(t)\, dt} \cdot e^{-\lambda t_B} + \\
&\quad + p \cdot \lambda_m \cdot \sigma_m \cdot N_\tau \cdot e^{-\lambda t_B} \int_0^{t_B} \left[\int_0^{t_B} f(t)\, dt \frac{\left(\int_0^{t_B} f(t)\, e^{\lambda_m t}\, dt \right)}{\int_0^{t_B} f(t)\, dt} e^{-\lambda_m t_B} \right] e^{\lambda t}\, dt \;\Rightarrow \\
\Rightarrow\; N(t_B) &= \sigma \cdot N_\tau \cdot \Phi \cdot f_c + \\
&\quad + p \cdot \lambda_m \cdot \sigma_m \cdot N_\tau \cdot e^{-\lambda t_B} \int_0^{t_B} \Phi\, f_{c_m}\, e^{\lambda t}\, dt \;\Rightarrow \\
\Rightarrow\; N(t_B) &= \sigma \cdot N_\tau \cdot \Phi \cdot f_c + p \cdot \lambda_m \cdot \sigma_m \cdot N_\tau \cdot \Phi \cdot f_{c_m} \cdot e^{-\lambda t_B} \int_0^{t_B} e^{\lambda t}\, dt \;\Rightarrow \\
\Rightarrow\; N(t_B) &= \sigma \cdot N_\tau \cdot \Phi \cdot f_c + p \cdot \lambda_m \cdot \sigma_m \cdot N_\tau \cdot \Phi \cdot f_{c_m} \cdot e^{-\lambda t_B} \frac{1}{\lambda} \left(e^{\lambda t_B} - 1 \right) \Rightarrow \\
\Rightarrow\; N(t_B) &= \sigma \cdot N_\tau \cdot \Phi \cdot f_c + p \cdot \lambda_m \cdot \sigma_m \cdot N_\tau \cdot \Phi \cdot f_{c_m} \cdot \frac{1}{\lambda} \left(1 - e^{-\lambda t_B} \right) \Rightarrow \\
\Rightarrow\; N(t_B) &= \sigma \cdot N_\tau \cdot \Phi \cdot f_c + \sigma_m \cdot N_\tau \cdot \Phi \cdot p \cdot \lambda_m \cdot f_{c_m} \cdot \frac{\left(1 - e^{-\lambda t_B} \right)}{\lambda}
\end{aligned} \tag{AA.8}$$

This equation is used instead of Eq. AA.3, in the cases in which a second isomeric state, with σ_m cross section, exists and decays to the ground one. In the uncertainty estimation, this correction was not included, due to the fact that it was considered systematic.

A.1 Correction factor for the activation measurement

Once the irradiation has finished, the decay of the produced nuclei during irradiation starts, according to the following formalism:

$$\frac{dN}{dt} = -\lambda \cdot N \Rightarrow \frac{1}{N}\frac{dN}{dt} = -\lambda \Rightarrow \int \frac{1}{N}\frac{dN}{dt}\,dt = \int -\lambda\,dt \Rightarrow lnN = -\lambda\,t + C \Rightarrow$$

$$\Rightarrow N(t) = e^{-\lambda t + C} \Rightarrow N(t) = e^{-\lambda t}\,e^{C} \tag{AA.9}$$

But $N(0) = N_0 \Rightarrow e^{C} = N_0$, so Eq. AA.9 becomes:

$$N(t) = N_0 \cdot e^{-\lambda t} \tag{AA.10}$$

Eq. AA.10 is the radioactive decay law and gives the number of the radioactive nuclei that still exist after time t.

Therefore, the number of the nuclei that have decayed after a time period t_1 after the end of the irradiation, can be written as:

$$N(t_1) = N_0 - N_0 \cdot e^{-\lambda t_1} \Rightarrow N(t_1) = N_0 \cdot (1 - e^{-\lambda t_1}) \tag{AA.11}$$

The same holds for a time period t_2 after the end of the irradiation:

$$N(t_2) = N_0 - N_0 \cdot e^{-\lambda t_2} \Rightarrow N(t_2) = N_0 \cdot (1 - e^{-\lambda t_2}) \tag{AA.12}$$

Assuming that t_1 and t_2 correspond to the time periods between the end of the irradiation and the beginning and termination of the measurement with the HPGe detector, respectively, the number of the nuclei that decayed during the measurement can be written as:

$$\begin{aligned} N = N(t_2) - N(t_1) &\Rightarrow N = N_0 \cdot (1 - e^{-\lambda t_2}) - N_0 \cdot (1 - e^{-\lambda t_1}) \Rightarrow \\ &\Rightarrow N = N_0 \cdot (1 - e^{-\lambda t_1} - 1 + e^{-\lambda t_2}) \Rightarrow \\ &\Rightarrow N = N_0 \cdot \underbrace{(e^{-\lambda t_1} - e^{-\lambda t_2})}_{D} \end{aligned} \tag{AA.13}$$

Therefore, the correction factor for the initial number of the nuclei produced during the irradiation, which decayed during the measurement with the HPGe detector is:

$$D = e^{-\lambda t_1} - e^{-\lambda t_2} \tag{AA.14}$$

The aforementioned formalism is accurate for almost all the studied reactions. However, in the cases in which the second metastable (m2) decays to the ground one (i.e in the case of ^{196}Au, see Fig. 1.2), it has to be adjusted in order to describe this process. It should be noted that the ground along with the first isomeric state are assumed to be one state. Therefore, it is:

$$\begin{aligned}
\frac{dN}{dt} &= -\lambda \cdot N + p \cdot \lambda_m \cdot N_m \Rightarrow \\
\Rightarrow \frac{dN}{dt} \cdot e^{\lambda t} &= -\lambda \cdot N \cdot e^{\lambda t} + p \cdot \lambda_m \cdot N_m \cdot e^{\lambda t} \Rightarrow \\
\Rightarrow \frac{dN}{dt} \cdot e^{\lambda t} + \lambda \cdot N \cdot e^{\lambda t} &= p \cdot \lambda_m \cdot N_m \cdot e^{\lambda t} \xrightarrow{N_m(t)=N_{m_0} \cdot e^{-\lambda_m t}} \\
\Rightarrow \frac{d(N \cdot e^{\lambda t})}{dt} &= p \cdot \lambda_m \cdot N_{m_0} \cdot e^{-\lambda_m t} \cdot e^{\lambda t} \Rightarrow \\
\Rightarrow \int_0^{t_B} \frac{d(N \cdot e^{\lambda t})}{dt}\, dt &= \int_0^{t_B} p \cdot \lambda_m \cdot N_{m_0} \cdot e^{(\lambda - \lambda_m) t}\, dt \Rightarrow \\
\Rightarrow N \cdot e^{\lambda t} - N_0 &= p \cdot \lambda_m \cdot N_{m_0} \cdot \left[\frac{e^{(\lambda - \lambda_m) t}}{\lambda - \lambda_m} \right]_0^t \Rightarrow \\
\Rightarrow N \cdot e^{\lambda t} - N_0 &= p \cdot N_{m_0} \cdot \frac{\lambda_m}{\lambda - \lambda_m} \left(e^{(\lambda - \lambda_m) t} - 1 \right) \Rightarrow \\
\Rightarrow N - N_0 \cdot e^{-\lambda t} &= p \cdot N_{m_0} \cdot \frac{\lambda_m}{\lambda - \lambda_m} \left(e^{(\lambda - \lambda_m) t} - 1 \right) \cdot e^{-\lambda t} \Rightarrow \\
\Rightarrow N &= N_0 \cdot e^{-\lambda t} + p \cdot N_{m_0} \cdot \frac{\lambda_m}{\lambda - \lambda_m} \left(e^{\lambda t - \lambda_m t - \lambda t} - e^{-\lambda t} \right) \Rightarrow \\
\Rightarrow N &= N_0 \cdot e^{-\lambda t} + p \cdot N_{m_0} \cdot \frac{\lambda_m}{\lambda - \lambda_m} \left(e^{-\lambda_m t} - e^{-\lambda t} \right) \qquad \text{(AA.15)}
\end{aligned}$$

Eq. AA.15 gives the number of the radioactive nuclei that still exist after time t.

Therefore, the number of the nuclei that have decayed after a time period t_1 after the end of the irradiation, can be written as:

$$N(t_1) = N_0 - N_0 \cdot e^{-\lambda t_1} + p \cdot N_{m_0} \cdot \frac{\lambda_m}{\lambda - \lambda_m} \left(e^{-\lambda_m t_1} - e^{-\lambda t_1} \right) \qquad \text{(AA.16)}$$

The same holds for a time period t_2 after the end of the irradiation:

$$N(t_2) = N_0 - N_0 \cdot e^{-\lambda t_2} + p \cdot N_{m_0} \cdot \frac{\lambda_m}{\lambda - \lambda_m} \left(e^{-\lambda_m t_2} - e^{-\lambda t_2} \right) \qquad \text{(AA.17)}$$

Assuming that t_1 and t_2 correspond to the time periods between the end of the irradiation and the beginning and termination of the measurement with the HPGe detector, respectively,

the number of the nuclei that decayed during the measurement can be written as:

$$
\begin{aligned}
& N = N(t_2) - N(t_1) \Rightarrow \\
\Rightarrow\ & N = N_0 - N_0 \cdot e^{-\lambda t_2} + p \cdot N_{m_0} \cdot \frac{\lambda_m}{\lambda - \lambda_m} \left(e^{-\lambda_m t_2} - e^{-\lambda t_2} \right) \\
& \quad - N_0 + N_0 \cdot e^{-\lambda t_1} - p \cdot N_{m_0} \cdot \frac{\lambda_m}{\lambda - \lambda_m} \left(e^{-\lambda_m t_1} - e^{-\lambda t_1} \right) \Rightarrow \\
\Rightarrow\ & N = N_0 \cdot \underbrace{\left(e^{-\lambda t_1} - e^{-\lambda t_2} \right)}_{D} + p \cdot N_{m_0} \cdot \frac{\lambda_m}{\lambda - \lambda_m} \left(\underbrace{\left(e^{-\lambda t_1} - e^{-\lambda t_2} \right)}_{D} - \underbrace{\left(e^{-\lambda_m t_1} - e^{-\lambda_m t_2} \right)}_{D_m} \right) \Rightarrow \\
\Rightarrow\ & N = N_0 \cdot D + p \cdot N_{m_0} \cdot \frac{\lambda_m}{\lambda - \lambda_m} \left(D - D_m \right) \Rightarrow \\
\Rightarrow\ & N = N_0 \cdot D \left(1 + p \cdot \frac{N_{m_0}}{N_0} \cdot \frac{\lambda_m}{\lambda - \lambda_m} - p \cdot \frac{N_{m_0}}{N_0} \cdot \frac{\lambda_m}{\lambda - \lambda_m} \cdot \frac{D_m}{D} \right) \Rightarrow \\
\Rightarrow\ & N = N_0 \cdot \underbrace{D \left[1 + p \cdot \frac{N_{m_0}}{N_0} \cdot \frac{\lambda_m}{\lambda - \lambda_m} \left(1 - \frac{D_m}{D} \right) \right]}_{D'}
\end{aligned}
\tag{AA.18}
$$

where

$$N_{m_0} = N_m(t_B) = \sigma_m \cdot N_\tau \cdot \Phi \cdot f_{c_m} \tag{AA.19}$$

$$N_0 = N(t_B) = \sigma \cdot N_\tau \cdot \Phi \cdot f_c + \sigma_m \cdot N_\tau \cdot \Phi \cdot p \cdot \lambda_m \cdot f_{c_m} \cdot \frac{1 - e^{-\lambda t_B}}{\lambda} \tag{AA.20}$$

Therefore, the correction factor for the initial number of the nuclei produced during the irradiation, which decayed during the measurement with the HPGe detector is:

$$D' = D \left[1 + p \cdot \frac{N_{m_0}}{N_0} \cdot \frac{\lambda_m}{\lambda - \lambda_m} \left(1 - \frac{D_m}{D} \right) \right] \tag{AA.21}$$

where

$$D = e^{-\lambda t_1} - e^{-\lambda t_2} \tag{AA.22}$$

$$D_m = e^{-\lambda_m t_1} - e^{-\lambda_m t_2} \tag{AA.23}$$

B

MCNP5 input files - Irradiation setups

The end of the irradiation line along with the Al flange and Ti-tritiated target were numbered for convenience according to Fig. B.1.

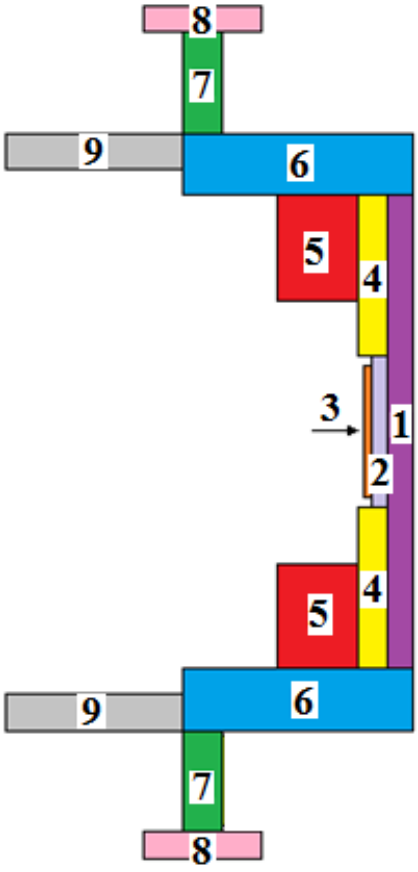

Figure B.1: The end of the irradiation line along with the Al flange and the Ti-tritiated target divided in surfaces and numbered in order to be described easier in MCNP5 input code comments.

B.1 MCNP5 input for the irradiation at 15.3 MeV

```
c       ----------------------Cells-------------------------
    1     1 -0.001225 -1 #2 #3 #4 #5 #6 #7 #8 #9 #10 #11 #12
             #13 #14 #15 #16 #17 #18 #19
c                  ---------Flange--------
    2     2    -2.7 -2  $             Al (cylinder 1)
    3     2    -2.7 -3 4 5 -6  $      Al (ring 4)
    4     2    -2.7 -7 8 9 -5  $      Al (ring 5)
    5     2    -2.7 -10 11 12 -13  $  Al (ring 6)
    6     2    -2.7 -14 15 12 -16  $  Al (ring 7)
    7     2    -2.7 -17 18 19 -20  $  Al (ring 8)
c                 --------Beam pipe-------
    8     4      -8 -21 22 23 -12  $  Steel (ring 9)
c                  ---------Holder---------
    9     2    -2.7 -27 26 -29 28  $  Al
c                  ---------Tritium---------
   10     3    -8.9 -24  $            Cu (cylinder 2)
   11     9  -4.506 -25  $            TiT (cylinder 3)
c                  ---------Foils---------
   12     2    -2.7 -30  $            AlA
   13     7 -19.282 -31  $            AuB
   14     2    -2.7 -32  $            AlC
   15    10  -13.31 -33  $            Hf4
   16     2    -2.7 -34  $            Al8
   17    11   -22.4 -35  $            Ir4
   18     2    -2.7 -36  $            Al9
   19     8   -8.57 -37  $            Nb2
c               -------Outside world-------
   20     0         1  $              Outside world

c     ----------------------Surfaces-------------------------
    1        so 100  $  Room
c                  ---------Flange--------
    2       rcc -0.2 0 0 0.2 0 0 4.5  $    Al (cylinder 1)
    3       rcc -0.7 0 0 0.5 0 0 4.5  $    Al (ring 4-outer)
    4       rcc -0.7 0 0 0.5 0 0 1.425  $  Al (ring 4-inner)
    5        px -0.7  $          auxilliary surfaces
    6        px -0.2  $          auxilliary surfaces
    7       rcc -2 0 0 1.3 0 0 4.5  $      Al (ring 5-outer)
    8       rcc -2 0 0 1.3 0 0 2.5  $      Al (ring 5-inner)
    9        px -2  $           auxilliary surfaces
   10       rcc -2.7 0 0 2.7 0 0 5.7  $    Al (ring 6-outer)
   11       rcc -2.7 0 0 2.7 0 0 4.5  $    Al (ring 6-inner)
```

```
43    12        px -2.7  $         auxilliary surfaces
44    13        px 0  $           auxilliary surfaces
45  c                ---------Ring--------
46    14       rcc -2.7 0 0 0.68 0 0 7.6  $  Al (ring 7-outer)
47    15       rcc -2.7 0 0 0.68 0 0 5.7  $  Al (ring 7-inner)
48    16        px -2.05  $       auxilliary surfaces
49    17       rcc -3.36 0 0 2 0 0 8.1  $     Al (ring 8-outer)
50    18       rcc -3.36 0 0 2 0 0 7.6  $     Al (ring 8-inner)
51    19        px -3.36  $       auxilliary surfaces
52    20        px -1.36  $       auxilliary surfaces
53  c               -----Irradiation line------
54    21       rcc -5.7 0 0 3 0 0 5.7  $      Steel (ring 9-outer)
55    22       rcc -5.7 0 0 3 0 0 4.985  $    Steel (ring 9-inner)
56    23        px -5.7  $        auxilliary surfaces
57  c                -------Tritium--------
58    24       rcc -0.3 0 0 0.1 0 0 1.425  $  Cu (cylinder 2)
59    25       rcc -0.31 0 0 0.01 0 0 1.27  $ TiT (cylinder 3)
60  c                -------Holder-------
61    26       rcc 2 0 0 0.5 0 0 0.8  $       Al (ring inner)
62    27       rcc 2 0 0 0.5 0 0 1.3  $       Al (ring outer)
63    28        px 2  $           auxilliary surface
64    29        px 2.5  $         auxilliary surface
65  c                --------Foils---------
66    30       rcc 2 0 0 0.055 0 0 0.7175  $           AlA
67    31       rcc 2.055 0 0 0.053 0 0 0.711  $         AuB
68    32       rcc 2.108 0 0 0.054 0 0 0.7175  $        AlC
69    33       rcc 2.162 0 0 0.054 0 0 0.706  $         Hf4
70    34       rcc 2.216 0 0 0.06 0 0 0.68  $          Al8
71    35       rcc 2.276 0 0 0.034 0 0 0.666  $         Ir4
72    36       rcc 2.31 0 0 0.052 0 0 0.688  $          Al9
73    37       rcc 2.362 0 0 0.05 0 0 0.6635  $         Nb2
74
75  mode  n
76  c     ------------------Materials-----------------------
77  m1    7014.         -0.755636  $                    Air
78        8016.         -0.231475 18000.        -0.012889
79  m2    13027.              -1  $                    Al
80  m3    29065.              -1  $                    Cu
81  m4    26056.           -0.74  $                    Steel
82        28000.           -0.18 24000.           -0.08
83  m5    42000.              -1  $                    Pb
84  m7    79197.              -1  $                    Au
85  m8    41093.              -1  $                    Nb
86  m9    22000.         0.39324  $                    TiT
87        1003.          0.60676
88  m10   72000.              -1  $                    Hf
```

```
m11   77000.               -1  $                    Ir
c     ------------------Importances--------------------
imp:n             1 18r                    0  $ 1, 20
c     ---------------Source definition-----------------
c
[...] sdef card from NeuSDesc
c
c     ----------------------Tally-----------------------
f4:n 12 13 14 15 16 17 18 19 $      Average neutron flux
e0 0 1e-3 40i 18 $                  Energy bins for tally
c       --------------History cutoff-----------------
nps 100000000        $        Limiting how long MCNP runs
```

B.2 MCNP5 input for the irradiation at 17.1 MeV

```
c       ---------------------Cells-------------------------
    1     1 -0.001225 -1 #2 #3 #4 #5 #6 #7 #8 #9 #10 #11 #12
             #13 #14 #15 #16 #17 #18 #19 #20 #21 #22 #23 #24
             #25 #26 #27 #28 #29 #30 #31 #32 #33
c                  ---------Flange--------
    2     2    -2.7 -2  $               Al (cylinder 1)
    3     2    -2.7 -3 4 5 -6  $        Al (ring 4)
    4     2    -2.7 -7 8 9 -5  $        Al (ring 5)
    5     2    -2.7 -10 11 12 -13  $    Al (ring 6)
    6     2    -2.7 -14 15 12 -16  $    Al (ring 7)
    7     2    -2.7 -17 18 19 -20  $    Al (ring 8)
c                 --------Beam pipe-------
    8     4      -8 -21 22 23 -12  $  Steel (ring 9)
c                  ---------Holder---------
    9     2    -2.7 -24 #6  $         Al (cylinder 10)
   10     2    -2.7 -25  $            Al (cylinder 11)
   11     2    -2.7 -26  $            Al (parallil. 12)
   12     2    -2.7 -27  $            Al (parallil. 13)
   13     2    -2.7 28 29 -30 31 -32 33 -34  $     ouf!
c                 ---------Tritium---------
   14     3    -8.9 -35  $            Cu (cylinder 2)
   15     9  -4.506 -36  $            TiT (cylinder 3)
c                -------Pb shielding-------
   16     5 -11.342 -37  $            Pb (cylider 16)
   17     5 -11.342 -38 39 40 -41  $  Pb (ring 21)
   18     5 -11.342 -42  $            Pb (ring 24)
c                --------Al shielding-------
   19     2    -2.7 -43  $            Al (cylinder 17)
```

```
   20     2    -2.7 -44 45 46 -47  $  Al (ring 20)
   21     2    -2.7 -48  $            Al (cylinder 19)
   22     2    -2.7 -49 50 51 -52  $  Al (ring 22)
   23     2    -2.7 -53 54 52 -55  $  Al (ring 23)
c                --------Am source--------
   24     6  -1.716 -56  $            Am (cylinder 18)
c                 ---------Foils---------
   25     2    -2.7 -57  $            AlF
   26     2    -2.7 -58  $            AlB
   27     7 -19.282 -59  $            Au1
   28     8   -8.57 -60  $            Nb1
   29     2    -2.7 -61  $            Al1
   30    11  -13.31 -62  $            Hf3
   31     2    -2.7 -63  $            Al6
   32    10   -22.4 -64  $            Ir2
   33     2    -2.7 -65  $            Al-B
c              -------Outside world-------
   34     0         1  $            Outside world

c     ----------------------Surfaces-----------------------
    1        so 100  $  Room
c                ---------Flange--------
    2       rcc -0.2 0 0 0.2 0 0 4.5  $    Al (cylinder 1)
    3       rcc -0.7 0 0 0.5 0 0 4.5  $    Al (ring 4-outer)
    4       rcc -0.7 0 0 0.5 0 0 1.425  $  Al (ring 4-inner)
    5        px -0.7  $         auxilliary surfaces
    6        px -0.2  $         auxilliary surfaces
    7       rcc -2 0 0 1.3 0 0 4.5  $      Al (ring 5-outer)
    8       rcc -2 0 0 1.3 0 0 2.5  $      Al (ring 5-inner)
    9        px -2  $           auxilliary surfaces
   10       rcc -2.7 0 0 2.7 0 0 5.7  $    Al (ring 6-outer)
   11       rcc -2.7 0 0 2.7 0 0 4.5  $    Al (ring 6-inner)
   12        px -2.7  $         auxilliary surfaces
   13        px 0  $            auxilliary surfaces
c                ---------Ring--------
   14       rcc -2.7 0 0 0.68 0 0 7.6  $  Al (ring 7-outer)
   15       rcc -2.7 0 0 0.68 0 0 5.7  $  Al (ring 7-inner)
   16        px -2.05  $       auxilliary surfaces
   17       rcc -3.36 0 0 2 0 0 8.1  $     Al (ring 8-outer)
   18       rcc -3.36 0 0 2 0 0 7.6  $     Al (ring 8-inner)
   19        px -3.36  $       auxilliary surfaces
   20        px -1.36  $       auxilliary surfaces
c                -----Irradiation line------
   21       rcc -5.7 0 0 3 0 0 5.7  $      Steel (ring 9-outer)
   22       rcc -5.7 0 0 3 0 0 4.985  $    Steel (ring 9-inner)
   23        px -5.7  $        auxilliary surfaces
```

```
c                -------Holder-------
   24       rcc -3.2 -6.625 0 8 0 0 0.85  $     Al (cylinder 10)
   25       rcc 3.3 -5.775 0 0 3.617 0 0.15  $  Al (cylinder 11)
   26       box 4.8 -2.158 -1.5 -3 0 0 0 0.864 0 0 0 3  $ Al 12
   27       box 4.8 -1.293 -1.5 -3 0 0 0 2.706 0 0 0 0.207  $13
   28       rcc 1.8 0 0 3 0 0 1.293  $  air (cylinder 14)
   29        px 1.8  $         auxilliary surfaces
   30        px 4.8  $         auxilliary surfaces
   31        py -1.294  $      auxilliary surfaces
   32        py 1.413  $       auxilliary surfaces
   33        pz -1.293  $      auxilliary surfaces
   34        pz 0  $
c                -------Tritium--------
   35       rcc -0.3 0 0 0.1 0 0 1.425  $     Cu (cylinder 2)
   36       rcc -0.31 0 0 0.01 0 0 1.27  $    TiT (cylinder 3)
c                -------Pb shielding-------
   37       rcc 2.06 0 0 0.3 0 0 1.293  $     Pb (cylinder 16)
   38       rcc 2.36 0 0 0.84 0 0 1.293  $    Pb (ring 21-outer)
   39       rcc 2.36 0 0 0.84 0 0 1  $        Pb (ring 21-inner)
   40        px 2.36  $        auxilliary surfaces
   41        px 3.2  $         auxilliary surfaces
   42       rcc 3.2 0 0 0.325 0 0 1.293  $    Pb (cylinder 24)
c               --------Al shielding-------
   43       rcc 2.36 0 0 0.05 0 0 0.9  $      Al (cylinder 17)
   44       rcc 2.41 0 0 0.21 0 0 0.9  $      Al (ring 20-outer)
   45       rcc 2.41 0 0 0.21 0 0 0.615  $    Al (ring 20-inner)
   46        px 2.41  $        auxilliary surfaces
   47        px 2.62  $        auxilliary surfaces
   48       rcc 2.62 0 0 0.05 0 0 0.9  $      Al (cylinder 19)
   49       rcc 2.67 0 0 0.3 0 0 0.9  $       Al (ring 22-outer)
   50       rcc 2.67 0 0 0.3 0 0 0.7  $       Al (ring 22-inner)
   51        px 2.67  $        auxilliary surfaces
   52        px 2.97  $        auxilliary surfaces
   53       rcc 2.97 0 0 0.2 0 0 1  $         Al (ring 23-outer)
   54       rcc 2.97 0 0 0.2 0 0 0.7  $       Al (ring 23-inner)
   55        px 3.17  $        auxilliary surfaces
c                ---------Am source--------
   56       rcc 2.41 0 0 0.21 0 0 0.615  $    Am (cylinder 18)
c                 ---------Foils---------
   57       rcc 2 0 0 0.06 0 0 0.6  $           AlF
   58       rcc 3.525 0 0 0.058 0 0 0.599  $    AlB
   59       rcc 3.583 0 0 0.038 0 0 0.665  $    Au1
   60       rcc 3.621 0 0 0.05 0 0 0.664  $     Nb1
   61       rcc 3.671 0 0 0.051 0 0 0.649  $    Al1
   62       rcc 3.722 0 0 0.048 0 0 0.651  $    Hf3
   63       rcc 3.77 0 0 0.05 0 0 0.655  $      Al6
```

```
121    64       rcc 3.82 0 0 0.04 0 0 0.653  $      Ir2
122    65       rcc 3.86 0 0 0.056 0 0 0.723  $     Al-B
123 c             ------Extra for cylinder 7------
124    66        px -3.88  $      auxilliary surfaces
125
126 mode  n
127 c     ------------------Materials-----------------------
128 m1    7014.         -0.755636  $                        Air
129       8016.         -0.231475 18000.        -0.012889
130 m2    13027.              -1  $                        Al
131 m3    29065.              -1  $                        Cu
132 m4    26056.           -0.74  $                        Steel
133       28000.           -0.18 24000.           -0.08
134 m5    42000.              -1  $                        Pb
135 m6    95241.         0.008762  $                        Am
136       8016.          0.601752 13027.         0.389486
137 m7    79197.              -1  $                        Au
138 m8    41093.              -1  $                        Nb
139 m9    22000.          0.39324  $                        TiT
140       1003.           0.60676
141 m10   77000.              -1  $                        Ir
142 m11   72000.              -1  $                        Hf
143 c     ------------------Importances--------------------
144 imp:n             1 32r                    0  $ 1, 34
145 c     ----------------Source definition-----------------
146 c
147 [...] sdef card from NeuSDesc
148 c
149 c     ----------------------Tally-----------------------
150 f4:n 25 24 26 27 28 29 30 31 32 33 $ Average neutron flux
151 e0 0 1e-3 40i 18 $                  Energy bins for tally
152 c       ---------------History cutoff-----------------
153 nps 100000000        $        Limiting how long MCNP runs
```

B.3 MCNP5 input for the irradiation at 17.9 MeV

```
1  c       ----------------------Cells-------------------------
2      1     1 -0.001225 -1 #2 #3 #4 #5 #6 #7 #8 #9 #10 #11 #12
3                #13 #14 #15 #16 #17 #18
4  c                   ---------Flange--------
5      2     2    -2.7 -2  $             Al (cylinder 1)
6      3     2    -2.7 -3 4 5 -6  $      Al (ring 4)
7      4     2    -2.7 -7 8 9 -5  $      Al (ring 5)
```

```
    5     2    -2.7 -10 11 12 -13  $  Al (ring 6)
    6     2    -2.7 -14 15 12 -16  $  Al (ring 7)
    7     2    -2.7 -17 18 19 -20  $  Al (ring 8)
c                 --------Beam pipe-------
    8     4      -8 -21 22 23 -12  $  Steel (ring 9)
c                  ---------Holder---------
    9     2    -2.7 -27 26 -29 28  $  Al
c                  ---------Tritium---------
   10     3    -8.9 -35  $            Cu (cylinder 2)
   11     7  -4.506 -36  $            TiT (cylinder 3)
c                 --------Foils---------
   12     2    -2.7 -57  $            AlB
   13     5 -19.282 -58  $            Au2
   14     8   -22.4 -59  $            Ir2
   15     2    -2.7 -60  $            AlA
   16     9    -3.8 -61  $            ErB
   17     2    -2.7 -63  $            Al8
   18     5 -19.282 -64  $            Au11
c              -------Outside world-------
   19     0         1  $              Outside world

c     ----------------------Surfaces-----------------------
    1        so 100  $  Room
c                 ---------Flange--------
    2       rcc -0.2 0 0 0.2 0 0 4.5  $    Al (cylinder 1)
    3       rcc -0.7 0 0 0.5 0 0 4.5  $    Al (ring 4-outer)
    4       rcc -0.7 0 0 0.5 0 0 1.425  $  Al (ring 4-inner)
    5        px -0.7  $          auxilliary surfaces
    6        px -0.2  $          auxilliary surfaces
    7       rcc -2 0 0 1.3 0 0 4.5  $      Al (ring 5-outer)
    8       rcc -2 0 0 1.3 0 0 2.5  $      Al (ring 5-inner)
    9        px -2  $            auxilliary surfaces
   10       rcc -2.7 0 0 2.7 0 0 5.7  $    Al (ring 6-outer)
   11       rcc -2.7 0 0 2.7 0 0 4.5  $    Al (ring 6-inner)
   12        px -2.7  $          auxilliary surfaces
   13        px 0  $             auxilliary surfaces
c                 ---------Ring--------
   14       rcc -2.7 0 0 0.68 0 0 7.6  $  Al (ring 7-outer)
   15       rcc -2.7 0 0 0.68 0 0 5.7  $  Al (ring 7-inner)
   16        px -2.05  $        auxilliary surfaces
   17       rcc -3.36 0 0 2 0 0 8.1  $     Al (ring 8-outer)
   18       rcc -3.36 0 0 2 0 0 7.6  $     Al (ring 8-inner)
   19        px -3.36  $        auxilliary surfaces
   20        px -1.36  $        auxilliary surfaces
c                  -----Irradiation line------
   21       rcc -5.7 0 0 3 0 0 5.7  $     Steel (ring 9-outer)
```

```
   22       rcc -5.7 0 0 3 0 0 4.985  $   Steel (ring 9-inner)
   23        px -5.7  $        auxilliary surfaces
c                -------Holder-------
   26       rcc 2.0 0 0 0.5 0 0 0.8  $    Al (ring inner)
   27       rcc 2.0 0 0 0.5 0 0 1.3  $    Al (ring outer)
   28        px 2.0  $         auxilliary surface
   29        px 2.5  $         auxilliary surface
c                -------Tritium--------
   35       rcc -0.3 0 0 0.1 0 0 1.425  $    Cu (cylinder 2)
   36       rcc -0.31 0 0 0.01 0 0 1.27  $   TiT (cylinder 3)
c                --------Foils---------
   57       rcc 2.0 0 0 0.056 0 0 0.713  $       AlB
   58       rcc 2.056 0 0 0.053 0 0 0.71  $      Au2
   59       rcc 2.109 0 0 0.033 0 0 0.652  $     Ir2
   60       rcc 2.142 0 0 0.054 0 0 0.714  $     AlA
   61       rcc 2.196 0 0 0.199 0 0 0.648  $     ErB
c             ------Extra for cylinder 7------
   62        px -3.88  $       auxilliary surfaces
c                -------Extra Foils--------
   63       rcc 2.395 0 0 0.057 0 0 0.664  $     Al8
   64       rcc 2.452 0 0 0.027 0 0 0.669  $     Au11

mode  n
c     ------------------Materials-----------------------
m1    7014.         -0.755636  $                        Air
      8016.         -0.231475 18000.        -0.012889
m2    13027.              -1  $                        Al
m3    29065.              -1  $                        Cu
m4    26056.           -0.74  $                        Steel
      28000.           -0.18 24000.           -0.08
m5    79197.              -1  $                        Au
m6    41093.              -1  $                        Nb
m7    22000.         0.39324  $                        TiT
      1003.          0.60676
m8    77000.              -1  $                        Ir
m9    72000.             0.6  $    Er2O3(Hf instead of Er)
      8016.              0.4
c     ------------------Importances---------------------
imp:n            1 17r                    0  $ 1, 19
c     ----------------Source definition-----------------
c
[...] sdef card from NeuSDesc
c
c     ----------------------Tally-----------------------
f4:n 12 13 14 15 16 17 18 $        Average neutron flux
e0 0 1e-3 1000i 20 $               Energy bins for tally
```

```
c       ---------------History cutoff-----------------
nps 100000000        $        Limiting how long MCNP runs
```

B.4 MCNP5 input for the irradiation at 18.9 MeV

```
c       ----------------------Cells-------------------------
    1     1 -0.001225 -1 #2 #3 #4 #5 #6 #7 #8 #9 #10 #11 #12
             #13 #14 #15 #16 #17 #18 #19 #20 #21
c                  ---------Flange--------
    2     2    -2.7 -2  $             Al (cylinder 1)
    3     2    -2.7 -3 4 5 -6  $      Al (ring 4)
    4     2    -2.7 -7 8 9 -5  $      Al (ring 5)
    5     2    -2.7 -10 11 12 -13  $  Al (ring 6)
    6     2    -2.7 -14 15 12 -16  $  Al (ring 7)
    7     2    -2.7 -17 18 19 -20  $  Al (ring 8)
c                 --------Beam pipe-------
    8     4      -8 -21 22 23 -12  $  Steel (ring 9)
c                  ---------Holder---------
    9     2    -2.7 -27 26 -29 28  $  Al
c                  ---------Tritium---------
   10     3    -8.9 -35  $            Cu (cylinder 2)
   11     7  -4.506 -36  $            TiT (cylinder 3)
c                 --------Foils---------
   12     2    -2.7 -57  $            Al1
   13     5 -19.282 -58  $            Au2
   14     2    -2.7 -59  $            Al10
   15     8   -22.4 -60  $            Ir4
   16     6   -8.57 -61  $            Nb1
   17     9  -13.31 -63  $            Hf4
   18     2    -2.7 -64  $            Al4
   19    10   -8.65 -65  $            Cd1
   20     5 -19.282 -66  $            Au1
   21    10   -8.65 -67  $            Cd2
c               -------Outside world-------
   22     0         1  $            Outside world

c     ----------------------Surfaces-------------------------
    1        so 100  $  Room
c                  ---------Flange--------
    2       rcc -0.2 0 0 0.2 0 0 4.5  $    Al (cylinder 1)
    3       rcc -0.7 0 0 0.5 0 0 4.5  $    Al (ring 4-outer)
    4       rcc -0.7 0 0 0.5 0 0 1.425  $  Al (ring 4-inner)
    5        px -0.7  $         auxilliary surfaces
```

```
39      6         px -0.2  $          auxilliary surfaces
40      7        rcc -2 0 0 1.3 0 0 4.5  $      Al (ring 5-outer)
41      8        rcc -2 0 0 1.3 0 0 2.5  $      Al (ring 5-inner)
42      9         px -2  $           auxilliary surfaces
43     10        rcc -2.7 0 0 2.7 0 0 5.7  $    Al (ring 6-outer)
44     11        rcc -2.7 0 0 2.7 0 0 4.5  $    Al (ring 6-inner)
45     12         px -2.7  $         auxilliary surfaces
46     13         px 0  $            auxilliary surfaces
47  c                  ---------Ring--------
48     14        rcc -2.7 0 0 0.68 0 0 7.6  $  Al (ring 7-outer)
49     15        rcc -2.7 0 0 0.68 0 0 5.7  $  Al (ring 7-inner)
50     16         px -2.05  $       auxilliary surfaces
51     17        rcc -3.36 0 0 2 0 0 8.1  $     Al (ring 8-outer)
52     18        rcc -3.36 0 0 2 0 0 7.6  $     Al (ring 8-inner)
53     19         px -3.36  $       auxilliary surfaces
54     20         px -1.36  $       auxilliary surfaces
55  c               -----Irradiation line------
56     21        rcc -5.7 0 0 3 0 0 5.7  $      Steel (ring 9-outer)
57     22        rcc -5.7 0 0 3 0 0 4.985  $    Steel (ring 9-inner)
58     23         px -5.7  $        auxilliary surfaces
59  c                  -------Holder-------
60     26        rcc 1.8 0 0 0.5 0 0 0.8  $     Al (ring inner)
61     27        rcc 1.8 0 0 0.5 0 0 1.3  $     Al (ring outer)
62     28         px 1.8  $         auxilliary surface
63     29         px 2.3  $         auxilliary surface
64  c                  -------Tritium--------
65     35        rcc -0.3 0 0 0.1 0 0 1.425  $     Cu (cylinder 2)
66     36        rcc -0.31 0 0 0.01 0 0 1.27  $    TiT (cylinder 3)
67  c                --------Foils---------
68     57        rcc 1.93 0 0 0.052 0 0 0.652  $      Al1
69     58        rcc 1.982 0 0 0.05 0 0 0.715  $      Au2
70     59        rcc 2.032 0 0 0.052 0 0 0.655  $     Al10
71     60        rcc 2.084 0 0 0.032 0 0 0.661  $     Ir4
72     61        rcc 2.116 0 0 0.03 0 0 0.666  $      Nb1
73  c              ------Extra for cylinder 7------
74     62         px -3.88  $          auxilliary surfaces
75  c                -------Extra Foils--------
76     63        rcc 2.146 0 0 0.051 0 0 0.704  $     Hf4
77     64        rcc 2.197 0 0 0.058 0 0 0.707  $     Al4
78  c                --------- Cd1 ------------
79     65        box 2.3 1.003 -0.965 0 -2.006 0 0.107 0 0 0 0 1.93
80     66        rcc 2.407 0 0 0.029 0 0 0.665  $     Au1
81  c                --------- Cd2 ------------
82     67        box 2.436 1.012 -0.979 0 -2.024 0 0.103 0 0 0 0 ↩
        1.959
83
```

```
mode  n
c     ------------------Materials-----------------------
m1    7014.         -0.755636  $                        Air
      8016.         -0.231475 18000.        -0.012889
m2    13027.             -1  $                        Al
m3    29065.             -1  $                        Cu
m4    26056.           -0.74  $                        Steel
      28000.           -0.18 24000.           -0.08
m5    79197.             -1  $                        Au
m6    41093.             -1  $                        Nb
m7    22000.         0.39324  $                        TiT
      1003.          0.60676
m8    77000.             -1  $                        Ir
m9    72000.             -1  $                        Hf
m10   48000.             -1  $                        Cd
c     ------------------Importances--------------------
imp:n            1 20r                    0  $ 1, 22
c     ----------------Source definition-----------------
c
[...] sdef card from NeuSDesc
c
c     ----------------------Tally-----------------------
f4:n 12 13 14 15 16 17 18 20 $      Average neutron flux
e0 0 1e-3 10000i 20 $               Energy bins for tally
c       ---------------History cutoff-----------------
nps 100000000        $        Limiting how long MCNP runs
```

B.5 MCNP5 input for the irradiation at 20.0 MeV

```
c       ----------------------Cells-------------------------
    1     1 -0.001225 -1 #2 #3 #4 #5 #6 #7 #8 #9 #10 #11 #12
             #13 #14 #15 #16 #17 #18 #19
c                  ---------Flange--------
    2     2    -2.7 -2  $               Al (cylinder 1)
    3     2    -2.7 -3 4 5 -6  $        Al (ring 4)
    4     2    -2.7 -7 8 9 -5  $        Al (ring 5)
    5     2    -2.7 -10 11 12 -13  $    Al (ring 6)
    6     2    -2.7 -14 15 62 -16  $    Al (ring 7)
    7     2    -2.7 -17 18 19 -20  $    Al (ring 8)
c                   --------Beam pipe-------
    8     4      -8 -21 22 23 -12  $  Steel (ring 9)
c                  ---------Holder---------
    9     2    -2.7 -27 26 -29 28  $  Al
```

```
c                 ---------Tritium---------
   10     3    -8.9 -35  $            Cu (cylinder 2)
   11     9  -4.506 -36  $            TiT (cylinder 3)
c                 --------Foils---------
   12     2    -2.7 -57  $            Al5
   13     7 -19.282 -58  $            Au62
   14    11   -22.4 -59  $            Ir2
   15    10  -13.31 -60  $            Hf4
   16     2    -2.7 -61  $            Al3
   17     8   -8.57 -63  $            Nb1
   18    12   -7.31 -64  $            In2
   19     2    -2.7 -65  $            Al4
c              -------Outside world-------
   20     0         1  $            Outside world

c     ----------------------Surfaces-----------------------
    1        so 100  $  Room
c                ---------Flange--------
    2       rcc -0.2 0 0 0.2 0 0 4.5  $    Al (cylinder 1)
    3       rcc -0.7 0 0 0.5 0 0 4.5  $    Al (ring 4-outer)
    4       rcc -0.7 0 0 0.5 0 0 1.425  $  Al (ring 4-inner)
    5        px -0.7  $          auxilliary surfaces
    6        px -0.2  $          auxilliary surfaces
    7       rcc -2 0 0 1.3 0 0 4.5  $      Al (ring 5-outer)
    8       rcc -2 0 0 1.3 0 0 2.5  $      Al (ring 5-inner)
    9        px -2  $           auxilliary surfaces
   10       rcc -2.7 0 0 2.7 0 0 5.7  $    Al (ring 6-outer)
   11       rcc -2.7 0 0 2.7 0 0 4.5  $    Al (ring 6-inner)
   12        px -2.7  $         auxilliary surfaces
   13        px 0  $            auxilliary surfaces
c                ---------Ring--------
   14       rcc -2.7 0 0 0.68 0 0 7.6  $  Al (ring 7-outer)
   15       rcc -2.7 0 0 0.68 0 0 5.7  $  Al (ring 7-inner)
   16        px -2.05  $       auxilliary surfaces
   17       rcc -3.36 0 0 2 0 0 8.1  $     Al (ring 8-outer)
   18       rcc -3.36 0 0 2 0 0 7.6  $     Al (ring 8-inner)
   19        px -3.36  $       auxilliary surfaces
   20        px -1.36  $       auxilliary surfaces
c               -----Irradiation line------
   21       rcc -5.7 0 0 3 0 0 5.7  $      Steel (ring 9-outer)
   22       rcc -5.7 0 0 3 0 0 4.985  $    Steel (ring 9-inner)
   23        px -5.7  $        auxilliary surfaces
c                -------Holder-------
   26       rcc 1.8 0 0 0.5 0 0 0.8  $     Al (ring inner)
   27       rcc 1.8 0 0 0.5 0 0 1.3  $     Al (ring outer)
   28        px 1.8  $         auxilliary surface
```

```
   29        px 2.3  $         auxilliary surface
c                -------Tritium--------
   35       rcc -0.3 0 0 0.1 0 0 1.425  $        Cu (cylinder 2)
   36       rcc -0.31 0 0 0.01 0 0 1.27  $      TiT (cylinder 3)
c               --------Foils---------
   57       rcc 1.8 0 0 0.061 0 0 0.699  $       Al5
   58       rcc 1.861 0 0 0.037 0 0 0.676  $     Au62
   59       rcc 1.898 0 0 0.033 0 0 0.653  $     Ir2
   60       rcc 1.931 0 0 0.053 0 0 0.703  $     Hf4
   61       rcc 1.984 0 0 0.061 0 0 0.72  $      Al3
c             ------Extra for cylinder 7------
   62        px -3.88  $         auxilliary surfaces
c               -------Extra Foils--------
   63       rcc 2.045 0 0 0.051 0 0 0.664  $     Nb1
   64       rcc 2.096 0 0 0.035 0 0 0.695  $     In2
   65       rcc 2.131 0 0 0.058 0 0 0.704  $     Al4

mode  n
c     ------------------Materials-----------------------
m1    7014.         -0.755636  $                        Air
      8016.         -0.231475 18000.        -0.012889
m2    13027.              -1  $                        Al
m3    29065.              -1  $                        Cu
m4    26056.           -0.74  $                        Steel
      28000.           -0.18 24000.           -0.08
m5    42000.              -1  $                        Pb
m7    79197.              -1  $                        Au
m8    41093.              -1  $                        Nb
m9    22000.         0.39324  $                        TiT
      1003.          0.60676
m10   72000.              -1  $                        Hf
m11   77000.              -1  $                        Ir
m12   49000.              -1  $                        In
c     ------------------Importances---------------------
imp:n             1 18r                    0  $ 1, 20
c     ----------------Source definition-----------------
c
[...] sdef card from NeuSDesc
c
c     ----------------------Tally-----------------------
f4:n 12 13 14 15 16 17 18 19 $       Average neutron flux
e0 0 1e-3 100i 22 $                  Energy bins for tally
c       --------------History cutoff-----------------
nps 100000000        $        Limiting how long MCNP runs
```

B.6 MCNP5 input for the irradiation at 20.9 MeV

```
c       ----------------------Cells-----------------------
    1     1 -0.001225 -1 #2 #3 #4 #5 #6 #7 #8 #9 #10 #11 #12
             #13 #14 #15 #16 #17 #18 #19
c                  ---------Flange--------
    2     2    -2.7 -2  $               Al (cylinder 1)
    3     2    -2.7 -3 4 5 -6  $        Al (ring 4)
    4     2    -2.7 -7 8 9 -5  $        Al (ring 5)
    5     2    -2.7 -10 11 12 -13  $    Al (ring 6)
    6     2    -2.7 -14 15 62 -16  $    Al (ring 7)
    7     2    -2.7 -17 18 19 -20  $    Al (ring 8)
c                 --------Beam pipe-------
    8     4      -8 -21 22 23 -12  $  Steel (ring 9)
c                  ---------Holder---------
    9     2    -2.7 -27 26 -29 28  $  Al
c                  ---------Tritium---------
   10     3    -8.9 -35  $            Cu (cylinder 2)
   11     9  -4.506 -36  $            TiT (cylinder 3)
c                 --------Foils---------
   12     2    -2.7 -57  $            Al2
   13     7 -19.282 -58  $            Au1
   14    11   -22.4 -59  $            Ir4
   15    10  -13.31 -60  $            Hf3
   16     2    -2.7 -61  $            Al10
   17     8   -8.57 -63  $            Nb2
   18    12   -7.31 -64  $            In1
   19     2    -2.7 -65  $            Al6
c              -------Outside world-------
   20     0         1  $            Outside world

c     ----------------------Surfaces-----------------------
    1        so 100  $  Room
c                  ---------Flange--------
    2       rcc -0.2 0 0 0.2 0 0 4.5  $    Al (cylinder 1)
    3       rcc -0.7 0 0 0.5 0 0 4.5  $    Al (ring 4-outer)
    4       rcc -0.7 0 0 0.5 0 0 1.425  $  Al (ring 4-inner)
    5        px -0.7  $          auxilliary surfaces
    6        px -0.2  $          auxilliary surfaces
    7       rcc -2 0 0 1.3 0 0 4.5  $      Al (ring 5-outer)
    8       rcc -2 0 0 1.3 0 0 2.5  $      Al (ring 5-inner)
    9        px -2  $           auxilliary surfaces
   10       rcc -2.7 0 0 2.7 0 0 5.7  $    Al (ring 6-outer)
   11       rcc -2.7 0 0 2.7 0 0 4.5  $    Al (ring 6-inner)
```

```
   12        px -2.7  $         auxilliary surfaces
   13        px 0  $            auxilliary surfaces
c                 ---------Ring--------
   14       rcc -2.7 0 0 0.68 0 0 7.6  $  Al (ring 7-outer)
   15       rcc -2.7 0 0 0.68 0 0 5.7  $  Al (ring 7-inner)
   16        px -2.05  $        auxilliary surfaces
   17       rcc -3.36 0 0 2 0 0 8.1  $     Al (ring 8-outer)
   18       rcc -3.36 0 0 2 0 0 7.6  $     Al (ring 8-inner)
   19        px -3.36  $       auxilliary surfaces
   20        px -1.36  $       auxilliary surfaces
c                -----Irradiation line------
   21       rcc -5.7 0 0 3 0 0 5.7  $      Steel (ring 9-outer)
   22       rcc -5.7 0 0 3 0 0 4.985  $    Steel (ring 9-inner)
   23        px -5.7  $        auxilliary surfaces
c                 -------Holder-------
   26       rcc 1.7 0 0 0.5 0 0 0.8  $     Al (ring inner)
   27       rcc 1.7 0 0 0.5 0 0 1.3  $     Al (ring outer)
   28        px 1.7  $         auxilliary surface
   29        px 2.2  $         auxilliary surface
c                 -------Tritium--------
   35       rcc -0.3 0 0 0.1 0 0 1.425  $     Cu (cylinder 2)
   36       rcc -0.31 0 0 0.01 0 0 1.27  $    TiT (cylinder 3)
c                  --------Foils---------
   57       rcc 1.7 0 0 0.056 0 0 0.712  $       Al2
   58       rcc 1.756 0 0 0.03 0 0 0.664  $      Au1
   59       rcc 1.786 0 0 0.04 0 0 0.66  $       Ir4
   60       rcc 1.826 0 0 0.05 0 0 0.65  $       Hf3
   61       rcc 1.876 0 0 0.053 0 0 0.653  $     Al10
c              ------Extra for cylinder 7------
   62        px -3.88  $         auxilliary surfaces
c                 -------Extra Foils--------
   63       rcc 1.929 0 0 0.043 0 0 0.633  $     Nb2
c                  --------- In2 ------------
   64       box 1.972 -0.526 -0.505 0 1.052 0 0.124 0 0 0 0 1.01
   65       rcc 2.096 0 0 0.06 0 0 0.688  $      Al6

mode  n
c     ------------------Materials-----------------------
m1    7014.         -0.755636  $                        Air
      8016.         -0.231475 18000.        -0.012889
m2    13027.              -1  $                        Al
m3    29065.              -1  $                        Cu
m4    26056.           -0.74  $                        Steel
      28000.           -0.18 24000.           -0.08
m5    42000.              -1  $                        Pb
m7    79197.              -1  $                        Au
```

```
m8    41093.              -1  $                        Nb
m9    22000.         0.39324  $                        TiT
      1003.          0.60676
m10   72000.              -1  $                        Hf
m11   77000.              -1  $                        Ir
m12   49000.              -1  $                        In
c     ------------------Importances---------------------
imp:n            1 18r                    0  $ 1, 20
c     ----------------Source definition-----------------
c
[...] sdef card from NeuSDesc
c
c     ----------------------Tally-----------------------
f4:n 12 13 14 15 16 17 18 19 $       Average neutron flux
e0 0 1e-3 100i 23 $                  Energy bins for tally
c       ---------------History cutoff-----------------
nps 100000000        $        Limiting how long MCNP runs
```

C

Covariance of σ_1 and σ_2 values

As mentioned in section 3.3, the covariance of σ_1 and σ_2 values is given by the following expression:

$$
\begin{aligned}
V_{12} &= cov(\sigma_1, \sigma_2) \Rightarrow \\
\Rightarrow V_{12} &= \left(\frac{\theta\sigma}{\theta\sigma_{ref}}\right)_1 cov(\sigma_{ref_1}, \sigma_{ref_2}) \left(\frac{\theta\sigma}{\theta\sigma_{ref}}\right)_2 + \\
&+ \left(\frac{\theta\sigma}{\theta(N_\gamma)_{meas}}\right)_1 cov((N_\gamma)_{meas_1}, (N_\gamma)_{meas_2}) \left(\frac{\theta\sigma}{\theta(N_\gamma)_{meas}}\right)_2 + \\
&+ \left(\frac{\theta\sigma}{\theta(N_\gamma)_{ref}}\right)_1 cov((N_\gamma)_{ref_1}, (N_\gamma)_{ref_2}) \left(\frac{\theta\sigma}{\theta(N_\gamma)_{ref}}\right)_2 + \\
&+ \left(\frac{\theta\sigma}{\theta(\varepsilon_\gamma)_{meas}}\right)_1 cov((\varepsilon_\gamma)_{meas_1}, (\varepsilon_\gamma)_{meas_2}) \left(\frac{\theta\sigma}{\theta(\varepsilon_\gamma)_{meas}}\right)_2 + \\
&+ \left(\frac{\theta\sigma}{\theta(\varepsilon_\gamma)_{ref}}\right)_1 cov((\varepsilon_\gamma)_{ref_1}, (\varepsilon_\gamma)_{ref_2}) \left(\frac{\theta\sigma}{\theta(\varepsilon_\gamma)_{ref}}\right)_2 + \\
&+ \left(\frac{\theta\sigma}{\theta(N_\tau)_{meas}}\right)_1 cov((N_\tau)_{meas_1}, (N_\tau)_{meas_2}) \left(\frac{\theta\sigma}{\theta(N_\tau)_{meas}}\right)_2 + \\
&+ \left(\frac{\theta\sigma}{\theta(N_\tau)_{ref}}\right)_1 cov((N_\tau)_{ref_1}, (N_\tau)_{ref_2}) \left(\frac{\theta\sigma}{\theta(N_\tau)_{ref}}\right)_2
\end{aligned}
\tag{C.1}
$$

As shown in this equation, the covariance of σ_1 and σ_2 values depends on seven other covariances, as many as are the factors which were taken into account in the determination of the uncertainty of each cross section value.

For the fully correlated factors, the covariance is equal to the square of the corresponding uncertainty. In this category belong the factors of the following covariances:

- $cov(\sigma_{ref_1}, \sigma_{ref_2})$

  The reference reaction cross section in measurements 1 and 2 is the same ($\sigma_{ref_1} = \sigma_{ref_2}$), since both measurements are obtained from the same irradiation, which means same reference (Al) foil and same neutron beam energy. Therefore, it is:

$$
cov(\sigma_{ref_1}, \sigma_{ref_2}) = \delta\sigma_{ref_1}^2 = \delta\sigma_{ref_2}^2 = \delta\sigma_{ref}{}^2 \tag{C.2}
$$

- $cov((N_\gamma)_{ref_1}, (N_\gamma)_{ref_2})$

  Since in both measurements the reference foil is the same, the integral of the γ-ray peak (1368.6 keV for the ^{27}Al(n,α)^{24}Na reaction) is also the same ($(N_\gamma)_{ref_1} = (N_\gamma)_{ref_2}$)). Therefore, it is:

$$cov((N_\gamma)_{ref_1}, (N_\gamma)_{ref_2}) = \delta(N_\gamma)_{ref_1}^2 = \delta(N_\gamma)_{ref_2}^2 = \delta(N_\gamma)_{ref}{}^2 \tag{C.3}$$

- $cov((\varepsilon_\gamma)_{ref_1}, (\varepsilon_\gamma)_{ref_2})$

  For the same reasons, $(\varepsilon_\gamma)_{ref_1} = (\varepsilon_\gamma)_{ref_2}$ and thus it is:

$$cov((\varepsilon_\gamma)_{ref_1}, (\varepsilon_\gamma)_{ref_2}) = \delta(\varepsilon_\gamma)_{ref_1}^2 = \delta(\varepsilon_\gamma)_{ref_2}^2 = \delta(\varepsilon_\gamma)_{ref}{}^2 \tag{C.4}$$

- $cov((N_\tau)_{ref_1}, (N_\tau)_{ref_2})$

  Similarly, it is $(N_\tau)_{ref_1} = (N_\tau)_{ref_2}$ and therefore:

$$cov((N_\tau)_{ref_1}, (N_\tau)_{ref_2}) = \delta(N_\tau)_{ref_1}^2 = \delta(N_\tau)_{ref_2}^2 = \delta(N_\tau)_{ref}{}^2 \tag{C.5}$$

- $cov((N_\tau)_{meas_1}, (N_\tau)_{meas_2})$

  Due to the fact that the two γ-rays, that give the two cross section values, are emitted from the same measured foil (either Au or Ir) it is $(N_\tau)_{meas_1} = (N_\tau)_{meas_2}$ and therefore:

$$cov((N_\tau)_{meas_1}, (N_\tau)_{meas_2}) = \delta(N_\tau)_{meas_1}^2 = \delta(N_\tau)_{meas_2}^2 = \delta(N_\tau)_{meas}{}^2 \tag{C.6}$$

For the uncorrelated factors, the covariance is equal to zero and in this category belong only the factors of the following covariance:

- $cov((N_\gamma)_{meas_1}, (N_\gamma)_{meas_2})$

  It doesn't matter if the two γ-rays are emitted from the same measured foil (either Au or Ir). The integrals of the γ-ray peaks were considered uncorrelated. Therefore, it is:

$$cov((N_\gamma)_{meas_1}, (N_\gamma)_{meas_2}) = 0 \tag{C.7}$$

Eq. C.1 by substituting Eqs. C.2-C.7 becomes:

$$\begin{aligned}
V_{12} = & \left(\frac{\theta\sigma}{\theta\sigma_{ref}}\right)_1 \delta\sigma_{ref}{}^2 \left(\frac{\theta\sigma}{\theta\sigma_{ref}}\right)_2 + \\
& + \left(\frac{\theta\sigma}{\theta(N_\gamma)_{ref}}\right)_1 \delta(N_\gamma)_{ref}{}^2 \left(\frac{\theta\sigma}{\theta(N_\gamma)_{ref}}\right)_2 + \\
& + \left(\frac{\theta\sigma}{\theta(\varepsilon_\gamma)_{meas}}\right)_1 cov((\varepsilon_\gamma)_{meas_1}, (\varepsilon_\gamma)_{meas_2}) \left(\frac{\theta\sigma}{\theta(\varepsilon_\gamma)_{meas}}\right)_2 + \\
& + \left(\frac{\theta\sigma}{\theta(\varepsilon_\gamma)_{ref}}\right)_1 \delta(\varepsilon_\gamma)_{ref}{}^2 \left(\frac{\theta\sigma}{\theta(\varepsilon_\gamma)_{ref}}\right)_2 + \\
& + \left(\frac{\theta\sigma}{\theta(N_\tau)_{meas}}\right)_1 \delta(N_\tau)_{meas}{}^2 \left(\frac{\theta\sigma}{\theta(N_\tau)_{meas}}\right)_2 + \\
& + \left(\frac{\theta\sigma}{\theta(N_\tau)_{ref}}\right)_1 \delta(N_\tau)_{ref}{}^2 \left(\frac{\theta\sigma}{\theta(N_\tau)_{ref}}\right)_2
\end{aligned} \tag{C.8}$$

Now, it remains only the determination of the $cov((\varepsilon_\gamma)_{meas_1}, (\varepsilon_\gamma)_{meas_2})$ term. This term is referred to the correlation of the absolute efficiency of the HPGe detector in which the Au or the Ir foils were measured, in two different energies. In order to find this covariance, one has to go back to the efficiency curve.

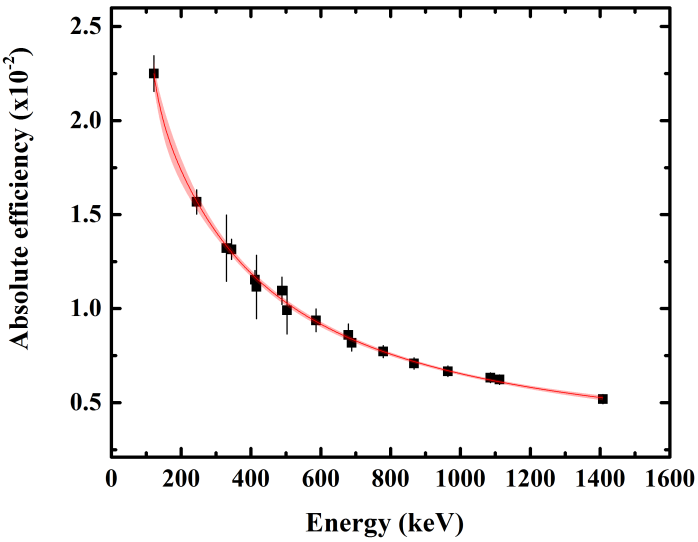

Figure C.1: The absolute efficiency with respect to the γ-ray energy for the 100% relative efficiency HPGe detector. The red hatched region denotes the confidence bands at a 95% level.

All the absolute efficiency experimental data were fitted by means of a function proposed by the International Atomic Energy Agency (IAEA), namely the:

$$\varepsilon(x) = A_0 + \frac{A_1}{x} + \frac{A_2}{x^2} + \frac{A_3}{x^3} \tag{C.9}$$

one, where ε is the absolute efficiency of the detector and x is the γ-ray energy in keV.

In order to find the covariance between two values of the absolute efficiency $cov(\varepsilon(x_1), \varepsilon(x_2))$ deduced by the same IAEA fitting function, the same formalism with the one used in Ref. [106] in order to find the covariance for an exponential fitting function (Eqs. (37) and (38)) was implemented and is the following:

$$\begin{aligned}
cov(\varepsilon(x_1), \varepsilon(x_2)) = & \left(\frac{\theta\varepsilon}{\theta A_0}\right)_{x_1}\left(\frac{\theta\varepsilon}{\theta A_0}\right)_{x_2} {\delta A_0}^2 + \\
& + \left(\frac{\theta\varepsilon}{\theta A_1}\right)_{x_1}\left(\frac{\theta\varepsilon}{\theta A_1}\right)_{x_2} {\delta A_1}^2 + \\
& + \left(\frac{\theta\varepsilon}{\theta A_2}\right)_{x_1}\left(\frac{\theta\varepsilon}{\theta A_2}\right)_{x_2} {\delta A_2}^2 + \\
& + \left(\frac{\theta\varepsilon}{\theta A_3}\right)_{x_1}\left(\frac{\theta\varepsilon}{\theta A_3}\right)_{x_2} {\delta A_3}^2 + \\
& + \left(\frac{\theta\varepsilon}{\theta A_0}\right)_{x_1}\left(\frac{\theta\varepsilon}{\theta A_1}\right)_{x_2} cov(A_0, A_1) + \\
& + \left(\frac{\theta\varepsilon}{\theta A_0}\right)_{x_1}\left(\frac{\theta\varepsilon}{\theta A_2}\right)_{x_2} cov(A_0, A_2) +
\end{aligned}$$

$$
\begin{aligned}
&+ \left(\frac{\theta\varepsilon}{\theta A_0}\right)_{x_1} \left(\frac{\theta\varepsilon}{\theta A_3}\right)_{x_2} cov(A_0, A_3) + \\
&+ \left(\frac{\theta\varepsilon}{\theta A_1}\right)_{x_1} \left(\frac{\theta\varepsilon}{\theta A_2}\right)_{x_2} cov(A_1, A_2) + \\
&+ \left(\frac{\theta\varepsilon}{\theta A_1}\right)_{x_1} \left(\frac{\theta\varepsilon}{\theta A_3}\right)_{x_2} cov(A_1, A_3) + \\
&+ \left(\frac{\theta\varepsilon}{\theta A_2}\right)_{x_1} \left(\frac{\theta\varepsilon}{\theta A_3}\right)_{x_2} cov(A_2, A_3) + \\
&+ \left(\frac{\theta\varepsilon}{\theta A_0}\right)_{x_2} \left(\frac{\theta\varepsilon}{\theta A_1}\right)_{x_1} cov(A_0, A_1) + \\
&+ \left(\frac{\theta\varepsilon}{\theta A_0}\right)_{x_2} \left(\frac{\theta\varepsilon}{\theta A_2}\right)_{x_1} cov(A_0, A_2) + \\
&+ \left(\frac{\theta\varepsilon}{\theta A_0}\right)_{x_2} \left(\frac{\theta\varepsilon}{\theta A_3}\right)_{x_1} cov(A_0, A_3) + \\
&+ \left(\frac{\theta\varepsilon}{\theta A_1}\right)_{x_2} \left(\frac{\theta\varepsilon}{\theta A_2}\right)_{x_1} cov(A_1, A_2) + \\
&+ \left(\frac{\theta\varepsilon}{\theta A_1}\right)_{x_2} \left(\frac{\theta\varepsilon}{\theta A_3}\right)_{x_1} cov(A_1, A_3) + \\
&+ \left(\frac{\theta\varepsilon}{\theta A_2}\right)_{x_2} \left(\frac{\theta\varepsilon}{\theta A_3}\right)_{x_1} cov(A_2, A_3)
\end{aligned}
\tag{C.10}
$$

By substituting the partial derivatives, becomes:

$$
\begin{aligned}
cov(\varepsilon(x_1), \varepsilon(x_2)) \;=\; & 1 \cdot 1 \cdot \delta {A_0}^2 + \\
& + \frac{1}{x_1}\,\frac{1}{x_2}\,\delta {A_1}^2 + \\
& + \frac{1}{{x_1}^2}\,\frac{1}{{x_2}^2}\,\delta {A_2}^2 + \\
& + \frac{1}{{x_1}^3}\,\frac{1}{{x_2}^3}\,\delta {A_3}^2 + \\
& + 1\,\frac{1}{x_2}\,cov(A_0, A_1) + \\
& + 1\,\frac{1}{{x_2}^2}\,cov(A_0, A_2) + \\
& + 1\,\frac{1}{{x_2}^3}\,cov(A_0, A_3) + \\
& + \frac{1}{x_1}\,\frac{1}{{x_2}^2}\,cov(A_1, A_2) + \\
& + \frac{1}{x_1}\,\frac{1}{{x_2}^3}\,cov(A_1, A_3) + \\
& + \frac{1}{{x_1}^2}\,\frac{1}{{x_2}^3}\,cov(A_2, A_3) + \\
& + 1\,\frac{1}{x_1}\,cov(A_0, A_1) + \\
& + 1\,\frac{1}{{x_1}^2}\,cov(A_0, A_2) +
\end{aligned}
$$

$$
\begin{aligned}
&+1\,\frac{1}{{x_1}^3}\,cov(A_0,A_3)+\\
&+\frac{1}{x_2}\,\frac{1}{{x_1}^2}\,cov(A_1,A_2)+\\
&+\frac{1}{x_2}\,\frac{1}{{x_1}^3}\,cov(A_1,A_3)+\\
&+\frac{1}{{x_2}^2}\,\frac{1}{{x_1}^3}\,cov(A_2,A_3)
\end{aligned}
\tag{C.11}
$$

Eq. C.11 can be summarized to the following expression:

$$
\begin{aligned}
cov(\varepsilon(x_1),\varepsilon(x_2)) \;=\; \delta{A_0}^2 + \frac{\delta{A_1}^2}{x_1\,x_2} + \frac{\delta{A_2}^2}{(x_1\,x_2)^2} + \frac{\delta{A_3}^2}{(x_1\,x_2)^3} \;+\\
+\,cov(A_0,A_1)\left(\frac{x_1+x_2}{x_1\,x_2}\right)\\
+\,cov(A_0,A_2)\left(\frac{x_1^2+x_2^2}{(x_1\,x_2)^2}\right)\\
+\,cov(A_0,A_3)\left(\frac{x_1^3+x_2^3}{(x_1\,x_2)^3}\right)\\
+\,cov(A_1,A_2)\left(\frac{x_1+x_2}{(x_1\,x_2)^2}\right)\\
+\,cov(A_1,A_3)\left(\frac{x_1^2+x_2^2}{(x_1\,x_2)^3}\right)\\
+\,cov(A_2,A_3)\left(\frac{x_1+x_2}{(x_1\,x_2)^3}\right)
\end{aligned}
\tag{C.12}
$$

The covariances $cov(A_i,A_j)$ between the fit parameters can be found with the Origin Program, if the appropriate button is enabled (see Fig. C.2). Eq. C.12 is the one that leads to the missing covariance in Eq. C.8. So, the latter, by substituting the partial derivatives becomes:

$$
\begin{aligned}
V_{12} \;=\; &\frac{\sigma_1}{\sigma_{ref}}\;\;\delta{\sigma_{ref}}^2\;\;\frac{\sigma_2}{\sigma_{ref}}\;\;+\\
&+\;\frac{\sigma_1}{(N_\gamma)_{ref}}\;\;\delta{(N_\gamma)_{ref}}^2\;\;\frac{\sigma_2}{(N_\gamma)_{ref}}\;\;+\\
&+\;\frac{\sigma_1}{\varepsilon(x_1)_{meas}}\;\;cov(\varepsilon(x_1),\varepsilon(x_2))\;\;\frac{\sigma_2}{\varepsilon(x_2)_{meas}}\;\;+\\
&+\;\frac{\sigma_1}{(\varepsilon_\gamma)_{ref}}\;\;\delta{(\varepsilon_\gamma)_{ref}}^2\;\;\frac{\sigma_2}{(\varepsilon_\gamma)_{ref}}\;\;+\\
&+\;\frac{\sigma_1}{(N_\tau)_{meas}}\;\;\delta{(N_\tau)_{meas}}^2\;\;\frac{\sigma_2}{(N_\tau)_{meas}}\;\;+\\
&+\;\frac{\sigma_1}{(N_\tau)_{ref}}\;\;\delta{(N_\tau)_{ref}}^2\;\;\frac{\sigma_2}{(N_\tau)_{ref}}\qquad\qquad\Rightarrow
\end{aligned}
$$

$$
\begin{aligned}
\Rightarrow\quad \frac{V_{12}}{\sigma_1\,\sigma_2} \;=\; &\left(\frac{\delta\sigma_{ref}}{\sigma_{ref}}\right)^2+\left(\frac{\delta(N_\gamma)_{ref}}{(N_\gamma)_{ref}}\right)^2+\left(\frac{cov(\varepsilon(x_1),\varepsilon(x_2))}{\varepsilon(x_1)_{meas}\,\varepsilon(x_2)_{meas}}\right)+\\
&+\left(\frac{\delta(\varepsilon_\gamma)_{ref}}{(\varepsilon_\gamma)_{ref}}\right)^2+\left(\frac{\delta(N_\tau)_{meas}}{(N_\tau)_{meas}}\right)^2+\left(\frac{\delta(N_\tau)_{ref}}{(N_\tau)_{ref}}\right)^2
\end{aligned}
\tag{C.13}
$$

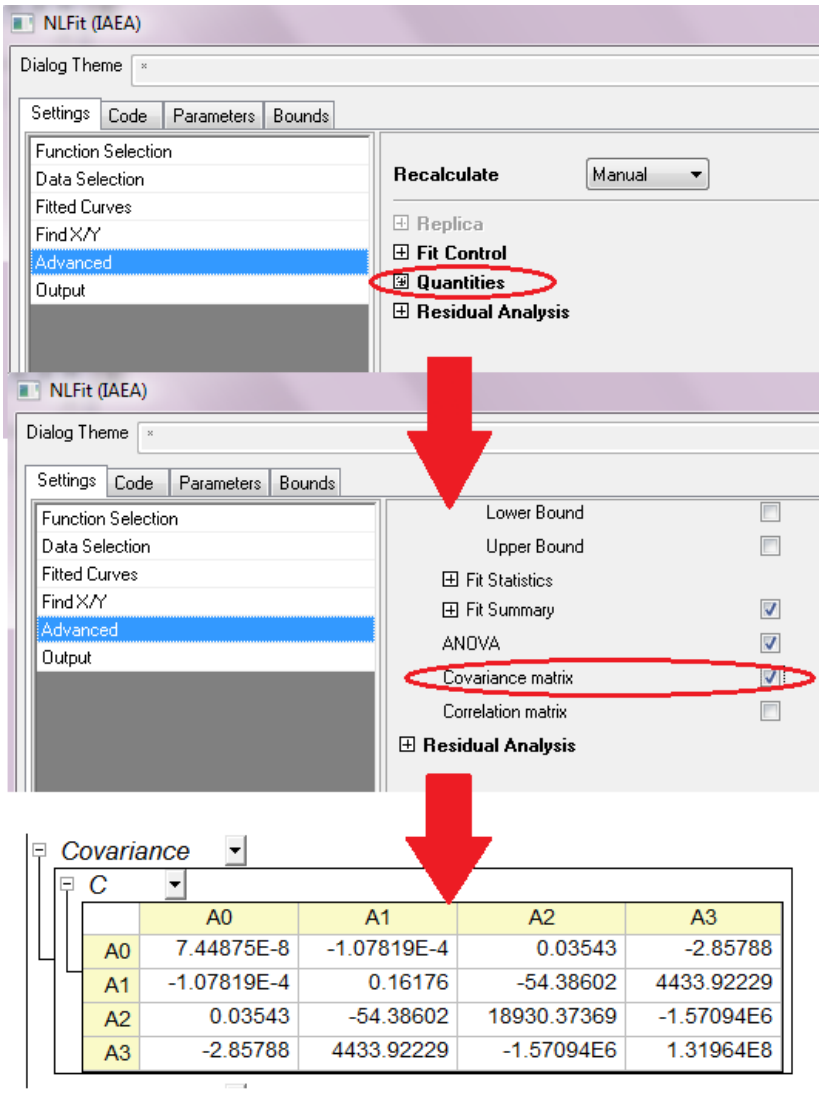

Figure C.2: Guide to find in Origin 2016 the right button to enable the covariance presentation between the fit parameters.

Finally, the covariance V_{12} can be determined by using Eqs. C.12 and C.13.

D

Weights and uncertainties for weighted averages of σ_1, σ_2 and σ_3 values

According to the formalism mentioned in Appendix 2 of Ref. [105], the weighted average cross section is given by the following expression:

$$\bar{\sigma} = \Sigma \cdot W^{\top} \Rightarrow \bar{\sigma} = \begin{bmatrix} \sigma_1 \\ \sigma_2 \\ \sigma_3 \end{bmatrix} \cdot \begin{bmatrix} w_1 & w_2 & w_3 \end{bmatrix} \Rightarrow \bar{\sigma} = w_1 \cdot \sigma_1 + w_2 \cdot \sigma_2 + w_3 \cdot \sigma_3 \tag{D.1}$$

where w_i are the weights, which in general form can be written as:

$$w_i = \frac{\sum\limits_{j} V_{ji}^{-1}}{\sum\limits_{k}\sum\limits_{l} V_{kl}^{-1}} \tag{D.2}$$

The covariances V_{ij} are determined as presented in Eq. 3.8 for i=1 and j=2 (see also Appendix C). The term V_{ji}^{-1} corresponds to the matrix element of V^{-1} matrix, which lies in the ij position. It is:

$$V = \begin{bmatrix} V_{11} & V_{12} & V_{13} \\ V_{21} & V_{22} & V_{23} \\ V_{31} & V_{32} & V_{33} \end{bmatrix} \Rightarrow V^{-1} = \frac{1}{\mid V \mid} \begin{bmatrix} V_{22}V_{33}-V_{23}^2 & V_{13}V_{32}-V_{33}V_{12} & V_{12}V_{23}-V_{22}V_{13} \\ V_{23}V_{31}-V_{33}V_{21} & V_{11}V_{33}-V_{13}^2 & V_{13}V_{21}-V_{23}V_{11} \\ V_{21}V_{32}-V_{31}V_{22} & V_{12}V_{31}-V_{32}V_{11} & V_{11}V_{22}-V_{12}^2 \end{bmatrix} \tag{D.3}$$

Thus, according to Eq. D.2, the weight for $i = 1$, can be written as:

$$\begin{aligned} w_1 &= \frac{V_{11}^{-1} + V_{21}^{-1} + V_{31}^{-1}}{V_{11}^{-1} + V_{12}^{-1} + V_{13}^{-1} + V_{21}^{-1} + V_{22}^{-1} + V_{23}^{-1} + V_{31}^{-1} + V_{32}^{-1} + V_{33}^{-1}} \Rightarrow \\ \Rightarrow w_1 &= \frac{V_{11}^{-1} + V_{21}^{-1} + V_{31}^{-1}}{V_{11}^{-1} + V_{22}^{-1} + V_{33}^{-1} + 2\,V_{12}^{-1} + 2\,V_{13}^{-1} + 2\,V_{23}^{-1}} \end{aligned} \tag{D.4}$$

Eq. D.4, by substituting the appropriate matrix elements of V^{-1} matrix (Eq. D.3), becomes:

$$w_1 = \underbrace{\frac{(V_{22}V_{33} - {V_{23}}^2) + (V_{23}V_{31} - V_{33}V_{12}) + (V_{12}V_{23} - V_{13}V_{22})}{\begin{array}{l}(V_{22}V_{33} - {V_{23}}^2) + (V_{11}V_{33} - {V_{13}}^2) + (V_{11}V_{22} - {V_{12}}^2) + \\ + 2\,(V_{13}V_{23} - V_{33}V_{12}) + 2\,(V_{12}V_{23} - V_{22}V_{13}) + 2\,(V_{13}V_{21} - V_{23}V_{11})\end{array}}}_{D\,=\,Denominator} \tag{D.5}$$

The denominator of Eq. D.5 is the same for all the weights (i=1,2 or 3), so for convenience will be symbolized with D. Therefore, the weight for $i = 2$, can be written as:

$$\begin{aligned} w_2 &= \frac{V_{12}^{-1} + V_{22}^{-1} + V_{32}^{-1}}{D} \Rightarrow \\ \Rightarrow\ w_2 &= \frac{(V_{13}V_{23} - V_{33}V_{12}) + (V_{11}V_{33} - {V_{13}}^2) + (V_{12}V_{13} - V_{23}V_{11})}{D} \end{aligned} \tag{D.6}$$

And similarly, for $i = 3$, it is:

$$\begin{aligned} w_3 &= \frac{V_{13}^{-1} + V_{23}^{-1} + V_{33}^{-1}}{D} \Rightarrow \\ \Rightarrow\ w_2 &= \frac{(V_{12}V_{23} - V_{22}V_{13}) + (V_{13}V_{12} - V_{23}V_{11}) + (V_{11}V_{22} - {V_{12}}^2)}{D} \end{aligned} \tag{D.7}$$

The uncertainty of the weighted average cross section is given by the following expression:

$$\delta\sigma = \sqrt{W \cdot V \cdot W^{\top}} \Rightarrow \delta\sigma = \left(\begin{bmatrix} w_1 & w_2 & w_3 \end{bmatrix} \cdot \begin{bmatrix} V_{11} & V_{12} & V_{13} \\ V_{21} & V_{22} & V_{23} \\ V_{31} & V_{32} & V_{33} \end{bmatrix} \cdot \begin{bmatrix} w_1 \\ w_2 \\ w_3 \end{bmatrix} \right)^{1/2} \Rightarrow$$

$$\Rightarrow \delta\sigma^2 = \begin{bmatrix} w_1V_{11}+w_2V_{21}+w_3V_{31} & w_1V_{12}+w_2V_{22}+w_3V_{32} & w_1V_{13}+w_2V_{23}+w_3V_{33} \end{bmatrix} \cdot \begin{bmatrix} w_1 \\ w_2 \\ w_3 \end{bmatrix}$$

$$\begin{aligned} \Rightarrow \delta\sigma^2 &= w_1\left(w_1V_{11} + w_2V_{21} + w_3V_{31}\right) + \\ &+ w_2\left(w_1V_{12} + w_2V_{22} + w_3V_{32}\right) + \\ &+ w_3\left(w_1V_{13} + w_2V_{23} + w_3V_{33}\right) \end{aligned} \tag{D.8}$$

where every term is known.

E

MCNP5 input files - Full room geometry

In this appendix the input file of the MCNP5 code, actually the part of the geometry description, will be presented for the irradiations at 10.0 and 15.3 MeV neutron beam energies. Concerning the measurements at higher energies (15.3 - 20.9 MeV), since the information on the sequence of the targets in the experimental setups exists in Appendix B, there is no need to give the input file for all the irradiations. The same holds regarding the lower energies (10.0 - 11.3 MeV), due to the fact that the sequence of the targets in the experimental setup was the same in all the irradiations. Apart from the neutron source description card, the tally card (more specifically the energy binning) will also be excluded from this appendix, due to its large size.

E.1 MCNP5 input for the irradiation at 10.0 MeV (Full room geometry)

```
1  c       ----------------------Cells-------------------------
2  c                ------------- Floor --------------
3  c                      ------Concrete---------
4      1     8   -2.35 (-14 -64 -65 -67 ):(-14 -64 66 ):
5                (-14 -64 46 -65 68 ):(-14 -64 -69 46 )
6      2     1 -0.0014 -14 -64 #1  $           Air
7  c                      ---Polyethylene---
8      3    14   -0.94 -12.2 -12.1 12.6 63 -14
9      4    12   -7.86 -12.2 -12.1 -63 64 -14  $ Fe
10 c                  ----------- Walls --------------
11     5     8   -2.35 -19  $         Concrete
12     6     8   -2.35 -20 -24 -12  $ Walls-Accelerator angle
13     7     8   -2.35 12 -13  $      Walls (without floor)
14 c                  ------------ Water --------------
15     8     9      -1 -15 :-16 :-17 :-18
16 c                       ---Water tanks---
```

```
     9    12   -7.86 (-16.2 16.3 17.2 -38 -51 -12.6 ):
              (17.2 38 39 -17.3 -51 -12.6 ):(17.3 39 -42 -40 -12.6
              -51 ):(-18.3 -43 18.1 -18.4 -51 -12.6 ):(44 18.4 -43
              16.1 -51 -12.6 ):(-42 16.1 -44 45 -51 -12.6 ):(45
              -15.3 -16.1 15.1 -51 -12.6 ):(-48 -45 15.1 46 -51
              -12.6 ):(46 15.4 -15.1 47 -51 -12.6 ):(47 15.2 -15.4
              -50 -51 -12.6 ):(-15.2 16.2 -50 15.3 -51 -12.6 ):
              (50 -38 16.2 49 -12.6 -51 ):(18.3 -41 42 -43 -51
              -12.6 ):(16.1 -42 -40 18.3 -51 -12.6 )
c               ----------- Al box --------------
   10     6    -2.7 -26  $     Box behind the source
   11     6    -2.7 -35  $     High voltage behind the wall
c                ---------- BF3 detector ----------
   12     6    -2.7 -34 61  $  Al wall
   13    13 -0.0028 -62  $     BF3
   14    11   -0.93 62 -61  $  Paraffin
c                -------- Irradiation Lines -------
   15     2      -8 -37  $   Neutrons
   16     2      -8 -36  $   Charged particles
   17     2      -8 -218  $  Charged particle (atomic physics)
c                ------------ Other --------------
   18    12   -7.86 -219  $        Table
   19    11   -0.93 -220 #5 #7  $  Paraffin blocks
   20    10    -8.9 -221 #5 #7  $  Quadrupoles
   21    18 -11.342 -222 #5 #7  $  Pb blocks
c                 --------Beam pipe-------
   25     2      -8 -80 81 82 -83  $     Al
   28     2      -8 -101 102 103 -82  $  Stainless steel
   29     0        -102 :-81 #25  $     Vacuum
c                  -------Holder-------
   30     6    -2.7 -107 106 -109 108  $ Al
c                ---------Gas cell---------
   22     4  -10.28 -125  $            Mo
   31     2      -8 115 -116  $        Gas cell wall
   32    19 -0.000122 -115 #22 #23  $  Deuterium
   23    20  -21.45 -126  $            Pt
c                --------Foils---------
   33     7 -19.282 -117  $              Au4
   34     6    -2.7 -118  $              Al4
   35    15   -22.4 -119  $              Ir3
   36    15   -22.4 -120  $              Ir4
   37     6    -2.7 -121  $              Al3
   38     7 -19.282 -122  $              Au3
c               -------Outside world-------
   41     1 -0.0014 -25 #1 #2 #3 #4 #5 #6 #7 #8 #9 #10 #11
             #12 #13 #14 #15 #16 #17 #18 #19 #20 #21 #25 #28
```

```
             #29 #30 #33 #34 #35 #36 #37 #31 #32 #22 #23 #38
   42     0         25  $                 Outside World

c     ----------------------Surfaces-----------------------
   12     1 rpp 0 1768 0 1683 0 667  $       Room (inner)
   13     1 rpp -124 1892 -124 1807 0 717  $ Room (outer)
c               ------------- Floor --------------
   14     1 rpp -50 1818 -50 1733 -80 0
   65       px 300
   66       px 400
   67     2  py -100
   68       px -300
   69       px -400
   63     1  pz -0.2  $                     Polyethylene
   64     1  pz -0.65  $                    Fe
c                ------------ Water --------------
   15     2 rpp 1 301 1 24 0 250
   16     2 rpp 26 326 24 49 0 250
   17     2 rpp 304 326 49 169 0 250
   18     2 rpp 326 352 36 154 0 250
c             ------------ Water tanks --------------
   38     2  py 50
   39     2  px 303
   40     2  py 170
   41     2  py 155
   42     2  px 327
   43     2  px 353
   44     2  py 35
   45     2  py 23
   46     2  py 0
   47     2  px 0
   48     2  px 302
   49     2  px 25
   50     2  py 25
   51     1  pz 251
c                ------------ Other --------------
   19     1 rpp 970 1768 265 345 0 250  $   Wall (right, back)
   20     1 c/z 0 1683 300  $               Cylinder corner
   24     1  pz 600
   25     1 rpp -200 2000 -200 2000 -100 1000  $ Boundary
   26       rpp -150 -10 -30 30 -174 -15  $Box behind the source
c                ---------- BF3 detector ----------
   34     5 rcc 200 0 0 30 0 0 20  $             Al wall
   61     5 rcc 200 0 0 30 0 0 19.5  $           BF3
   62     5 rcc 200 0 0 30 0 0 1  $              Paraffin
c                -------- Irradiation Lines -------
```

```
   36     3 rpp 153 1323 0 30 0 155  $        Charged particles
   37       rpp -687 -150 -15 15 -175 -5.8  $ Neutrons
  218     4 rpp 153 953 0 30 0 175  $Charged part. (atom. phys.)
c                 ------------ Other -------------
  219       rcc -100 -670 -20 0 0 40 200  $   Table
   35     1 rpp 1200 1690 80 170 0 170  $ High vol. beh. wall
  220     1 rpp 500 650 1600 1680 0 150  $    Paraffin blocks
  221     6 rpp -50 50 100 270 -50 50  $      Quadrupoles
  222     1 rpp 1700 1768 500 700 0 80  $     Pb blocks
c                --------Beam pipe-------
  101       rcc -687 0 0 684.3 0 0 5.7  $   Steel (ring 9-outer)
  102       rcc -687 0 0 684.3 0 0 4.985  $ Steel (ring 9-inner)
  103        px -687  $         auxilliary surfaces
c                 -------Holder-------
  106       rcc 6.865 0 0 0.5 0 0 0.8  $     Al (ring inner)
  107       rcc 6.865 0 0 0.5 0 0 1.3  $     Al (ring outer)
  108        px 6.865  $         auxilliary surface
  109        px 7.365  $         auxilliary surface
c                ---------Gas cell---------
  115       rcc -1.985 0 0 3.7 0 0 0.48  $       In
  116       rcc -1.985 0 0 3.7 0 0 0.5  $        Out
  125       rcc -1.985 0 0 0.0005 0 0 0.48  $    Mo
  126       rcc 1.695 0 0 0.02 0 0 0.48  $       Pt
c                --------Foils---------
  117       rcc 6.865 0 0 0.025 0 0 0.65  $      Au
  118       rcc 6.89 0 0 0.05 0 0 0.65  $        Al
  119       rcc 6.94 0 0 0.05 0 0 0.65  $        Ir
  120       rcc 6.99 0 0 0.05 0 0 0.65  $        Ir
  121       rcc 7.04 0 0 0.05 0 0 0.65  $        Al
  122       rcc 7.09 0 0 0.025 0 0 0.65  $       Au
c          -------Extra for cylinder 7--------
  212        px -3.88  $         auxilliary surfaces

c    ------------------- Transformations --------------------
c              ------- °-33.85 for x (Room)--------
*tr1 -50 -1397 -175 -33.85 56.15 90 -123.85 -33.85 90 90 90 0
c              ------- °22.15 for x (Water)---------
*tr2 -131 -322 -175 22.15 112.15 90 -67.85 22.15 90 90 90 0
c            ---- °40.18 ton x (Charged particles)-----
*tr3 -850 -60 -175 40.15 130.15 90 -49.85 40.15 90 90 90 0
c         -- °20 ton x (Charged particles- atomic physics)--
*tr4 -845 -50 -175 10 100 90 -80 10 90 90 90 0
c               ------- °-50 for x (BF3)-------
*tr5 250 200 0 -50 40 90 -140 -50 90 90 90 0
c            ------- °-45 ton z (Quadrupoles)-------
*tr6 300 500 0 -45 90 45 90 0 90 -135 90 -45
```

```
mode  n
c     ------------------Materials----------------------
m1    7014.             -0.78  $        Air
      8016.             -0.21 18000.      -0.01
m2    26056.            -0.74  $        Stainless steel
      28000.            -0.18 24000.      -0.08
m3    22000.          0.39324  $        TiT (Tritium target)
      1003.           0.60676
m4    42000.               -1  $           Mo
m5    41093.               -1  $           Nb
m6    13027.               -1  $           Al
m7    79197.               -1  $           Au
m8    8016.          -0.50086  $       Concrete(with ENDF-VI)
      11023.        -0.017197 12000.        -0.002579
      13027.        -0.046002 14000.        -0.316853
      16000.         -0.00129 19000.        -0.019347
      20000.        -0.083405 26054.        -0.000711
      26056.        -0.011454 26057.        -0.000266
      26058.        -3.6e-005
m9    1001.         -0.111915  $       Water
      8016.         -0.888085
m10   29000.               -1  $       Cu
m11   1001.         -0.148605  $       Paraffin
      6012.         -0.851395
m12   26054.        -0.056988  $       Fe (with ENDF-VI)
      26056.        -0.918697 26057.         -0.02141
      26058.        -0.002905
m13   5010.        -0.0315707  $       BF3
      9019.         -0.840552 5011.        -0.1278773
m14   1001.         -0.143711  $       Polyethylene
      6012.         -0.856289
m15   77000.               -1  $       Ir
m16   72000.               -1  $       Hf
m17   48000.               -1  $       Cd
m18   82000.               -1  $       Pb
m19   1002.                -1  $       Deuterium
m20   78000.               -1  $       Pt
c     ------------------Importances---------------------
imp:n             1 35r                     0  $ 1, 37
c     -------------- Cut for neutrons ------------------
cut:n j 0.00000000001
c     ----------------Source definition------------------
c
[...] sdef card from NeuSDesc
c Gas pressure: 110 kPa
c Gas cell length: 37mm
```

```
c 5000 nm Mo (entrance) foil
c D(d,pn)D, D break-up gas target enabled
c
c     ----------------------Tally-----------------------
f4:n 33 34 35 36 37 38 $       Average neutron flux
e0 0.00000000001 &
c
[...] energy binning from the ENDF/B-VII.1 library
c
c       ---------------History cutoff------------------
nps 1000000000        $       Limiting how long MCNP runs
```

E.2 MCNP5 input for the irradiation at 15.3 MeV (Full room geometry)

```
c       ----------------------Cells-------------------------
c               ------------- Floor --------------
c                     ------Concrete---------
    1     8   -2.35 (-14 -64 -65 -67 ):(-14 -64 66 ):
            (-14 -64 46 -65 68 ):(-14 -64 -69 46 )
    2     1 -0.0014 -14 -64 #1  $               Air
c                     ---Polyethylene---
    3    14   -0.94 -12.2 -12.1 12.6 63 -14
    4    12   -7.86 -12.2 -12.1 -63 64 -14  $   Fe
c                 ----------- Walls --------------
    5     8   -2.35 -19  $            Concrete
    6     8   -2.35 -20 -24 -12  $    Walls-Accelerator angle
    7     8   -2.35 12 -13  $         Walls (without floor)
c                ------------ Water --------------
    8     9      -1 -15 :-16 :-17 :-18
c                      ---Water tanks---
    9    12   -7.86 (-16.2 16.3 17.2 -38 -51 -12.6 ):
           (17.2 38 39 -17.3 -51 -12.6 ):(17.3 39 -42 -40 -12.6
           -51 ):(-18.3 -43 18.1 -18.4 -51 -12.6 ):(44 18.4 -43
           16.1 -51 -12.6 ):(-42 16.1 -44 45 -51 -12.6 ):(45
           -15.3 -16.1 15.1 -51 -12.6 ):(-48 -45 15.1 46 -51
           -12.6 ):(46 15.4 -15.1 47 -51 -12.6 ):(47 15.2 -15.4
           -50 -51 -12.6 ):(-15.2 16.2 -50 15.3 -51 -12.6 ):(50
           -38 16.2 49 -12.6 -51 ):(18.3 -41 42 -43 -51 -12.6 )
           :(16.1 -42 -40 18.3 -51 -12.6 )
c               ----------- Al box -------------
   10     6    -2.7 -26  $          Box behind the source
   11     6    -2.7 -35  $          High voltage behind the wall
```

```
c                ---------- BF3 detector ----------
   12     6    -2.7 -34 61  $       Al wall
   13    13 -0.0028 -62  $          BF3
   14    11   -0.93 62 -61  $       Paraffin
c                -------- Irradiation Lines -------
   15     2      -8 -37  $    Neutrons
   16     2      -8 -36  $    Charged particles
   17     2      -8 -218  $   Charged particles (atomic physics)
c                ------------ Other --------------
   18    12   -7.86 -219  $            Table
   19    11   -0.93 -220 #5 #7  $      Paraffin blocks
   20    10    -8.9 -221 #5 #7  $      Quadrupoles
   21    18 -11.342 -222 #5 #7  $      Pb blocks
c                  ---------Flange--------
   22     6    -2.7 -72  $              Al (cylinder 1)
   23     6    -2.7 -73 74 75 -76  $    Al (ring 4)
   24     6    -2.7 -77 78 79 -75  $    Al (ring 5)
   25     6    -2.7 -80 81 82 -83  $    Al (ring 6)
   26     6    -2.7 -94 95 212 -96  $   Al (ring 7)
   27     6    -2.7 -97 98 99 -100  $   Al (ring 8)
c                 --------Beam pipe-------
   28     2      -8 -101 102 103 -82  $ Stainless steel (ring 9)
c                    -----Vacuum-----
   29     0         -102 :-81 #22 #23 #24 #25 #26 #27 #31 #32
c                   -------Holder-------
   30     6    -2.7 -107 106 -109 108  $  Al
c                  -------Tritium--------
   31    10    -8.9 -115  $              Cu (cylinder 2)
   32     3  -4.506 -116  $              TiT (cylinder 3)
c                 --------Foils---------
   33     6    -2.7 -117  $              AlA
   34     7 -19.282 -118  $              AuB
   35     6    -2.7 -119  $              AlC
   36    16  -13.31 -120  $              Hf4
   37     6    -2.7 -121  $              Al8
   38    15   -22.4 -122  $              Ir4
   39     6    -2.7 -123  $              Al9
   40     5   -8.57 -124  $              Nb2
c              -------Outside world-------
   41     1 -0.0014 -25 #1 #2 #3 #4 #5 #6 #7 #8 #9 #10 #11 #12
                    #13 #14 #15 #16 #17 #18 #19 #20 #21 #22 #23
                    #24 #25 #26 #27 #28 #29 #30 #31 #32 #33 #34
                    #35 #36 #37 #38 #39 #40
   42     0         25  $                Outside World

c     ----------------------Surfaces-----------------------
```

```
   12     1 rpp 0 1768 0 1683 0 667  $          Room (inner)
   13     1 rpp -124 1892 -124 1807 0 717  $   Room (outer)
c              ------------ Floor --------------
   14     1 rpp -50 1818 -50 1733 -80 0
   65       px 300
   66       px 400
   67     2  py -100
   68       px -300
   69       px -400
   63     1  pz -0.2  $                         Polyethylene
   64     1  pz -0.65  $                        Fe
c               ------------ Water --------------
   15     2 rpp 1 301 1 24 0 250
   16     2 rpp 26 326 24 49 0 250
   17     2 rpp 304 326 49 169 0 250
   18     2 rpp 326 352 36 154 0 250
c             ------------ Water tanks --------------
   38     2  py 50
   39     2  px 303
   40     2  py 170
   41     2  py 155
   42     2  px 327
   43     2  px 353
   44     2  py 35
   45     2  py 23
   46     2  py 0
   47     2  px 0
   48     2  px 302
   49     2  px 25
   50     2  py 25
   51     1  pz 251
c                ------------ Other --------------
   19     1 rpp 970 1768 265 345 0 250  $     Wall (right, back)
   20     1 c/z 0 1683 300  $                 Cylinder corner
   24     1  pz 600
   25     1 rpp -200 2000 -200 2000 -100 1000  $ Boundary
   26       rpp -150 -10 -30 30 -174 -15  $Box behind the source
c               ---------- BF3 detector ----------
   34     5 rcc 200 0 0 30 0 0 20  $             Wall (outer)
   61     5 rcc 200 0 0 30 0 0 19.5  $           Wall (inner)
   62     5 rcc 200 0 0 30 0 0 1  $              Gas
c               ------------ Other --------------
   35     1 rpp 1200 1690 80 170 0 170  $  High vol. behind wall
c               -------- Irradiation Lines -------
   36     3 rpp 153 1323 0 30 0 155  $        Charged particles
   37       rpp -687 -150 -15 15 -175 -5.8  $ Neutrons
```

```
  218     4 rpp 153 953 0 30 0 175  $  Charged particles (atom.)
c                ------------ Other --------------
  219       rcc -100 -670 -20 0 0 40 200  $   Table
  220     1 rpp 500 650 1600 1680 0 150  $    Paraffin blocks
  221     6 rpp -50 50 100 270 -50 50  $      Quadrupoles
  222     1 rpp 1700 1768 500 700 0 80  $     Pb blocks
c                  ---------Flange--------
   72       rcc -0.2 0 0 0.2 0 0 4.5  $     Al (cylinder 1)
   73       rcc -0.7 0 0 0.5 0 0 4.5  $     Al (ring 4-outer)
   74       rcc -0.7 0 0 0.5 0 0 1.425  $   Al (ring 4-inner)
   75        px -0.7  $          auxilliary surfaces
   76        px -0.2  $          auxilliary surfaces
   77       rcc -2 0 0 1.3 0 0 4.5  $       Al (ring 5-outer)
   78       rcc -2 0 0 1.3 0 0 2.5  $       Al (ring 5-inner)
   79        px -2  $           auxilliary surfaces
   80       rcc -2.7 0 0 2.7 0 0 5.7  $     Al (ring 6-outer)
   81       rcc -2.7 0 0 2.7 0 0 4.5  $     Al (ring 6-inner)
   82        px -2.7  $          auxilliary surfaces
   83        px 0  $             auxilliary surfaces
c                 ---------Ring--------
   94       rcc -3.88 0 0 0.68 0 0 7.6  $   Al (ring 7-outer)
   95       rcc -3.88 0 0 0.68 0 0 5.7  $   Al (ring 7-inner)
   96        px -3.2  $          auxilliary surfaces
   97       rcc -4.5 0 0 2 0 0 8.1  $       Al (ring 8-outer)
   98       rcc -4.5 0 0 2 0 0 7.6  $       Al (ring 8-inner)
   99        px -4.5  $          auxilliary surfaces
  100        px -2.5  $          auxilliary surfaces
c                 --------Beam pipe-------
  101       rcc -687 0 0 684.3 0 0 5.7  $   Steel (ring 9-outer)
  102       rcc -687 0 0 684.3 0 0 4.985  $ Steel (ring 9-inner)
  103        px -687  $          auxilliary surfaces
c                  -------Holder-------
  106       rcc 2.0 0 0 0.5 0 0 0.8  $      Al (ring inner)
  107       rcc 2.0 0 0 0.5 0 0 1.3  $      Al (ring outer)
  108        px 2.0  $           auxilliary surface
  109        px 2.5  $           auxilliary surface
c                 -------Tritium--------
  115       rcc -0.3 0 0 0.1 0 0 1.425  $   Cu (cylinder 2)
  116       rcc -0.31 0 0 0.01 0 0 1.27  $  TiT (cylinder 3)
c                --------Foils---------
  117       rcc 2.0 0 0 0.055 0 0 0.7175  $          AlA
  118       rcc 2.055 0 0 0.053 0 0 0.711  $         AuB
  119       rcc 2.108 0 0 0.054 0 0 0.7175  $        AlC
  120       rcc 2.162 0 0 0.054 0 0 0.706  $         Hf4
  121       rcc 2.216 0 0 0.06 0 0 0.68  $          Al8
  122       rcc 2.276 0 0 0.034 0 0 0.666  $         Ir4
```

```
  123       rcc 2.31 0 0 0.052 0 0 0.688  $          Al9
  124       rcc 2.362 0 0 0.05 0 0 0.6635  $         Nb2
c            -------Extra for cylinder 7--------
  212        px -3.88  $         auxilliary surfaces

c    ------------------- Transformations --------------------
c             ------- °-33.85 for x (Room)--------
*tr1 -50 -1397 -175 -33.85 56.15 90 -123.85 -33.85 90 90 90 0
c              ------- °22.15 for x (Water)---------
*tr2 -131 -322 -175 22.15 112.15 90 -67.85 22.15 90 90 90 0
c            ---- °40.18 ton x (Charged particles)-----
*tr3 -850 -60 -175 40.15 130.15 90 -49.85 40.15 90 90 90 0
c         -- °20 ton x (Charged particles- atomic physics)--
*tr4 -845 -50 -175 10 100 90 -80 10 90 90 90 0
c               ------- °-50 for x (BF3)-------
*tr5 250 200 0 -50 40 90 -140 -50 90 90 90 0
c            ------- °-45 ton z (Quadrupoles)-------
*tr6 300 500 0 -45 90 45 90 0 90 -135 90 -45
mode  n
c     ------------------Materials-----------------------
m1    7014.             -0.78  $                          Air
      8016.             -0.21 18000.           -0.01
m2    26056.            -0.74  $                          Steel
      28000.            -0.18 24000.           -0.08
m3    22000.          0.39324  $                          TiT
      1003.           0.60676
m5    41093.               -1  $                          Nb
m6    13027.               -1  $                          Al
m7    79197.               -1  $                          Au
m8    8016.          -0.50086  $       Concrete(with ENDF-VI)
      11023.  -0.017197 12000.   -0.002579 13027.    -0.046002
      14000.  -0.316853 16000.    -0.00129 19000.    -0.019347
      20000.  -0.083405 26054.   -0.000711 26056.    -0.011454
      26057.  -0.000266 26058.   -3.6e-005
m9    1001.         -0.111915  $                          Water
      8016.         -0.888085
m10   29000.               -1  $                          Cu
m11   1001.         -0.148605  $                   Paraffin
      6012.         -0.851395
m12   26054.        -0.056988  $            Fe (with ENDF-VI)
      26056.  -0.918697 26057.    -0.02141 26058.    -0.002905
m13   5010.        -0.0315707  $                          BF3
      9019.    -0.840552 5011.  -0.1278773
m14   1001.         -0.143711  $                 Polyethylene
      6012.         -0.856289
m15   77000.               -1  $                          Ir
```

```
213 m16   72000.              -1  $                          Hf
214 m17   48000.              -1  $                          Cd
215 m18   82000.              -1  $                          Pb
216 c     ------------------Importances--------------------
217 imp:n             1 40r                    0  $ 1, 42
218 c     -------------- Cut for neutrons ------------------
219 cut:n j 0.00000000001
220 c     ----------------Source definition------------------
221 c
222 [...] sdef card from NeuSDesc
223 c
224 c     ----------------------Tally-----------------------
225 f4:n 33 34 35 36 37 38 39 40 $       Average neutron flux
226 e0 0.00000000001 &
227 0.0000000000110304 &
228 c
229 [...] energy binning from the ENDF/B-VII.1 library
230 c
231 c       ---------------History cutoff-----------------
232 nps 1000000000        $       Limiting how long MCNP runs
```

In the description of the complex materials, the spaces between the numbers do not correspond to the real input file. Some spaces have been erased for better presentation of the numbers.

Concerning the energy binning, the bins from the ENDF/B-VII.1 library [28] for the ^{197}Au(n,γ)^{198}Au and ^{191}Ir(n,γ)^{192}Ir reactions have been merged in order to create a binning which covers the resonance region for both reactions.

Bibliography

[1] P. Talou, T. Kawano, P. G. Young, M. B. Chadwick, and R. E. MacFarlane, "Improved Evaluations of Neutron-Induced Reactions on Americium Isotopes," *Nuclear Science and Engineering*, vol. 155, no. 1, pp. 84–95, 2007.

[2] A. Fessler, A. J. M. Plompen, D. L. Smith, J. W. Meadows, and Y. Ikeda, "Neutron Activation Cross-Section Measurements from 16 to 20 MeV for isotopes of F, Na, Mg, Al, Si, P, Cl, Ti, V, Mn, Fe, Nb, Sn, and Ba," *Nuclear Science and Engineering*, vol. 134, no. 2, pp. 171–200, 2000.

[3] J. Chadwick, "Possible existence of a neutron," *Nature*, vol. 129, p. 312, 1932.

[4] S. Pomp, "Tutorial on Neutron Physics in Dosimetry," *Uppsala University*.

[5] J. A. B. Gibson and E. Piesch, *Neutron Monitoring for Radiological Protection*. Technical Reports Series No. 252, National Atomic Energy Agency, Vienna, 1985.

[6] S. Kopecky, F. Emiliani, K. Kauwenberghs, C. Lampoudis, C. Massimi, P. Schillebeeckx, I. Sirakov, and K. Volev, "Evaluation of neutron induced reaction cross sections in the resolved and unresolved resonance region at EC - JRC - IRMM," *EPJ Web of Conferences*, vol. 42, p. 02001, 2013.

[7] L. R. Greenwood and A. L. Nichols, "Review of the Requirements to Improve and Extend the IRDF Library, International Reactor Dosimetry File (IRDF-2002), IAEA," vol. INDC(NDS)-0507, 01 2007.

[8] M. Chadwick, S. Frankle, H. Trellue, P. Talou, T. Kawano, P. Young, R. MacFarlane, and C. Wilkerson, "Evaluated Iridium, Yttrium, and Thulium Cross Sections and Integral Validation Against Critical Assembly and Bethe Sphere Measurements," *Nuclear Data Sheets*, vol. 108, no. 12, pp. 2716 – 2741, 2007. Special Issue on Evaluations of Neutron Cross Sections.

[9] "EXFOR." http://www.nndc.bnl.gov/exfor/exfor.htm.

[10] http://nuclearphysics.ntua.gr/home.php, Group of Nuclear Physics NTUA, Copyright ©2017.

[11] N. Patronis, C. T. Papadopoulos, S. Galanopoulos, M. Kokkoris, G. Perdikakis, R. Vlastou, A. Lagoyannis, and S. Harissopulos, "Activation cross section and isomeric cross-section ratio for the (n,2n) reaction on ^{191}Ir," *Physical Review C, Nuclear Physics*, vol. 75, p. 034607, 2007.

[12] A. Tsinganis, M. Diakaki, M. Kokkoris, A. Lagoyannis, E. Mara, C. T. Papadopoulos, and R. Vlastou, "Isomeric cross section of the $^{197}\mathrm{Au}(n, 2n)$ reaction," *Phys. Rev. C*, vol. 83, p. 024609, Feb 2011.

[13] H. A. Tewes, A. A. Caretto, A. E. Miller, and D. R. Nethaway, "Excitation functions of neutron-induced reactions," *Lawrence Rad. Lab. (Berkeley and Livermore*, vol. 6028, 1960.

[14] S. K. Ghorai, K. Hayworth, J. Williams, and W. L. Alford, "Isomeric yield ratios and isomeric cross sections for the ^{197}Au(n,2n) reaction," *Bulletin of the American Physical Society*, vol. 29, p. 1117, 1984.

[15] Y. Uno, S. Meigo, S. Chiba, T. Fukahori, Y. Kasugai, O. Iwamoto, P. Siegler, and Y. Ikeda, "Measurements of activation cross sections for the neutron dosimetry at an energy range from 17.5 to 30 MeV by using the ^{7}Li(p,n) quasi-mono-energetic neutron source," *Proceedings of the 9th International Symposium on Reactor Dosimetry, Prague, Czech Republic*, 1996. (World Scientific, Singapore, 1996).

[16] R. J. Prestwood and B. P. Bayhurst, "(n, 2n) Excitation Functions of Several Nuclei from 12.0 to 19.8 MeV," *Phys. Rev.*, vol. 121, pp. 1438–1441, Mar 1961.

[17] M. Majerle, P. Bém, J. Novák, E. Šimečková, and M. Štefánik, "Au, Bi, Co and Nb cross-section measured by quasimonoenergetic neutrons from p + ^{7}Li reaction in the energy range of 18{36 MeV," *Nuclear Physics A*, vol. 953, pp. 139 – 157, 2016.

[18] B. P. Bayhurst, J. S. Gilmore, R. J. Prestwood, J. B. Wilhelmy, N. Jarmie, B. H. Erkkila, and R. A. Hardekopf, "Cross sections for (n, xn) reactions between 7.5 and 28 MeV," *Phys. Rev. C*, vol. 12, pp. 451–467, Aug 1975.

[19] A. A. Filatenkov, "Neutron activation cross sections measured at KRI in neutron energy region 13.4 - 14.9 MeV," 2016. INDC(CCP)-0460 Rev.

[20] J. K. Temperley and D. E. Barnes, "Neutron Activation Cross Sections for Some Isotopes of Ruthenium, Palladium, Indium, Tin, and Iridium," Tech. Rep. 1491, 1970. Ballistic Research Labs Reports.

[21] M. Herman, A. Marcinkowski, and K. Stankiewicz, "Statistical Multi-step Compound Emission in (n,2n) Reactions," *Nuclear Physics, Section A*, vol. 430, p. 69, 1984.

[22] Z. Feng, K. Xiang-Zhong, P. Zhong-Sheng, and Z. Xue-Bin, "Measurement of cross sections for 185-Re(n,2n)184g,m-Re and 191-Ir(n,2n)190-Ir reactions by 14 MeV neutrons," *High Energy Physics and Nucl.Physics,Chinese ed.*, vol. 26, no. 7, p. 678, 2002.

[23] M. Bormann, H. H. Bissem, E. Magiera, and R. Warnemunde, "Total Cross Sections and Isomeric Cross-Section Ratios for (n,2n) Reactions in the Energy Region 12-18 MeV," *Nuclear Physics, Section A*, vol. 157, p. 481, 1970.

[24] C. Konno, Y. Ikeda, K. Oishi, K. Kawade, H. Yamamoto, and H. Maekawa, "Activation Cross section measurements at neutron energy from 13.3 to 14.9 MeV," Tech. Rep. 1329, 1993. JAERI Reports.

[25] A. A. Druzhinin, N. I. Ivanova, and A. A. Lbov, "The (n,2n) Reaction Cross Sections for Tu, Ir, Tl and Pb Isotopes at 14.8 MeV Neutron Energy," *Yadernaya Fizika*, vol. 14, no. 4, p. 682, 1971.

[26] http://tandem.inp.demokritos.gr/, TANDEM Accelerator Laboratory, Institute of Nuclear Physics, NCSR "Demokritos".

[27] P. Reimer, "Fast neutron induced reactions leading to activation products: selected cases relevant to development of low activation materials, transmutation and hazard assessment of nuclear wastes," 2002.

[28] ENDF, "https://www-nds.iaea.org/exfor/endf.htm."

[29] M. Drosg, "Monoenergetic neutron production by two-body reactions in the energy range from 0.0001 to 500 MeV." Institute of Experimental Physics, University of Vienna, A-1090 Wien, AUSTRIA.

[30] V. Michalopoulou *et al.*, "Measurements of the ^{234}U and ^{234}U cross-sections between 15 and 20 MeV with MicroMegas detectors," in *HNPS: Advances in Nuclear Physics, Proceedings of the 26th Hellenic Conference on Nuclear Physics*, pp. 239–243, Hellenic Nuclear Physics Society, 2017.

[31] NNDC Q-value calculator, https://www.nndc.bnl.gov/qcalc/.

[32] G. Perdikakis, *Study of neutron induced reactions (n,2n) on nuclei in the region of Actinides*. PhD thesis, National Technical University of Athens, 2006.

[33] A. Kalamara, "Implementation of the ^{3}H(d,n)^{4}He reaction for the production of a high energy neutron beam at 17.5 MeV to study the ^{241}Am(n,2n)^{240}Am reaction," 2013. Master thesis, National Technical University of Athens.

[34] E. Birgersson and G. Loevestam, "NeuSDesc-Neutron Source Description Software Manual," 2009. JRC Scientific and Technical Reports.

[35] F. Brown *et al. Trans. Am. Nucl. Soc.*, vol. 87, p. 273, 2002.

[36] X-5 Monte Carlo team, *MCNP-A General Monte Carlo N-ParticleTransport Code, version 5*, April 2003. LA-UR-03-1987, LA-CP-03-0245 and LA-CP-03-0284.

[37] R. B. Firestone and C. M. Baglin, *Table of Isotopes*. New York: John Wiley and Sons, 8^{th} edition ed., 1999.

[38] M. Majerle, M. Stefanik, J. Kamenik, E. Simeckova, D. Venosa, A. Kalamara, and R. Vlastou, "The intensities of γ-rays from the decay of ^{196m2}Au," *Applied Radiation and Isotopes*, 2018. https://doi.org/10.1016/j.apradiso.2018.07.026.

[39] "https://www.nndc.bnl.gov/," tech. rep.

[40] M. Herman, R. Capote, B. Carlson, P. Oblozinsky, M. Sin, A. Trkov, H. Wienke, and V. Zerkin, "Empire: Nuclear Reaction Model Code System for Data Evaluation," *Nuclear Data Sheets*, vol. 108, no. 12, pp. 2655 – 2715, 2007. Special Issue on Evaluations of Neutron Cross Sections.

[41] tech. rep. https://www-nds.iaea.org/index-meeting-crp/EmpireWorkshop2013/downloadEmpire322win.htm.

[42] A. Koning, S. Hilaire, and S. Goriely, "TALYS-1.8," tech. rep., 2015.

[43] tech. rep. http://www.talys.eu/download-talys/.

[44] W. Hauser and H. Feshbach, "The Inelastic Scattering of Neutrons," *Phys. Rev.*, vol. 87, pp. 366–373, Jul 1952.

[45] A. D. Arrigo, G. Giardina, M.Herman, A. Ignatyuk, and A. Taccone *J. Phys.*, vol. G20, p. 305, 1994.

[46] R. Capote and et. al., "https://www-nds.iaea.org/ripl-3/," 2009.

[47] A. Koning and J. Delaroche, "Local and global nucleon optical models from 1 kev to 200 mev," *Nuclear Physics A*, vol. 713, no. 3, pp. 231 – 310, 2003.

[48] V. Avrigeanu, P. E. Hodgson, and M. Avrigeanu, "Global optical potentials for emitted alpha particles," *Phys. Rev. C*, vol. 49, pp. 2136–2141, Apr 1994.

[49] D. Wilmore and P. Hodgson, "The calculation of neutron cross-sections from optical potentials," *Nuclear Physics*, vol. 55, no. Supplement C, pp. 673 – 694, 1964.

[50] J. J. Griffin, "Statistical Model of Intermediate Structure," *Phys. Rev. Lett.*, vol. 17, pp. 478–481, Aug 1966.

[51] J. Griffin, "Energy dependence of average direct reaction cross sections and partial nuclear level densities," *Physics Letters B*, vol. 24, no. 1, pp. 5 – 7, 1967.

[52] M. Herman, R. Capote, B. Carlson, P. Oblozinsky, M. Sin, A. Trkov, H. Wienke, and V. Zerkin, "Empire: Nuclear reaction model code system for data evaluation," *Nuclear Data Sheets*, vol. 108, no. 12, pp. 2655 – 2715, 2007. Special Issue on Evaluations of Neutron Cross Sections.

[53] J. Raynal Tech. Rep. SMR-9/8, IAEA (unpublished).

[54] J. Raynal, "Computing as a language of physics," *IAEA, ICTP International Seminar Course*, 1972.

[55] T. Belgya and *et. al.*, "IAEA-TECDOC-1506," 2006. https://www-nds.iaea.org/RIPL-2/.

[56] V. Avrigeanu, M. Avrigeanu, and C. Mănăilescu, "Further explorations of the α-particle optical model potential at low energies for the mass range $a \approx 45$ffl209," *Phys. Rev. C*, vol. 90, p. 044612, Oct 2014.

[57] N. Dzysiuk and A. Koning, "Improving activation cross section data with talys," vol. 146, p. 02047, 01 2017.

[58] T. Tamura, "Analyses of the scattering of nuclear particles by collective nuclei in terms of the coupled-channel calculation," *Rev. Mod. Phys.*, vol. 37, pp. 679–708, Oct 1965.

[59] S. M. Qaim, "Activation Cross Sections, Isomeric Cross-Section Ratios and Systematics of (n,2n) Reactions at 14-15 MeV," *Nucl. Phys. A*, vol. 185, p. 614, 1972.

[60] G. Li *et al.*, "Cross section measurements for (n,3n) reactions induced by 14.8 MeV neutrons," *Applied Radiation and Isotopes*, vol. 56, pp. 731–733, 2002.

[61] "https://www-nds.iaea.org/index-meeting-crp/EmpireWorkshop2013/docs/empire-3.2.pdf," tech.
rep.

[62] A. Kalamara, R. Vlastou, M. Kokkoris, N. G. Nicolis, N. Patronis, M. Serris, V. Michalopoulou, A. Stamatopoulos, A. Lagoyannis, and S. Harissopulos, "$^{197}\mathrm{Au}(n,2n)$ reaction cross section in the 15–21 mev energy range," *Phys. Rev. C*, vol. 97, p. 034615, Mar 2018.

[63] A. Kalamara, R. Vlastou, M. Kokkoris, S. Chasapoglou, A. Stamatopoulos, N. Patronis, M. Serris, A. Lagoyannis, and S. Harissopulos, "$^{191}\mathrm{Ir}(n,2n)$ and $^{191}\mathrm{Ir}(n,3n)$ reaction cross sections in the 15–21 mev energy range," *Phys. Rev. C*, vol. 98, p. 034607, Sep 2018.

[64] Y. D. Lee and Y. O. Lee, "Neutron Induced Cross Section Data for Ir-191 and Ir-193," *Nuclear Engineering and Technology*, vol. 38, pp. 803–808, 2006. No. 8.

[65] P. Talou, M. Chadwick, R. Nelson, N. Fotiades, M. Devlin, P. Garrett, W. Younes, and J. Becker, "Determination of partial (n, xngamma) cross-sections in 193-Ir," 01 2003.

[66] "AGATA|Advanced GAmma Tracking Array," *Nuclear Instruments and Methods in Physics Research Section A: Accelerators, Spectrometers, Detectors and Associated Equipment*, vol. 668, pp. 26 – 58, 2012. AGATA Collaboration.

[67] "IAEA CRP on Testing and Improving the International Reactor Dosimetry and Fusion File (IRDFF),"

[68] S. Simakov *et al.*, "Proposals for new measurements for IRDFF community and HPRL," September 2017.

[69] E. B. Paul and R. L. Clarke, "Cross-section measurements of reactions induced by neutrons of 14.5 MeV energy," *Canadian Journal of Physics*, vol. 31, pp. 267 – 277, 1953.

[70] V. J. Ashby, H. C. Catron, L. L. Newkirk, and C. J. Taylor, "Absolute Measurement of $(n,2n)$ Cross Sections at 14.1 MeV," *Phys. Rev.*, vol. 111, pp. 616–621, Jul 1958.

[71] W. Dilg, H. Vonach, G. Winkler, and P. Hille, "Messung von (n, 2n) wirkungsquerschnitten an schweren kernen," *Nuclear Physics A*, vol. 118, no. 1, pp. 9 – 16, 1968.

[72] D. S. Mather *et al.*, "Measurement of (n,2n) Cross Sections for Incident Energies between 6 and 14 MeV," 1972. AWRE Report No. 072/72.

[73] D. Nethaway, "Cross sections for several (n, 2n) reactions at 14 MeV," *Nuclear Physics A*, vol. 190, no. 3, pp. 635 – 644, 1972.

[74] A. Hankla, R. Fink, and J. Hamilton, "Neutron activation cross sections at 14.4 MeV For some naturally occurring heavy elements in the region $76 \leq z \leq 82$," *Nuclear Physics A*, vol. 180, no. 1, pp. 157 – 176, 1972.

[75] G. N. Maslov, F. Nasyrov, and N. F. Pashkin, "Experimental cross-sections for nuclear reactions involving neutrons with energies of about 14 MeV," *Yad. Konstanty*, vol. 9, p. 50, 1972.

[76] A. Paulsen, H. Liskien, and R. Widera, "Cross-sections of (n,2n) reactions for Ti 46, Zn 66, In 115 and Au 197," *Atomkernenergie*, vol. 26 (1), pp. 34–36, 1975.

[77] L. R. Veeser, E. D. Arthur, and P. G. Young, "Cross sections for $(n, 2n)$ and $(n, 3n)$ reactions above 14 MeV," *Phys. Rev. C*, vol. 16, pp. 1792–1802, Nov 1977.

[78] P. Andersson, S. Lundberg, and G. Magnusson, "Absolute measurements of some neutron activation cross sections in ^{27}Al, ^{115}In and ^{197}Au at 14.9 MeV," 1978.

[79] J. Frehaut, A. Bertin, R. Bois, J. Jary, and G. Mosinski, "Status of (n,2n) cross section measurements at Bruyeres-le-Chatel," 1980. (DOE/NDC–21/L(Vol1)). Pearlstein, S. (Ed.). United States.

[80] T. B. Ryves and P. Kolkowski, "The Au(n,2n) and Au(n,γ) cross sections at 14 MeV," *Journal of Physics G: Nuclear Physics*, vol. 7, no. 1, p. 115, 1981.

[81] J. Csikai, "Study of Excitation Functions Around 14 MeV Neutron Energy," *Nuclear Data for Science and Technology*, p. 414, 1983. Springer, Dordrecht.

[82] S. Daroczy, P. Raics, Z. Papp, I. Futo, J. Csikai, N. V. Kornilov, O. A. Salnikov, V. Y. Baryba, A. V. Balickij, and A. P. Rudenko, "Cross sections of the reactions Ni-58(n,p),Nb-93(n,2n) and Au-197(n,2n) between 7 and 9.9 MeV neutron energies," *Proc. of Conf. on Neutron Physics, Kiev*, vol. 191, 1983.

[83] I. Garlea, C. Miron, D. Dobrea, C. Roth, T. Musat, and H. N. Rosu, "Measurements of integral cross sections at 14 MeV for the following reactions: ^{115}In(n,n'), ^{197}Au(n,2n), ^{93}Nb(n,2n), ^{27}Al(n,α), ^{56}Fe(n,p), ^{235}U(n,f), ^{239}Pu(n,f), ^{237}Np(n,f), ^{238}U(n,f) and ^{232}Th(n,f)," Jan 1983. International Atomic Energy Agency, Vienna, Austria.

[84] Y. Ikeda, H. Miyade, K. Kawade, and H. Yamamoto, "Measurement of high threshold reaction cross sections for 13.5 to 15 MeV." Private communication, 1984.

[85] L. R. Greenwood, "Recent research in neutron dosimetry and damage analysis for materials irradiations," Conference Report 956, 1987. American Soc. of Testing and Materials Reports.

[86] I. Kimura and K. Kobayashi, "Calibrated Fission and Fusion Neutron Fields at the Kyoto University Reactor," *Nuclear Science and Engineering*, vol. 106, no. 3, pp. 332–344, 1990.

[87] I. Garlea, C. Miron-Garlea, H. N. Rosu, G. Fodor, and V. Raducu, "Integral Neutron Cross Sections Measured Around 14 MeV," *Rev. Roum. Phys.*, vol. 37, p. 19, 1992.

[88] Y. Uwamino, H. Sugita, Y. Kondo, and T. Nakamura, "Measurement of Neutron Activation Cross Sections of Energy Up to 40 MeV Using Semimonenergetic p-Be Neutrons," *Nucl. Sci. Eng.*, vol. 111, p. 391, 1992.

[89] M. Belgaid, M. Siad, and M. Allab, "Measurement of 14.7 MeV neutron cross sections for several isotopes," *Journal of Radioanalytical and Nuclear Chemistry Letters*, vol. 166, p. 493, 1992.

[90] S. Iwasaki, S. Matsuyama, T. Ohkubo, H. Fukuda, M. Sakuma, and M. Kitamura, "Measurement of activation cross-sections for several elements between 12 and 20 MeV," *JAERI-Conf, 95-008*, 1994.

[91] C. Zhu, Y. Chen, Y. Mou, P. Zheng, T. He, W. Xinhua, L. An, and H. Guo, "Measurements of (n, 2n) Reaction Cross Sections at 14 MeV for Several Nuclei," *Nuclear Science and Engineering*, vol. 169, no. 2, pp. 188–197, 2011.

[92] J. Vrzalova, O. Svoboda, A. Krasa, A. Kugler, M. Majerle, M. Suchopar, and V. Wagner, "Studies of (n,xn) cross-sections in Al, Au, Bi, Cu, Fe, I, In, Mg, Ni, Ta, Y, and Zn by the activation method," *Nuclear Instruments and Methods in Physics Research Section A: Accelerators, Spectrometers, Detectors and Associated Equipment*, vol. 726, pp. 84 – 90, 2013.

[93] "NNDC,AME:the Atomic Mass Evaluation." File: mass16.txt.

[94] M. Majerle *Private Communication*, 2017.

[95] S. Cowell *et al.*, "Evaluation of iridium (n,xn) reactions," *International Conference on Nuclear Data for Science and Technology*, 2007.

[96] P. E. Garrett *et al.*, "Long-lived isomers in 190Ir," *Nuclear Physics A*, vol. 11, pp. 68–84, 1996.

[97] https://ojs.ujf.cas.cz/∼wagner/transmutace/studentpraxe/stevenreferat.pdf, S. Peetermans, Neutron Activation Analysis, 2009.

[98] M. D. Glascock, "An Overview of Neutron Activation Analysis," 2004.

[99] M. Majerle, "Experimental studies and simulations of spallation neutron induced production on a thick lead target," in *Journal of Physics*, vol. 41 of *Conference Series*, pp. 331–339, 2006.

[100] https://nmi3.eu/neutron-research/techniques-for-/chemical-analysis.html.

[101] http://chiayolin.org/physics_mccc/.

[102] SODERN, https://www.sodern.com/website/en/ref/home.html.

[103] J. Ziegler and J. Biersack, "SRIM-2008." http://www.srim.org.

[104] C. Kalfas, M. Axiotis, and C. Tsabaris, "SPECTRW: A software package for nuclear and atomic spectroscopy," *Nuclear Instruments and Methods in Physics Research Section A: Accelerators, Spectrometers, Detectors and Associated Equipment*, vol. 830, no. C, pp. 265–274, 2016.

[105] W. Mannhart, "A Small Guide to Generating Covariances of Experimental Data," 2013. https://www-nds.iaea.org/publications/indc/indc-nds-0588r.pdf.

[106] N. Otuka *et al.*, "Uncertainty propagation in activation cross section measurements," *Radiation Physics and Chemistry*, vol. 140, pp. 502–510, 2017.

[107] V. Paneta, "Simulation of the neutron production experimental setup of the NCSR "Demokritos" by means of the MCNP code," 2009. Master thesis, National Technical University of Athens.

[108] N. Bohr, "Neutron Capture and Nuclear Constitution," *Nature*, vol. 137, p. 344, Feb 1936.

[109] A. Cole, *Statistical Models for Nuclear Decay: From Evaporation to Vaporization*. Series in Fundamental and Applied Nuclear Physics, CRC Press, 2000.

[110] J. M. Blatt and V. F. Weisskopf, *Theoretical Nuclear Physics*. Springer-Verlag New York, 1979.

[111] V. Weisskopf, "Statistics and Nuclear Reactions," *Phys. Rev.*, vol. 52, pp. 295–303, Aug 1937.

[112] V. F. Weisskopf and D. H. Ewing, "On the Yield of Nuclear Reactions with Heavy Elements," *Phys. Rev.*, vol. 57, pp. 472–485, Mar 1940.

[113] S. Fernbach, R. Serber, and T. B. Taylor, "The Scattering of High Energy Neutrons by Nuclei," *Phys. Rev.*, vol. 75, pp. 1352–1355, May 1949.

[114] S. N. Ghoshal, "An Experimental Verification of the Theory of Compound Nucleus," *Phys. Rev.*, vol. 80, pp. 939–942, Dec 1950.

[115] S. T. Butler, "Stripping and the Nuclear Shell Model," *Phys. Rev.*, vol. 88, pp. 685–685, Nov 1952.

[116] H. A. Bethe and S. T. Butler, "A Proposed Test of the Nuclear Shell Model," *Phys. Rev.*, vol. 85, pp. 1045–1046, Mar 1952.

[117] H. Feshbach, C. E. Porter, and V. F. Weisskopf, "Model for Nuclear Reactions with Neutrons," *Phys. Rev.*, vol. 96, pp. 448–464, Oct 1954.

[118] C. Cline and M. Blann, "The pre-equilibrium statistical model: Description of the nuclear equilibration process and parameterization of the model," *Nuclear Physics A*, vol. 172, no. 2, pp. 225 – 259, 1971.

[119] M. Blann, "Preequilibrium Decay," *Annual Review of Nuclear Science*, vol. 25, no. 1, pp. 123–166, 1975.

[120] G. D. Harp, J. M. Miller, and B. J. Berne, "Attainment of Statistical Equilibrium in Excited Nuclei," *Phys. Rev.*, vol. 165, pp. 1166–1169, Jan 1968.

[121] E. Fabrici, E. Gadioli, E. Gadioli Erba, M. Galmarini, F. Fabbri, and G. Reffo, "Importance of nucleon-nucleon interactions in hardening nucleon spectra in heavy ion fusion," *Phys. Rev. C*, vol. 40, pp. 2548–2557, Dec 1989.

[122] D. Glas and U. Mosel, "On the critical distance in fusion reactions," *Nuclear Physics A*, vol. 237, no. 3, pp. 429 – 440, 1975.

[123] A. J. Koning and J. M. Akkermans, "Pre-equilibrium nuclear reactions: An introduction to classical and quantum-mechanical models," 1998.

[124] K. S. Krane, *Introductory Nuclear Physics*. Wiley, 1988.

[125] A. Tsinganis, "Experimental and Theoretical Study of the isomeric state production for ^{197}Au(n,2n) reaction," 2012. Master thesis, National Technical University of Athens.

[126] A. Kamal, *Nuclear Physics*. Murphy, TX, USA: Springer, 2014.

[127] E. Gadioli and P. E. Hodgson, *Pre-equilibrium nuclear reactions*, vol. 15. Oxford, New York: Clarendon Press, 8^{th} edition ed., 1992.

[128] P. E. Hodgson, G. M. Field, H. Gruppelaar, and P. Nagel, "Pre-equilibrium processes in nuclear reactions," *Radiation Effects*, vol. 95, pp. 1–4, 27–46, 1986.

[129] H. Feshbach, A. Kerman, and S. Koonin, "The statistical theory of multi-step compound and direct reactions," *Annals of Physics*, vol. 125, no. 2, pp. 429 – 476, 1980.

[130] B. V. Carlson, "Elastic scattering and the optical model," 2010.

[131] A. Koning and D. Rochman, "Modern Nuclear Data Evaluation with the TALYS Code System," *Nuclear Data Sheets*, vol. 113, no. 12, pp. 2841 – 2934, 2012. Special Issue on Nuclear Reaction Data.

[132] M. Diakaki, "Theoretical study of ^{197}Au(n,2n) reaction using the STAPRE-F code," 2011. Master thesis, National Technical University of Athens.

[133] C. Cline, "The pauli exclusion principle in pre-equilibrium decay," *Nuclear Physics A*, vol. 195, no. 2, pp. 353 – 360, 1972.

[134] F. Williams, "Intermediate state transition rates in the Griffin model," *Physics Letters B*, vol. 31, no. 4, pp. 184 – 186, 1970.

[135] H. A. Bethe, "Nuclear Physics B. Nuclear Dynamics, Theoretical," *Rev. Mod. Phys.*, vol. 9, pp. 69–244, Apr 1937.

[136] A. Koning, S. Hilaire, and S. Goriely, "Global and local level density models," *Nuclear Physics A*, vol. 810, no. 1, pp. 13 – 76, 2008.

[137] A. V. Ignatyuk, G. N. Smirenkin, and A. S. Tishin *Sov. J. Nucl. Phys.*, vol. 21, p. 255, 1975.

[138] A. V. Ignatyuk, K. K. Istekov, and G. N. Smirenkin *Sov. J. Nucl. Phys.*, vol. 29, p. 450, 1979.

[139] A. V. Ignatyuk, J. L. Weil, S. Raman, and S. Kahane, "Density of discrete levels in ^{116}Sn," *Phys. Rev. C*, vol. 47, pp. 1504–1513, Apr 1993.

[140] J. Bardeen, L. N. Cooper, and J. R. Schrieffer, "Microscopic Theory of Superconductivity," *Phys. Rev.*, vol. 106, pp. 162–164, Apr 1957.

[141] M. Avrigeanu, V. Avrigeanu, M. Diakaki, and R. Vlastou, "Isomeric cross sections of fast-neutron-induced reactions on ^{197}au," *Phys. Rev. C*, vol. 85, p. 044618, Apr 2012.

[142] H. Hofmann, J. Richert, J. Tepel, and H. Weidenmuller, "Direct reactions and hauser-feshbach theory," *Annals of Physics*, vol. 90, no. 2, pp. 403 – 437, 1975.

[143] V. A. Plujko, "A new closed-form thermodynamic approach for radiative strength functions," *Acta Physica Polonica B*, vol. 31, no. 2, pp. 435 – 441, 2000.

[144] R. C. Harper and W. L. Alford, "Experimental and theoretical neutron cross sections at 14 mev," *Journal of Physics G: Nuclear Physics*, vol. 8, no. 1, p. 153, 1982.

[145] J. P. Delaroche *Proceedings of an International Conference on Neutron Physics and Nuclear Data for Reactors and Other Applied Purposes*, p. 1232, 1978.

[146] O. Bersillon and N. Cindro *Proceedings of 5th International Symposium on the Interactions of Fast Neutrons with Nuclei, Gaussig (GDR)*, p. p.234, November 1975.

[147] A. Koning and J. Delaroche, "Local and global nucleon optical models from 1 kev to 200 mev," *Nuclear Physics A*, vol. 713, no. 3, pp. 231 – 310, 2003.

[148] E. Soukhovitskii and R. Capote, "Ripl { reference input parameter library for calculation of nuclear reactions and nuclear data evaluations," *Nuclear Data Sheets*, vol. 110, no. 12, pp. 3107 – 3214, 2009. Special Issue on Nuclear Reaction Data.

[149] A. Koning and J. Delaroche, "Local and global nucleon optical models from 1 kev to 200 mev," *Nuclear Physics A*, vol. 713, no. 3, pp. 231 – 310, 2003. (Global potential).

[150] B. Morillon and P. Romain, "Dispersive and global spherical optical model with a local energy approximation for the scattering of neutrons by nuclei from 1 keV to 200 MeV," *Phys. Rev. C*, vol. 70, p. 014601, Jul 2004.

[151] B. Morillon and P. Romain, "Bound single-particle states and scattering of nucleons on spherical nuclei with a global optical model," *Phys. Rev. C*, vol. 76, p. 044601, Oct 2007.

[152] F. D. Becchetti, J. Greenlees, and G. W. Greenlees, "Nucleon-nucleus optical-model parameters, a>40, e<50 mev," *Phys. Rev.*, vol. 182, p. 1190, 1969.

[153] J. C. Ferrer, J. D. Carlson, and J.Rapaport, "Neutron elastic scattering at 11 mev and the isospin dependence of the neutron-nucleus optical potential," *Nucl. Phys. A*, vol. 275, p. 325, 1977.

[154] P. A. Moldauer, "Optical model of low energy neutron interactions with spherical nuclei," *Nucl. Phys.*, vol. 47, p. 65, 1963.

[155] C. A. Engelbrecht and H. Fiedeldey, "Nonlocal potentials and the energy dependence of the optical model for neutrons," *Ann. Phys.*, vol. 42, pp. 262–295, 1967.

[156] D. G. Madland, "Nucleon nucleus optical model up to 200 mev," *OECD/NEA Proceedings of a Specialist Meeting*, p. 129, 1997. Paris.

[157] R. Macklin and P. G. Young, "Neutron capture cross sections of rhenium from 3 to 1900 keV," *Nucl. Sci. Eng.*, vol. 97, p. 239, 1987.

[158] R. L. Varner *et al.*, "A global nucleon optical model potential," *Phys. Rep.*, vol. 201, p. 57, 1991.

[159] R. L. Walter and P. P. Guss, "A global optical model for neutron scattering for a $>$ 53 and 10 MeV $<$ e $<$ 80 MeV," *Rad. Effects*, vol. 95, p. 73, 1986. [1985 Santa Fe Conf. Proc.].

[160] G. Satchler, *Direct nuclear reactions*. International series of monographs on physics, Clarendon Press, 1983.